

# **Studies on the Initiation, Propagation, and Extinction of Premixed Flames**

**Zheng Chen**

A DISSERTATION PRESENTED TO THE FACULTY OF  
PRINCETON UNIVERSITY  
IN CANDIDACY FOR THE DEGREE OF  
DOCTOR OF PHILOSOPHY

RECOMMENDED FOR ACCEPTANCE  
BY THE DEPARTMENT OF  
MECHANICAL AND AEROSPACE ENGINEERING

Advisor: Yiguang Ju

January, 2009

To My Parents and Advisors

© Copyright by Zheng Chen, 2009.

All rights reserved.

## **Abstract**

Premixed flames are widely utilized in spark ignition engines for automobiles and in advanced gas turbine engine systems for power generation. In the present study, the fundamental properties of premixed flames such as initiation, propagation, and extinction are systematically investigated using asymptotic theoretical analysis, detailed numerical simulations, and/or experimental measurements.

A general theory on spherical flame initiation and propagation and an accurate numerical algorithm for adaptive simulation of unsteady reactive flow are first developed. The general theory describes different flame regimes and transitions among them. This could be utilized to study effects of radiative heat loss, ignition power, and preferential diffusion on spherical flame initiation, propagation, and extinction. The numerical solver is thoroughly tested and validated. It is shown to be able to accurately and efficiently model propagating flames with detailed chemical mechanisms.

With the help of the general theory and the numerical solver, the controlling factor for spherical flame initiation and how it relates to the minimum ignition energy are then investigated. It is found that there exists a critical flame radius controlling the spherical flame initiation and that the minimum ignition energy is proportional to the cube of the critical flame radius. Moreover, results show that the preferential diffusion between heat and mass (Lewis number) plays an important role in the spherical flame initiation. Both the critical flame radius and the minimum ignition energy are found to increase with the Lewis number.

The general theory and the numerical solver are also employed to study the accuracy of laminar flame speed measurements utilizing propagating spherical flames.

Different effects such as ignition, unsteadiness, compression, and stretch are found to decrease the accuracy of these measurements. New flame speed determination methods to obtain more accurate flame speeds by correcting for these effects are developed. For example, both the Compression-Corrected Flame Speed (CCFS) and the Stretch-Corrected Flame Speed (SCFS) are demonstrated not only to significantly improve the accuracy of the flame speed measurements but also to greatly extend the parameter range of experimental conditions.

The effects of radiation on flame propagation, extinction, and flammability limits are also investigated. Opposite trends for the change of flame propagation speed and flame extinction/flammability limits are found for the outwardly and inwardly propagating spherical flames. A functional expression for the Markstein length is found in terms of the Lewis number and the radiative heat loss. Moreover, the spectrally dependent radiation absorption effect on propagating spherical flames is measured by using CO<sub>2</sub>-diluted CH<sub>4</sub>/O<sub>2</sub>/He mixtures at normal and elevated pressures. Radiation absorption is found to increase the flame speed and extend the flammability limit. In addition, the combined effects of flame curvature, radiation, and stretch on flame extinction are revealed via premixed tubular flames. It is found that the coupling between radiation and flame curvature leads to multiple flame bifurcations and extinction limits.

Finally, the effects of kinetic and transport coupling on ignition and flame propagation are investigated by using dimethyl ether (DME) blended methane/air mixtures. It is shown that the addition of a small amount of DME to methane leads to a significant decrease in the ignition time, while the flame speed of DME/CH<sub>4</sub>/air mixture is only linearly proportional to the DME fraction.

## Acknowledgements

Many people contributed, in different ways, to the realization of the research work that resulted in this thesis.

First and foremost, I would like to express my most sincere gratitude to my advisor, Professor Yiguang Ju, for his invaluable support, guidance, and encouragement through my graduate study at Princeton. Professor Ju is the greatest mentor and it is my great fortune to have him as my academic advisor. I am immensely grateful that he has taken every step possible to nurture my personal as well as professional growth, and to help me develop my career in an academia position. I am also grateful to Mrs. Limei Zhu. On holidays she often threw a party chaired by Professor Ju in their house. The parties I attended in these years gave me warmth as well as delicious Chinese food.

I thank Professor Chung K. Law and Professor Frederick L. Dryer for their service on my doctoral committee and for their help on my study and research. The outstanding teaching and continuous encouragement from Professor Law are greatly appreciated. The inspiring discussions with Professor Dryer during lunch-time are also greatly appreciated. Thanks also go to Professor Chung K. Law and Professor Paul D. Ronney for reading my thesis and providing many helpful feedbacks which have greatly improved the final form of this dissertation and to Professor Alexander Smits and Professor Luigi Martinelli for taking the time to be my examiner.

I wish to acknowledge my colleagues and collaborators: Dr. Xiao Qin and Mr. Michael Burke for collaborations on spherical flames; Dr. Xiaolong Gou and Mr. Wenting Sun for collaborations on multi-scale modeling and mechanism reduction; Dr. Zhenwei Zhao, Dr. Marcos Chaos, and Professor Frederick L. Dryer for collaborations on

studying dimethyl ether/methane dual-fuel; Dr. Genyuan Li and Professor Herschel Rabitz for collaborations on applications of the high dimensional model representation; and Dr. Takeshi Yokomori for collaborations on tubular flames.

I would like also thank other colleagues of the Princeton combustion group: Yuan Xue, Bo Xu, Timothy Ombrello, Sang-Hee Won, Wenjun Kong, Jingning Shan, Tianfeng Lu, Hoi Dick Ng, Heyang Wang, Jiao Yuan, Juan Li, Peng Zhang, Wei Liu, Kenneth Kroenlein, Mac Hass, and Kenichi Takita. I am grateful to them for their friendship and for inspiring me during daily interactions. Besides, thanks also go to the MAE staff for their excellent professional work and especially to Jessica O'Leary and Kelley Lynn Garza for administrative help during my graduate study.

I wish to acknowledge my master-course advisor, Professor Zi-Niu Wu, and other teachers at Tsinghua University. I would never be able to finish the current research work without the fundamentals on mathematics, fluid mechanics, and thermal engineering I learned at Tsinghua University.

Finally, it is with profound gratitude that I thank my parents, Jinya Chen and Guiying Liu, and my sister, Mei Chen, for their love and support. It is my parents' hard work over the years that made it possible for me to attend college and graduate school.

This dissertation carries the number 3196-T in the records of the Department of Mechanical and Aerospace Engineering.

# Table of Contents

<b>Abstract</b> .....	<b>iii</b>
<b>Acknowledgements</b> .....	<b>v</b>
<b>Table of Contents</b> .....	<b>vii</b>
<b>Chapter 1: Introduction</b> .....	<b>1</b>
1.1 Overview and Significance .....	1
1.2 Historical Perspectives .....	2
1.2.1 Flame Initiation and Minimum Ignition Energy .....	2
1.2.2 Flame Propagation and Laminar Flame Speed .....	7
1.2.3 Flame Extinction and Flammability Limit.....	11
1.3 Motivation and Objectives .....	14
1.4 Organization of the Dissertation .....	21
1.5 List of Publications .....	23
<b>Chapter 2: Theoretical Analysis on Spherical Flame Initiation and Propagation</b> .....	<b>25</b>
2.1 Mathematical Model .....	25
2.2 Theoretical Analysis.....	28
2.2.1 Analytical Solution without External Energy Addition .....	29
2.2.2 Validation in Limiting Cases.....	31
2.2.3 Effect of Radiative Heat Loss .....	34
2.2.4 Correlation among Different Flame Regimes.....	37
2.2.5 Effects of Ignition Energy .....	40
2.3 Numerical Modeling of the Unsteady Effect .....	43
2.6 Conclusions.....	46
Appendix: Solutions for Cylindrical Flames .....	47
<b>Chapter 3: Adaptive Simulation of Unsteady Reactive Flow (A-SURF)</b> .....	<b>61</b>
3.1 Governing Equations for Unsteady Reactive Flows .....	61
3.1.1 General Conservation Equations.....	61
3.1.2 Transport and Chemistry Models.....	63

3.2 Numerical Methods.....	66
3.2.1 Fractional-step Procedure .....	67
3.2.2 Finite Volume Method .....	69
3.2.3 Locally Adaptive Mesh.....	70
3.3 Validation and Examples.....	71
<b>Chapter 4: Critical Flame Radius and Minimum Ignition Energy for Spherical Flame Initiation.....</b>	<b>88</b>
4.1 Theoretical Analysis.....	88
4.1.1 Analytical Solutions.....	88
4.1.2 Results and Discussions.....	89
4.2 Numerical Validation .....	94
4.2.1 Numerical Specifications.....	94
4.2.2 Results and Discussions.....	95
4.3 Conclusions.....	98
<b>Chapter 5: On the Determination of Laminar Flame Speed using Propagating Spherical Flames .....</b>	<b>108</b>
5.1 Introduction.....	108
5.2 Constant Pressure Method .....	111
5.2.1 Validity of the Linear Relationship between Flame Speed and Stretch... ..	114
5.2.2 Effects of Ignition and Unsteady Transition .....	116
5.2.3 Effect of Compression .....	121
5.3 Constant Volume Method.....	128
5.3.1 Effect of Stretch Rate.....	130
5.4 Conclusions.....	137
<b>Chapter 6: Effect of Radiation on Flame Propagation and Extinction .....</b>	<b>155</b>
6.1 Radiation Effect on Propagating Spherical Flames .....	155
6.1.1 Introduction.....	155
6.1.2 Mathematical Model and Asymptotic Solutions.....	156
6.1.3 Results and Discussions.....	160
6.1.4 Summary .....	163

6.2 Radiation Reabsorption Effect on Flame Speed and Flammability Limits .....	164
6.2.1 Introduction.....	164
6.2.2 Experimental and Numerical Specifications.....	164
6.2.3 Results and Discussions.....	165
6.2.4 Summary .....	170
6.3 Radiation Effect on Premixed Counterflow and Tubular Flames .....	171
6.3.1 Introduction.....	171
6.3.2 Mathematical Model and Asymptotic Solutions.....	171
6.3.3 Results and Discussions.....	179
6.3.4 Summary .....	187
<b>Chapter 7: Ignition and Burning Properties of DME/methane Mixtures .....</b>	<b>202</b>
7.1 Introduction.....	202
7.2 Experimental/numerical Specifications and Kinetic Model Selection .....	202
7.3 Results and Discussions.....	205
7.3.1 Ignition Enhancement by DME Addition .....	205
7.3.2 Flame Speed and Burned Markstein Length of DME/CH <sub>4</sub> Dual Fuel.....	209
7.4 Conclusions.....	213
<b>Chapter 8: Summary and Recommendations .....</b>	<b>221</b>
8.1 Summary .....	221
8.2 Recommendations for Future Work.....	225
<b>References.....</b>	<b>228</b>

# Chapter 1: Introduction

## 1.1 Overview and Significance

Combustion has had significant impact on our daily lives since the beginning of human history. It is the primary means by which mankind produces power: about 85% of the world's energy comes from combustion of fossil fuels. Meanwhile, combustion is also responsible for nearly all of the anthropogenic emission of nitrogen oxides (NO<sub>x</sub>), carbon monoxide (CO), particulates (such as soot and aerosols), and other by-products that are harmful to human health and the environment. In recent years, environmental regulations throughout the world have been tightened for engine emissions. The emission standards for both NO<sub>x</sub> and particulates have been tightened and more restrictive measures will be implemented in the coming years. Meeting these requirements is becoming increasingly difficult and developing high-efficiency, low-emission devices for the conversion of fossil energy is currently a major research goal in combustion and engine design communities. For example, radically new engine designs are the only hope for meeting the near-zero NO<sub>x</sub> and particulate emission commitments proposed for implementation by 2012.

To facilitate the exploration of radically new concepts for high-performance engines, science-based predictive models for fundamental combustion processes such as ignition, flame propagation, and flame extinction should be developed. For example, ultra-lean combustion is currently one of the most promising concepts for substantial reduction of emissions while maintaining high efficiency. Operating near the lean flammability limit poses significant challenges such as flame blow-off, combustion

instabilities, auto-ignition, and flashback. In addition, the slowdown of combustion heat release at near-limit conditions encourages the coupling between chemistry and transport. Therefore, understanding and controlling near limit combustion are crucial for the successful design of ultra-lean combustion gas turbines and burners.

This study is focused on the fundamental properties of premixed flames, which are widely utilized in spark ignition engines for automobiles and in advanced gas turbine engine systems for power generation. Using combined modeling and experimental approaches, this thesis includes investigations on the ignition, propagation, and extinction of premixed flames.

## **1.2 Historical Perspectives**

### **1.2.1 Flame Initiation and Minimum Ignition Energy**

Ignition is the process whereby a medium capable of reacting exothermically is brought to a state of rapid combustion (Williams 1985). It is one of the most important problems in combustion. Understanding of flame initiation is important not only for fundamental combustion research but also for fire safety control and the development of low emission gasoline and homogeneous charge compression ignition (HCCI) engines and alternative fuels. Phenomenologically, ignition can be classified into two modes: self-ignition and forced-ignition (Glassman 1996). Self-ignition, which is also called auto-ignition or spontaneous ignition, is caused by chain branching or thermal feedback in a homogeneous mixture without input of either an external source of thermal energy or active radicals into the system. Unlike self-ignition, forced-ignition is a result of electrical discharge (spark), heated surface, shock wave, or pilot flame, with the locally initiated

flame front subsequently reaching a self-propagating state where the ignition source can be removed without extinguishing the combustion process.

For self-ignition, there are two different modes according to the mechanisms of ignition. The first mode is chain self-ignition, in which the chain branching factor at a given temperature and pressure exceeds a critical value (Glassman 1996). The second mode is thermal self-ignition, in which the thermal energy release rate is greater than the heat loss rate and the temperature consequently increases exponentially until a flame appears (Glassman 1996). Theory on chain self-ignition was first developed by Semenov (1935) and Hinshelwood (1940). The thermal self-ignition was first presented in analytical form by Semenov (1935) and later in more exact form by Frank-Kamenetskii (1955).

For forced-ignition, there are many means, among which the spark ignition is the first and most prevalent form. Most practical combustion devices require combustion events to be initiated at predetermined locations and times, and spark ignition is the primary means of accomplishing this task (Ronney 1994). Successful spark ignition depends on the amount of energy in the form of heat and/or radicals deposited into the combustible mixture. If the energy is smaller than a so-called minimum ignition energy (MIE), the resulting flame kernel decays rapidly because heat/radicals conducts/diffuse away from the surface of the ignition kernel and the dissociated species recombine faster than they are generated by the chain-branching reactions within the ignition kernel. Comprehensive experiments on spark ignition of different hydrocarbon fuels were conducted by Lewis and von Elbe and large amounts of experimental data on the MIE were reported (Lewis and Von Elbe 1961). To explain their observations of the MIE for

different mixtures, Lewis and von Elbe (1961) postulated the first theory of spark ignition. They proposed that the spark heated the surrounding mixture and ensured continued flame propagation. The minimum size of this heated “spark kernel” was dictated by the condition that heat transferred from its surface by conduction was balanced by heat generated by combustion inside the kernel. If the kernel volume was too small, the heat conduction rate was greater than the heat generation rate and the flame kernel would be extinguished. The minimum spark kernel size was believed to be related to the quenching distance which the authors had observed in their experiments (Lewis and Von Elbe 1961). It was then postulated that the MIE,  $E_{min}$ , was the spark energy necessary to heat a sphere of gas whose diameter was equal to the quenching distance,  $d_q$ , to the flame temperature,  $T_f$ , of the mixture

$$E_{min} = \frac{\pi}{6} (d_q)^3 \rho C_p (T_f - T_0) \quad (1.1)$$

Similarly, based on the thermal-diffusion theory considering the competition between the reaction heat release and conductive heat loss, Zeldovich (Zeldovich et al. 1985) proposed that the minimal ignition kernel radius for successful spherical flame initiation was related to the laminar premixed flame thickness,  $\delta_f^0$ , and the MIE was proportional to the cube of the flame thickness

$$E_{min} = \frac{4\pi}{3} (\delta_f^0)^3 \rho C_p (T_f - T_0) \quad (1.2)$$

Unfortunately, the above models could only phenomenologically describe the spark ignition since the fuel consumption and thus mass diffusion were not considered. More accurate description of flame ignition including the effect of preferential diffusion of heat and mass (Lewis number effect) was proposed later based on the studies about

flame balls (Deshaies and Joulin 1984; Zeldovich et al. 1985; Champion et al. 1986). Zel'dovich (Zeldovich et al. 1985) found that for any premixed mixture there could exist a diffusion controlled stationary flame ball with a characteristic equilibrium radius – the flame ball radius. A stability analysis (Deshaies and Joulin 1984) showed that adiabatic flame balls were inherently unstable: a small perturbation would cause the flame to propagate either inward and eventually extinguish, or outward and evolve into a planar flame. The unstable equilibrium flame ball radius was therefore considered to be a critical parameter in controlling flame initiation and the MIE was proposed to be proportional to the cube of the flame ball radius instead of the flame thickness (Zeldovich et al. 1985; Champion et al. 1986). Since the flame ball radius strongly depends on the Lewis number (Zeldovich et al. 1985), the MIE for mixtures with different Lewis numbers is totally different. This was confirmed by numerical simulation using a one-step chemical mechanism (Tromans and Furzeland 1988). Recently, He (2000) studied mixtures with larger Lewis numbers and found that propagating spherical flames with radius less than the flame ball radius could exist when the Lewis number was larger than a critical value. Therefore, it was concluded that flame initiation for mixtures with large Lewis numbers was not controlled by the radius of stationary flame ball (He 2000). All the above theoretical studies were based on the quasi-steady assumption, neglecting the unsteadiness of flame initiation. Using large activation energy asymptotic analysis, Joulin (1985) studied the dynamics of flame kernels whose evolution was triggered by a time-dependent point-source of energy and a parameter-free flame front evolution equation for mixtures with Lewis numbers smaller than and bounded away from unity was obtained.

While the simplified models (such as one-step chemistry, constant thermal properties, quasi-steadiness, energy deposition as a boundary condition independent of time and space) considered in the above theoretical studies are adequate to describe many important qualitative features of the ignition process, they do not appear to be adequate for quantitative accuracy (Ronney 1994). To include more quantitatively accurate and perhaps even more qualitatively realistic models, numerical simulations were employed to study the ignition process. Maas and Warnatz (1988) simulated the ignition process in hydrogen/air mixtures by solving the corresponding conservation equations (total mass, momentum, energy, and species mass) for one-dimensional geometries using a detailed reaction mechanism and a multi-species transport model. Sloane and Ronney (1993) compared the MIE for a stoichiometric methane/air mixture using a one-step chemical mechanism and a detailed mechanism, and found that the differences in chemical mechanisms had a substantial effect on the MIE. Other effects such as composition, size of ignition source, duration of energy deposition, method of energy deposition, and flow environment on the MIE were also investigated via numerical simulations, which were reviewed by Ronney (1994). Spherical symmetry was usually assumed and one-dimensional simulations of flame initiation were conducted for simplicity. To provide a better understanding of the spark discharge process, two-dimensional simulations were recently carried out and more sophisticated models including ionization were employed (Akram 1996; Thiele et al. 2000; Thiele et al. 2002; Ekici et al. 2007).

Despite the extensive research on the flame initiation over many decades, the determination of MIE still remains empirical and could not be predicted even qualitatively by theory. To get a better understanding of the flame initiation and more

accurate prediction of the MIE, flame propagation after spark ignition should be studied since successful ignition critically depends on whether the expanding flame kernel would be able to maintain its propagation to reach a self-propagating state.

### **1.2.2 Flame Propagation and Laminar Flame Speed**

When a sufficient amount of energy is locally deposited into a quiescent homogeneous combustible mixture, a sustainable combustion wave can be initiated. For some specific conditions of strong ignition, the combustion wave takes the form of a detonation characterized by the supersonic propagation speed in the fresh mixture. The detonation has a propagating shock front which is coupled with and sustained by chemical heat release behind it (Williams 1985). For mild ignition, deflagrations (called premixed flames in the following) can be initiated. In this study, the focus will be on these premixed flames which propagate with a subsonic speed into the chemically-frozen, fresh mixture.

The thickness of premixed flames is usually much smaller than the characteristic length of the gas flow. Therefore, the flame front can be considered as a hydrodynamic discontinuity between two non-reactive flows, the fresh mixture and the burnt gases, both at thermo-chemical equilibrium (Clavin 1994). The motion of the flame front is controlled not only by its inner structure where diffusion and chemical reaction dominate, but also by the outer flow around it. Due to the coupling between diffusion and hydrodynamics, the dynamics and structure of premixed flames cannot be described completely by ordinary diffusion-reaction equations and thus are difficult to be analyzed theoretically. Therefore, either only hydrodynamics or only diffusion was considered in most of the previous studies. In the pioneering studies by Darrieus (1938) and Landau

(1944), the first stability analysis of a flame front was conducted and hydrodynamic instability, induced by the thermal expansion across the flame front, was found to be the main cause of the formation of cellular patterns on the flame front. The diffusive processes inside the flame front were completely neglected in their studies. On the other hand, other studies (Sivashinsky 1977; Joulin and Clavin 1979) deliberately neglected the hydrodynamic effect by using the thermal-diffusive model in which the density was assumed to be constant and the flame reduced to a simpler reaction-diffusion problem. Extensive studies on the reaction-diffusion problem using asymptotic methods and multiscale analyses were conducted, which were reviewed in the monograph by Buckmaster and Lundford (1982).

The first study on the coupling of diffusion and hydrodynamics was carried out by Markstein (1951). Based on semi-phenomenological considerations, the following correlation between the local flame speed,  $S_u$ , and the mean flame radius of curvature,  $R$ , was proposed (Markstein 1951)

$$S_u / S_u^0 = 1 + L_u / R \quad (1.3)$$

where  $S_u^0$  is the laminar flame speed of an adiabatic freely-propagating planar flame and  $L_u$  is a length called the “Markstein length”.  $L_u$  depends on the diffusive properties of the reactive mixture and has the same order in magnitude as the flame thickness,  $\delta_f^0$ . Later, the curvature of the flow (defined as the divergence of the unit flow velocity taken just upstream of the flame front) was included (Markstein 1964)

$$S_u / S_u^0 = 1 + L_u [1 / R + \bar{\nabla} \cdot (\bar{u} / |\bar{u}|)_-] \quad (1.4)$$

Another point of view was developed in a different context by Karlovitz (Karlovitz et al. 1953) who introduced the concept of “flame stretch” and proposed that

the local flame speed,  $S_u$ , was affected by the flame stretch. The flame stretch,  $K$ , was defined as  $K=A^{-1}dA/dt$ , where  $A$  is the elemental area of the flame front. It was shown that flame stretch was contributed by two sources: flame curvature and flow non-uniformity (Buckmaster 1982; Matalon 1983). For a weakly stretched flame, the following linear relationship was obtained (Clavin and Williams 1982)

$$S_u / S_u^0 = 1 - L_u K \quad (1.5)$$

For an outwardly propagating spherical flame resulted from central spark ignition in a quiescent homogeneous combustible mixture, the flame stretch is well defined as (Lewis and Von Elbe 1961)

$$K = \frac{1}{A} \frac{dA}{dt} = \frac{2}{R_f} \frac{dR_f}{dt} \quad (1.6)$$

where  $A=4\pi R_f^2$  is the surface area of the flame front and  $R_f$  is the flame radius. When the flame size is small, for example on the order of flame thickness, the propagating spherical flame is strongly stretched according to the definition given by equation (1.6) and therefore the flame speed is significantly affected by the flame stretch (Clavin 1985). To achieve successful ignition, the MIE must be able to support the flame kernel to survive the strong flame stretch and propagate out to reach a self-propagating state.

Extensively studies using asymptotic techniques were carried out to investigate the propagating spherical flames. Ronney and Sivashinsky (Ronney and Sivashinsky 1989) studied the expanding spherical flame within the framework of a slowly varying flame (SVF) theory. While reasonable predictions for Lewis number ( $Le$ ) less than unity were obtained, the results of the SVF theory were found to be physically unrealistic for  $Le>1$ . Bechtold and co-workers (Bechtold and Matalon 1987; Addabbo et al. 2003;

Bechtold et al. 2005) investigated the hydrodynamic and thermal-diffusion instabilities and effects of radiative loss in self-extinguishing and self-wrinkling spherical flames. Frankel and Sivashinsky (1983, 1984) examined the thermal expansion effect in propagating spherical flames in the limit of  $Le \rightarrow 1$ . Chung and Law (Chung and Law 1988) conducted integral analysis for propagating spherical flames for  $Le=1$ . All the above studies were based on the assumption of large normalized flame radius ( $R_f/\delta_f^0 \gg 1$ ). The recent work by He (2000) and Chen and Ju (2007) spanned all the spherical flame sizes and transitions between flames at small and large radii.

One of the most important applications of propagating spherical flames in fundamental combustion research is for laminar flame speed measurements. Recently, the propagating spherical flames have been popularly utilized to measure the laminar flame speed,  $S_u^0$ . The laminar flame speed, defined as the speed relative to the unburned gas with which a planar one-dimensional flame front travels along the normal to its surface (Andrews and Bradley 1972), is one of the most important parameters of a combustible mixture. On the practical level, it affects the fuel burning rate in internal combustion engines and the engine's performance and emissions (Metghalchi and Keck 1980). On a more fundamental level, it is an important target for the validation of kinetic mechanisms (Law et al. 2003). In the last fifty years, substantial attention has been given to the development of new techniques and the improvement of existing methodologies for experimental determination of the laminar flame speed. Various experimental approaches, reviewed in (Andrews and Bradley 1972; Rallis and Garforth 1980), have been developed to measure the laminar flame speed utilizing different flame configurations, including the outwardly propagating spherical flame (Lewis and Von

Elbe 1961; Bradley and Mitcheson 1976; Metghalchi and Keck 1980; Rallis and Garforth 1980; Hill and Hung 1988; Taylor 1991; Kwon et al. 1992; Aung et al. 1997; Bradley et al. 1998; Tse et al. 2000), counterflow or stagnation flame (Tsuji 1982; Egolfopoulos et al. 1989; Wu et al. 1999; Huang et al. 2004), Bunsen flame (Lewis and Von Elbe 1961), and burner stabilized flat flame (Levy and Weinberg 1959; Van maaren et al. 1994). Due to the lack of uniformity of the flame speed over the flame surface in the Bunsen flame and the wall effects in the flat flame, the propagating spherical flame and the stationary counterflow flame are among the most successful systems for flame speed measurements (Rallis and Garforth 1980; Tse et al. 2000). However, due to the Reynolds number limit, the counterflow flame method is difficult to apply at high pressures (e.g. above 10 atm)(Tse et al. 2000). Consequently, tracking the evolution of an outwardly propagating spherical flame in a confined bomb is the most favourable method for measuring the flame speed, especially at pressure above 10 atmosphere (Metghalchi and Keck 1980; Bradley et al. 1998; Tse et al. 2000). This method will be investigated and utilized in the present study.

### **1.2.3 Flame Extinction and Flammability Limit**

For ultra-lean combustion utilized in high-efficiency low-emission engines such as the HCCI, flame extinction is one of the most important problems on engine performance. A fundamental understanding of flame extinction is therefore essential for developing radically new engines.

Flame extinction usually occurs for near-limit mixtures and it could be caused by different effects such as radiative heat loss, flame stretch, and flame curvature (Ju et al. 2001). It is well known that radiation heat transfer is a dominant mechanism for

near-limit flame extinction. Indeed the flammability limit is determined by the radiative heat loss for unstretched premixed planar flames (Spalding 1957; Buckmaster 1976). For non-adiabatic planar flames, the following relationship between the normalized flame speed,  $U$ , and the normalized heat loss (which strongly depends on the fuel concentration),  $L$ , was derived (Spalding 1957; Buckmaster 1976)

$$U^2 \ln(U^2) + L = 0 \quad (1.7)$$

According to the above relationship, the flammability limit is defined by  $L^* = 1/e$  and  $U^* = e^{-1/2}$ . For each combustible mixture above the flammability limit, i.e.  $L < L^* = 1/e$ , there exist two laminar flame speed solutions and only the higher one is stable and thus could be observed in experiments (Joulin and Clavin 1979).

The above theory works only for planar flames which are unstretched. For stretched flames, the flammability limit can be modified by the combined effects of thermal radiation and flame stretch. The effects of radiation and stretch were extensively studied by using the counterflow flames (Sohrab and Law 1984; Maruta et al. 1996; Sung and Law 1996; Buckmaster 1997; Ju et al. 1997; Ju et al. 1999a; Ju et al. 2000). These studies showed that the flammability limit of stretched flames below a critical Lewis number can be lower than that of unstretched flames. The extended flammable region was found due to the existence of the Near Stagnation plane Flame (NSF) and the flammability of the stretched flame below the critical Lewis number is characterized by the limit of the NSF (Ju et al. 1999a). It was shown that the flammable region of premixed counterflow flames was bounded by the stretch extinction limit at large stretch rate and the radiation extinction limit at low stretch rate. Multi-flame bifurcations were found theoretically (Buckmaster 1997) and numerically (Ju et al. 1997; Ju et al. 1999a) to

be intrinsic phenomena caused by the combined effects of radiation and flame stretch, and the limits of these flame regimes were shown to be sensitive to the Lewis numbers of reactants and to radiative heat losses.

Unlike the counterflow flames, practical flames such as the laminar propagating spherical flames used in experiments and the flamelets in turbulent flames are not only stretched but also curved. To include the curvature effect, the tubular flames (Ishizuka 1993; Ju et al. 1999b) and propagating spherical flames (Bechtold et al. 2005; Chen and Ju 2007) have been utilized to study the combined effects of flame radiation, stretch, and curvature on premixed flames. It has been shown that the interaction of flame curvature with radiation or stretch greatly affects the flame strength and extinction.

In most of the studies mentioned above, radiation was only considered as heat loss from the combustion system. However, radiation emission and reabsorption occur simultaneously in combustion, and radiation from the downstream hot products could be reabsorbed by the upstream cold mixture. The effect of radiation absorption on the flame speed was first analyzed by Joulin and Deshaies (1986) using a gray gas model. It was shown that there was no flammability limit when radiation absorption is considered. The gray gas model was also used to study flame ball dynamics (Lozinski et al. 1994). However, radiation of most species is not gray. For example, CO<sub>2</sub> radiation is strongly spectral dependent and has temperature and pressure broadening. Ju et al. (Guo et al. 1998; Ju et al. 1998) first used the non-gray statistical narrow band (SNB) model to study CO<sub>2</sub>-diluted propagating flames and showed that a “fundamental” flammability limit exists because of the emission-absorption spectra difference between the reactants and products and band broadening. This model was later used in flame balls (Wu et al. 1999)

and high-pressure planar flames (Ruan et al. 2001). All these studies showed that radiation absorption plays an important role in flame extinction and flammability limits for CO<sub>2</sub>-diluted mixtures.

### **1.3 Motivation and Objectives**

Flame initiation, propagation, and extinction are intriguing combustion phenomena that also have substantial practical applications and deserve further research. The motivation and objectives of the present study are listed below:

(1) When an external energy is locally deposited into a combustible mixture, there are four possible outcomes: evolution from the outwardly propagating spherical flame to a planar flame, a stationary flame ball, a propagating self-extinguishing flame, or a decaying ignition kernel (Ronney 1988; He and Law 1999; Ju et al. 2001). The planar flame, flame ball, and self-extinguishing flame have been extensively studied (Spalding 1957; Deshaies and Joulin 1984; Zeldovich et al. 1985; Ronney 1988; Buckmaster et al. 1990; Ronney 1990; Clavin 1994). However, previous studies only focused on the dynamics of the separate phenomena such as flame balls and self-extinguishing flames, and thus the propagating flames were isolated from flame balls and self-extinguishing flames. As a result, the relation between self-extinguishing flames and flame balls and the relation between the flame ball size and successful initiation of outwardly propagating flames were not well understood. Recognizing the importance of the missing relationship between flame balls and propagating flames, a theoretical analysis by He and Law (He and Law 1999) was conducted to examine the transition of a flame ball to a propagating spherical flame. Although it was concluded that radiative heat loss has a significant effect on flame transition, the impact of radiative heat loss in the unburned region was not

considered. A recent study by He (2000) was motivated to study the flame initiation at large Lewis numbers, but it did not consider radiative heat loss either. This makes the results less realistic because near-limit flame initiation is dominantly affected by radiative heat loss. Therefore, the role of heat loss on flame transition and the correlation among the flame regimes from ignition kernels to flame balls and propagating flames remain unknown.

In view of the above considerations, the first objective is to develop a general theory which could describe the flame regimes and transitions among the flame kernel, the flame ball, the self-extinguishing flame, the outwardly propagating spherical flame, and the propagating planar flame, and to investigate the effects of radiative heat loss, ignition energy, and preferential diffusion between heat and mass (Lewis number) on flame transitions based on the general theory.

(2) As mentioned before, theoretical models usually only give qualitative rather than quantitative predictions due to the simplify assumptions employed. For example, for outwardly propagating spherical flames, it is unrealistic to obtain the flame propagation speed as a function of flame radius predicted by theory to agree well with experimental measurements because the theory is usually based on the assumption of one-step irreversible chemical reaction with large activation energy. In order to get quantitative results which could be utilized to compare with the experimental data, numerical simulations including detailed chemical kinetics and accurate transport properties need to be conducted. Besides, numerical simulation has many other advantages that make it an attractive tool for scientific research and engineering design. For example, computer simulations allow the user to interrogate the flow domain at any point in a non-intrusive

manner. Thus, field information such as pressure, temperature, velocity, and species concentration could be obtained without altering the flow field. Moreover, numerical simulation also enables the user to separate the various processes that occur in a flow and study the many complex interactions of these processes. For example, the role of radiation on flame initiation and propagation may be better understood by studying cases without radiation and then introducing radiation to isolate and thereby identify the radiation effect on flame initiation and propagation. It would be exceptionally difficult, or impossible, to accomplish this decoupling and removal of processes in experiments.

Therefore, the second objective is to develop a time-accurate and space-adaptive numerical solver for the adaptive simulation of unsteady reactive flow. High-fidelity numerical simulations of flame initiation, propagation, and/or extinction will be carried out to validate the theoretical models and/or to explain experimental measurements.

(3) Flame initiation plays an important role in the performance of combustion engines and a fundamental understanding of ignition is essential for a better control of fuel efficiency, exhaust emission, and idle stability of the engine operation. Despite extensive research effort over many decades on the determination of the MIE, it remains unclear as the length scale controlling the spherical flame initiation and how it is related to the MIE. Quenching distance or flame thickness was first considered to be the controlling length scale and the MIE was proposed to be proportional to the cube of the quenching distance or flame thickness (Lewis and Von Elbe 1961; Zeldovich et al. 1985). Later, the unstable flame ball radius was considered to be the controlling length scale for flame initiation and the MIE was proposed to be proportional to the cube of the flame ball radius instead of the flame thickness (Deshaies and Joulin 1984; Zeldovich et al. 1985;

Champion et al. 1986). A recent study (He 2000) showed that propagating spherical flame with radius less than the flame ball radius could exist when the Lewis number is larger than a critical value. It was concluded that flame initiation for mixtures with large Lewis numbers was not controlled by the radius of the stationary flame ball (He 2000). More recent experiments (Kelley et al. 2008) on hydrogen/air ignition at different equivalence ratios and pressures showed that there was a critical flame radius for spherical flame initiation and successful ignition depended on whether the initially ignited flame kernel can attain this critical radius. However, the relation between the critical flame radius and the MIE was not examined in those studies. Therefore, more studies should be carried out to clarify what is the controlling length scale for spherical flame initiation. Moreover, since the MIE is a very important parameter, the next question needs to be answered is how the controlling length scale is related to the MIE.

The third object of this study is therefore to find the controlling length scale for spherical flame initiation and to reveal its relationship with the MIE.

(4) Currently the propagating spherical flame is popularly utilized to measure the laminar flame speed and many experiments on different fuels at different conditions have been conducted. However, it was found that large discrepancies exist among flame speed data obtained from measurements using spherical flames and counterflow flames (Farrell et al. 2004). The reason for this discrepancy has yet to be explained. The accuracy and the validity of the employed models for flame speed measurements over a certain parameter range in the spherical flame methods still remain unclear due to the complexity of flame stretch, flow compression, flame structure, chamber geometry, and thermal radiation. For example, in the constant-pressure method using propagating spherical

flames, the stretched flame speed is first obtained from the flame front history  $R_f=R_f(t)$  and then is linearly extrapolated to zero stretch rate to obtain the unstretched flame speed (Taylor 1991; Tseng et al. 1993; Bradley et al. 1996). Flame speeds are commonly extrapolated over ranges of flame radius data,  $[R_{fL}, R_{fU}]$ . The lower bound,  $R_{fL}$ , is often chosen to reduce the effects of initial spark ignition, flame curvature, and unsteadiness on the flame propagation speed, and to make stretch rate small such that the linear relationship between the stretched flame speed and stretch rate is satisfied (Taylor 1991; Tseng et al. 1993; Bradley et al. 1996). The upper bound,  $R_{fU}$ , is frequently chosen to ensure that the pressure change is “small”. Historically, the choice of the data range has been somewhat arbitrary — different researchers made different choices without giving quantitative justification. To the authors’ knowledge, there is no quantitative study on how the flame radii range,  $[R_{fL}, R_{fU}]$ , affects the measured flame speed and how to choose the proper  $R_{fL}$  and  $R_{fU}$  in the literature. Similarly, in the constant-volume method using propagating spherical flames (Lewis and Von Elbe 1961; Metghalchi and Keck 1980; Hill and Hung 1988), stretch effect on the laminar flame speed might be too large to be neglected and thus the stretch correction for obtaining accurate unstretched laminar flame speed is indispensable (Wu et al. 1999). However, in all previous studies using the constant-volume method, the effect of flame stretch was neglected (Lewis and Von Elbe 1961; Metghalchi and Keck 1980; Hill and Hung 1988; Parsinejad et al. 2006). The stretch effect for the constant-volume method addresses two concerns: how much does the stretch affect the accuracy of flame speed measurement; and how does one correct the stretch effect in the flame speed measurements.

The fourth objective is therefore to answer the questions posed above. Different effects such as ignition and unsteady transition, compression, and flame stretch on the accuracy of laminar flame speed measurements using propagating spherical flames will be investigated and new methods to obtain more accurate flame speeds in a broader experimental range by correcting for these effects will be developed.

(5) It is well known that curved flame fronts prevail in turbulent combustion and the effect of curvature on flame propagation is important, especially for near-limit flames. Therefore, in order to extend the flammability and to improve flame stability for ultra lean combustion engines, it is particularly important to understand how the coupling of thermal radiation, flame curvature, and flame stretch affects the flame speed and extinction limits. Extensive studies have been conducted to investigate the effects of radiation, stretch, and curvature on flame extinction by using the counterflow flames and outwardly propagating spherical flames (Frankel and Sivashinsky 1984; Sohrab and Law 1984; Flaherty et al. 1985; Maruta et al. 1996; Sung and Law 1996; Buckmaster 1997; Ju et al. 1997; Ju et al. 1999a; Ju et al. 2000; Bechtold et al. 2005; Chen and Ju 2007). However only radiation together with stretch or stretch together with curvature was considered and the combined effects of radiation with both stretch and curvature were not addressed in all the previous studies except for the numerical study by Ju et al. (Ju et al. 1999b). Therefore, to gain a clear understanding of the extinction mechanism and to obtain an explicit correlation of the flammability limit, it is necessary to perform an analytical study to investigate the combined effects of radiation, stretch, and curvature on flame propagation and extinction.

Furthermore, with the recent development of high pressure combustor for high

energy efficiency and low NO<sub>x</sub> and soot emission technology, a large amount of CO<sub>2</sub> is recycled to the unburned mixture. As such, the strong spectral radiation absorption of CO<sub>2</sub> and the appearance of large amount of CO<sub>2</sub> in the recirculated exhausted gas raise the following question: what is the role of CO<sub>2</sub> radiation in flame speed and flammability limit? This concern becomes more serious with increasing ambient pressure. In most of previous studies, only radiative heat loss was considered. However, CO<sub>2</sub> not only is a radiation emitter but also an absorber. Therefore, it is important to know the effect of radiation absorption due to CO<sub>2</sub> on flame extinction and flammability limit.

Based on the above considerations, the fifth objective is to study the combined effects of radiation, stretch, and curvature on flame propagation and extinction, and to investigate the extension of flammability limits and the increase of laminar flame speeds due to the spectral dependent radiation absorption.

(6) Dimethyl ether (DME) is emerging as a substitute for Liquefied Petroleum Gas (LPG), diesel fuels, and Liquefied Natural Gas (LNG) because it has low soot emission, no air or ground-water pollution effects, and can be mass produced from natural gas, coal or biomass (Semelsberger et al. 2006; Arcounianis et al. 2008). Recently, the study of DME combustion has received significant attention. DME has shown promise as an additive and/or fuel extender. Yao et al. (2005) have undertaken studies on DME addition to methane for homogeneous charge compression ignition (HCCI) engines. In such cases, the coupling of DME kinetics with those of methane involves the low temperature kinetics of DME. On the other hand, DME/methane utilization in burners and in gas turbine applications is expected to involve principally high temperature kinetic coupling effects. However, the underlying kinetic coupling between DME and CH<sub>4</sub>

responsible for the observed ignition enhancement was not explored in any detail. In addition, kinetic coupling effects on flame properties and auto-ignition in non-premixed systems have not been studied.

Moreover, it is well known that flame properties such as burning rate and flame stability depend on the overall activation energy and the Lewis number or the Markstein length (Clavin 1985; Law 2006). Kinetic coupling may result in a dramatic change in the overall activation energy with a small amount of DME addition to methane. Furthermore, DME has a molecular weight larger than air so that the  $Le$  is larger than unity for lean DME/air mixtures in comparison to methane/air mixtures. On the other hand, DME is expected to react more quickly in the preheating zone by decomposing to lighter molecules. Therefore, it is of interest to investigate how the effective mixture Lewis number or the Markstein length depends on the blending ratio of dual fuels with disparate molecular weights, such as DME/CH<sub>4</sub> mixtures.

Thus the sixth and last objective of the present study is to investigate the kinetic coupling effects of DME addition on the high temperature ignition and burning properties of methane/air mixtures.

The above motivation and objectives basically provide the guideline for the dissertation research, with the following structure.

## **1.4 Organization of the Dissertation**

Chapter 2 presents a general theory on spherical flame initiation, propagation, and extinction. Based on this theory, the dynamics of flame kernel evolution with and without ignition energy deposition is studied and the effects of radiative heat loss and Lewis number on flame propagation are investigated.

Chapter 3 describes the numerical solver for Adaptive Simulation of Unsteady Reactive Flow (A-SURF). The details on the governing equations, numerical methods, and code validation for A-SURF are reported.

Chapter 4 is concerned with flame initiation. The critical flame radius and minimum ignition energy for spherical flame initiation are studied. The emphasis is on investigating the effect of preferential diffusion between heat and mass on the flame kernel evolution and the minimum ignition energy.

Chapter 5 is focused on flame propagation. The constant pressure and constant volume methods utilizing propagating spherical flames for laminar flame speed measurements are investigated. New methods to obtain more accurate flame speed in a broader experimental range are presented.

Chapter 6 is focused on flame extinction. Different effects such as radiative heat loss, stretch, curvature, and preferential diffusion on flame extinction are identified. The extension of flammability limits and the increase of laminar flame speeds due to the spectral-dependent radiation reabsorption are also discussed.

Chapter 7 reports the ignition and burning properties of the dimethyl ether/methane dual fuel. The effect of dimethyl ether addition to methane-air mixtures on ignition, flame speed, and Markstein length is studied. New experimental data were obtained for the validation of existing chemical mechanisms.

Chapter 8 summarizes the present theoretical analysis, numerical modeling, and experimental work, and provides recommendations for future work.

## 1.5 List of Publications

Chapter 2: Z. Chen, Y. Ju, “Theoretical analysis of the evolution from ignition kernel to flame ball and planar flame,” *Combustion Theory and Modelling*, **11** (2007) 427-453.

Chapter 4: Z. Chen, M.P. Burke, Y. Ju, “On the critical flame radius and minimum ignition energy for spherical flame initiation,” In preparation, 2009.

Chapter 5: Z. Chen, M.P. Burke, Y. Ju, “Effects of Lewis number and ignition energy on the determination of laminar flame speed using propagating spherical flames,” *Proceedings of the Combustion Institute*, **32** (2009) In press.

Z. Chen, M.P. Burke, Y. Ju, “Effects of compression and stretch on the determination of laminar flame speed using propagating spherical flames,” *Combustion Theory and Modelling*, (2009) In press.

Chapter 6: Z. Chen, Y. Ju, “Combined effects of curvature, radiation, and stretch on the propagation and extinction of spherical flames,” In preparation, 2009.

Z. Chen, X. Qin, B. Xu, Y. Ju, F. Liu, “Studies of radiation absorption on flame speed and flammability limit of CO<sub>2</sub> diluted methane flames at elevated pressures,” *Proceedings of the Combustion Institute*, **31** (2007) 2693-2700.

Z. Chen, Y. Ju, “Combined effects of curvature, radiation, and stretch on the extinction of premixed tubular flames,” *International Journal of Heat and Mass Transfer*, **51** (2008) 6118-6125.

Chapter 7: Z. Chen, X. Qin, Y. Ju, Z. Zhao, M. Chaos, F.L. Dryer, “High temperature ignition and combustion enhancement by dimethyl ether addition to

methane-air mixtures,” *Proceedings of the Combustion Institute*, **31** (2007)  
1215-1222.

Note that the experimental work published in the papers related to Chapters 4 and 5 was conducted by Mr. M.P. Burke and thus not presented in the dissertation. The experimental work reported in Chapters 6 and 7 and their related papers was conducted by the author with the help of Dr. X. Qin. The analysis on ignition presented in Chapter 7 and its related paper was carried out jointly with Drs. Z. Zhao, M. Chaos, and F.L. Dryer.

## Chapter 2: Theoretical Analysis on Spherical Flame Initiation and Propagation

In this chapter, a general theory on spherical flame initiation and propagation is presented. The dynamics of flame kernel evolution with and without external energy deposition is studied using large-activation-energy asymptotic analysis. The effects of radiative heat loss, ignition energy, and Lewis number on the correlation and transition among the initial flame kernel, the self-extinguishing flame, the flame ball, the outwardly propagating spherical flame, and the propagating planar flame are investigated. The theory will be utilized to study ignition and flame speed measurement in Chapter 4 and Chapter 5, respectively.

### 2.1 Mathematical Model

We consider the evolution of an unsteady, one-dimensional spherical flame kernel with and without an external energy source at the center. By assuming constant thermal properties, the conservation equations for energy and fuel mass in a quiescent flow are given as

$$\tilde{\rho}\tilde{C}_p \frac{\partial \tilde{T}}{\partial \tilde{t}} = \frac{1}{\tilde{r}^2} \frac{\partial}{\partial \tilde{r}} (\tilde{r}^2 \tilde{\lambda} \frac{\partial \tilde{T}}{\partial \tilde{r}}) - \tilde{H} + \tilde{q} \tilde{\omega} \quad (2.1a)$$

$$\tilde{\rho} \frac{\partial \tilde{Y}}{\partial \tilde{t}} = \frac{1}{\tilde{r}^2} \frac{\partial}{\partial \tilde{r}} (\tilde{r}^2 \tilde{\rho} \tilde{D} \frac{\partial \tilde{Y}}{\partial \tilde{r}}) - \tilde{\omega} \quad (2.1b)$$

where  $\tilde{t}$ ,  $\tilde{r}$ ,  $\tilde{\rho}$ ,  $\tilde{T}$  and  $\tilde{Y}$  are time, radial coordinate, density, temperature, and fuel mass fraction, respectively.  $\tilde{q}$  is the chemical heat release per unit mass of fuel,  $\tilde{C}_p$  the specific heat capacity at constant pressure,  $\tilde{\lambda}$  the thermal conductivity, and  $\tilde{D}$  the

fuel mass diffusivity. To further simplify the problem in theoretical analysis, we also adopt the commonly used constant density assumption (Joulin and Clavin 1979) so that the convection flux is absent.  $\tilde{\omega}$  is the reaction rate for a one-step irreversible reaction,  $\tilde{\rho}\tilde{A}\tilde{Y}\exp(-\tilde{E}/\tilde{R}^0\tilde{T})$ , in which  $\tilde{A}$  is the pre-factor of Arrhenius law,  $\tilde{E}$  the activation energy, and  $\tilde{R}^0$  the universal gas constant. The volumetric radiative heat loss  $\tilde{H}$  is estimated by using the optically thin model,  $\tilde{H} = 4\tilde{\sigma}\tilde{K}_p(\tilde{T}^4 - \tilde{T}_\infty^4)$ , where  $\tilde{\sigma}$  is the Stefan-Boltzmann constant and  $\tilde{K}_p$  denotes the Planck mean absorption coefficient of the mixture.

By using the adiabatic planar flame speed,  $\tilde{S}_u^0$ , and the flame thickness,  $\tilde{\delta}_f^0 = \tilde{\lambda}/(\tilde{\rho}\tilde{C}_p\tilde{S}_u^0)$ , the flow velocity, length, time, temperature, and reactant (fuel) mass fraction can be normalized as

$$u = \frac{\tilde{u}}{\tilde{S}_L^0}, \quad r = \frac{\tilde{r}}{\tilde{\delta}_f^0}, \quad t = \frac{\tilde{t}}{\tilde{\delta}_f^0/\tilde{S}_u^0}, \quad T = \frac{\tilde{T} - \tilde{T}_\infty}{\tilde{T}_{ad} - \tilde{T}_\infty}, \quad Y = \frac{\tilde{Y}}{\tilde{Y}_\infty} \quad (2.2)$$

where  $\tilde{T}_\infty$  and  $\tilde{Y}_\infty$  denote the temperature and fuel mass fraction in the fresh mixture, respectively, and  $\tilde{T}_{ad} = \tilde{T}_\infty + \tilde{Y}_\infty\tilde{q}/\tilde{C}_p$  is the adiabatic flame temperature. By further attaching the coordinate to the moving flame front,  $R=R(t)$ , the non-dimensional equations take the following form

$$\frac{\partial T}{\partial t} - U \frac{\partial T}{\partial r} = \frac{1}{r^2} \frac{\partial}{\partial r} \left( r^2 \frac{\partial T}{\partial r} \right) - H + \omega \quad (2.3a)$$

$$\frac{\partial Y}{\partial t} - U \frac{\partial Y}{\partial r} = \frac{Le^{-1}}{r^2} \frac{\partial}{\partial r} \left( r^2 \frac{\partial Y}{\partial r} \right) - \omega \quad (2.3b)$$

where  $Le = \tilde{\lambda} / \tilde{\rho} \tilde{C}_p \tilde{D}$  is the Lewis number and  $U = dR/dt$  is the flame front propagating speed. The radiative heat loss and chemical reaction rate are normalized, respectively, as

$$H = \frac{\tilde{H} \tilde{\delta}_f^0}{\tilde{\rho} \tilde{C}_p \tilde{S}_u^0 (\tilde{T}_{ad} - \tilde{T}_\infty)}, \quad \omega = \frac{\tilde{\omega} \tilde{\delta}_f^0}{\tilde{\rho} \tilde{S}_u^0 \tilde{Y}_\infty} \quad (2.4)$$

One can see that the present model extends the previous theoretical flame ball models (Zeldovich et al. 1985; Buckmaster et al. 1990; Buckmaster et al. 1991) by including propagating flames and radiative heat loss in both the burned and unburned zones. Therefore the correlation between flame ball and propagating flames and the impact of radiation on the flame transition among different flame regimes can be examined.

In the limit of large activation energy, chemical reaction occurs only within a very thin zone of high temperature and the reaction rate can be replaced by a Delta function with jump conditions used at the flame front (Sivashinsky 1977; Joulin and Clavin 1979; Law 2006)

$$\omega = \exp \left[ \frac{Z}{2} \frac{T_f - 1}{\sigma + (1 - \sigma) T_f} \right] \cdot \delta(r - R) \quad (2.5)$$

where  $Z = \tilde{E}(1 - \sigma) / \tilde{R}^0 \tilde{T}_{ad}$  is the Zel'dovich number and  $\sigma = \tilde{T}_\infty / \tilde{T}_{ad}$  the expansion ratio. By integrating the conservation equations (2.3a) and (2.3b) around the flame front ( $r=R$ ), the jump relations for temperature and fuel mass fraction can be obtained as (Sivashinsky 1977; Joulin and Clavin 1979)

$$\left. \frac{dT}{dr} \right|_{R^-} - \left. \frac{dT}{dr} \right|_{R^+} = \frac{1}{Le} \left( \left. \frac{dY}{dr} \right|_{R^+} - \left. \frac{dY}{dr} \right|_{R^-} \right) = \exp \left[ \frac{Z}{2} \frac{T_f - 1}{\sigma + (1 - \sigma) T_f} \right] \quad (2.6)$$

In this study, we shall also examine the impact of external energy deposition on the flame initiation and flame transition. A constant energy flux is locally deposited in an initially homogeneous mixture. For an initial flame kernel with a radius of  $R$ , the center of the flame kernel is located at  $r = 0$ , and  $0 \leq r \leq R$  and  $R \leq r < \infty$  are respectively the burned and unburned regions. By defining the flame as the location where the fuel concentration goes to zero, the boundary conditions for temperature and fuel mass fraction can be given as

$$r = 0, \quad r^2 \partial T / \partial r = -Q, \quad Y = 0 \quad (2.7a)$$

$$r = R, \quad T = T_f, \quad Y = 0 \quad (2.7b)$$

$$r = \infty, \quad T = 0, \quad Y = 1 \quad (2.7c)$$

where  $Q$  is the normalized ignition power given by

$$Q = \frac{\tilde{Q}}{4\pi\tilde{\lambda}\tilde{\delta}_f^0(\tilde{T}_{ad} - \tilde{T}_\infty)} \quad (2.8)$$

## 2.2 Theoretical Analysis

The unsteady problem given by equations (2.3a, 2.3b) cannot be solved analytically. In fact, as will be demonstrated later by numerical simulations, it is reasonable to assume that in the attached coordinate moving with the flame front, the flame can be considered as in quasi-steady state ( $\partial/\partial t=0$ ). This assumption has also been used in previous studies (Frankel and Sivashinsky 1983; Deshaies and Joulin 1984; Frankel and Sivashinsky 1984; He 2000). Therefore, the governing equations can be simplified to

$$-U \frac{dT}{dr} = \frac{1}{r^2} \frac{d}{dr} \left( r^2 \frac{dT}{dr} \right) - h \cdot T + \omega \quad (2.9a)$$

$$-U \frac{dY}{dr} = \frac{Le^{-1}}{r^2} \frac{d}{dr} \left( r^2 \frac{dY}{dr} \right) - \omega \quad (2.9b)$$

In addition, for the convenience of the algebraic manipulation the heat loss term  $H$  is approximated by a linear function of the normalized temperature as  $H = h \cdot T$ , where  $h$  is the heat loss constant taking the following form

$$h = \frac{4\tilde{\sigma}\tilde{K}_p\tilde{\delta}_f^0(\tilde{T}^4 - \tilde{T}_\infty^4)}{\tilde{\rho}\tilde{C}_p\tilde{S}_L^0(\tilde{T} - \tilde{T}_\infty)} \approx \frac{4\tilde{\sigma}\tilde{K}_p\tilde{\lambda}}{(\tilde{\rho}\tilde{C}_p\tilde{S}_L^0)^2} \tilde{T}_{ad}^3 \quad (2.10)$$

Note that the radiative heat loss constant involves the radiation intensity and the fuel concentration. For any mixtures, a decrease of fuel concentration (decrease of flame speed) means an increase of  $h$ . For methane-air flames, the heat loss constant,  $h$ , calculated according to equation (2.10) is in the range of 0.001 to 0.05.

### 2.2.1 Analytical Solution without External Energy Addition

Equation (2.9) with boundary conditions given by equation (2.7) can be solved analytically for  $Q=0$ . An exact solution of temperature and fuel mass fraction distribution is presented below. For fuel lean cases, the fuel mass fraction in burned gas region ( $0 \leq r \leq R$ ) is zero and that in unburned gas region ( $R \leq r < \infty$ ) is obtained by solving equation (2.9b) with boundary conditions given by equations (2.7b, 2.7c)

$$Y(r) = 1 - \int_r^\infty \frac{e^{-ULe\tau}}{\tau^2} d\tau / \int_R^\infty \frac{e^{-ULe\tau}}{\tau^2} d\tau \quad \text{for } r \geq R \quad (2.11)$$

As to the temperature distribution, for adiabatic flames ( $h=0$ ), the analytical solution is

$$T(r) = \begin{cases} T_f & \text{for } 0 \leq r \leq R \\ T_f \int_r^\infty \frac{e^{-U\tau}}{\tau^2} d\tau / \int_R^\infty \frac{e^{-U\tau}}{\tau^2} d\tau & \text{for } r \geq R \end{cases} \quad (2.12)$$

For nonadiabatic flames, since the radiation properties in burned and unburned gases may be different, we use  $h_1$  and  $h_2$  to represent the heat loss constants in the burned and unburned regions, respectively. Therefore, the individual contribution of the radiative heat loss from these two regions can be examined. By defining  $k_i = \sqrt{U^2 + 4h_i}$  ( $i=1,2$ ), an analytical solution of the temperature distribution is obtained as

$$T(r) = \begin{cases} T_f \cdot e^{[0.5(U+k_1)(R-r)]} \frac{F(k_1 r, U/k_1, -U/k_1)}{F(k_1 R, U/k_1, -U/k_1)} & \text{for } 0 \leq r \leq R \\ T_f \cdot e^{[0.5(U+k_2)(R-r)]} \frac{G(-k_2 r, U/k_2, -U/k_2)}{G(-k_2 R, U/k_2, -U/k_2)} & \text{for } r \geq R \end{cases} \quad (2.13)$$

where  $F(a, b, c) = \int_0^1 e^{at} t^b (1-t)^c dt$  and  $G(a, b, c) = \int_0^\infty e^{at} t^b (1+t)^c dt$ .

Note that this exact solution removes the assumption of small heat loss ( $h \sim 1/Z \ll 1$ ) which is commonly employed in previous studies (Joulin and Clavin 1979; Buckmaster et al. 1990; Buckmaster et al. 1991). Therefore, the present study provides a more rigorous consideration of radiation modelling to understand the relation between spherical flames and the far field propagating planar flames in the limit of  $R \rightarrow \infty$ .

By using the jump relations given by equation (2.6), one obtains the following algebraic system of equations for the flame propagation speed,  $U$ , flame radius,  $R$ , and flame temperature,  $T_f$

$$\Omega \cdot T_f = \frac{1}{Le} R^{-2} e^{-ULeR} / \int_R^\infty \tau^{-2} e^{-ULe\tau} d\tau = \exp \left[ \frac{Z}{2} \frac{T_f - 1}{\sigma + (1-\sigma)T_f} \right] \quad (2.14a)$$

where

$$\Omega = \begin{cases} R^{-2} e^{-UR} / \int_R^{\infty} \tau^{-2} e^{-U\tau} d\tau & \text{if } h_1 = 0, h_2 = 0 \\ -\frac{U+k_1}{2} + k_1 \frac{F(k_1 R, 1+U/k_1, -U/k_1)}{F(k_1 R, U/k_1, -U/k_1)} + R^{-2} e^{-UR} / \int_R^{\infty} \tau^{-2} e^{-U\tau} d\tau & \text{if } h_1 \neq 0, h_2 = 0 \\ \frac{U+k_2}{2} + k_2 \frac{G(-k_2 R, 1+U/k_2, -U/k_2)}{G(-k_2 R, U/k_2, -U/k_2)} & \text{if } h_1 = 0, h_2 \neq 0 \\ \frac{k_2 - k_1}{2} + k_1 \frac{F(k_1 R, 1+U/k_1, -U/k_1)}{F(k_1 R, U/k_1, -U/k_1)} + k_2 \frac{G(-k_2 R, 1+U/k_2, -U/k_2)}{G(-k_2 R, U/k_2, -U/k_2)} & \text{if } h_1 h_2 \neq 0 \end{cases} \quad (2.14b)$$

The present work extends the study of He (He 2000) by considering the coupling of radiative heat loss with the flame kernel evolution, which is the key mechanism for near-limit flames, and allows bridging between the spherical flame limits and the flammability limit of planar flames. By solving equation (2.14) numerically, the relation for the flame propagation speed, flame radius, and flame temperature and the existence of different flame regimes at different radiative heat loss intensities (or different fuel concentrations) and/or different Lewis numbers can be obtained.

## 2.2.2 Validation in Limiting Cases

In the following, it will be shown that in different limiting cases the present model recovers the previous results of stationary flame balls (Buckmaster et al. 1990; Buckmaster et al. 1991), outwardly propagating spherical flames (Frankel and Sivashinsky 1984), and planar flames (Joulin and Clavin 1979).

### 2.2.2.1 Stationary Flame Balls

In previous studies (Buckmaster et al. 1990; Buckmaster et al. 1991), the non-adiabatic stationary flame ball was investigated via asymptotic analysis under the assumption of small heat loss ( $h_1 = h_{in} / Z$ ,  $h_2 = h_{out} / Z^2$ ). The relation between heat loss and flame radius was

$$\ln\left(\frac{R}{R_Z}\right) = L_{in}\left(\frac{R}{R_Z}\right)^2 + L_{out}\left(\frac{R}{R_Z}\right) \quad (2.15)$$

where  $L_{in} = \frac{h_{in}}{6} \frac{R_Z^2 T_{fz}}{[\sigma + (1-\sigma)T_{fz}]^2}$  and  $L_{out} = \frac{\sqrt{h_{out}}}{2} \frac{R_Z T_{fz}}{[\sigma + (1-\sigma)T_{fz}]^2}$ .  $T_{fz}$  and  $R_Z$  are flame temperature and radius of adiabatic stationary flame ball (Zeldovich et al. 1985).

$$T_{fz} = \frac{1}{Le}, \quad R_Z = \frac{1}{Le} \cdot \exp\left[-\frac{Z}{2} \frac{1-Le}{1-\sigma(1-Le)}\right] \quad (2.16)$$

In the present study, the exact solution for the fuel mass fraction and temperature distribution is obtained without using the small heat loss assumption. In the limit of  $U = 0$  for flame balls, equation (2.14) reduces to the following form for the nonadiabatic stationary flame ball

$$T_f \sqrt{h_2} + T_f \frac{\sqrt{h_1}}{\tanh(\sqrt{h_1} R)} = \frac{1}{R \cdot Le} = \exp\left[\frac{Z}{2} \frac{T_f - 1}{\sigma + (1-\sigma)T_f}\right] \quad (2.17)$$

If the small heat loss assumption ( $h_1 = h_{in}/Z$ ,  $h_2 = h_{out}/Z^2$ ) is used and high-order terms of  $1/Z$  are neglected, the above relation can be reduced to the same form as equation (2.15). Therefore, the flame ball solution (Buckmaster et al. 1990; Buckmaster et al. 1991) is a limiting case of the present result.

### 2.2.2.2 Outwardly Propagating Spherical Flames

A flame speed relation for propagating spherical flames was obtained by Frankel and Sivashinsky (1984). It is readily seen that the present result given by equation (2.14) recovers the same result in the limit of zero heat loss and large flame radius ( $h_1 = h_2 = 0$  and  $R \gg 1$ ). Specifically, for  $R \gg 1$ , the exponential integral can be represented by an asymptotic series

$$R^{-2}e^{-ULeR} / \int_R^{\infty} \tau^{-2}e^{-ULe\tau} d\tau \approx ULe + \frac{2}{R} \quad (2.18)$$

By using the above expansion, equation (2.14) reduces to the following form

$$T_f(U + \frac{2}{R}) = U + \frac{1}{Le} \frac{2}{R} = \exp\left[\frac{Z}{2} \frac{T_f - 1}{\sigma + (1 - \sigma)T_f}\right] \quad (2.19)$$

The following relation can be immediately derived from equation (2.19), which is similar to the theory presented in (Frankel and Sivashinsky 1984)

$$(U + \frac{2}{R}) \ln(U + \frac{2}{R}) = \frac{Z}{R} (\frac{1}{Le} - 1) - \frac{2}{R} (\frac{1}{Le} - 1) \quad (2.20)$$

The only difference between equation (2.20) and the relation from Frenkel and Sivashinsky (Frankel and Sivashinsky 1984) is the additional second term on the right hand side of equation (2.20), which was not considered by Frenkel and Sivashinsky for  $Z \rightarrow \infty$  and  $Le \rightarrow 1$ . Since the Zel'dovich number for most mixtures is in the range of 5~15 such that the deviation of Lewis number from unity can be of order of unity, the second term on the right hand side of equation (2.20) can not be neglected.

As such, the present model is valid in both limits of flame ball and propagating flames and can provide the relationship and transition mechanism between these two flames during the flame kernel growth.

### 2.2.2.3 Planar Flames

In the limit of  $R \rightarrow \infty$ , the functions  $F$  and  $G$  respectively become

$$\frac{F(k_1 R, 1 + U/k_1, -U/k_1)}{F(k_1 R, U/k_1, -U/k_1)} \rightarrow 1, \quad \frac{G(-k_2 R, 1 + U/k_2, -U/k_2)}{G(-k_2 R, U/k_2, -U/k_2)} \rightarrow 0$$

Therefore, equation (2.14) reduces to

$$T_f \frac{k_1 + k_2}{2} = U = \exp \left[ \frac{Z}{2} \frac{T_f - 1}{\sigma + (1 - \sigma)T_f} \right] \quad (2.21)$$

Asymptotically, when the heat loss is of the order of  $1/Z$  in the limit of large Zel'dovich number ( $h_1 = h_{in}/Z$ ,  $h_2 = h_{out}/Z$ , and  $Z \gg 1$ ), equation (2.21) recovers the classical theory of flammability limit for planar flames (Joulin and Clavin 1979)

$$L = -U^2 \ln(U^2) \quad \text{with} \quad L = h_{in} + h_{out} = Z(h_1 + h_2) \quad (2.22)$$

The flammability limit is defined by  $L = 1/e$  and  $U = e^{-1/2}$ . Therefore, equation (2.14) is a general solution to describe the dynamics of flame kernel growth and depicts a clear correlation among the ignition kernel, flame ball, propagating curved flames, and planar flames. In the following section, we will demonstrate the role of radiative heat loss, Lewis number, and external energy addition in the various flame regimes and flame initiation.

### 2.2.3 Effect of Radiative Heat Loss

Radiative heat losses from the burned and unburned zones affect the flame temperature in different ways. The heat loss from the unburned zone will directly reduce the flame temperature. However, the heat loss from the burned region only affects the flame temperature via the heat conduction loss from the flame. In addition, the impact of radiative heat loss on the flame depends on the ratio of the burned gas volume to the surface area of the flame front. As the flame kernel grows, the volume to surface area ratio changes significantly. For example, the normalized radiative heat loss from the burned and unburned zones can be given as

$$H_{in} = h_1 \int_0^R T(r) \cdot r^2 dr / \left( R^2 \frac{dT}{dr} \Big|_{R^-} - R^2 \frac{dT}{dr} \Big|_{R^+} \right) \quad (2.23a)$$

$$H_{out} = h_2 \int_R^{\infty} T(r) \cdot r^2 dr / \left( R^2 \frac{dT}{dr} \Big|_{R^-} - R^2 \frac{dT}{dr} \Big|_{R^+} \right) \quad (2.23b)$$

where  $\left( R^2 \frac{dT}{dr} \Big|_{R^-} - R^2 \frac{dT}{dr} \Big|_{R^+} \right)$  is the total heat generation from chemical reaction. By using the temperature distribution obtained in equation (2.13), the ratio of the heat loss in the limit of small and large flame radius becomes

$$\frac{H_{in}}{H_{out}} = \begin{cases} 0 & \text{if } R \rightarrow 0 \\ h_1 \cdot \frac{\sqrt{1 + 4h_2/U^2} + 1}{h_2 \cdot \sqrt{1 + 4h_1/U^2} - 1} & \text{if } R \rightarrow \infty \end{cases} \quad (2.24)$$

The above qualitative result shows that the radiative heat loss from burned and unburned zones will have different impacts on the flame temperature and flame transition. Since the radiative heat loss in the unburned region was neglected in the previous theoretical studies (He and Law 1999; He 2000), the competing role of radiative heat loss from the unburned and burned zones as the flame kernel grew was not identified.

In the following we will take an example of CH<sub>4</sub>/air flames and use equation (2.14) to demonstrate how differently the radiative heat losses from the burned and unburned regions affect the flame temperature and flame propagation speed. For flames around the stoichiometric equivalence ratio, we choose  $Z = 10$  and  $\sigma = 0.15$ . Equation (2.23) is utilized to evaluate the radiative heat loss from different zones and the total normalized radiative heat loss is their summation:  $H_{all} = H_{in} + H_{out}$ .

Figure 2.1 shows the dependence of normalized heat loss and flame propagation speed on the flame radius for  $Le = 1$  and  $h = 0.015$ . It is seen that there are two flame branches in the  $U - R$  diagram: the fast stable flame branch  $abc$  and the slow unstable

flame branch *cde*. At point *c*, the flame is extinguished at a finite propagating speed because the normalized heat loss reaches its maximum on the fast flame branch *abc*. It is also observed that the normalized total heat loss changes nonmonotonically as the flame radius increases. There exists a minimum value as the flame reaches point *b* on the fast branch and point *d* on the slow branch, respectively. This phenomenon can only be explained by considering the individual contributions of heat loss in the burned and unburned zones.

The dependence of the normalized radiative heat loss in the burned and unburned zones,  $H_{in}$  and  $H_{out}$ , on flame radius are shown in figure 2.1(b). It is seen that  $H_{in}$  increases monotonically with flame radius while  $H_{out}$  decreases monotonically with flame radius. It is shown that the radiative heat loss from the unburned zone  $H_{out}$  remains nearly constant when the flame radius is larger than 20 and is an order smaller than  $H_{in}$  ( $H_{out}/H_{in} < 0.1$  when  $R > 20$ ). This means that the effect of heat loss in the unburned zone becomes weaker as the flame grows. However, it does not mean that heat loss from the unburned zone can be neglected because the heat loss from these zones affect the flame temperature in different ways. The rapid increase of flame speed and the peak of the radiative heat loss in the region of  $R < 20$  are caused by the competition of radiative heat loss from the burned and unburned zones.

When the radiative loss is larger than the critical loss ( $L = 1/e$  and  $h_c = 0.0184$ ) at the flammability of the planar flame, a flame does not exist at larger flame radii. Figure 2.2 shows the dependence of the normalized heat loss and flame propagation speed on the flame radius for  $Le = 1$  and  $h = 0.0197$ . It is interesting to note that a propagating spherical flame still exists at intermediate flame radii and has two extinction limits,

respectively, at small and large flame radii. The normalized total heat loss also changes non-monotonically and peaks at both extinction limits. This indicates that the extinction at small flame radius is caused by the heat loss in the unburned zone and the extinction at large flame radius by that from the burned zone (figure 2.2b). The appearance of the extinction limit at small flame radius has not been reported in previous studies and the existence of this extinction limit will significantly affect the ignition kernel size for successful flame initiation. Therefore, adequate inclusion of radiative loss from unburned gas is particularly important for understanding the flame kernel evolution.

#### **2.2.4 Correlation among Different Flame Regimes**

Figure 2.3(a) shows the flame propagation speed as a function of flame radius for various radiative loss constants (or different fuel concentrations) at  $Le = 1$ . To further demonstrate the importance of heat loss in the unburned zone, the results with radiative loss only from the burned gas is shown in figure 2.3(b). In figure 2.3, solutions on the horizontal axis of  $U = 0$  denote the stationary flame balls (equation 2.17) and those on the vertical axis at large flame radius denote the planar flame (equation 2.21). The solution curves between the flame ball solutions and the planar flame solutions represent the travelling spherical flames. It is seen from figure 2.3(a) that for adiabatic flame ( $h = 0$ ), the quasi-steady state flame ball exists at small radius,  $R=1$ . As the flame size grows the flame speed increases rapidly because of the increase of diffusion flux and eventually reaches the planar flame speed ( $U = 1$ ) at a large flame radius. When there is a small radiative loss ( $h = 0.005$ ), the quasi-steady state flame ball solution does not exist, and at a small flame radius, the flame extinguishes at a finite flame speed. As the flame radius increases, flame speed increases and ultimately reaches the corresponding

nonadiabatic planar flame speed. As the radiative loss further increases and becomes larger than the critical heat loss associated with the flammability limit, as explained in figure 2.2(a), sub-limit flames only exist at intermediate flame radii and the radiative loss from the unburned and burned zones yield two extinction limits at small and large flame radii, respectively. To distinguish this flame regime from the self-extinguishing flame observed in the microgravity experiments (Ronney 1985; Ronney 1988), we will refer to it as an isolated self-extinguishing flame because this flame cannot be initiated by a small localized ignition source. When only the radiative loss in the burned zone is considered (figure 2.3b), it is seen that the quasi-steady state solution of the stationary flame ball exists for all heat losses. This obviously contradicts the experimental observation (Ronney 1990). Therefore, it can be concluded that the present model can successfully predict the existence of multiple flame regimes and the transition between flame balls and travelling flames. Radiation from the unburned zone yields a new flame regime at intermediate flame radii. The exclusion of radiative loss from unburned zone prevents correct prediction of the flame regimes and their transitions.

The flame speed dependence on flame radius for  $Le = 0.8$  and  $1.2$  is shown in figures 2.4(a) and 2.5(a), respectively. For comparison, results without radiative loss in the unburned zone are shown in figures 2.4(b) and 2.5(b). Effects of Lewis number on the flame regime and the flame transition can be found by comparing these results with figure 2.3. It is seen that in a mixture of  $Le = 0.8$ , depending on the fuel concentration, there exists five different flames: the flame ball, the outwardly propagating spherical flame, the planar flame, the self-extinguishing flame (SEF), and the isolated self-extinguishing flame (ISEF). Because of the Lewis number effect, the sub-limit SEF

and ISEF can exist at much lower concentrations than the flammability limit of the planar flame. In addition, stationary flame balls start to appear at small radiative losses. These results are consistent with the experimental observation (Ronney 1985; Ronney and Wachman 1985; Ronney 1988; Ronney and Sivashinsky 1989; Ronney 1990). At  $Le = 1.2$ , figure 2.5(a) shows that neither flame ball nor sub-limit SEF or ISEF exists. At large radiative loss or low fuel concentrations, a flame does not exist because of the combined effect of radiative loss in the unburned gas and of the flame stretch. Obviously, predictions without inclusion of radiative heat loss in the unburned zone (figures 2.4b, 2.5b) do not correctly predict this phenomenon. For example, figure 2.5b shows that flame balls exist at all fuel concentrations. This is contrary to experimental observations.

The effects of radiative loss on the critical Lewis number below which a quasi-steady state flame ball solution exists are shown in figure 2.6 for different radiation intensities. It is seen that for a large radiative loss constant, stationary flame balls exist only for small Lewis number, which is consistent with the experimental results in microgravity (Ronney 1985; Ronney and Wachman 1985; Ronney 1988; Ronney and Sivashinsky 1989; Ronney 1990). The importance of radiative loss in the unburned zone can also be observed from figure 2.6. It is seen that the effect of radiative heat loss on the critical Lewis number for flame ball is dominated by the heat loss in the unburned zone. This conclusion is different from previous studies in which the radiative loss in the unburned region was often ignored. This is because the flame ball size is very small and the diffusion zone is very broad at zero and small flame speed. As a result, the radiative loss in the burned zone plays a negligible role in affecting the critical Lewis number.

### 2.2.5 Effects of Ignition Energy

We now consider the case in which an external energy flux is deposited in the center of a quiescent mixture and to examine how the ignition energy affects the flame diagram and the transition trajectory.

In the quasi-steady model, the ignition energy  $Q$  is modelled as a boundary condition (related discussions are presented at the end of this section), that is

$$r^2 \partial T / \partial r|_{r=\varepsilon} = -Q \quad \text{with } \varepsilon \rightarrow 0 \quad (2.25)$$

The fuel mass fraction distribution is the same as that obtained in section 3.1 and the temperature distribution in the burned gas region ( $0 \leq r \leq R$ ) is given by

$$T(r) = T_0(r) + Q \cdot T_Q(r) \quad (2.26)$$

where  $T_0(r)$  is the solution in the case of  $Q = 0$  (equations 2.12, 2.13) and  $T_Q(r)$  is the temperature increase caused by the external ignition power

$$T_Q(r) = \begin{cases} \int_r^R \frac{e^{-U\tau}}{\tau^2} d\tau & \text{if } h_1 = 0 \\ e^{-0.5(U+k_1)r} \left[ C_1 \cdot G\left(-k_1 r, \frac{U}{k_1}, -\frac{U}{k_1}\right) + C_2 \cdot F\left(k_1 r, \frac{U}{k_1}, -\frac{U}{k_1}\right) \right] & \text{if } h_1 \neq 0 \end{cases} \quad (2.27)$$

$$\text{with } C_1 = \left[ \varepsilon^2 \frac{U+k_1}{2} G(-k_1 \varepsilon, U/k_1, -U/k_1) + \varepsilon^2 k_1 G(-k_1 \varepsilon, 1+U/k_1, -U/k_1) \right]^{-1} \quad \text{and}$$

$$C_2 = -C_1 \cdot G(-k_1 R, U/k_1, -U/k_1) / F(k_1 R, U/k_1, -U/k_1).$$

By using the jump relations given by equation (2.6), the flame speed equation can be obtained as

$$\Omega \cdot T_f + \Omega_Q \cdot Q = \frac{1}{Le} R^{-2} e^{-ULeR} / \int_R^\infty \tau^{-2} e^{-ULe\tau} d\tau = \exp \left[ \frac{Z}{2} \frac{T_f - 1}{\sigma + (1 - \sigma)T_f} \right] \quad (2.28a)$$

where  $\Omega$  is given by equation (2.14b) and

$$\Omega_Q = \begin{cases} -R^{-2}e^{-UR} & \text{if } h_1 = 0 \\ k_1 e^{-0.5(U+k_1)R} \left[ -C_1 \cdot G\left(-k_1 R, 1 + \frac{U}{k_1}, -\frac{U}{k_1}\right) + C_2 \cdot F\left(k_1 R, 1 + \frac{U}{k_1}, -\frac{U}{k_1}\right) \right] & \text{if } h_1 \neq 0 \end{cases} \quad (2.28b)$$

The effects of ignition power and Lewis number on flame transition can be studied by solving equation (2.28) numerically. Figures 2.7 to 2.9 show the flame speed as a function of flame radius with different values of ignition power, radiative loss constant, and Lewis number. Figure 2.7(a) shows the results for  $Le = 1.0$  and  $h = 0$ . The solid line  $ab$  shows the result of zero ignition energy ( $Q = 0$ ) which is the same as that in figure 2.3(a). In this case, the outwardly propagating spherical flame only exists beyond a finite flame radius  $R_b = 1.0$ . When an external energy is deposited, it is seen that the flame transition trajectory is changed. At a low ignition energy of  $Q = 0.05$ , due to the increase of flame temperature, the propagating flame branch  $ab$  is extended to branch  $ac$  and the critical flame initiation radius is reduced to  $R_c = 0.72$ . At the same time, a new flame branch (ignition kernel)  $de$  is formed at small flame radius and the flame quenches as it grows. Therefore, flame initiation is not successful. However, by increasing the ignition power to  $Q = 0.092$ , a new ignition kernel branch  $fg$  starts to merge with the propagating flame branch  $ag$ , indicating that an outwardly propagating spherical flame can be successfully initiated via the flame transition along  $fga$ . Therefore, we can define the critical ignition power ( $Q_c = 0.092$ ) above which the flame kernel branch always merges with the travelling flame branch.

Figure 2.7(b) shows the results of nonadiabatic flame evolution diagram for  $Le = 1.0$  and  $h = 0.01$ . Unlike the adiabatic case, no flame ball solution exists and the

outwardly propagating spherical flame only exists at a much larger flame radius with a finite flame speed due to the effects of radiative loss. When the ignition energy is deposited, the new flame kernel branch starts to merge with the travelling flame branch at  $Q = 0.107$  and forms three new flame branches, a fast flame transition branch *dja*, a slow isolated branch *ic*, and an ISEF branch *egh*. As the ignition power increases, the ISEF branch degenerates and the fast transition branch becomes more monotonic, indicating a successful flame transition from the ignition kernel to a travelling flame. Note that the radiative loss not only changes the flame bifurcation but also significantly increases the critical ignition radius (from  $R_f = 0.3$  to 0.6) and the critical ignition energy (from  $Q = 0.092$  to 0.107). Therefore, the adiabatic model does not adequately describe the flame initiation trajectory. This conclusion is different from that of a previous study (He 2000).

The adiabatic and nonadiabatic flame trajectories with external ignition energy for  $Le = 0.8$  and 1.2 are shown in figures 2.8 and 2.9. For the case of a small Lewis number (figure 2.8), due to the Lewis number effect, the critical ignition radius becomes much smaller and the critical ignition power decreases. Moreover, the radiation effect becomes weaker with the decrease of Lewis number. However, at a large Lewis number (figure 2.9), both the critical ignition radius and the critical ignition power significantly increase. In particular, compared with the non-adiabatic model (figure 2.9b), the adiabatic model (figure 2.9a) not only does not predict the correct flame bifurcation but also fails to predict the size of critical ignition kernel.

It is noted that ignition is an essentially transient process. Depending on the relative magnitude of the characteristic times of external heating, chemical reaction,

travelling acoustic wave and heat conduction, there are fast-nondiffusive-ignition (Vazquez-Espi and Linan 2001) and thermal-diffusive-ignition (Vazquez-Espi and Linan 2002). In the present study, the constant density assumption is used and the acoustic effect is neglected because its time scale is far shorter than the thermal diffusion time scale. Therefore, only the thermal-diffusive-ignition is investigated here. It is reasonable because in practical devices the initial flame kernel size is much smaller than the volume of combustion chamber so that the pressure increase can be neglected. Unlike the work of Vazquez-Espi and Liñán (Vazquez-Espi and Linan 2002), in which the unsteady-diffusion-reaction equations similar to equation (2.1) were solved numerically and radiative loss was not considered, here we present a general theory (equation 2.28) based on the quasi-steady assumption in which radiative loss is included. The shortcoming of the present analysis is that the ignition energy deposition is modelled as a boundary condition (equation 2.25); while in practice it should be resolved in time and space. The employment of such a steady state energy deposition is for the purpose to obtain an analytical solution. However, this simplification does not prevent the model from producing qualitatively correct results. It will be shown in the next section that results from the present theoretical analysis based on the quasi-steady assumption agree well with those from fully transient numerical simulations.

### **2.3 Numerical Modeling of the Unsteady Effect**

In order to confirm the validity of the quasi-steady state assumption used in the previous analysis, we performed numerical simulations of the time-dependent flame initiation problem. The nondimensional form of equations (2.1a, 2.1b) under the constant density assumption is solved numerically by means of an implicit finite volume method.

To numerically resolve the moving flame front, a ten-level adaptive grid algorithm has been developed (Chen et al. 2007a) and utilized here. The mesh addition and removal are based on the first and second order gradients of the temperature and reaction rate distributions. Uniform grids of 0.00125~0.01 (length normalized by flame thickness) are used in the reaction zone and kept moving with the flame front. The following finite reaction rate is used in the numerical simulation,

$$\omega = \frac{1}{2Le} \cdot Y \cdot Z^2 \cdot \exp\left[\frac{Z(T-1)}{\sigma + (1-\sigma)T}\right] \quad (2.29)$$

The boundary conditions are the same as those given by equations (2.7a, 2.7c). With an initial uniform temperature and fuel mass fraction distribution of  $T(r)=1-Y(r)=0$ , the unsteady flame initiation problem is resolved.

To justify the validity of the quasi-steady state assumption used in theoretical analysis, flame speeds at different flame radii predicted from theoretical analysis were compared with those from numerical simulations, in which the flame propagation speed was calculated from the flame front history, i.e.  $U=dR/dt$  (the flame front,  $R$ , is defined as the position where the maximum heat release appears). Figure 2.10 shows the results for  $Le=1$  without and with radiative loss. It is seen that the results from the theory agree reasonably well with those from the unsteady simulations. Comparisons for other Lewis numbers without and with radiative loss are also made and qualitative agreement is obtained.

In order to evaluate quantitatively the magnitude of the unsteady term, numerical results from unsteady simulation were transformed into the coordinate attached to the flame front (in which theoretical analysis was carried out). The magnitudes of unsteady term ( $\partial T/\partial t$ ), convection term ( $U\partial T/\partial r$ ), diffusion term ( $r^2\partial(r^2\partial T/\partial r)/\partial r$ ), and reaction

term ( $\omega$ ) in equations (2.3a, 2.3b) are evaluated and compared in the transformed coordinate. The importance of the unsteady effects is shown by comparing the unsteady term with other terms. Figure 2.11 shows the distributions of the unsteady, convection, diffusion, and reaction terms in energy equation (2.3a) for flames at different flame radii with  $Le=1.0$  and  $Q=0.2$ . When the flame radius is large,  $R=5.0$  in figure 2.11(a), the unsteady term is one order smaller than all other terms, therefore it is negligible. For the cases of larger flame radii, the unsteady term becomes much smaller. Therefore, it is reasonable to employ the quasi-steady state assumption. When the flame radius is small,  $R=0.5$  in figure 2.11(b), the diffusion and reaction terms will dominate, while the unsteady and convection terms are relatively small near the flame front. However, near the center where energy deposition exists, the unsteady term is very large and is balanced by the convection term. This is because the energy deposited in the center (modelled as a boundary condition) is moving away from the flame front in the coordinate attached to the flame front.

Furthermore, to investigate the effect of the time scale of energy deposition on the flame trajectory, we compared the flame-front trajectories obtained from time dependent numerical computations with different duration time,  $t_s$  at a given energy flux,  $Q$  (there is zero heat flux from the center when  $t > t_s$ ). In numerical simulation, the energy flux  $Q$  at the boundary is set to be zero when the time is greater than the duration time ( $t_s$ ). Figure 2.12 shows the results for  $Le=1.0$ ,  $h=0.01$  and  $Q=0.2$ . It is seen that the flame initiation fails when the duration is too small. However, when  $t_s \geq 6.5$  the flame-front trajectory (which is the same as that of  $t_s=6.5$ ) is not affected by the change of the time scale of energy deposition. Therefore, in this case, the duration must be large than 6.5 (time

normalized by flame thickness divided by planar flame speed) to make the quasi-steady model consistent. Similar results were also presented in (He 2000).

## **2.6 Conclusions**

A general solution to describe the flame regimes and transitions among the flame kernel, the flame ball, the self-extinguishing flame, the outwardly propagating spherical flame, and the propagating planar flame is obtained. The results show that radiative heat loss significantly affects the flame regime, flame transition, and critical ignition radius and power. It is found that radiative loss from the unburned and burned zones play different roles in affecting the flame propagation speed. With the increase of flame radius, the radiative loss from the burned zone increases, while the radiative loss from the unburned zone decreases. As a result, there is a peak radiation loss at an intermediate flame radius, which dramatically affects the flame regimes and critical flame initiation parameters. It is also found that the radiative loss from the unburned zone results in a new flame regime: the isolated self-extinguishing flame with two radiation extinction limits respectively at small and large flame radius. In addition, it is shown that the critical Lewis number for the stationary flame ball is dominated by the heat loss from the unburned gas. The results also show that radiative loss significantly affects the transition history of flame initiation with external energy deposition. The critical radius for successful flame initiation of radiative flames is much larger than that of adiabatic flames. Furthermore, this difference increases dramatically with the increase of the Lewis number.

## Appendix: Solutions for Cylindrical Flames

Following the same asymptotic analysis procedure, solutions for cylindrical flame initiation and propagation can also be obtained. The following equations provide the general solutions for both cylindrical and spherical flames, with a geometrical factor  $N$  utilized for these two flames ( $N=1$ , cylindrical flames;  $N=2$ , spherical flames):

$$\Omega \cdot T_f + \Omega_Q \cdot Q = \frac{1}{Le} R^{-N} e^{-ULeR} / \int_R^\infty \tau^{-N} e^{-ULe\tau} d\tau = \exp \left[ \frac{Z}{2} \frac{T_f - 1}{\sigma + (1 - \sigma)T_f} \right]$$

where

$$\Omega = \begin{cases} R^{-N} e^{-UR} / \int_R^\infty \tau^{-N} e^{-U\tau} d\tau & \text{if } h_1 = 0, h_2 = 0 \\ -\frac{U + k_1}{2} + k_1 \frac{F \left[ k_1 R, \frac{N}{2} \left( \frac{U}{k_1} + 1 \right), -\frac{N}{2} \left( \frac{U}{k_1} - 1 \right) - 1 \right]}{F \left[ k_1 R, \frac{N}{2} \left( \frac{U}{k_1} + 1 \right) - 1, -\frac{N}{2} \left( \frac{U}{k_1} - 1 \right) - 1 \right]} + \frac{R^{-N} e^{-UR}}{\int_R^\infty \tau^{-N} e^{-U\tau} d\tau} & \text{if } h_1 \neq 0, h_2 = 0 \\ T_f \frac{U + k_2}{2} + T_f k_2 \frac{G \left[ -k_2 R, \frac{N}{2} \left( \frac{U}{k_2} + 1 \right), -\frac{N}{2} \left( \frac{U}{k_2} - 1 \right) - 1 \right]}{G \left[ -k_2 R, \frac{N}{2} \left( \frac{U}{k_2} + 1 \right) - 1, -\frac{N}{2} \left( \frac{U}{k_2} - 1 \right) - 1 \right]} & \text{if } h_1 = 0, h_2 \neq 0 \\ \frac{k_2 - k_1}{2} + k_1 \frac{F \left[ k_1 R, \frac{N}{2} \left( \frac{U}{k_1} + 1 \right), -\frac{N}{2} \left( \frac{U}{k_1} - 1 \right) - 1 \right]}{F \left[ k_1 R, \frac{N}{2} \left( \frac{U}{k_1} + 1 \right) - 1, -\frac{N}{2} \left( \frac{U}{k_1} - 1 \right) - 1 \right]} & \text{if } h_1 h_2 \neq 0 \\ + k_2 \frac{G \left[ -k_2 R, \frac{N}{2} \left( \frac{U}{k_2} + 1 \right), -\frac{N}{2} \left( \frac{U}{k_2} - 1 \right) - 1 \right]}{G \left[ -k_2 R, \frac{N}{2} \left( \frac{U}{k_2} + 1 \right) - 1, -\frac{N}{2} \left( \frac{U}{k_2} - 1 \right) - 1 \right]} & \end{cases}$$

$$\Omega_Q = \begin{cases} -R^{-N} e^{-UR} & \text{if } h_1 = 0 \\ k_1 e^{-0.5(U+k_1)R} \begin{cases} -C_1 \cdot G \left[ -k_1 R, \frac{N}{2} \left( \frac{U}{k_1} + 1 \right), -\frac{N}{2} \left( \frac{U}{k_1} - 1 \right) - 1 \right] \\ + C_2 \cdot F \left[ k_1 R, \frac{N}{2} \left( \frac{U}{k_1} + 1 \right), -\frac{N}{2} \left( \frac{U}{k_1} - 1 \right) - 1 \right] \end{cases} & \text{if } h_1 \neq 0 \end{cases}$$

$$C_1 = \left[ \begin{array}{l} \varepsilon^N \frac{U+k_1}{2} G[-k_1 \varepsilon, \frac{N}{2} (\frac{U}{k_1} + 1) - 1, -\frac{N}{2} (\frac{U}{k_1} - 1) - 1] \\ + \varepsilon^N k_1 G[-k_1 \varepsilon, \frac{N}{2} (\frac{U}{k_1} + 1), -\frac{N}{2} (\frac{U}{k_1} - 1) - 1] \end{array} \right]^{-1}$$

$$C_2 = -C_1 \cdot \frac{G[-k_1 R, \frac{N}{2} (\frac{U}{k_1} + 1) - 1, -\frac{N}{2} (\frac{U}{k_1} - 1) - 1]}{F[k_1 R, \frac{N}{2} (\frac{U}{k_1} + 1) - 1, -\frac{N}{2} (\frac{U}{k_1} - 1) - 1]}.$$

The effects of radiation, ignition, and Lewis number on cylindrical flame initiation and propagation can be investigated based on the above analytical solutions in the same way as that for spherical flames.

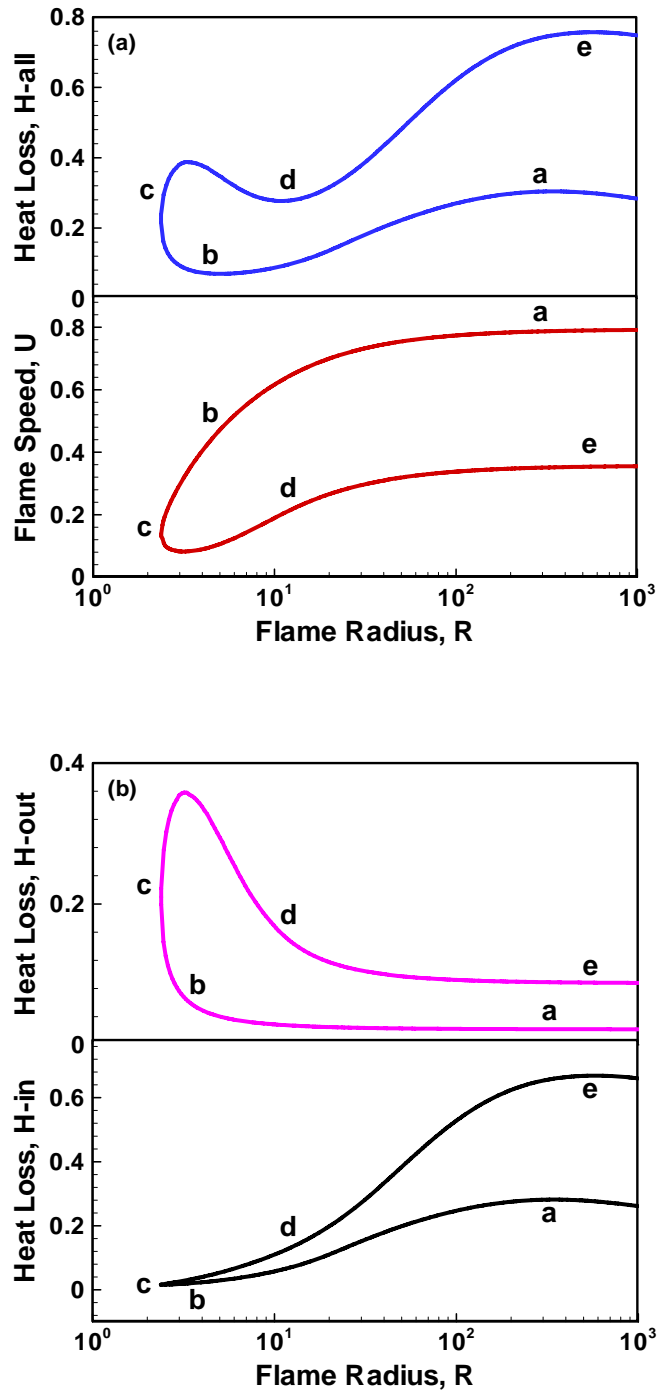


Figure 2.1: The dependence of normalized radiative heat loss and flame propagation speed on flame radius for  $Le=1$  and  $h=0.015$ , (a),  $H_{all}-R$  and  $U-R$ ; (b),  $H_{in}-R$  and  $H_{out}-R$ .

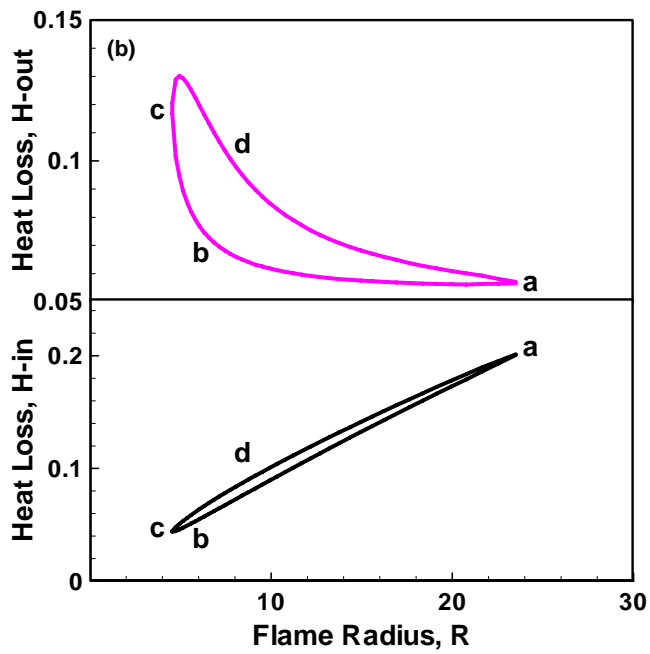
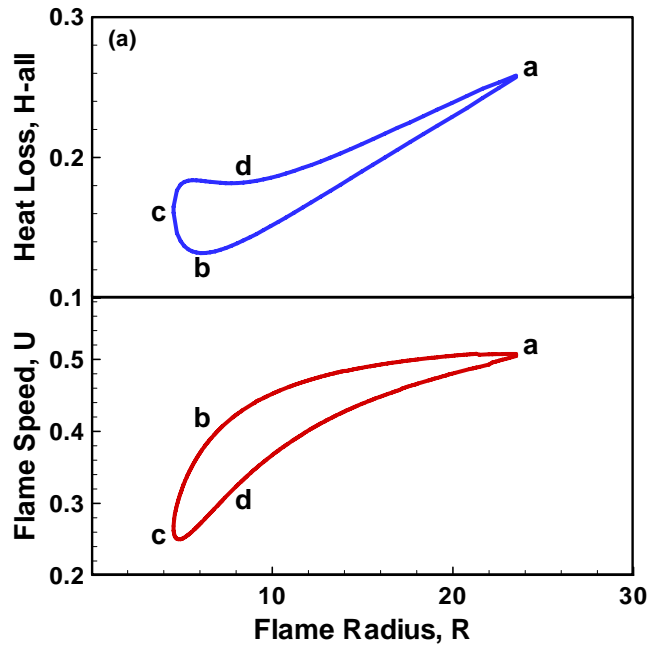


Figure 2.2: The dependence of normalized radiative heat loss and flame propagation speed on flame radius for  $Le=1$  and  $h=0.0197$ , (a),  $H_{all}-R$  and  $U-R$ ; (b),  $H_{in}-R$  and  $H_{out}-R$ .

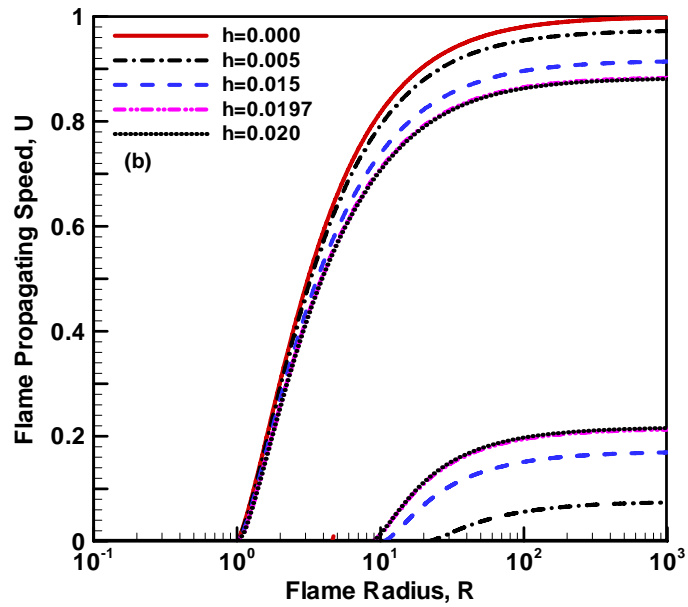
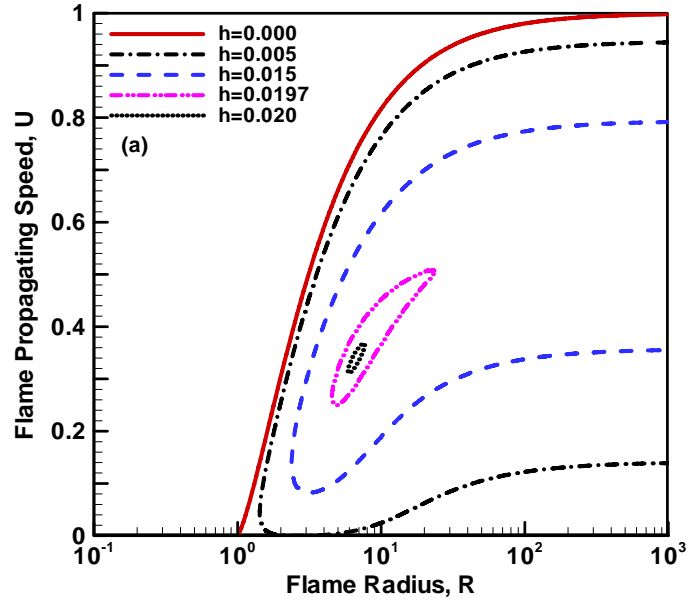


Figure 2.3: Flame propagation speed as a function of flame radius for  $Le=1.0$  with different values of radiative heat loss constants, (a), with heat losses in both the burned and unburned zones; (b), with heat loss only in the burned zone.

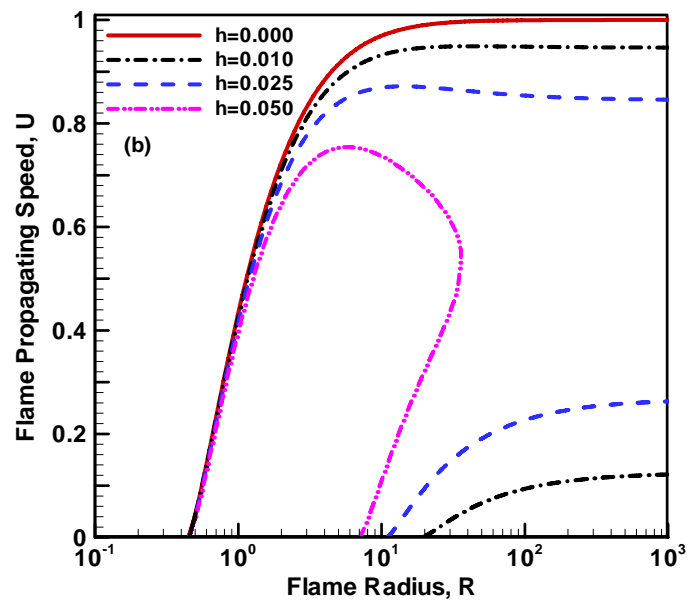
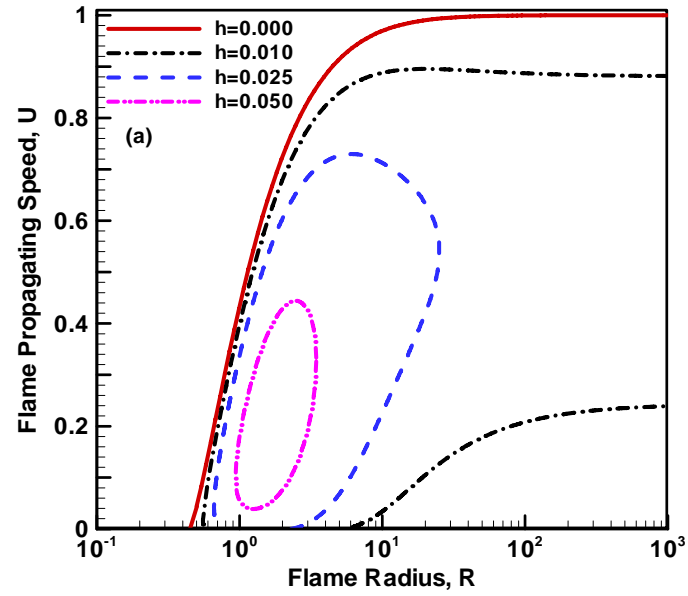


Figure 2.4: Flame propagation speed as a function of flame radius for  $Le=0.8$  with different values of radiative heat loss constants, (a), with heat losses in both the burned and unburned zones; (b), with heat loss only in the burned zone.

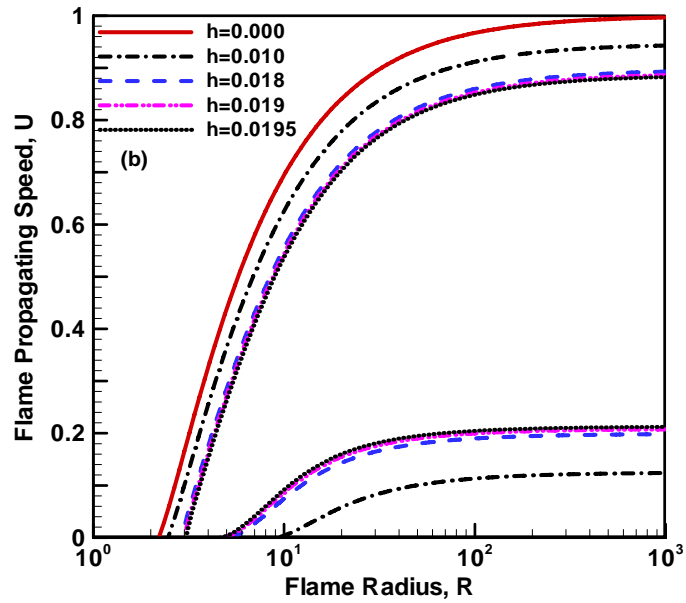
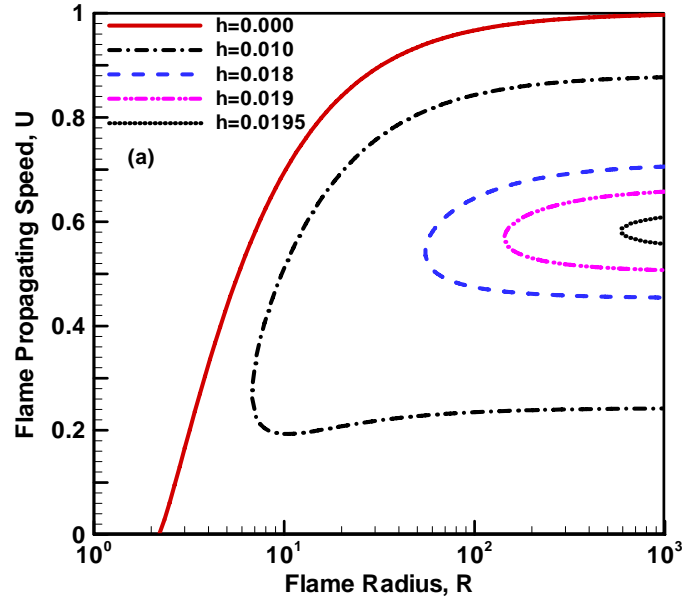


Figure 2.5: Flame propagation speed as a function of flame radius for  $Le=1.2$  with different values of radiative heat loss constants, (a), with heat losses in both the burned and unburned zones; (b), with heat loss only in the burned zone.

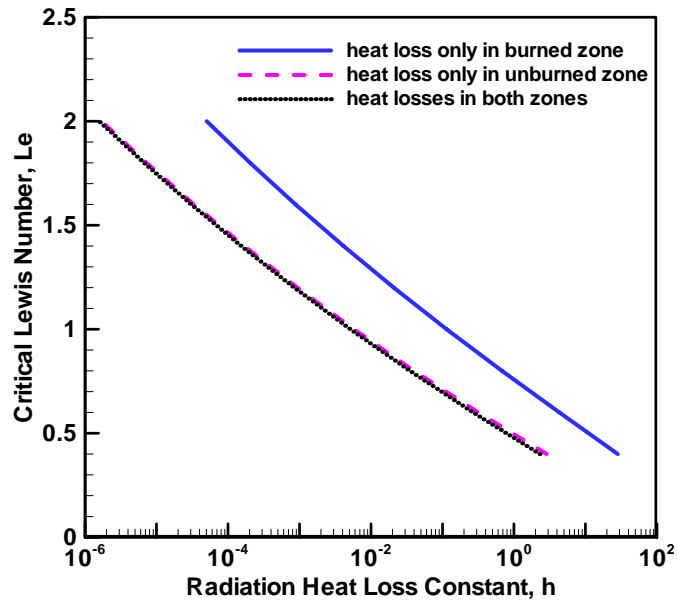


Figure 2.6: The dependence of critical Lewis number above which no solution exists for stationary flame ball for a given heat loss constant.

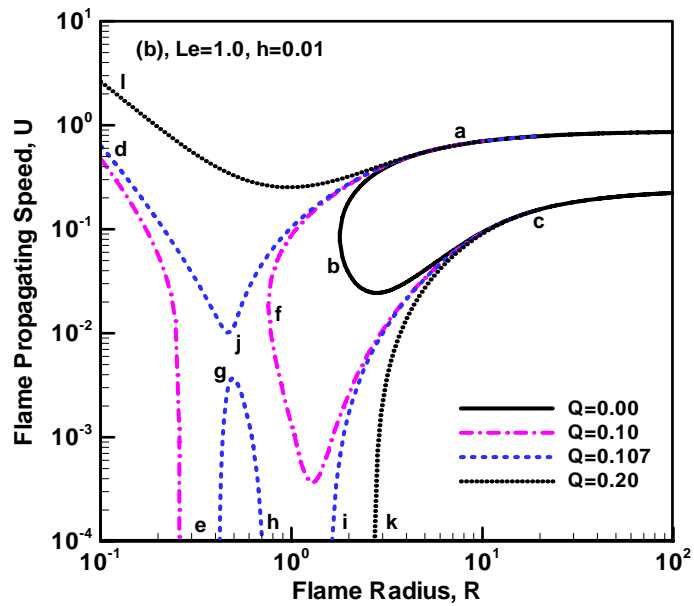
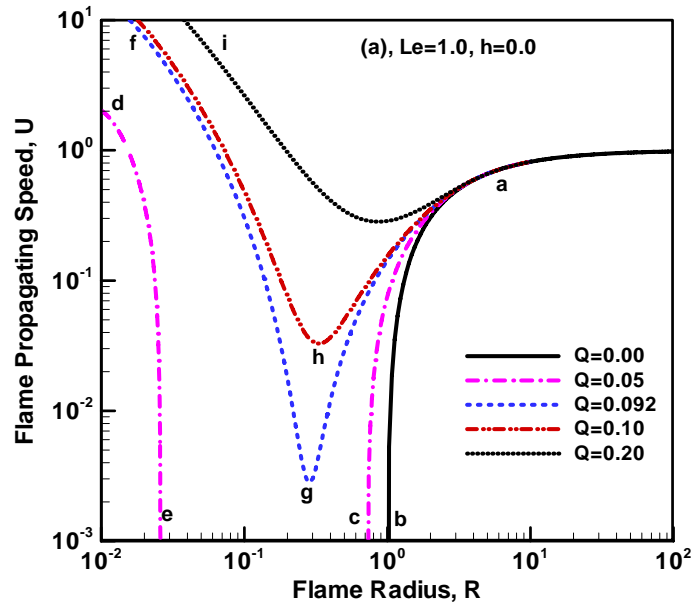


Figure 2.7: Flame propagation speed as a function of flame radius with different values of ignition power for  $Le=1.0$ , (a),  $h=0.0$ ; (b),  $h=0.01$ .

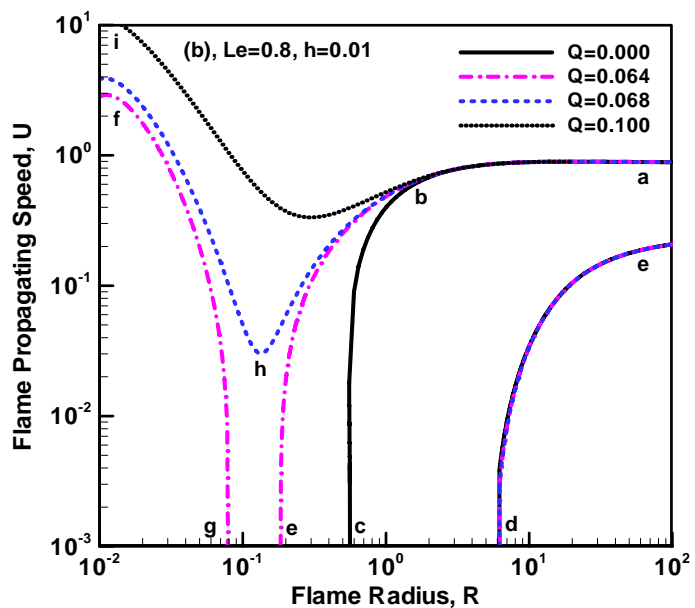
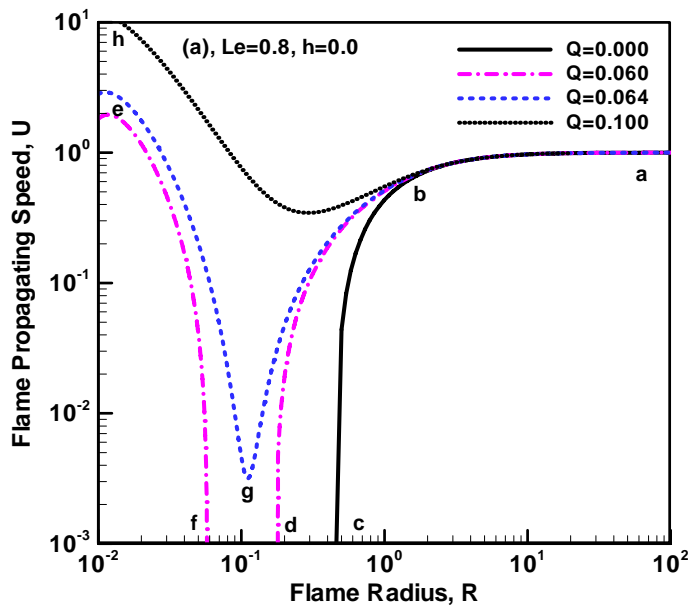


Figure 2.8: Flame propagation speed as a function of flame radius with different values of ignition power for  $Le=0.8$ , (a),  $h=0.0$ ; (b),  $h=0.01$ .

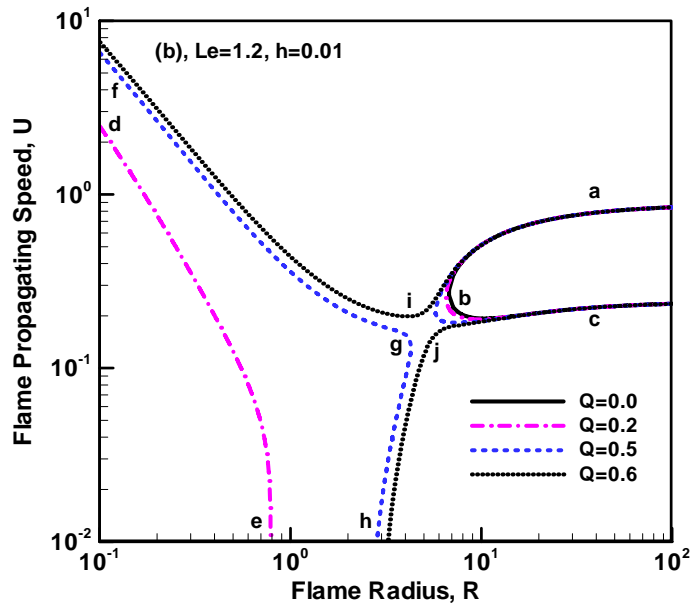
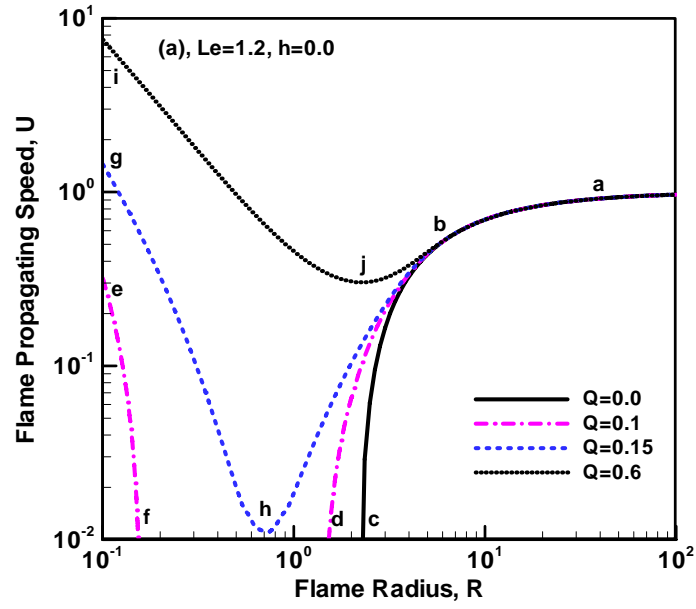


Figure 2.9: Flame propagation speed as a function of flame radius with different values of ignition power for  $Le=1.2$ , (a),  $h=0.0$ ; (b),  $h=0.01$ .

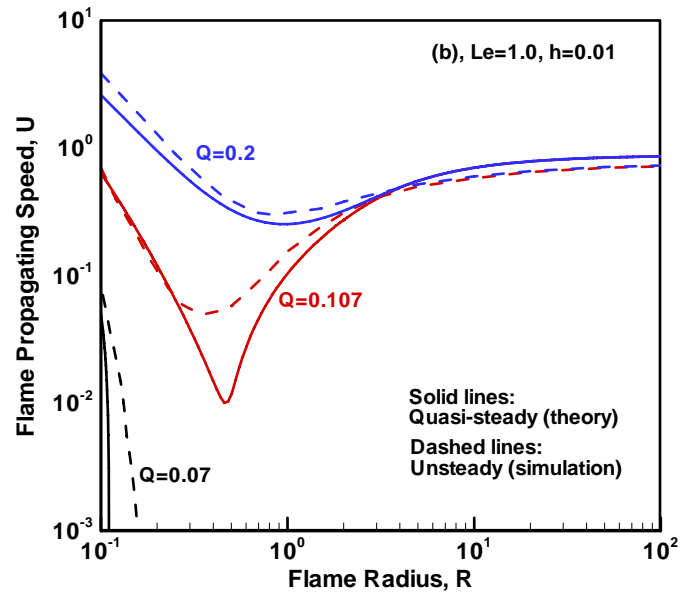
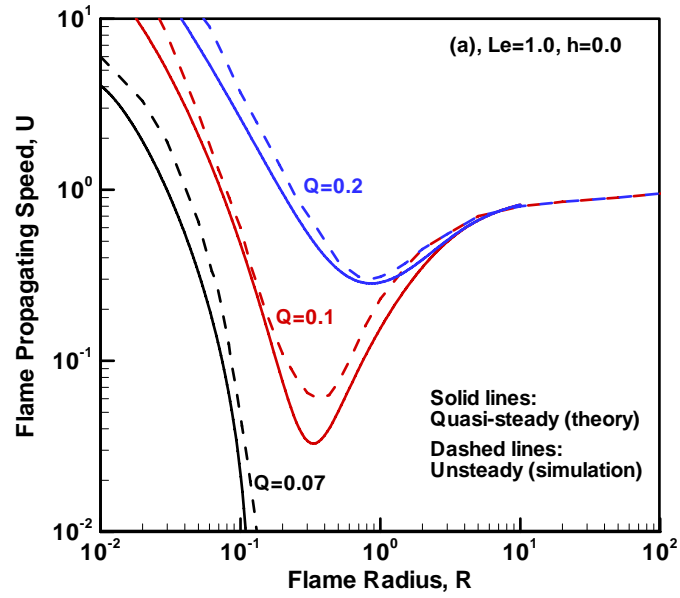


Figure 2.10: Comparison of flame propagation speeds predicted by numerical simulation and theoretical analysis for  $Le=1.0$ , (a),  $h=0.0$ ; (b),  $h=0.01$ .

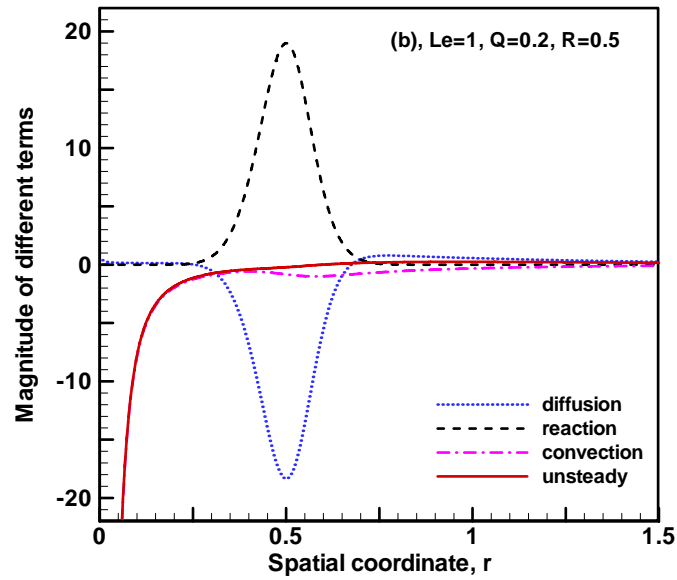
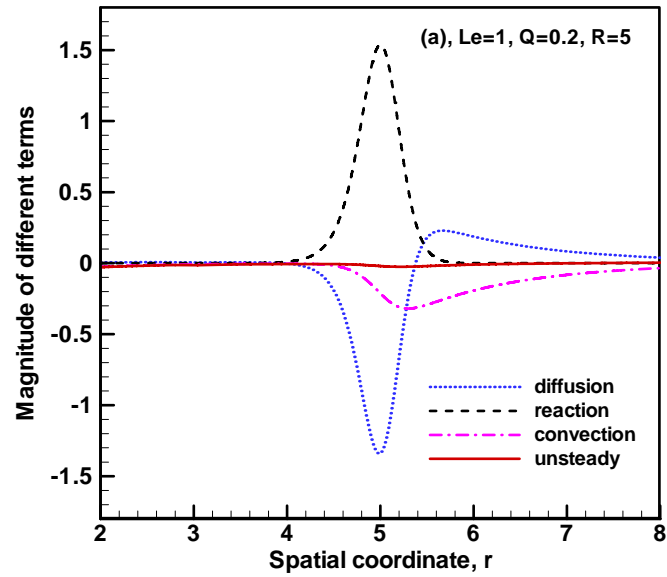


Figure 2.11: The unsteady term ( $\partial T/\partial t$ ), convection term ( $U\partial T/\partial r$ ), diffusion term ( $\partial(\partial T/r^2\partial r)/r^2\partial r$ ), and reaction term ( $\omega$ ) in equations (2.3a) predicted from numerical simulation for flames at different flame radii with  $Le=1.0$  and  $Q=0.2$ , (a),  $R=5.0$ ; (b),  $R=0.5$ .

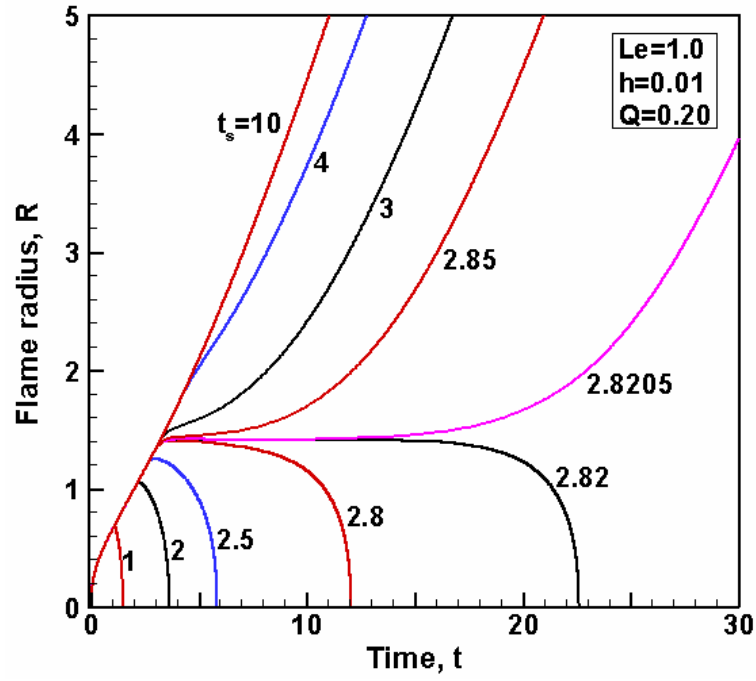


Figure 2.12: Flame-front trajectories obtained from numerical computations with different duration time ( $t_s$ ) at a given energy flux ( $Q=0.2$ ) for  $Le=1.0$  and  $h=0.01$ .

# **Chapter 3: Adaptive Simulation of Unsteady Reactive Flow (A-SURF)**

A time-accurate and space-adaptive numerical solver for A d a p t i v e s i m u l a t i o n o f U n s t e a d y R e a c t i v e F l o w, A-SURF, has been developed. The details on the governing equations, numerical methods, and code validations are presented in this chapter. By using A-SURF, high-fidelity numerical simulations will be carried out to validate the theoretical results and the kinetic models on spherical flame initiation and propagation in the following chapters.

## **3.1 Governing Equations for Unsteady Reactive Flows**

In A-SURF, the unsteady compressible Navier-Stokes equations are solved in order to account for the pressure change and pressure-induced compression waves produced during the flame propagation. The general conservation equations are presented in Section 3.1.1. The conservation equations require modelling of the viscous stress tensor, the diffusion velocities, the heat flux, and the chemical source terms. These models are shown in Section 3.1.2. The detailed description and/or derivation of the conservation and transport equations presented in this section can be found in (Williams 1985; Poinsoot and Veynante 2005; Law 2006).

### **3.1.1 General Conservation Equations**

#### ***3.1.1.1 Mass Conservation***

Conservation of mass is given by the continuity equation

$$\frac{\partial \rho}{\partial t} + \nabla \cdot (\rho V) = 0 \quad (3.1)$$

where  $\rho$  is the density and  $V=(u, v, w)$  is the velocity vector.

### 3.1.1.2 Momentum Conservation

Conservation of momentum is described by the Navier-Stokes equations

$$\frac{\partial(\rho V)}{\partial t} + \nabla \cdot (\rho V V) = \rho \sum (Y_k f_k) + \nabla \cdot \Pi \quad (3.2)$$

with  $f_k$  being the body force on species  $k$  (not considered in the present study) and  $\Pi$  the stress tensor, which is define as

$$\Pi = -PI + \tau \quad (3.3)$$

where  $P$  is the hydrostatic pressure,  $I$  the unit tensor, and  $\tau$  the viscous stress tensor. In this chapter,  $\sum$  denotes the summation with respect to  $k$  from 1 to  $NS$ , the total number of species.

### 3.1.1.3 Species Conservation

Conservation of species  $k$  is given by the species-mass-balance equation:

$$\frac{\partial(\rho Y_k)}{\partial t} + \nabla \cdot [\rho(V + V'_k)Y_k] = \omega_k \quad (3.4)$$

where  $Y_k$ ,  $V'_k$ , and  $\omega_k$  are the mass fraction, diffusion velocity vector and the production rate of species  $k$ , respectively. Note that the summation of the conservation equations for each species should recover to the mass conservation equation, equation (3.1). Therefore

$$\sum (\rho Y_k V'_k) = 0, \quad \sum \omega_k = 0 \quad (3.5)$$

### 3.1.1.4 Energy Conservation

Conservation of total energy is described by the following equation

$$\frac{\partial E}{\partial t} + \nabla \cdot [V(E + P)] = -\nabla \cdot q + \nabla \cdot (V \cdot \Pi) + Q_R + \rho \sum [Y_k f \cdot (V + V'_k)] \quad (3.6)$$

where  $E$ ,  $q$ , and  $Q_R$  are the total energy per unit volume, heat flux, and the heat source term (due, for example, to an electric spark, a laser or a radiative flux), respectively. The total energy is defined as

$$E = -P + \rho V^2 / 2 + \rho h, \quad h = \sum (Y_k h_k), \quad h_k = h_{k,0} + \int_{T_0}^T C_{P,k}(T) dT \quad (3.7)$$

where  $T$  is the temperature,  $h_k$ , the enthalpy of species  $k$ ,  $h_{k,0}$  the species enthalpy of formation at the reference temperature  $T_0$ , and  $C_{P,k}$  the specific heat of species  $k$  at constant pressure.

### 3.1.1.5 Equation of State

Assuming all species in the reactive flow to be ideal gas, the equation of state that couples density,  $\rho$ , partial pressure,  $P_k$ , and temperature,  $T$ , reads

$$P_k = Y_k \rho R^0 T / M_k \quad (3.8)$$

where  $R^0$  is the universal gas constant (8.314 J/(molK)) and  $M_k$  is the molecular weight of species  $k$ . The hydrostatic pressure  $P$  is equal to the summation of the partial pressures  $P_k$  of all species

$$P = \sum P_k = \rho R^0 T / \bar{M} \quad (3.9)$$

with  $\bar{M} = 1 / [\sum (Y_k / M_k)]$  being the mean molecular weight of the mixture.

## 3.1.2 Transport and Chemistry Models

### 3.1.2.1 Viscous Stress

The gas mixture is assumed to behave as a Newtonian fluid. Therefore, the viscous stress tensor can be modelled with Stokes' law of friction,

$$\Pi = -PI + \mu [(\nabla V + (\nabla V)^T - \frac{2}{3}(\nabla \cdot V)I)] \quad (3.10)$$

where  $\mu$  is the dynamic viscosity of the mixture. Note that Stokes' assumption of zero bulk viscosity is employed here.

### 3.1.2.2 Diffusion Velocity

The diffusion velocity can be obtained by solving the following system of equations

$$\begin{aligned} \nabla X_i = & \sum_{j=1}^{NS} \left( \frac{X_i X_j}{D_{i,j}} \right) (V'_j - V'_i) + (Y_i - X_i) \left( \frac{\nabla P}{P} \right) + \left( \frac{\rho}{P} \right) \sum_{j=1}^{NS} Y_i Y_j (f_i - f_j) \\ & + \sum_{j=1}^{NS} \left( \frac{X_i X_j}{\rho D_{i,j}} \right) \left( \frac{D_{T,j}}{Y_j} - \frac{D_{T,i}}{Y_i} \right) \left( \frac{\nabla T}{T} \right) \quad i = 1, \dots, NS \end{aligned} \quad (3.11)$$

where  $D_{i,j}$  is the binary mass diffusion coefficient of species  $i$  into species  $j$ ,  $X_k = Y_k \bar{M} / M_k$  the mole fraction, and  $D_{T,k}$  the thermal diffusion (the diffusion of mass due to temperature gradients: Soret effect) coefficient of species  $k$ . Mathematically, it is difficult and costly to solve these equations and simplified approach (for example Fick's law) is usually used. In the present study, the mixture-averaged formula (Kee et al. 1985) is employed. The diffusion velocity is composed of three parts (Kee et al. 1985):

$$V'_k = V'_{k,Y} + V'_{k,T} + V'_{k,C} \quad (3.12)$$

where  $V'_{k,Y}$  is the ordinary diffusion velocity and is given in the Curtiss-Hirschfelder approximation by

$$Y_k V'_{k,Y} = -D_{km} \nabla (Y_k \bar{M}) / \bar{M} \quad (3.13)$$

and  $D_{km}$  is the mixture-averaged diffusion coefficient of species  $k$ .

Furthermore,  $V'_{k,T}$  is the thermal diffusion velocity, which is included only for low molecular weight species (H, H<sub>2</sub> and He)

$$Y_k V'_{k,T} = -D_{km} \Theta_k M_k \nabla T / (T \bar{M}) \quad (3.14)$$

where  $\Theta_k$  is the thermal diffusion ratio of species  $k$ , the sign of which makes the lower molecular weight species diffuse from low to high temperature regions.

The correction velocity  $V'_{k,C}$  is included to insure compatibility of species and mass conservation equations. It is calculated according to the requirement given by the first equation in (3.5).

### 3.1.2.3 Heat Flux

The heat flux  $q$  includes a heat diffusion term expressed by the Fourier's law and a second term associated with the diffusion of species with different enthalpies.

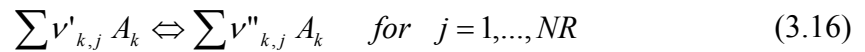
$$q = -\lambda \nabla T + \rho \sum h_k Y_k V'_k \quad (3.15)$$

where  $\lambda$  is the thermal conductivity of the gas mixture. Note that the Dufour effect (heat flux due to a mass gradient) is usually negligible and thus is not included in the present study.

In A-SURF, the CHEMKIN-TRANSPROT package (Kee et al. 1989) is implemented to calculate all the transport coefficients,  $\mu$ ,  $D_{km}$ ,  $\Theta_k$ , and  $\lambda$ .

### 3.1.2.4 Chemical Model

Consider a chemical system of  $NS$  species reacting through  $NR$  reactions



where  $A_k$  is a symbol for species  $k$ ,  $v'_{k,j}$  and  $v''_{k,j}$  are the molar stoichiometric coefficients of species  $k$  in reaction  $j$ . The production rate of species  $k$  is given by a general form of the law of mass action

$$\omega_k = M_k \sum_{j=1}^{NR} (v''_{k,j} - v'_{k,j}) \Psi_j \quad (3.17)$$

where  $\Psi_j$  is the progress rate of reaction  $j$ , written as

$$\Psi_j = K_{f,j} \prod_{k=1}^{NS} \left( \frac{\rho Y_k}{M_k} \right)^{v'_{k,j}} - K_{b,j} \prod_{k=1}^{NS} \left( \frac{\rho Y_k}{M_k} \right)^{v''_{k,j}} \quad (3.18)$$

where  $K_{f,j}$  and  $K_{b,j}$  are the forward and reverse rates of reaction  $j$ . The reaction rate for each elementary reaction is usually modeled using the empirical Arrhenius law

$$K_{f,j} = A_{f,j} T^{\beta_j} \exp\left(-\frac{E_j}{RT}\right) \quad (3.19)$$

where  $A_{f,j}$  is the pre-exponential constant,  $\beta_j$  the temperature exponent, and  $E_j$  the activation energy. These parameters are given by the detailed reaction mechanism and the CHEMKIN package (Kee et al. 1985; Kee et al. 1989) is used to evaluate the production rate.

In A-SURF, different detailed chemical mechanisms are utilized for different fuels. For example, the recent mechanism of 9 species and 25 reactions developed by Li et al. (Li et al. 2004) is employed for H<sub>2</sub>/air flames, and the GRI-MECH 3.0 mechanism (Smith et al.) is utilized for CH<sub>4</sub>/air flames.

### 3.2 Numerical Methods

Finite volume method is employed for discretizing the governing equations given in the previous section. The conservation equations for one-dimensional, multi-component, reactive compressible flows can be written as

$$\frac{\partial U}{\partial t} + \frac{\partial F(U)}{\partial x} + N \frac{G(U)}{x} = \frac{\partial F_v(U)}{\partial x} + S_R(U) \quad (3.20)$$

where the vectors  $U$ ,  $F(U)$ ,  $G(U)$ ,  $F_v(U)$ , and  $S_R(U)$  are defined as

$$\begin{aligned}
U &= \begin{pmatrix} \rho Y_1 \\ \rho Y_2 \\ \vdots \\ \rho Y_{NS} \\ \rho u \\ E \end{pmatrix}, & F(U) &= \begin{pmatrix} \rho u Y_1 \\ \rho u Y_2 \\ \vdots \\ \rho u Y_{NS} \\ \rho u^2 + P \\ (E + P)u \end{pmatrix}, & G(U) &= \begin{pmatrix} \rho u Y_1 \\ \rho u Y_2 \\ \vdots \\ \rho u Y_{NS} \\ \rho u^2 \\ (E + P)u \end{pmatrix}, \\
F_v(U) &= \begin{pmatrix} -x^{-N} (x^N \rho Y_1 V'_1)_x \\ -x^{-N} (x^N \rho Y_2 V'_2)_x \\ \vdots \\ -x^{-N} (x^N \rho Y_{NS} V'_{NS})_x \\ x^{-N} (x^N \tau_1)_x - N \tau_2 / x \\ -x^{-N} q + \Phi + Q_R \end{pmatrix}, & S_R &= \begin{pmatrix} \omega_1 \\ \omega_2 \\ \vdots \\ \omega_{NS} \\ 0 \\ 0 \end{pmatrix} \quad (3.21)
\end{aligned}$$

where  $N$  is the geometry factor ( $N=0$ , rectangular coordinate;  $N=1$ , cylindrical coordinate;  $N=2$  spherical coordinate).  $u$  is the flow velocity and  $x(=r)$  is the spatial coordinate.

The viscous stress and dissipation energy are:

$$\begin{aligned}
\tau_1 &= 2\mu \partial u / \partial x - (2/3)\mu x^{-N} \partial(x^N u) / \partial x \\
\tau_2 &= 2\mu u / x - (2/3)\mu x^{-N} \partial(x^N u) / \partial x \\
\Phi &= u[x^{-N} \partial(x^N \tau_1) / \partial x - N \tau_2 / x] + \Phi' \\
\Phi' &= \mu \{ 2(\partial u / \partial x)^2 + 2N(u/x)^2 - (2/3)[x^{-N} \partial(x^N u) / \partial x]^2 \}
\end{aligned} \quad (3.22)$$

The heat flux is:

$$q = -x^N K \partial T / \partial x + x^N \rho \sum (h_k Y_k V'_k) \quad (3.23)$$

The corrected diffusion velocities (to ensure  $\sum Y_k V'_k = 0$ ) are:

$$\begin{aligned}
-Y_k V'_k &= D_{km} \nabla(Y_k \bar{M}) / \bar{M} + D_{km} \Theta_k M_k \nabla T / (T \bar{M}) - Y_k V'_{k,C} \\
\text{with } V'_{k,C} &= \sum [D_{km} \nabla(Y_k \bar{M}) / \bar{M} + D_{km} \Theta_k M_k \nabla T / (T \bar{M})]
\end{aligned} \quad (3.24)$$

### 3.2.1 Fractional-step Procedure

To solve the conservation system (3.20), the stiff source term  $S_R$  is treated by the

fractional-step procedure (Toro 1999). In the first fractional step, the non-reactive flow is solved

$$\left. \begin{array}{l} PDE : \frac{\partial U}{\partial t} + \frac{\partial F(U)}{\partial x} + N \frac{G(U)}{x} = \frac{\partial F_v(U)}{\partial x} \\ IC : U(x, t^n) = U^n \end{array} \right\} \Rightarrow \bar{U}^{n+1} \quad (3.25)$$

The chemistry is solved in the second fractional step for a homogeneous system

$$\left. \begin{array}{l} ODE : \frac{dU}{dt} = S_R(U) \\ IC : \bar{U}^{n+1} \end{array} \right\} \Rightarrow U^{n+1} \quad (3.26)$$

The two steps given by equations (3.25) and (3.26) are denoted by operator  $C^{(t)}$  and operator  $S^{(t)}$ , respectively. Based on the above splitting, the solution can be evolved from its initial value  $U^n$  at time  $t^n$ , by one time step of size  $\Delta t$ , to a value  $U^{n+1}$  at time  $t^{n+1} = t^n + \Delta t$ ,

$$U^{n+1} = S^{\Delta t} C^{\Delta t} (U^n) \quad (3.27)$$

The above procedure for solving the inhomogeneous system given by equation (3.20) is exceedingly simple but only has first-order accuracy in time, when  $S$  and  $C$  are at least first-order accurate solution operators (Toro 1999). A scheme with second-order accuracy in time called Strang splitting (Strang 1968) is

$$U^{n+1} = S^{\Delta t/2} C^{\Delta t} S^{\Delta t/2} (U^n) \quad (3.28)$$

where  $S$  and  $C$  are at least second-order accurate solution operators in time.

For the  $S$  operator, the mass fraction of species are updated by using the VODE solver (Brown et al. 1989). Note that the density  $\rho$ , momentum  $\rho u$ , and total energy  $E$  remain to be constant during updating the mass fraction of all the species, after which the temperature is solved according to the definition of total energy, equation (3.7):

$$F(T) = R^0 T / \bar{M} - u^2 / 2 - h + E / \rho = 0 \quad (3.29)$$

where the equation of state, equation (3.9), is utilized to eliminate the pressure term. The above equation can be solved numerically by using the Newton iteration method and the updated temperature at each iteration step is

$$T^{new} = T^{old} - F(T^{old}) / (R^0 / \bar{M} - C_p) \quad (3.30)$$

For the  $C$  operator, the details are presented in the following.

### 3.2.2 Finite Volume Method

The unsteady convection-diffusion system solved in the  $C$  operator is discretized by applying a Godunov-type upwind finite volume spatial discretization procedure (Toro 1999). The integral form of the conservation system (3.20) without the source term is

$$\int \frac{\partial U}{\partial t} dx + \int \frac{\partial F(U)}{\partial x} dx + \int \frac{NG(U)}{x} dx = \int \frac{\partial F_v(U)}{\partial x} dx \quad (3.31)$$

A conservative finite-volume scheme can be obtained by evaluating the integral over a control volume representing the domain of interest. Here we consider the control volume over space from  $x_{i-1/2}$  to  $x_{i+1/2}$ . For this control volume, the above equation becomes

$$\begin{aligned} \frac{d}{dt} \int_{x_{i-1/2}}^{x_{i+1/2}} U(x,t) dx + [F(x_{i+1/2},t) - F(x_{i-1/2},t)] + \int_{x_{i-1/2}}^{x_{i+1/2}} \frac{NG(U)}{x} dx \\ = [F_v(x_{i+1/2},t) - F_v(x_{i-1/2},t)] \end{aligned} \quad (3.32)$$

Explicit time marching (Toro 1999) is utilized in the  $C$  operator and the above equation is solved to evolve the solution from the current time step  $t^n$  to the next time step  $t^{n+1} = t^n + \Delta t$ , where  $\Delta t$  is the time step length which is restricted by the CFL number for computational stability (Toro 1999).

The MUSCL-Hancock (van Leer 1984) and central difference schemes, both of second-order accuracy, are employed to evaluate the convective flux,  $F(x_{i+1/2},t)$ , and

diffusive flux,  $F_v(x_{i+1/2}, t)$ , in equation (3.32), respectively. The ordinary differential equation, (3.32), can be written in the following form

$$\frac{d\bar{U}}{dt} = L(\bar{U}) \quad (3.33)$$

where  $\bar{U}$  is the cell average of the solution state. At cell  $i$ , it is

$$\bar{U}_i(t) = \frac{1}{x_{i+1/2} - x_{i-1/2}} \int_{x_{i-1/2}}^{x_{i+1/2}} U(x, t) dx \quad (3.34)$$

To update the state  $\bar{U}^n$  at the current time step to state  $\bar{U}^{n+1}$  at the next time step according to equation (3.33), a second-order TVD Runge-Kutta method (Gottlieb and Shu 1998) can be utilized

$$\begin{aligned} \bar{U}^{(1)} &= \bar{U}^n + \Delta t L(\bar{U}^n) \\ \bar{U}^{n+1} &= \frac{1}{2} \bar{U}^n + \frac{1}{2} \bar{U}^{(1)} + \frac{1}{2} \Delta t L(\bar{U}^{(1)}) \end{aligned} \quad (3.35)$$

### 3.2.3 Locally Adaptive Mesh

Most combustion phenomena in nature contain many disparate length scales. Therefore, a numerical method should be able to adapt resolutions to regions with different length scales; otherwise computer resources will be largely wasted in regions where the solutions do not require the maximum resolution. Mesh adaptation is just a way to distribute mesh cells in the interested regions so as to resolve a physical phenomenon economically.

An unstructured  $h$ -refinement (the cells in the regions of interest are locally subdivided, and some other cells may be coarsened in the regions of less importance) is employed in A-SURF. Local mesh addition and removal are based on the first-order and second-order gradients of the temperature, velocity and major species distributions. The

present adaptive mesh for one-dimensional and two-dimensional simulations is based on the same algorithm developed in (Sun 1998; Sun and Takayama 1999). The details can be found in (Sun 1998; Sun and Takayama 1999) and thus not repeated here.

For propagating flames investigated in the present study, the reaction zone is usually very thin and the flame thickness is strongly affected by pressure. Therefore, in order to maintain adequate numerical resolution of a moving flame front without the need to use hundreds of thousands of grid points, adaptive mesh with seven to ten grid levels is utilized in this study and the moving reaction zone is always fully covered by the finest meshes of  $32 \mu m$  to  $4 \mu m$  in width.

It is noted that the numerical methods described above are for one-dimensional reactive flows whose conservation equations are given in (3.20). For two-dimensional problems, the same fractional-step procedure and finite volume method are implemented in A-SURF.

### **3.3 Validation and Examples**

To demonstrate the accuracy and robustness of A-SURF, simulation results from A-SURF for different problems are compared with their exact solutions or predictions by other well-developed algorithms.

Simulation of a modified version of the popular Sod's test (Sod 1978; Toro 1999) is carried out to illustrate the performance of A-SURF on one-dimensional, time dependent Euler equations. Figure 3.1 shows the comparison between numerical and exact solutions of the temperature distribution. It is seen that the left-propagating expansion fan, right-propagating contact line, and right-propagating shock wave are all well resolved and the numerical prediction agrees well with the exact solution. Moreover,

according to the mesh level distribution (the mesh size is inversely proportional to  $2^{\text{mesh level}}$ ), the finest meshes are focused on the expansion fan, contact line, and shock wave. Therefore, the adaptive mesh utilized in A-SURF helps to resolve these physical phenomena economically.

A one-dimensional, time dependent convection-diffusion problem is utilized to show the performance of A-SURF on the Navier-Stokes equations. The governing equations and initial conditions for unsteady convection (with constant velocity,  $u$ ) and diffusion (at constant mass diffusivity,  $D_{H_2}$ ) of hydrogen can be written as (assuming constant density,  $\rho(x,t) \equiv 1$ )

$$\frac{dY_{H_2}}{dt} + \frac{d}{dx}(uY_{H_2}) = \frac{d^2}{dx^2}(D_{H_2}Y_{H_2}) \quad (3.36)$$

$$Y_{H_2}(x, t = 0) = \begin{cases} 0.06 & x < 20\text{cm} \\ 0.0 & x > 20\text{cm} \end{cases} \quad (3.37)$$

The above problem has the following exact solution

$$Y_{H_2}(x, t) = 0.03 - 0.03 \cdot \text{erf}\left(\frac{x - ut}{2\sqrt{D_{H_2} \cdot t}}\right), \text{ with } \text{erf}(y) = \frac{2}{\sqrt{\pi}} \int_0^y e^{-s^2} ds \quad (3.38)$$

Figure 3.2 shows the hydrogen mass fraction profiles at different times. The numerical prediction by A-SURF is seen to agree very well with the exact solution given by equation (3.38). Also it is seen that the finest meshes are focused on the region with large gradient of hydrogen mass fraction due to the mesh adaptation. Therefore, A-SURF could be utilized to accurately and efficiently simulate one-dimensional unsteady convection-diffusion problems.

To illustrate the performance of A-SURF on one-dimensional propagating flames, PREMIX (Kee et al. 1985) is employed here to make comparison with A-SURF since

PREMIX is widely utilized to simulate one-dimensional planar flames in combustion research. Figure 3.3 shows the simulation results for a planar stoichiometric CH<sub>4</sub>/air flame from both A-SURF and PREMIX. The GRI-MECH 3.0 mechanism (Smith et al.) is utilized in both simulations. It is seen that the temperature distribution predicted by A-SURF is nearly the same as that by PREMIX. The relative differences of adiabatic flame temperature,  $T_{ad}$ , and laminar flame speed,  $S_u$ , between the predictions by A-SURF and PREMIX are 0.27% and 1.34%, respectively. Simulations of one-dimensional planar flames for other fuels were also conducted and very good agreements between predictions from A-SURF and PREMIX were obtained. Therefore, A-SURF can accurately model one-dimensional flames.

Figure 3.4 shows the temperature and mesh level distribution at different times for a propagating spherical CH<sub>4</sub>/O<sub>2</sub>/CO<sub>2</sub> (15%/30%/55% by volume) flame (the spectral-dependent radiation, discussed in Chapter 6, is not considered here). The flame front is shown to be covered by the finest meshes ( $L=6$  in mesh level and  $\Delta x=16 \mu m$  in mesh size). Moreover, the finest meshes move together with the flame front and thus the total mesh number does change during flame propagation. Figure 3.5 shows the flame propagation speed as a function of flame radius for different propagating spherical H<sub>2</sub>/air and CH<sub>4</sub>/air flames. The computation domain is a sphere of 30 cm in radius, which is the same that of the spherical chamber used in experiments (Taylor 1991). As shown in figure 3.5, good agreement between simulations and experiments is obtained. The laminar flame speeds of methane/air at different equivalence ratios from simulations (predicted by both A-SURF and PREMIX) and experiments (Gu et al. 2000; Rozenchan et al. 2003; Qin and Ju 2005) are shown in figure 3.6. It is observed that the laminar

flame speeds of methane/air predicted by A-SURF agree very well with those by PREMIX and the experimental results. The maximum relative differences between the predictions from A-SURF and PREMIX over the entire test range is less than 2%, which demonstrates the robustness and accuracy of the present computation methods. The laminar flame speeds and burned Markstein length of hydrogen/air flames as a function of equivalence ratio are shown in figure 3.7. Again, very good agreement among the predictions from A-SURF and PREMIX is obtained. According to all the tests shown in figures 3.3 to 3.7, A-SURF can accurately model the propagating flames. Therefore, it can be employed to validate the theoretical models for spherical flame initiation and propagation in the following chapters. To the authors' knowledge, A-SURF is currently the only code available to simulate propagating flames based on compressible governing equations (thus acoustics are resolved) using detailed chemical mechanisms and an adaptive mesh.

The above discussion is on one-dimensional problems. Some preliminary results on two-dimensional simulations using A-SURF are shown in figures 3.8 to 3.12.

In order to demonstrate the performance of two-dimensional adaptive mesh utilized in A-SURF, a propagating flame with specified propagating flame front,  $R_f(t) = (R_0 + U \cdot t) \cdot [1 + 0.05 \cdot \sin(24 \cdot \theta)]$ , is studied. No flow is considered in the simulation and mesh adaptation is based on the temperature gradient which changes with the propagation of the flame front,  $R_f(t)$ . The temperature distribution is given by

$$T(x, y, t) = 1300 - 1000 \frac{e^S - 1}{e^S + 1} \quad \text{with} \quad S = 200 \left( \frac{\sqrt{x^2 + y^2}}{R_f(t)} - 1 \right) \quad (3.39)$$

Therefore, the temperature of the unburned and burned gases is 300 K and 2300 K,

respectively. Adaptive mesh spanned seven levels, from the base mesh, level  $L=0$ , to the finest mesh, level  $L=6$  (mesh size changes from  $2048 \times 2048 \mu\text{m}^2$  to  $32 \times 32 \mu\text{m}^2$  for the rectangular meshes shown in figure 3.8) are implemented in the simulation. Figure 3.8 shows that the flame front is covered by the finest mesh (which moves together with the flame front) due to the appearance of the largest temperature gradient there, and that both quadrilateral and rectangular meshes can be utilized in the simulation. Therefore, this example shows that A-SURF can efficiently resolve two-dimensional propagating flames using locally adaptive meshes. Moreover, with the help of quadrilateral meshes, any two-dimensional computational domain with arbitrary boundary geometries can be accurately resolved by A-SURF.

To illustrate the performance of A-SURF on two-dimensional, time dependent Euler equations, a numerical simulation of cylindrical explosion by A-SURF was conducted. For this problem, the initial conditions are described by two thermodynamic states separated by a cylindrical interface: high pressure state inside and low pressure state outside. During the evolution, an outwardly-propagating shock, an outwardly-propagating contact surface, and an inwardly-propagating rarefaction wave appear. This is similar to the Sod's problem (Sod 1978; Toro 1999) discussed at the beginning of this section. Due to the axisymmetry of this problem, it can be studied by both one-dimensional and two-dimensional simulations. Figure 3.9(a) shows a comparison between the one-dimensional radial solution (very high resolution which could be regarded as the exact solution) and the two-dimensional solution along the radial line that is coincident with the x-axis. It is seen that the prediction from the two-dimensional simulation agrees very well with the exact solution. Comparison along

other radial directions gives virtually identical results. This is confirmed by the very symmetric character of the numerical solution of density distribution shown in figure 3.9(b), demonstrating that A-SURF can accurately resolve the rarefaction wave, contact surface, and shock wave in two-dimensional simulations. Similar to the one-dimensional simulation shown in figure 3.1, the finest meshes are focused on the expansion fan, contact line, and shock in the two-dimensional simulation. Moreover, nearly the same results were obtained from simulations using rectangular and quadrilateral meshes (similar to the two types of meshes shown in figure 3.8).

Another example of the two-dimensional simulation based on Euler equations is shown in figure 3.10. The wave interaction problem (Müller 2000) is studied using A-SURF. The initial configuration is determined by four states corresponding to the four quadrants of the coordinate system (Müller 2000):

$$(\rho, u_x, u_y, P) = \begin{cases} (1 \text{ Kg/m}^3, 1 \text{ m/s}, 1 \text{ m/s}, 1 \text{ atm}) & \text{if } x \cdot y \geq 0 \\ (4 \text{ Kg/m}^3, 0 \text{ m/s}, 0 \text{ m/s}, 4 \text{ atm}) & \text{if } x \cdot y < 0 \end{cases} \quad (3.40)$$

Away from the origin of the coordinate system, the solution, as shown in figure 3.10(a), exhibits a one-dimensional wave pattern consisting of a rarefaction wave, a contact surface and a shock wave. Close to the origin, the different one-dimensional waves interact forming a genuinely two-dimensional wave pattern. The density contours shown in figure 3.10(a) agree well with those reported in (Müller 2000). Moreover, figure 3.10(b) shows that the finest adaptive meshes efficiently cover the position where the waves and their interactions appear. These results show that the two-dimensional simulation can accurately resolve the wave interactions.

A-SURF is also utilized to simulate propagating two-dimensional premixed flames with one-step irreversible chemical mechanism. Figures 3.11 and 3.12 show the

flame fronts of outwardly propagating cylindrical flames at different times for mixtures with different Lewis numbers. It is well known that laminar premixed flames are subjected to two modes of cellular instability: hydrodynamic and thermal-diffusive (Williams 1985; Law 2006). Hydrodynamic instability is caused by the density disparity across the flame and it always exists; while thermal-diffusive instability is caused by the preferential diffusion between heat and mass and it occurs when the global Lewis number is less than one (Williams 1985; Law 2006). For an outwardly propagating flame, its positive stretch tends to inhibit the development of cellular instability, especially for mixtures with larger Lewis numbers (Law 2006; Jomaas 2008). As a result, the cellular instability occurs earlier as the flame expands when the Lewis number is smaller. Figure 3.11 shows that the cellular instability is strongest for flames at  $Le=0.5$ , since both hydrodynamic and thermal-diffusion instabilities occur. For  $Le=1.0$ , only the hydrodynamic instability occurs because the flame is highly stretched and curved when it is small, hence preventing the onset of cellular instabilities. Consequently, the flame front is smooth at the beginning. Cellular instabilities appear when the flame radius becomes larger because both the curvature and stretch are smaller, as shown by figure 3.12. For  $Le=2.0$ , the flame front is much smoother than that of  $Le=1.0$  due to the stabilization caused by the positive stretch. The results shown in figures 3.11 and 3.12 agree qualitatively with those from experiments on outwardly propagating spherical flames (Jomaas 2008). Figure 3.13 shows the flame front of a propagating cylindrical lean hydrogen/air flame at time  $t=3.92$  mS. Detailed chemical mechanism for hydrogen/air (Li et al. 2004) are employed in the simulation. For hydrogen/air at equivalence ratio  $\phi=0.5$ , the Lewis number is around 0.5 (Law 2006). Therefore strong cellular instabilities are

observed.

In summary, based on the numerical validations and tests presented above, A-SURF can be utilized to accurately and efficiently simulate one-dimensional propagating flames with detailed chemical mechanisms. For two-dimensional flame simulations with large detailed chemistry (for large hydrocarbon fuels) treated by a single computer, the computation time will be on the order of a month and thus effective parallelization and chemical mechanism reduction are needed. In the following chapters, only one-dimensional simulations using A-SURF will be conducted.

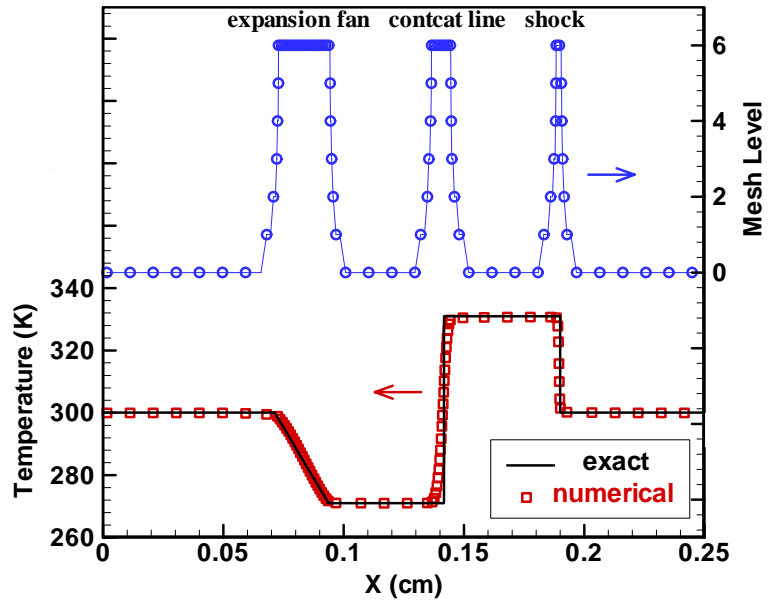


Figure 3.1: Mesh level and temperature distribution at time  $t=100 \mu s$ .

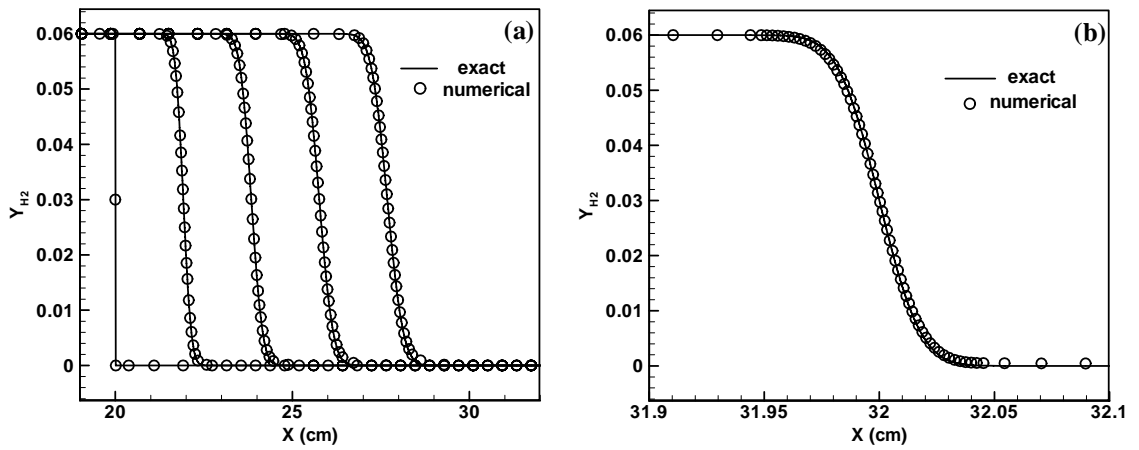


Figure 3.2: Distribution of hydrogen mass fraction: (a) at time  $t=0, 19200, 38400, 57600, 76800 \mu s$  with  $u=1 m/s$  and  $D_{H_2}=8 \cdot 10^{-5} m^2/s$ ; (b) at  $t=120 \mu s$  with  $u=1000 m/s$  and  $D_{H_2}=8 \cdot 10^{-5} m^2/s$ .

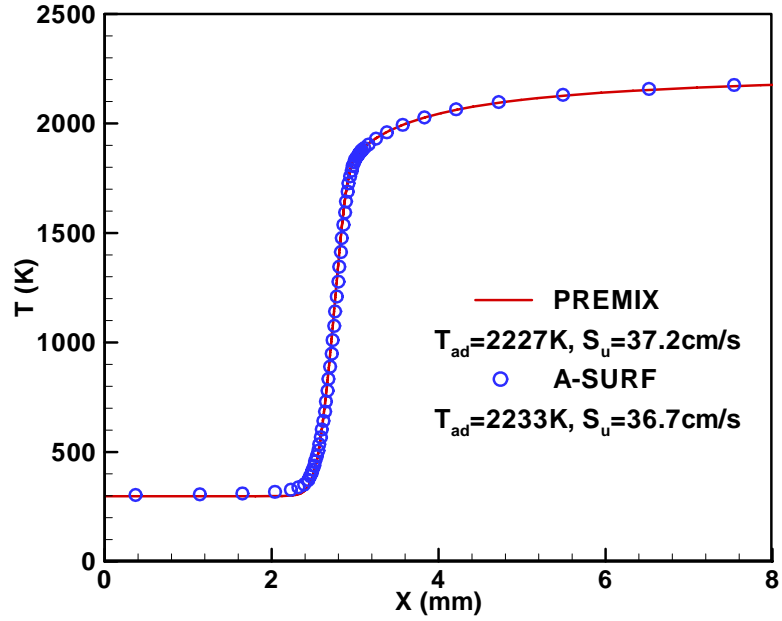


Figure 3.3: Temperature distribution for a propagating planar stoichiometric  $\text{CH}_4/\text{air}$  flame at  $T_u=298\text{ K}$  and  $P=1\text{ atm}$ .

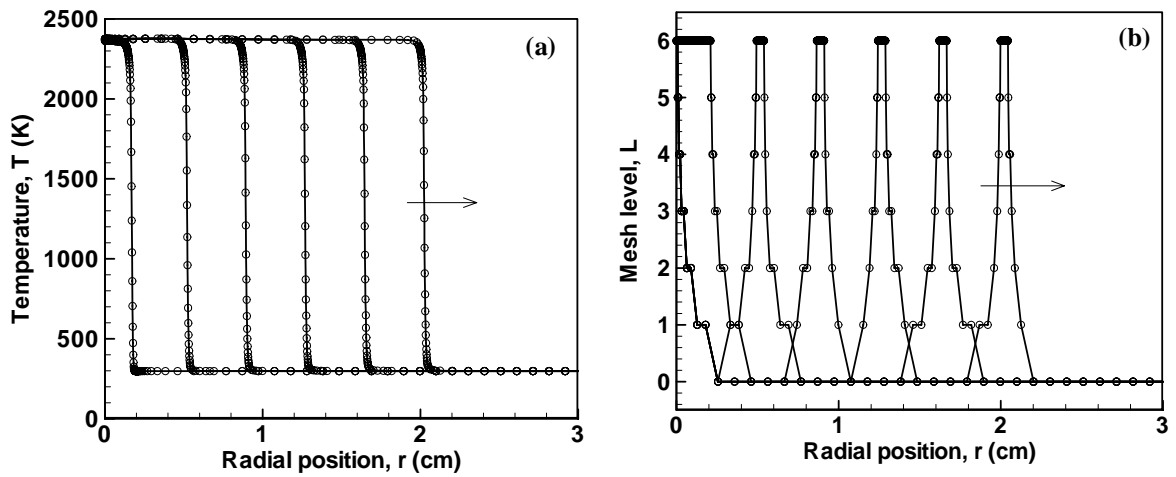


Figure 3.4: Temperature and mesh level distribution at different times for a propagating spherical  $\text{CH}_4/\text{O}_2/\text{CO}_2$  (15%/30%/55% in volume) flame at  $T_u=298\text{ K}$  and  $P=1\text{ atm}$ . The base mesh ( $L=0$ ) size is  $\Delta x=1024\ \mu\text{m}$  and the finest mesh ( $L=6$ ) size is  $\Delta x=16\ \mu\text{m}$ .

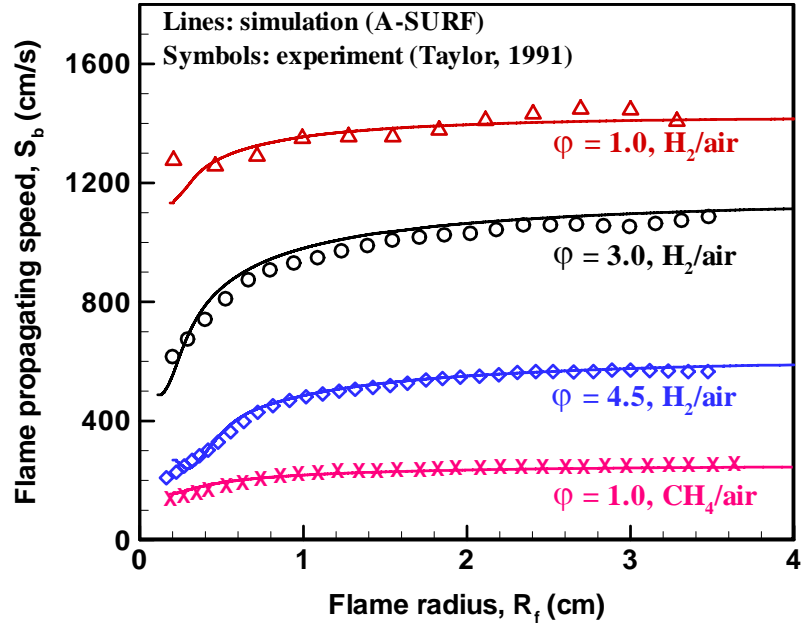


Figure 3.5: Flame propagation speed as a function of flame radius for different spherical  $\text{H}_2/\text{air}$  and  $\text{CH}_4/\text{air}$  flames.

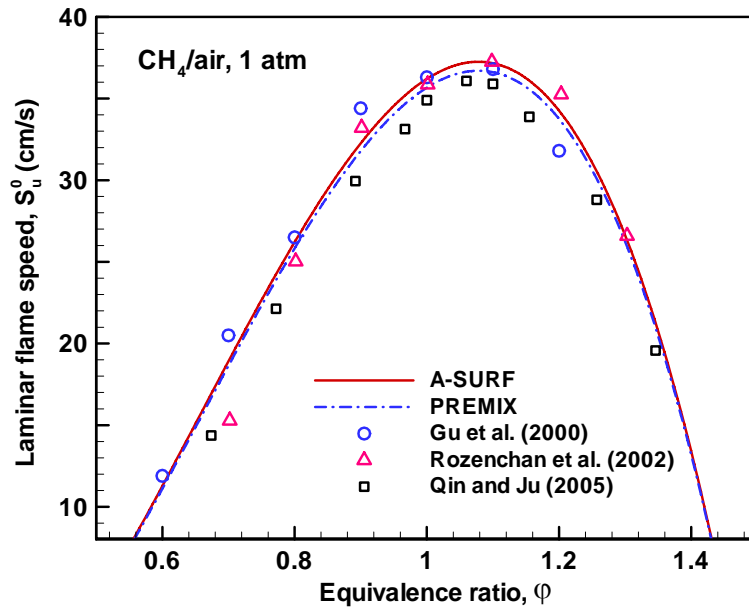


Figure 3.6: Laminar flame speed of  $\text{CH}_4/\text{air}$  flames as a function of equivalence ratio at  $T_u=298\text{ K}$  and  $P=1\text{ atm}$ .

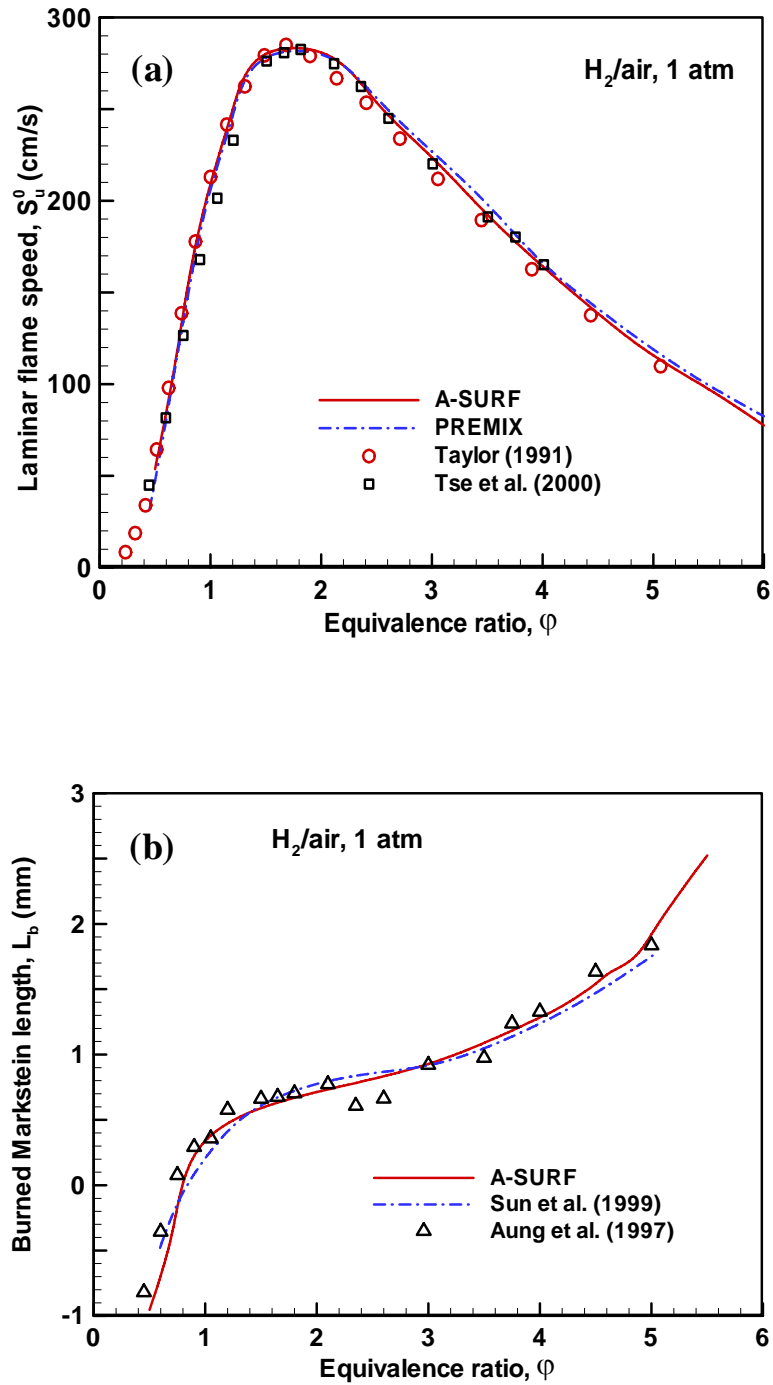


Figure 3.7: (a) Laminar flame speeds and (b) burned Markstein length of  $H_2/air$  flames as a function of equivalence ratio at  $T_u=298 K$  and  $P=1 atm$ .

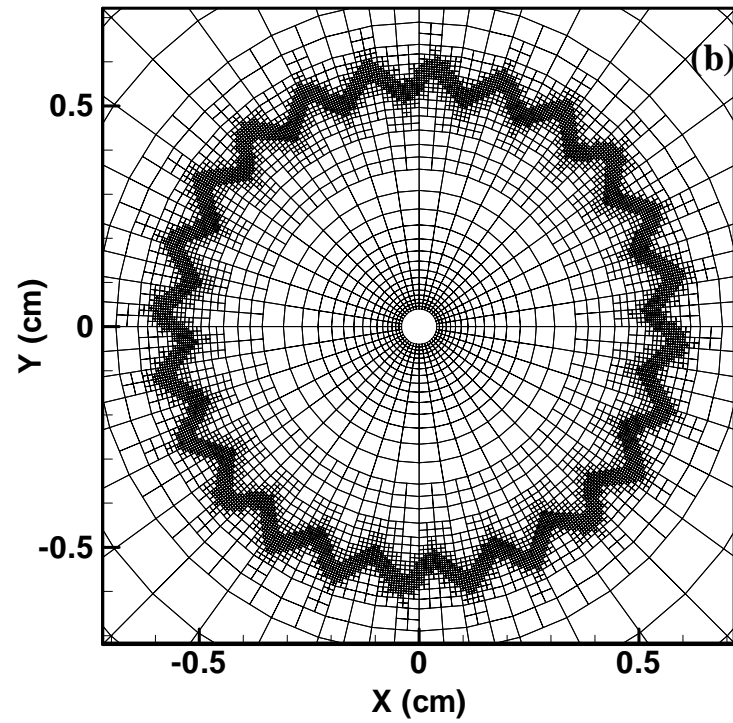
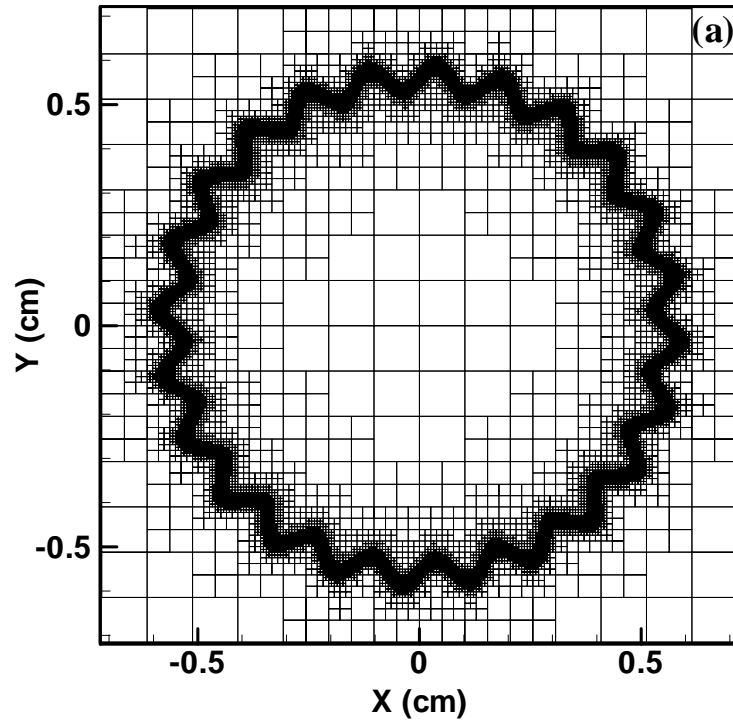


Figure 3.8: (a) Rectangular and (b) quadrilateral adaptive mesh following the moving flame front given by  $R_f(t) = (R_{f0} + U \cdot t) \cdot [1 + 0.05 \cdot \sin(24 \cdot \theta)]$  at time  $t = 0.01$  s ( $R_{f0} = 0.05$  cm,  $U = 50$  cm/s).

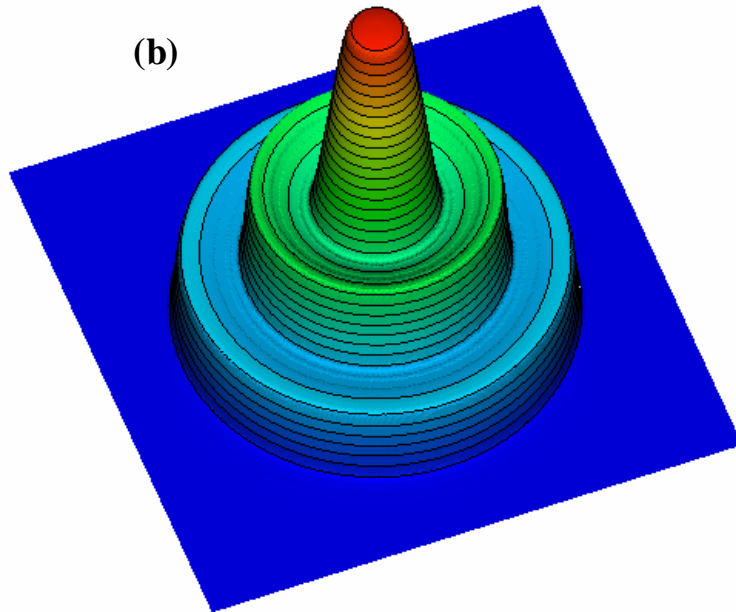
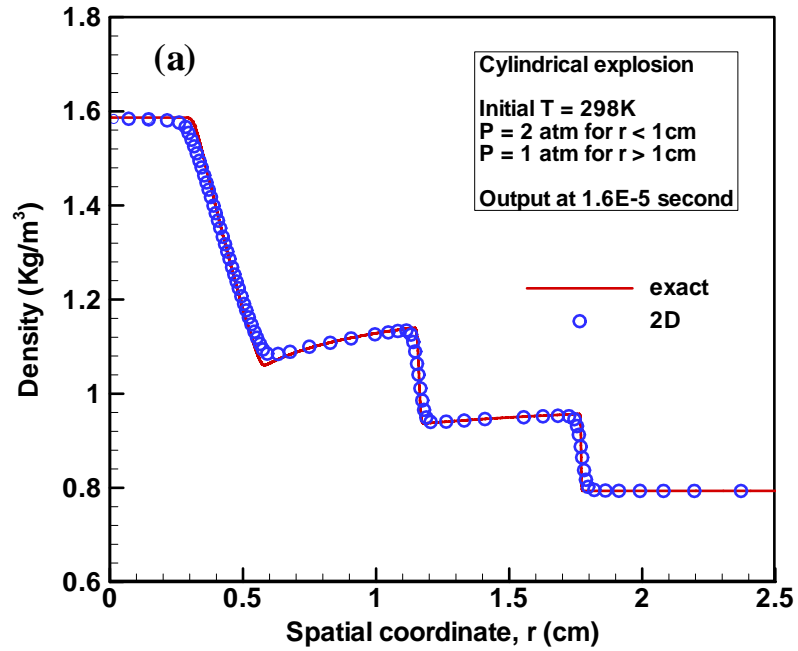


Figure 3.9: Two dimensional simulation of cylindrical explosion: (a), comparison between the exact and 2D solutions; (b), the density distribution.

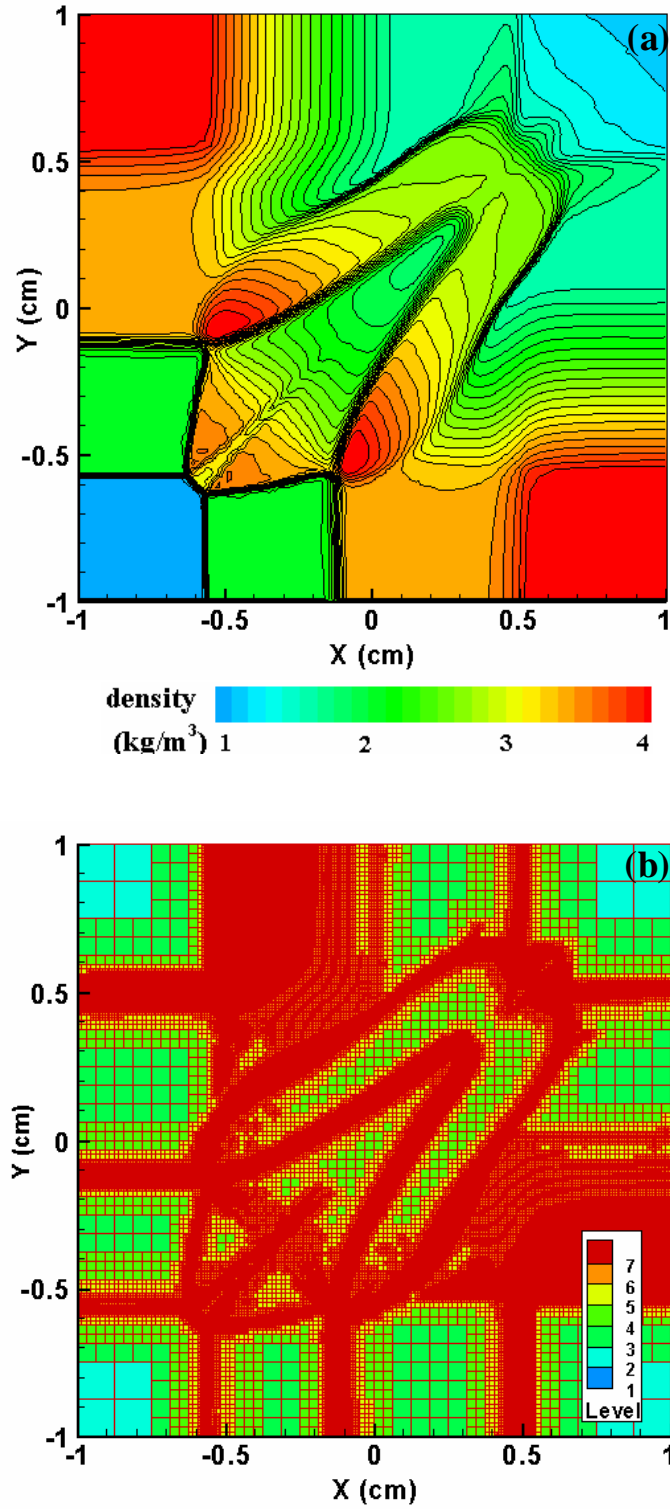


Figure 3.10: Two dimensional simulation of wave interactions: (a), density contours; (b), adaptive mesh. Output time:  $12 \mu\text{s}$ ; mesh size:  $\Delta x_0 = 5 \text{ mm}$ ,  $\Delta x = \Delta x_0 / 2^{\text{Level}}$ .

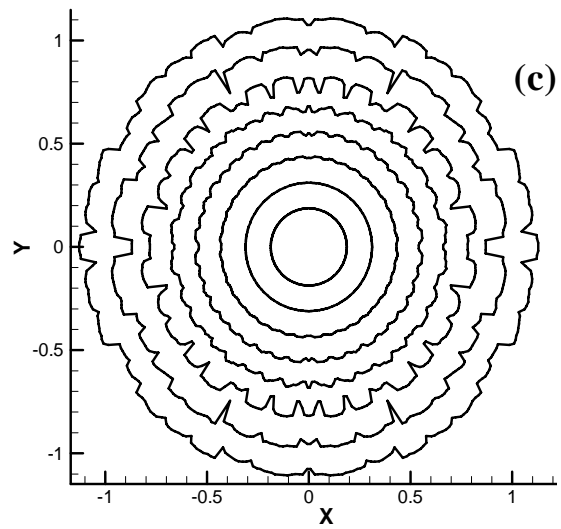
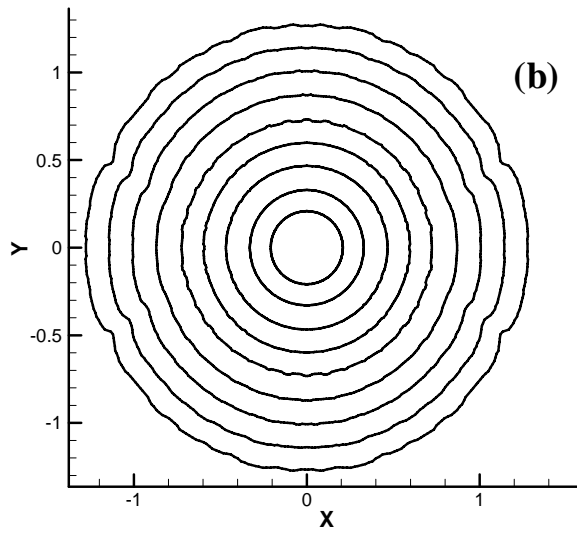
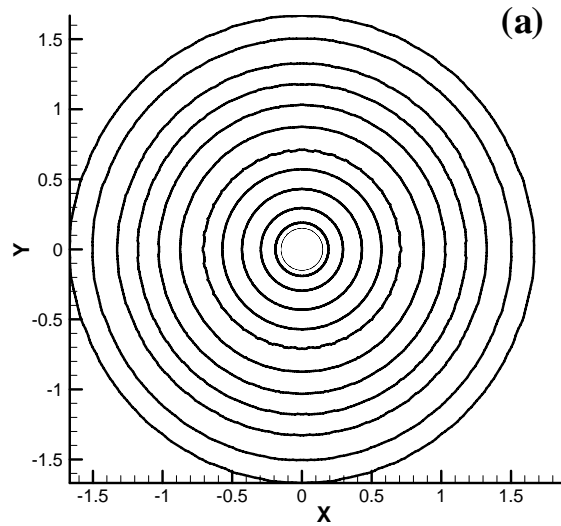


Figure 3.11: Flame fronts of propagating cylindrical flames at different times: (a),  $Le=2.0$ ; (b),  $Le=1.0$ ; (c),  $Le=0.5$  (the units of both  $x$  and  $y$  coordinates are  $cm$ ).

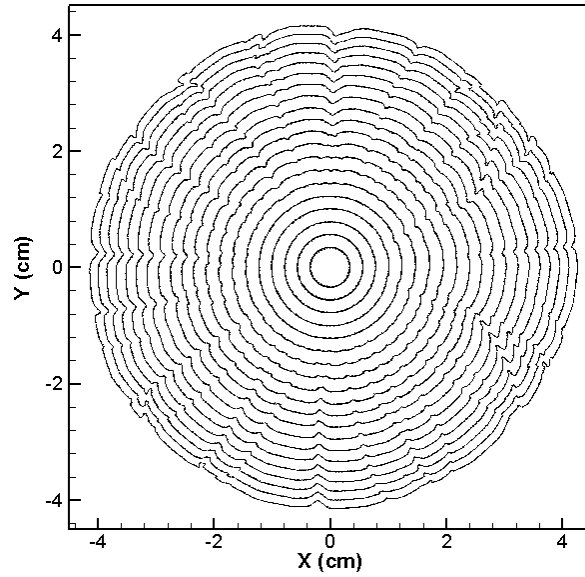


Figure 3.12: Flame fronts of a propagating cylindrical flame at different times with  $Le=1.0$ .

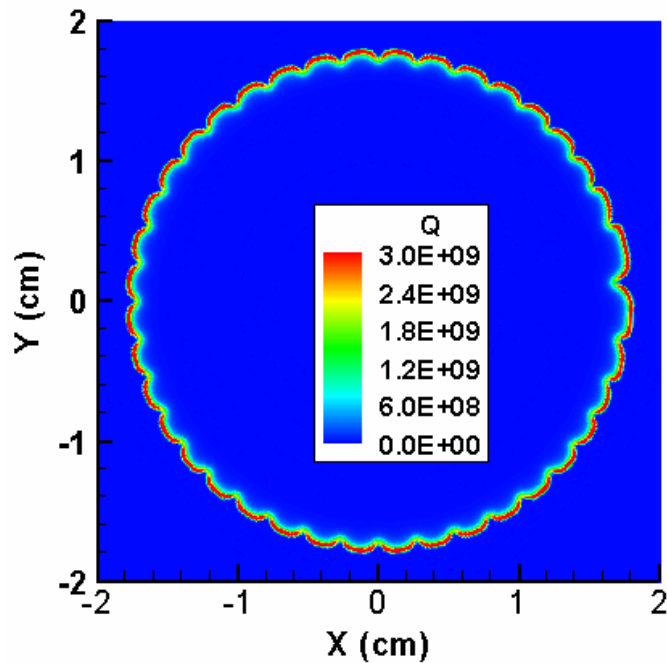


Figure 3.13: Flame front of a propagating cylindrical lean hydrogen/air (equivalence ratio  $\phi=0.5$ ) flame at time  $t=3.92$  ms.  $Q$  is the total heat release in the unit of  $J/(m^3S)$ .

## **Chapter 4: Critical Flame Radius and Minimum Ignition Energy for Spherical Flame Initiation**

In this chapter, the theory and numerical solver developed in the previous two chapters will be utilized to study spherical flame initiation. The objectives are to find the controlling length scale for spherical flame initiation and to reveal its relationship with the minimum ignition energy (MIE). In the following we shall first provide a summary of the theoretical results so as to provide a unified interpretation of the role of critical flame radius and the effect of preferential diffusion on spherical flame initiation. This will be followed by detailed numerical simulations of spherical flame initiation for different fuel/oxygen/helium/argon mixtures (hydrogen, methane, and propane), which demonstrates the validity of the theoretical results.

### **4.1 Theoretical Analysis**

#### **4.1.1 Analytical Solutions**

In Chapter 2, the spherical flame kernel evolution with and without an external ignition source at the center and/or radiative heat loss was investigated analytically. The theory developed in Chapter 2 will be utilized here with the main results briefly summarized below.

For a freely propagating spherical flame (i.e. a spherical flame without ignition energy deposition,  $Q=0$ ), the following algebraic system of equations (equation 2.14 in Chapter 2) for normalized flame propagation speed,  $U$ , flame radius,  $R$ , and flame temperature,  $T_f$ , were obtained

$$\frac{T_f R^{-2} e^{-UR}}{\int_R^\infty \tau^{-2} e^{-U\tau} d\tau} = \frac{1}{Le} \frac{R^{-2} e^{-ULeR}}{\int_R^\infty \tau^{-2} e^{-ULe\tau} d\tau} = \exp\left[\frac{Z}{2} \frac{T_f - 1}{\sigma + (1 - \sigma)T_f}\right] \quad (4.1)$$

When an external energy flux is continuously deposited in the center of the quiescent mixture ( $Q > 0$ ), the following relationship (equation 2.14 in Chapter 2) between  $U$ ,  $R$ ,  $T_f$ , and  $Q$  was obtained

$$\frac{T_f R^{-2} e^{-UR}}{\int_R^\infty \tau^{-2} e^{-U\tau} d\tau} - Q \cdot R^{-2} e^{-UR} = \frac{1}{Le} \frac{R^{-2} e^{-ULeR}}{\int_R^\infty \tau^{-2} e^{-ULe\tau} d\tau} = \exp\left[\frac{Z}{2} \frac{T_f - 1}{\sigma + (1 - \sigma)T_f}\right] \quad (4.2)$$

By solving equations (4.1) and (4.2) numerically, the relations for the flame propagation speed, flame radius, and flame temperature and the existence of different flame regimes for different Lewis numbers and/or ignition powers can be obtained. In the following, the critical flame radius and minimum ignition power will be investigated based on the quasi-steady solutions given by equations (4.1) and (4.2).

#### 4.1.2 Results and Discussions

As suggested in (Deshaies and Joulin 1984; He 2000), the critical conditions for a spherical flame to propagate in a self-sustained manner control the critical conditions for spherical flame initiation. Therefore, the critical conditions for the existence of a propagating spherical flame are first investigated for cases without ignition energy deposition by solving equation (4.1). Figure 4.1 shows the flame propagation speed as a function of flame radius for mixtures with different Lewis numbers. The Zel'dovich number,  $Z=10$ , and thermal expansion ratio,  $\sigma=0.15$ , are fixed for all the theoretical results except those in figure 4.5. For each mixture at a given Lewis number, there is a critical flame radius,  $R_C$ , as shown in figure 4.1. Above the critical flame radius, a flame

can successfully propagate outward. On the other hand, no quasi-steady solution exists below the critical flame radius. As shown in figure 4.1, the critical radius increases with the Lewis number. This is because the propagating spherical flame has positive stretch rate, and the highly curved spherical flame of small radius has high stretch rate, which makes the flame weaker at higher Lewis numbers (Law 2006). It is seen that for mixtures with small Lewis numbers ( $Le=0.5$ , and  $0.7$  in figure 4.1), the flame propagation speed could be higher than the adiabatic planar flame speed ( $U>1.0$ ). This is due to the enhancement by positive stretch rate for flames with Lewis number less than unity (Law 2006).

Figure 4.1 also shows that the adiabatic flame ball radius (Zeldovich et al. 1985),  $R_Z$ , corresponding to zero propagating flame speed ( $U=0$ ), increases with Lewis number. It is found that for  $Le<1.35$ , the critical flame radius,  $R_C$ , is equal to the flame ball radius,  $R_Z$ ; while for  $Le>1.35$ , we have  $R_C<R_Z$ . Therefore, the stationary flame ball radius,  $R_Z$ , is not the minimum radius for the existence of propagating spherical flames in mixtures with high Lewis numbers. This was first found by He (He 2000) and it was proposed that the flame initiation is not controlled by the radius of stationary flame ball for mixtures with high Lewis number (He 2000). As a result, the critical flame radius,  $R_C$ , is proposed to be the controlling length scale for spherical flame initiation, instead of the radius of stationary flame ball, which is commonly considered to be the minimum radius below which a spherical flame cannot propagate outwards (Deshaies and Joulin 1984; Champion et al. 1986).

We now consider the case in which an external energy flux is deposited in the center of a quiescent mixture and examine how the ignition power correlates with the

critical flame radius. The effect of ignition energy on the flame diagram and the transition trajectory has been studied in Chapter 2 for mixtures with Lewis number around unity ( $Le=0.8, 1.0, 1.2$ ). In the present study, mixtures with large Lewis numbers are investigated. Figure 4.2 shows the flame propagation speed as a function of flame radius at different ignition power for mixtures with  $Le=2$  and  $Le=2.5$ . For  $Q=0$ , only a  $C$  shaped flame branch for  $U-R$  exists (which is also shown in figure 4.1 for  $Le>1.3$ ), and there is a critical flame radius,  $R_C$ , at the turning point, and a flame ball radius,  $R_Z$ , at  $U=0$  (it is not shown in figure 4.2 since  $R_Z$  is larger than the upper bound of flame radius range). At low ignition power,  $Q=0.5$  for  $Le=2$  and  $Q=1.0$  for  $Le=2.5$ , there is a new branch (left branch) of solution for  $U-R$  at small flame radii with the flame propagation speed decreasing sharply to zero (flame ball solution). On the left branch, the maximum possible flame radius is defined as the lower critical flame radius,  $R_C^-$ , and the flame ball solution is defined as the lower flame ball radius,  $R_Z^-$ . The  $C$  shaped branch (right branch) is slightly shifted to the left side due to the ignition power deposition. On the right branch, the corresponding upper critical flame radius,  $R_C^+$ , and the upper flame ball radius,  $R_Z^+$  are defined in the opposite way. It is seen that the left and right branches move towards each other with increasing ignition power. Figure 4.2 shows that when the ignition power is larger than a critical value (0.968 for  $Le=2$  and 2.04 for  $Le=2.5$ ), defined as the minimum ignition power,  $Q_{min}$ , the two branches merge with each other, resulting in the new upper and lower branches. Spherical flame can thereafter propagate outward along the upper branch  $U-R$  correlation, and therefore successful spherical flame initiation is obtained.

The changes of the upper and lower critical flame radii and flame ball radii with the ignition power are shown in figure 4.3. It is seen that the upper and lower flame ball

radii are both strongly affected by the ignition power. However, for the critical flame radii,  $R_Z^-$  monotonically increases with  $Q$ , while  $R_Z^+$  remains almost constant at different  $Q$ . The lower critical flame radius and the flame ball radius are almost the same. Here the minimum ignition power is the power at which  $R_C^+=R_C^-$ . In (Champion et al. 1986), the minimum ignition power is defined as the power at which  $R_Z^+=R_Z^-$ . From figure 4.3, it is seen that the minimum ignition power defined according to  $R_Z^+=R_Z^-$  ( $Q'_{min}=1.048$  for  $Le=2$  and  $Q'_{min}=2.53$  for  $Le=2.5$ ) is higher than the  $Q_{min}$  defined based on the critical flame radius ( $Q_{min}=0.968$  for  $Le=2$  and  $Q_{min}=2.04$  for  $Le=2.5$ ). Therefore, the minimum ignition power is over-predicted in (Champion et al. 1986) based on the flame ball radius. For mixtures with Lewis number less than 1.3, there is no  $C$  shaped branch for  $U-R$  and the critical radius is the same as the flame ball radius. Therefore, the minimum ignition power based on the critical flame radius is the same as that based on flame ball radius.

It is noted that the critical flame radius,  $R_C^+=R_C^-$ , at the minimum ignition power is nearly the same as the critical flame radius,  $R_C$ , at the zero ignition power deposition since  $R_Z^+$  remains almost constant for different  $Q$  (figure 4.3). By comparing the critical flame radius and flame ball radius, over-prediction of the minimum ignition power based on flame ball radius instead of critical flame radius can be found. Figure 4.4 shows the critical flame radius and flame ball radius for different Lewis numbers at  $Q=0$ . It is seen that the critical flame radius strongly depends on the Lewis number and the flame ball radius increases exponentially with Lewis number – the adiabatic critical flame radius is it is more than one order larger for  $Le=2$  than  $Le=1$ . As a result, the minimum ignition power would be substantially over-predicted based on the flame ball radius for mixtures with large larger Lewis numbers. Therefore, the critical flame radius should be

considered as the controlling length scale for a spherical flame initiation for mixtures with Lewis number above a critical value,  $Le^* = 1.35$ . For  $Le < 1.35$ , the critical radius is the same as the flame ball radius, and the minimum ignition power can be correlated with either the critical radius or the flame ball radius.

To see how the critical flame radius is correlated with the minimum ignition power, the minimum ignition power,  $Q_{min}$ , and the cube of the critical flame radius,  $R_C^3$ , for mixtures with different Lewis numbers ( $Le = 1.4 \sim 2.5$ ) and Zel'dovich numbers ( $Z = 10, 13$ ) are plotted in figure 4.5. Both  $Q_{min}$  and  $R_C^3$  are shown to strongly depend on the Lewis number. It is seen that the minimum ignition power varies almost linearly with the cube of the critical flame radius, demonstrating a linear correlation:  $Q_{min} \sim R_C^3$ . Therefore it is the critical flame radius that controls successful spherical flame initiation. Furthermore, the minimum energy deposition for successful spherical flame initiation is proportional to the cube of the critical flame radius instead of the flame thickness or the flame ball radius.

The above results were obtained from theoretical analysis of spherical flames based on the assumption of quasi-steadiness in the flame-front attached coordinate. The shortcoming of this analysis is that the ignition energy deposition is modeled as a boundary condition in the center; while under most realistic conditions it is resolved in time and space. The steady-state energy deposition is employed in order to achieve an analytical solution. However, this simplification does not prevent the model from producing qualitatively correct results, as will be confirmed by results from unsteady simulation. In the next section, energy deposition similar to practical ignition will be utilized in detailed numerical simulation.

## 4.2 Numerical Validation

### 4.2.1 Numerical Specifications

In this section, the validity of the theoretical results presented in the previous section is demonstrated by numerical simulations using detailed chemistry. A-SURF developed in Chapter 3 is used here to simulate spherical flame initiation and propagation.

Symmetric conditions at the center ( $r=0$ ) and non-reactive, adiabatic condition at the wall ( $r=1.0\text{ m}$ ) are utilized in the simulation. At the initial state, the premixture is assumed quiescent and homogeneous at  $298\text{ K}$  and atmospheric pressure. Ignition is achieved by energy deposition resolved in time and space and the following term is added to the conservation equation of energy (Freni and Sibulkin 1990),

$$\dot{q}_{\text{ignit}} = \begin{cases} \frac{E}{4\pi r_{\text{ig}}^3 \tau_{\text{ig}} / 3} \exp\left[-\frac{\pi}{4} \left(\frac{r}{r_{\text{ig}}}\right)^6\right] & \text{if } t < \tau_{\text{ig}} \\ 0 & \text{if } t \geq \tau_{\text{ig}} \end{cases} \quad (4.3)$$

where  $E$  is the total ignition energy,  $\tau_{\text{ig}}=200\ \mu\text{s}$ , the duration of the source energy, and  $r_{\text{ig}}=200\ \mu\text{m}$ , the ignition kernel radius (large  $\tau_{\text{ig}}$  and  $r_{\text{ig}}$  are utilized here to prevent high temperature, ( $>5000\text{ K}$ ) in the center, above which the thermal and transport coefficients are difficult to be evaluated). It is noted that the duration of the source energy and the ignition kernel radius both affect the MIE,  $E_{\text{min}}$  (Lewis and Von Elbe 1961; Ronney 1994). In the present study, fixed values of  $\tau_{\text{ig}}$  and  $r_{\text{ig}}$  specified above are utilized, and the emphasis is on the correlation between the MIE and the critical flame radius, and the preferential diffusion effect on spherical flame initiation.

Simulations utilizing detailed chemical mechanisms for different fuels ( $\text{H}_2$ ,  $\text{CH}_4$  and  $\text{C}_3\text{H}_8$ ) have been conducted. To simulate the  $\text{H}_2/\text{O}_2/\text{He}/\text{Ar}$  and  $\text{H}_2/\text{air}$  flames, the

recent mechanism (Li et al. 2004) of 9 species and 25 reactions is employed. For CH<sub>4</sub>/O<sub>2</sub>/He/Ar, the GRI-MECH 3.0 mechanism (Smith et al.) is used. To save the computation time, the NO<sub>x</sub> sub-mechanism is not included and the resulting mechanism contains 36 species and 219 reactions. For C<sub>3</sub>H<sub>8</sub>/O<sub>2</sub>/He/Ar mixtures, the San-Diego Mechanism 20051201 (Williams) which consists of 46 species and 235 reactions is utilized.

The following homogeneous premixtures initially at room temperature (298 K) and atmospheric pressure (1 atm) were studied

$$0.3 \left( \frac{\varphi}{\varphi + r_s} \text{Fuel} + \frac{r_s}{\varphi + r_s} \text{O}_2 \right) + \alpha \text{He} + (0.7 - \alpha) \text{Ar} \quad (4.4)$$

where  $r_s$  is the stoichiometric oxygen-to-fuel mole ratio ( $r_s=0.5$  for H<sub>2</sub>, 2.0 for CH<sub>4</sub>, 5.0 for C<sub>3</sub>H<sub>8</sub>) and  $\varphi$  is the equivalence ratio. The volumetric fraction of fuel and oxygen is fixed to be 30%, while that of inert diluents, helium and argon, is fixed to be 70%. Different amount of helium fractions ( $\alpha=0\%$ , 25%, 50%, 70%) is used to investigate the preferential diffusion effect on spherical flame initiation. With the increase of the helium fraction, the thermal diffusivity of the mixture increases, resulting in higher Lewis numbers (Chen et al. 2007a). The laminar flame speed also increases with helium dilution, since it increases with the Lewis number (Law 2006). However, the adiabatic flame temperature does not change with the increase of helium fraction because the thermal capacities of helium and argon are almost the same.

#### 4.2.2 Results and Discussions

Figure 4.6 shows the flame radius evolution,  $R_f=R_f(t)$ , and the flame propagation speed,  $S_b=dR_f/dt$  for different ignition energies for H<sub>2</sub>/O<sub>2</sub>/Ar at  $\varphi=2.0$  and  $\alpha=0\%$ . The MIE for this mixture,  $E_{min}=0.165$  mJ, and for all other mixtures was calculated with an

error less than 3%. It is seen that there is a left branch of  $S_b-R_f$ , along which the spherical flame could not successfully propagate outwardly when the ignition energy is less than the MIE. Only when the ignition energy is above the MIE can a self-sustained propagating flame be successfully initiated. The results are similar to the theoretical results shown in figure 4.2, except the right and lower branches which could not be calculated from the transient numerical simulation. It is noted that the critical flame radius can not be defined in the same way as that in the quasi-steady theoretical analysis. Figure 4.2 shows that the critical flame radius is almost the same flame radius at which the minimum propagating speed occurs in case of the minimum ignition power deposition. According to this, in numerical simulations, we define the critical flame radius as the radius at which the minimum propagating speed occurs in case of MIE deposition. In the diagram of flame radius evolution,  $R_f=R_f(t)$ , the critical flame radius occurs at the inflection point for  $E=E_{min}=0.165 \text{ mJ}$ , which is  $R_C=0.11 \text{ cm}$ . Similar results to those shown in figure 4.6 were also obtained from simulation (one-step chemistry, constant thermal properties, and no thermal expansion) and experiments in (Champion et al. 1986).

To investigate the preferential diffusion effect on spherical flame initiation, numerical simulations on the initiation of  $\text{H}_2/\text{O}_2/\text{He}/\text{Ar}$  mixtures at different equivalence ratios and different amounts of helium dilution were conducted. The burned Markstein length, the MIE, and the critical flame radius of different  $\text{H}_2/\text{O}_2/\text{He}/\text{Ar}$  mixtures are shown in figures 4.7, 4.8, and 4.9, respectively. The burned Markstein length,  $L_b$ , is obtained from the linear extrapolation based on the plot of  $S_b-K$ , where the flame speed relative to the burned gas,  $S_b=dR_f/dt$ , and the flame stretch rate,  $K=(2/R_f)(dR_f/dt)$ ,

satisfying the following linear relation (Law 2006)

$$S_b = S_b^0 - L_b K \quad (4.5)$$

where  $S_b^0$  is the unstretched laminar flame speed relative to the burned gas. It is well known that the burned Markstein length increases with Lewis number and vice versa (Clavin 1985).

Figure 4.7 shows that the burned Markstein length increases with the increase of the helium fraction at each equivalence ratio. Therefore, the Lewis number increases with helium dilution, which is consistent with previous discussion that helium increases the Lewis number of the mixture by increasing its thermal diffusivity. Figure 4.7 also shows that the burned Markstein length increases with the equivalence ratio for fixed inert gas ratio. This is also reasonable since for hydrogen/air mixtures, the Lewis number monotonically increases with equivalence ratio (Law 2006). Therefore, the Lewis number of the H<sub>2</sub>/O<sub>2</sub>/He/Ar mixture increases with both the inert helium fraction and equivalence ratio. As a result, the MIE and the critical flame radius of the H<sub>2</sub>/O<sub>2</sub>/He/Ar mixture also increase with the inert helium fraction and the equivalence ratio, as shown in figures 4.8 and 4.9. This is consistent with the theoretical results on the Lewis number effect on the critical flame radius and the MIE shown in figures 4.4 and 4.5. It is noted that the increase of both the MIE and the critical flame radius with the helium fraction at higher equivalence ratios is much greater than that at lower equivalence ratios. This is because at a higher equivalence ratio, the H<sub>2</sub>/O<sub>2</sub>/He/Ar mixture has larger Lewis number, while the relative change of Lewis number and/or burned Markstein length is not strongly affected by equivalence ratio, which is shown in 4.7. According to results from the theoretical analysis shown in figure 4.5, at higher Lewis number, the same relative change of Lewis

number results in larger changes of both the MIE and the critical flame radius.

To see how the critical flame radius correlated with the minimum ignition power, the MIE,  $E_{min}$ , and the cube of the critical flame radius,  $R_C^3$ , for different H<sub>2</sub>/O<sub>2</sub>/He/Ar mixtures are shown in figure 4.10. Similar to the theoretical results (figure 4.5) based on the quasi-steady analysis with energy deposition as a steady boundary condition, the transient numerical simulation with energy deposition resolved in time and space also shows that the MIE changes almost linearly with the cube of critical flame radius, demonstrating a linear correlation:  $E_{min} \sim R_C^3$ . Therefore, it is the critical flame radius that controls the successful spherical flame initiation, and the minimum energy deposition for successful spherical flame initiation is proportional to the cube of the critical flame radius instead of the flame thickness or the flame ball radius. It is noted that the slope of  $E_{min}-R_C^3$  is different for mixtures with different equivalence ratios.

To further demonstrate the validity of the theoretical results, simulations for other fuels (CH<sub>4</sub> and C<sub>3</sub>H<sub>8</sub>) and hydrogen/air of different equivalence ratios ( $\phi = 3, 4, 4.2, 4.4, 4.5, 4.6, 4.8, 5$ ) were also conducted. Similar results to those of H<sub>2</sub>/O<sub>2</sub>/He/Ar were obtained. Figures 4.11 and 4.12 show that the linearly correlation,  $E_{min} \sim R_C^3$ , also holds for CH<sub>4</sub>/O<sub>2</sub>/He/Ar, C<sub>3</sub>H<sub>8</sub>/O<sub>2</sub>/He/Ar and H<sub>2</sub>/O<sub>2</sub>/N<sub>2</sub> mixtures. Therefore, the spherical flame initiation is controlled by the critical flame radius and the minimum ignition energy is proportional to the cube of the critical flame radius.

### 4.3 Conclusions

Spherical flame initiation is studied by asymptotic analysis and detailed numerical simulation. The results show that it is the critical flame radius, rather than the flame

thickness or flame ball radius, that controls spherical flame initiation. The minimum ignition energy for successful spherical flame initiation is shown to be proportional to the cube of the critical flame radius. Furthermore, the preferential diffusion between heat and mass (Lewis number effect) is found to play an important role in spherical flame initiation. It is shown that the critical flame radius and the minimum ignition energy increase significantly with the Lewis number. Therefore, for fuels with much higher thermal diffusivity than fuel mass diffusivity, larger ignition energy is needed to initiate a self-sustained propagating premixed flame.

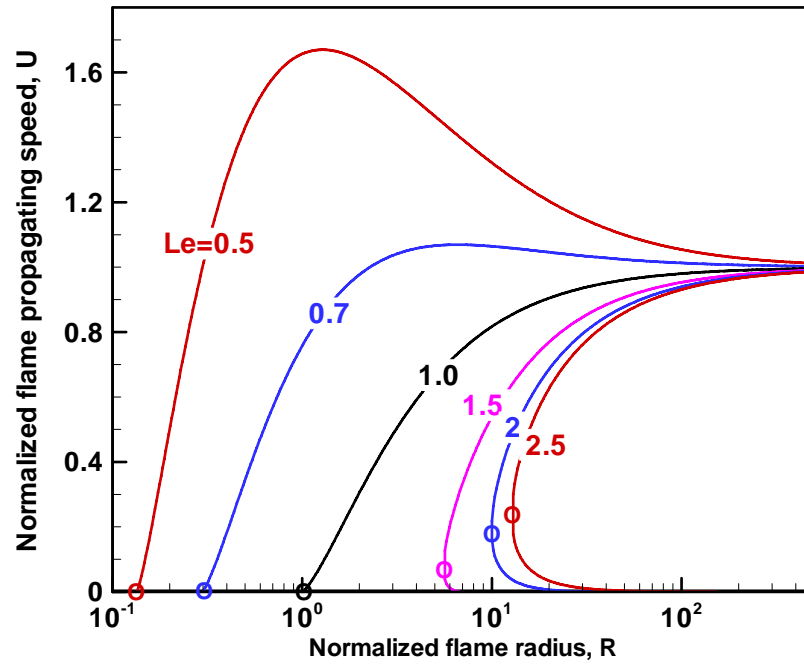


Figure 4.1: Normalized flame propagation speed as a function of flame radius for mixtures at different Lewis numbers (the critical flame radius for each case is denoted by a circle at the corresponding minimum flame radius).

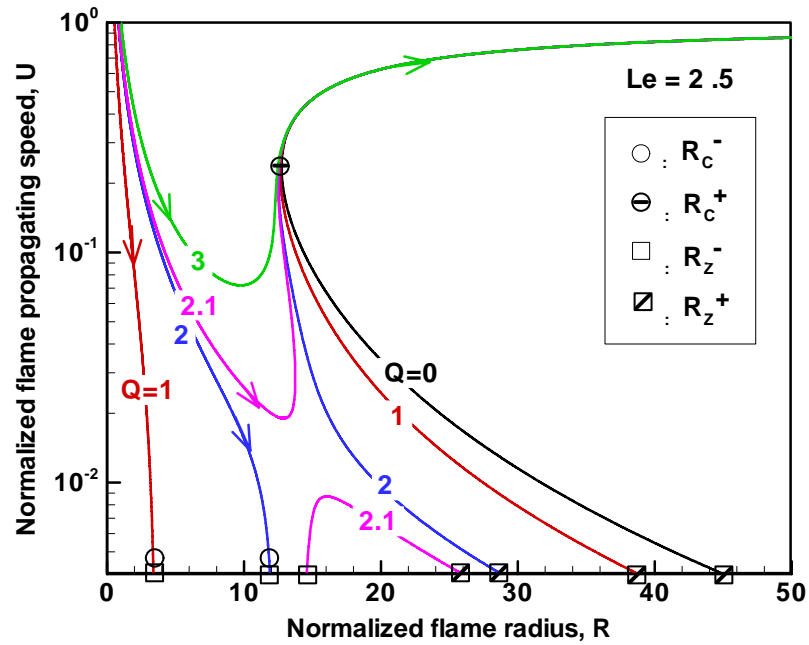
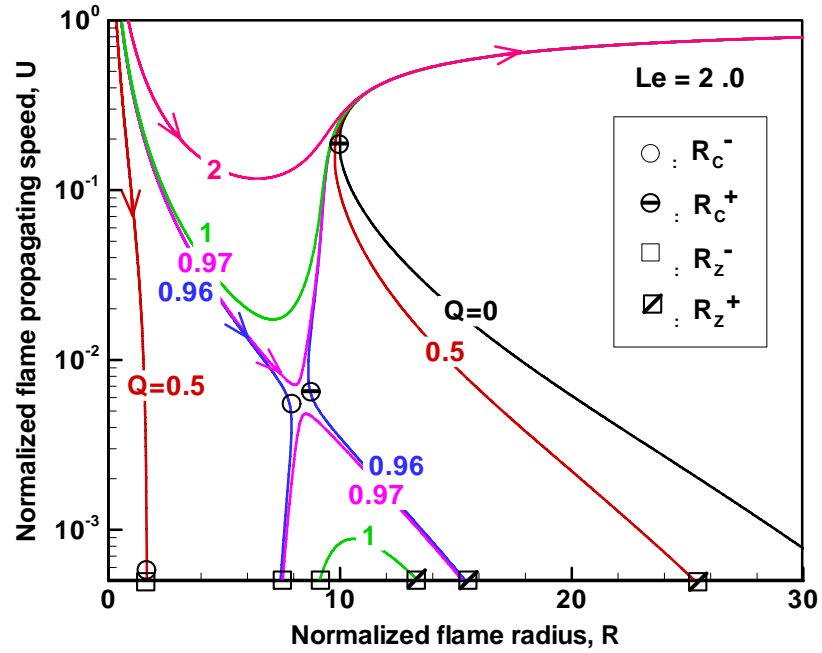


Figure 4.2: Normalized flame propagation speed as a function of flame radius at different ignition power for mixtures with (a),  $Le=2$ ; (b),  $Le=2.5$ .

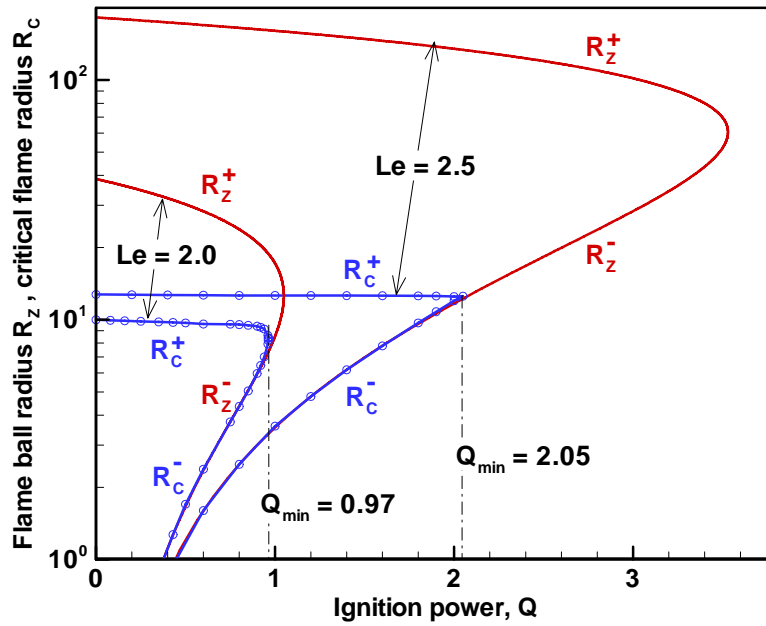


Figure 4.3: Change of upper and lower critical flame radii and flame ball radii with ignition power.

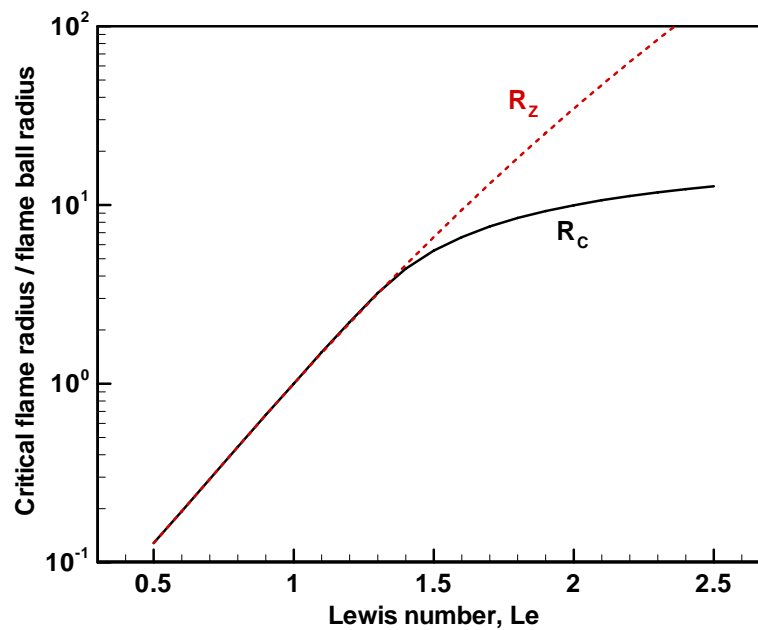


Figure 4.4: Critical flame radius and flame ball radius as functions of different Lewis numbers.

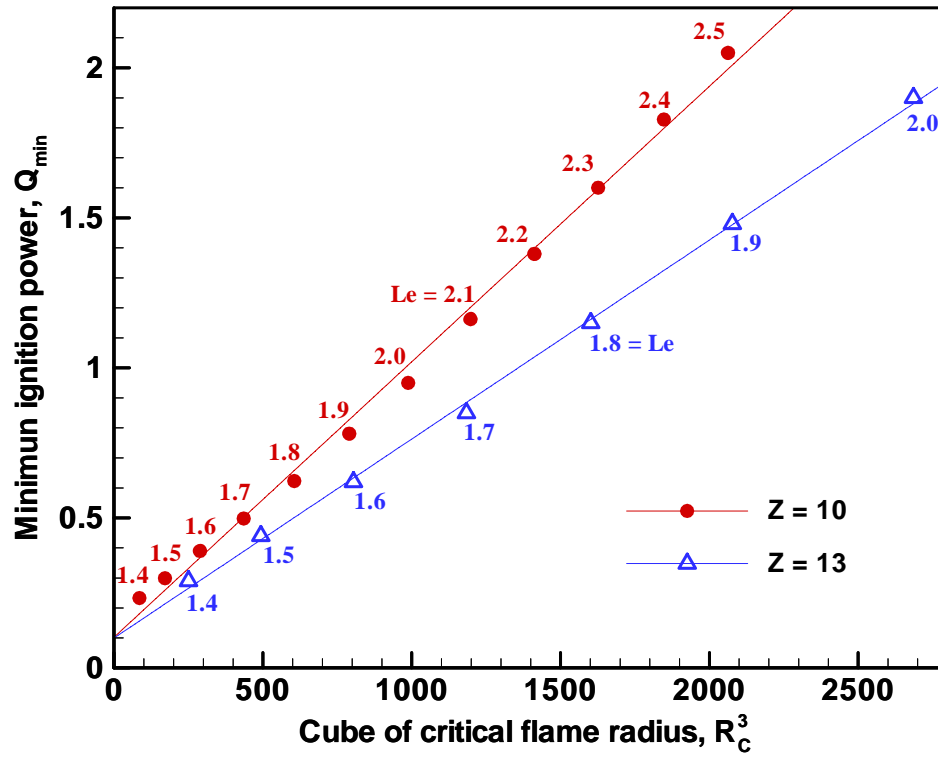


Figure 4.5: Minimum ignition power and cube of critical flame radius for mixtures with different Lewis numbers and Zel'dovich numbers.

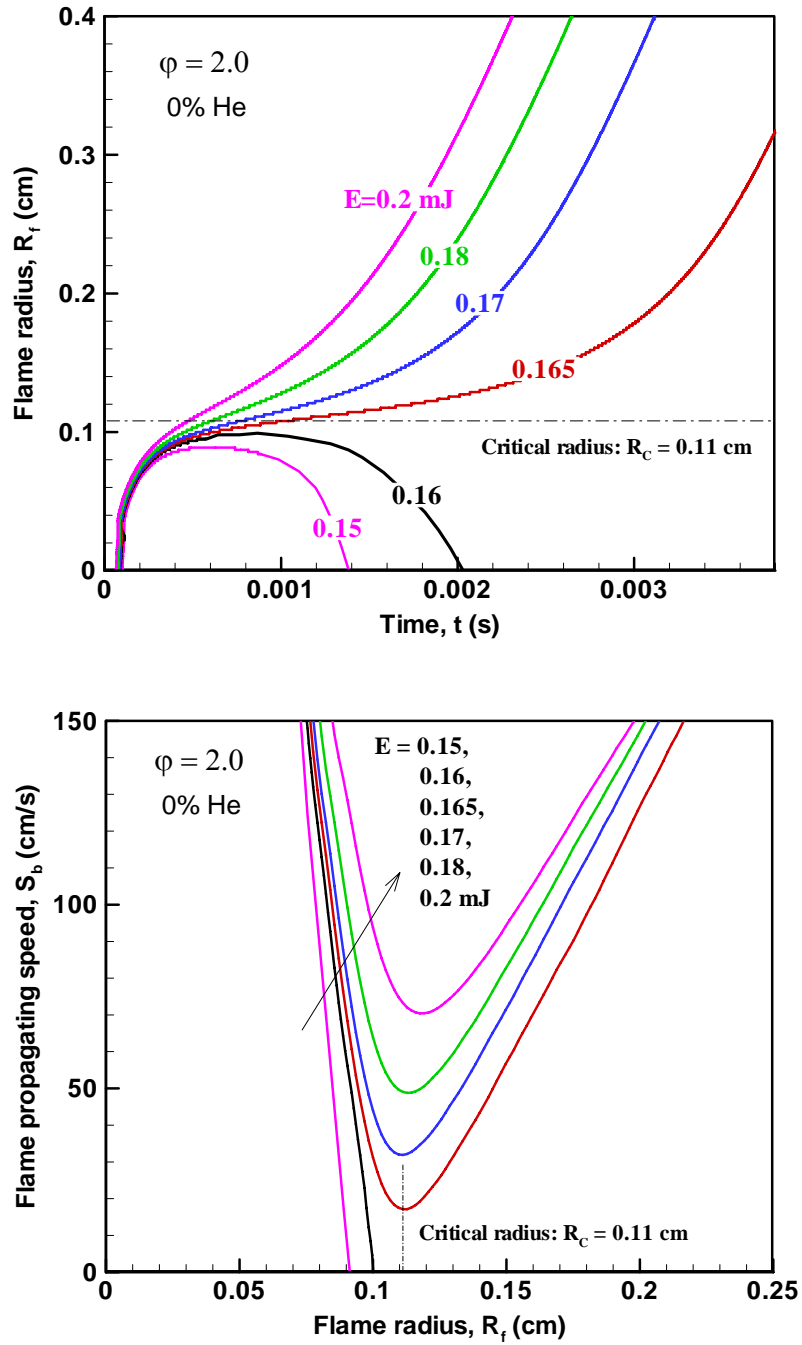


Figure 4.6: Spherical flame initiation for  $\text{H}_2/\text{O}_2/\text{He}/\text{Ar}$  mixtures at different ignition energies: (a), temporal variation of flame radius; (b), flame propagation speed at each radius.

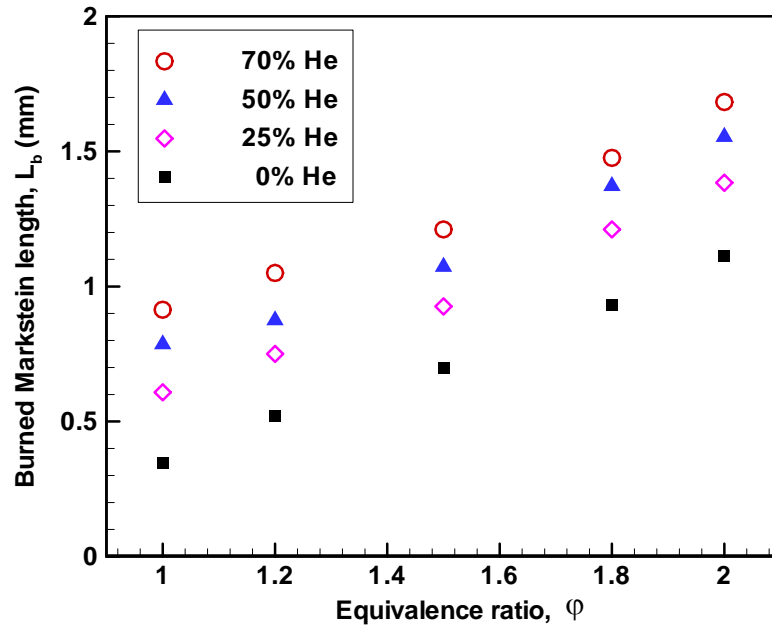


Figure 4.7: Burned Markstein length of  $H_2/O_2/He/Ar$  mixtures.

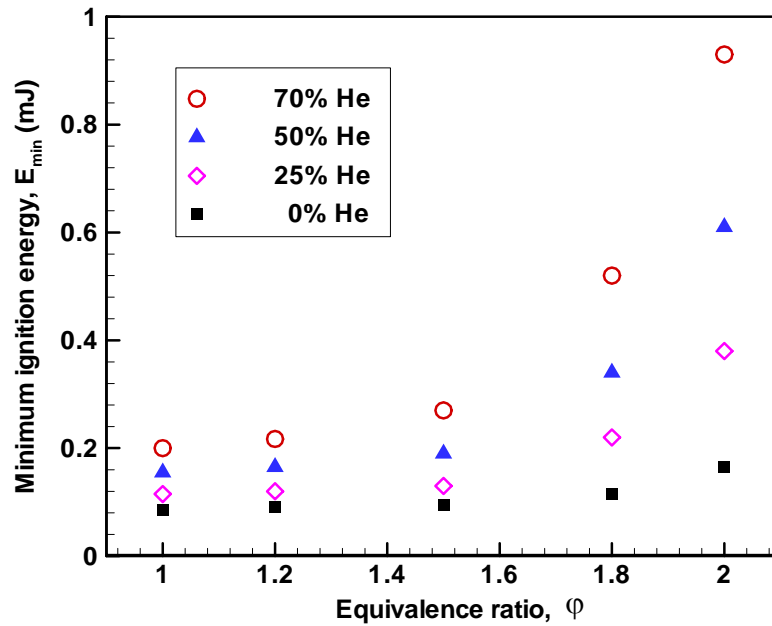


Figure 4.8: Minimum ignition energy for  $H_2/O_2/He/Ar$  mixtures.

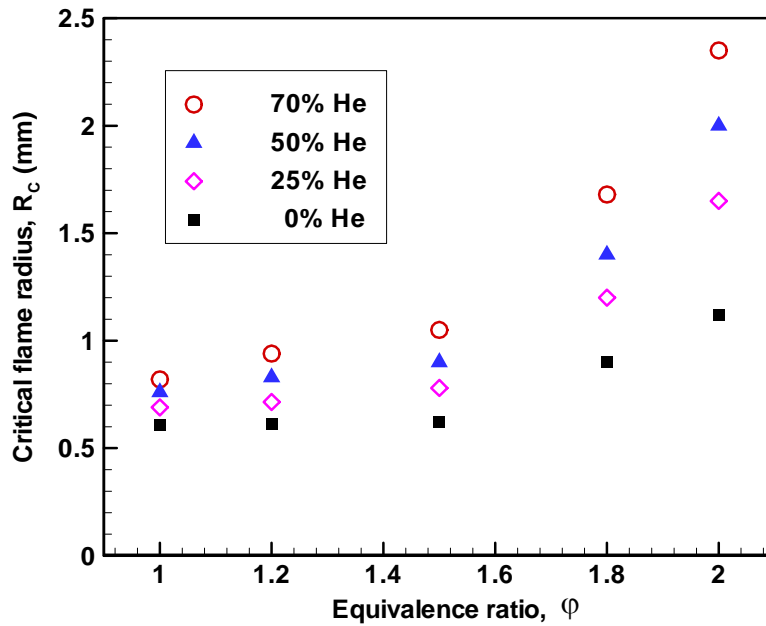


Figure 4.9: Critical flame radius of  $H_2/O_2/He/Ar$  mixtures.

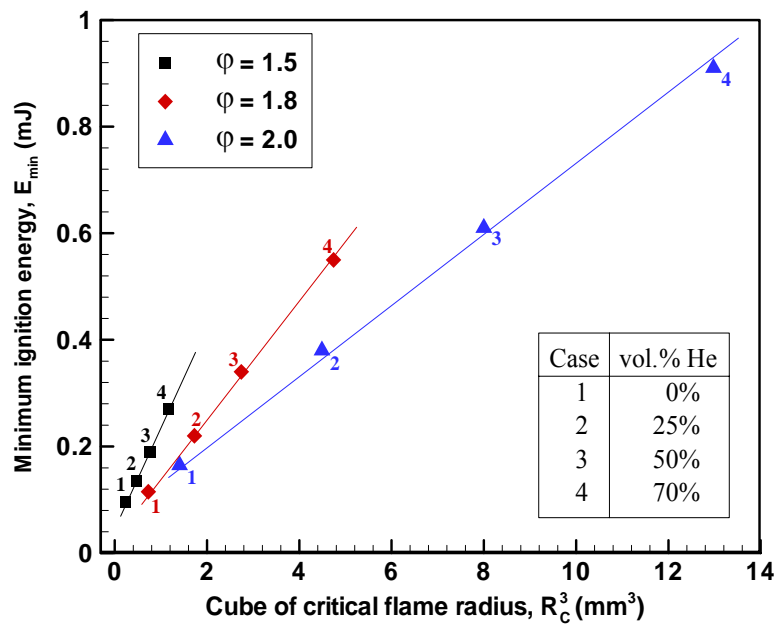


Figure 4.10: Minimum ignition energy and cube of critical flame radius of  $H_2/O_2/He/Ar$  mixtures

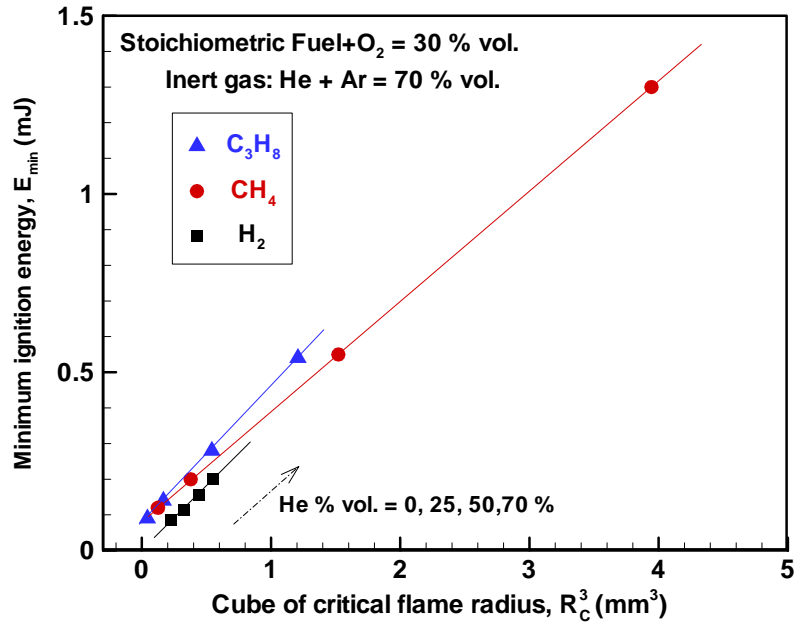


Figure 4.11: Minimum ignition energy and cube of critical flame radius of different fuels with different amount of He dilutions.

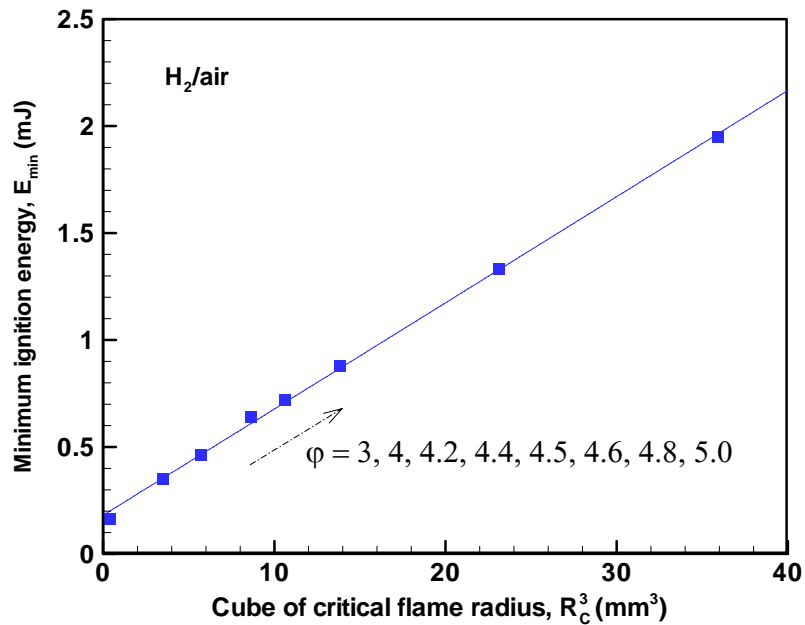


Figure 4.12: Minimum ignition energy and cube of critical flame radius of rich H<sub>2</sub>/air mixtures.

# **Chapter 5: On the Determination of Laminar Flame Speed using Propagating Spherical Flames**

In this chapter, the method of laminar flame speed measurement utilizing propagating spherical flames in a confined bomb is investigated theoretically and numerically. The emphasis is placed on how to improve the accuracy of flame speed measurement. It is found that the accuracy is affected by different effects such as Lewis number, ignition and unsteady flame transition, compression, and flame stretch. Rigorous determination of flame speeds could be achieved by using techniques developed in this chapter to correct these effects.

## **5.1 Introduction**

As discussed in Chapter 1, tracking the evolution of an outwardly propagating spherical flame in a confined bomb is currently the most preferred method for measuring the laminar flame speed at high pressures. In this method, a quiescent homogeneous combustible mixture in a closed chamber is centrally ignited by an electrical spark or a laser beam which results in an outwardly propagating spherical flame (Lewis and Von Elbe 1961; Rallis and Garforth 1980). The flame front history and/or the pressure rise history are/is recorded during the experiment and subsequently related to the laminar flame speed through theoretical models (described in the next two sections). Depending on the bomb design and the pressure change, there are two different methods for flame speed measurement by using the expanding spherical flames. The so-called constant pressure method uses Schlieren photograph to view the flame front propagation history of an expanding spherical flame in a large confined chamber or a pressure release

dual-chamber. There are two main advantages of this method. First, the propagating flame surface is observed such that any distortion of the flame morphology from being spherical or smooth can be detected; the former effect could occur for slow burning flames due to buoyancy while the later from the development of flame front instabilities especially those of cellular nature. Second, since the effect of the increase of the pressure and temperature within the chamber on the flame speed is minimal during the early stages, there exists a stage where the flame speed is purely a function of stretch — allowing for extrapolation to zero stretch and determination of stretch behaviour. Recently a great deal of effort has been devoted to obtaining accurate flame speeds utilizing this method. For example, Kelley and Law (Kelly and Law 2007) suggested that nonlinear extrapolation between the stretched flame speed and stretch rate should be used for mixtures with Lewis numbers appreciably different from unity in order to obtain accurate flame speed; Bradley et al. (Bradley et al. 2007) developed a method to correct the flame speed enhancement due to flame wrinkling arising from hydrodynamic and/or thermal-diffusive instabilities and measured laminar flame speed of lean hydrogen/air mixtures; Burke et al. (Burke et al. 2008) demonstrated that the effect of flow field deviation due to constant-pressure non-spherical chambers can significantly affect the accuracy of flame speed measurements and the Flow-Corrected Flame Speed (FCFS) was proposed to include the flow field deviation in order to improve the accuracy of flame speed measurements.

The other experimental technique, the so-called constant volume method (Lewis and Von Elbe 1961; Bradley and Mitcheson 1976; Metghalchi and Keck 1980; Hill and Hung 1988) employs a fast-response pressure transducer to measure the chamber

pressure history during the propagation of an expanding spherical flame in a closed thick-walled spherical vessel. Conversion of the reactants to hot products across the flame front results in a rapid pressure rise and a consequent temperature rise in unburned and burned gas. Therefore, this method has the advantage that the flame speed for a given mixture over a wide range of temperatures and pressures can be obtained from a single test (Metghalchi and Keck 1980). Recently, several improved theoretical models to relate the experimentally measured pressure history to the instantaneous flame speeds have been developed. Saeed and Stone (Saeed and Stone 2004) developed a multiple burned gas zone model to allow for a more realistic temperature distribution within the burned gas than the initially employed uniform temperature assumption. Metghalchi and co-workers (Parsinejad et al. 2006) considered a variable-temperature central burned gas core surrounded by a preheat zone, a uniform-temperature unburned gas shell, and a thermal boundary layer at the wall in their model, and they accounted for different sources of heat loss. Huzayyin et al. (Huzayyin et al. 2008) revealed that using different models to relate the same pressure history (from the same experimental data) to the laminar flame speed results in discrepancies up to 15% in the predicted flame speed. The result indicates the importance of accurate models and the need to improve them further.

The objective of the present study is to investigate different effects such as ignition and unsteady transition, compression, and flame stretch on the accuracy of laminar flame speed measurements using propagating spherical flames and to develop new methods to obtain more accurate flame speeds in a broader experimental range by correcting these effects. For the constant pressure method, the assumptions such as the linear relationship between the stretched flame speed and stretch rate, negligible effects

due to ignition and unsteady transition, and zero burned gas velocity will be investigated. For the constant volume method, the stretch effect on the measured flame speed will be studied. For both methods, the validity of the theoretical models and the improvement in the accuracy of measured flame speed will be demonstrated by numerical simulations using detailed chemistry for different fuels (hydrogen, methane, and propane). In this study, detailed numerical simulations instead of experimental measurement were utilized because: 1), the compression induced flow field (which is difficult to measure in experiments) can be readily obtained from simulation and thus it is compared with the theoretical prediction; and 2), other effects such as radiative loss (which always exists in experiments) can be included/excluded in simulations in order to isolate the effects of interest.

## 5.2 Constant Pressure Method

For the outwardly propagating spherical flame, the flame front,  $R_f=R_f(t)$ , has a propagation velocity,  $dR_f/dt$ . If the radial flow velocity is defined positive in the outward direction, and the flame front is assumed to be infinitely thin, the velocity of the flame front must be subtracted from that in the mass flow balance through the flame front (Peters 2000)

$$\rho_u \left( U_u - \frac{dR_f}{dt} \right) = \rho_b \left( U_b - \frac{dR_f}{dt} \right) \quad (5.1)$$

where  $\rho$  and  $U$  are density and flow velocity caused by thermal expansion across the flame front, respectively. The subscripts  $u$  and  $b$  refer to parameters for unburned and burned mixtures, respectively. At the flame front, the kinetic balance between the propagation velocity ( $dR_f/dt$ ), flow velocity ( $U_u$ ), and flame speed with respect to the

unburned gas ( $S_u$ ), is

$$\frac{dR_f}{dt} = U_u + S_u \quad (5.2)$$

Similarly, the kinetic balance with respect to the burned mixture is

$$\frac{dR_f}{dt} = U_b + S_b \quad (5.3)$$

According to the mass conservation given by equation (5.1), we have

$$S_u = aS_b \quad (5.4)$$

where  $a = \rho_b / \rho_u$  is the density ratio. Note that both  $S_u$  and  $S_b$  are laminar flame speeds under finite stretch rate. For outwardly propagating spherical flames, the flame stretch rate is (Clavin 1985)

$$K = \frac{1}{A} \frac{dA}{dt} = \frac{2}{R_f} \frac{dR_f}{dt} \quad (5.5)$$

where  $A = 4\pi R_f^2$  is the surface area of the flame front. The above flame stretch rate could be separated into two components: one due to the strain rate and the other due to the flame curvature (Bradley et al. 1996; Groot et al. 2002). Therefore, separate effects due to strain rate and curvature on flame speed can be studied (Bradley et al. 1996; Groot et al. 2002). However, it has been shown that the Markstein length with respect to the stretch due to strain rate is not unique while that with respect to the stretch rate given by equation (5.5) is unique (Groot et al. 2002). Moreover, in most of the previous experimental measurements (Brown et al. 1989; Dowdy et al. 1990; Tseng et al. 1993; Aung et al. 1997; Hassan et al. 1998; Tse et al. 2000; Rozenchan et al. 2003) the stretch rate defined by equation (5.5) was used. Therefore, it is also used in the present study and the separate effects by strain rate and curvature is not studied here. For weakly stretched

flames, a linear relationship between the stretched flame speed and the stretch rate exists that is quantified by a burned gas Markstein Length,  $L_b$  (Clavin 1985)

$$S_b = S_b^0 - L_b K \quad (5.6)$$

where  $S_b^0$  is the unstretched flame speed with respect to the burned mixture. The unstretched laminar flame speed with respect to the unburned mixture,  $S_u^0$ , is given through mass conservation

$$S_u^0 = a S_b^0 \quad (5.7)$$

By substituting equations (5.4) and (5.7) into (5.6), we have

$$S_u = S_u^0 - a L_b K \quad (5.8)$$

From equations (5.3) and (5.4), the stretched flame speed,  $S_u$ , is given by

$$S_u = a \frac{dR_f}{dt} - a U_b \quad (5.9)$$

In all previous studies utilizing the constant pressure method, data reduction was performed only for “small” pressure change and the burned gas is assumed to be quiescent ( $U_b \approx 0$ ). As a result, the moving velocity of the experimentally visualized flame front is the burned flame speed, and from equation (5.9) we have

$$S_u \approx a(dR_f / dt) \quad (5.10)$$

Therefore, according to equation (5.8), the unstretched laminar flame speed,  $S_u^0$ , and burned gas Markstein Length,  $L_b$  (or the unburned gas Markstein Length,  $L_u = aL_b$ ), can be obtained from the linear extrapolation based on the plot of  $S_u - K$ , where  $S_u$  and  $K$  are calculated from the flame front history,  $R_f = R_f(t)$ , according to equations (5.10) and (5.5), respectively. It should be noted that the flame front is assumed to be infinitely thin in the above discussions. The effect of finite flame thickness, discussed in (Bradley et al.

1996; Bradley et al. 1998; Gu et al. 2000; Groot et al. 2002), is not included here.

The constant pressure method discussed above is based on the following assumptions: linear relationship between the stretched flame speed and stretch rate, negligible effects due to ignition and unsteady transition, zero burned gas velocity, and negligible radiative loss. In the following, the conditions under which these assumptions hold and the corrections for circumstances that these assumptions do not hold will be investigated.

### 5.2.1 Validity of the Linear Relationship between Flame Speed and Stretch

To investigate under what conditions the stretched flame speed changes linearly with the stretch rate, the theory for propagating spherical flames presented in Chapter 2 is utilized here. By neglecting radiative loss, the relationship between the normalized flame radius,  $R=R/\delta$ , and the normalized flame speed,  $U=S_b/S_b^0$ , can be expressed as

$$T_f \cdot \frac{R^{-2} e^{-UR}}{\int_R^\infty \tau^{-2} e^{-U\tau} d\tau} - Q \cdot R^{-2} e^{-UR} = \frac{1}{Le} \frac{R^{-2} e^{-ULeR}}{\int_R^\infty \tau^{-2} e^{-ULe\tau} d\tau} = \exp\left[\frac{Z}{2} \frac{T_f - 1}{\sigma + (1 - \sigma)T_f}\right] \quad (5.11)$$

where  $T_f$ ,  $Q$ , and  $Z$  are, respectively, the normalized flame temperature, ignition power at the center, and Zel'dovich number, which are defined in Chapter 2. Equation (5.11) is valid for flames at both small and large radii. Hereafter, we refer to it as the detailed model (DM).

For spherical flames of large radii ( $R \gg 1$ ), the detailed model reduces to the simplified model (SM)

$$\left(U + \frac{2}{R}\right) \ln\left(U + \frac{2}{R}\right) = \frac{Z}{R} \left(\frac{1}{Le} - 1\right) - \frac{2}{R} \left(\frac{1}{Le} - 1\right) \quad (5.12)$$

For weakly stretched flames, the stretched flame speed is close to the adiabatic

unstretched flame speed (i.e.  $U=1+\varepsilon$  with  $\varepsilon\ll 1$ ). In this limit, equation (5.12) reduces to the linear model (LM)

$$U = 1 - Ma \cdot Ka \quad (5.13)$$

where  $Ka=2U/R=K\delta/S_u^0$  is the Karlovitz number and  $Ma=Le^{-1}-(Z/2)(Le^{-1}-1)$  the Markstein number, which is the same as that derived for premixed counterflow flame (Law 2006).

The linear relationship, equation (5.6) or (5.8), utilized for linear extrapolation for constant pressure method, is based on the LM given by equation (5.13). To find under which conditions the LM works well, the normalized flame speed predicted as a function of flame radius and the Karlovitz number (in figures 5.1(b) and 5.5(b),  $Ka=2U/(\sigma R)$  is used since the propagating speed, thus the flame stretch, is  $l/\sigma$  times of the laminar flame speed,  $S_u^0$ , to the zeroth order) by DM, SM, and LM for  $Z=10$ ,  $\sigma=0.15$  and  $Le=0.5, 1.0, 2.0$  is shown in figure 5.1. It is observed that SM and LM agree well with DM only for large flame radius. In addition, the difference among the prediction from DM, SM, and LM strongly depends on the Lewis number. Figure 5.1(b) reveals that for each Lewis number, there is a critical Karlovitz number above which the spherical flame does not exist, due to the quenching caused by the combined effects of flame curvature and stretch. The maximum Karlovitz number for  $Le=2$  is much smaller than that for  $Le=0.5$  and  $1.0$ , indicating that small spherical flames does not exist for large Lewis numbers. Finite flame curvature always decreases the flame speed (equation 5.12). However, the effect of flame stretch on flame speed depends strongly on the Lewis number derivation from unity (Law 2006). As a result, the critical Karlovitz number, denoted by the turning points in figure 5.1(b), decreases significantly with increasing Lewis number. As will be shown

later, this conclusion plays an important role in determining the experimental data range for flame speed measurement.

Figure 5.2 shows the critical flame radius above which the relative discrepancies between LM and DM and between SM and DM are less than 5%. It is seen that the critical flame radius of SM is much smaller than that of LM for a given Lewis number, which is consistent with the fact that the SM is more comprehensive than the LM (SM is based on the assumption of large flame radius; while LM is based on the assumption of large flame radius as well as small stretch rate). The nonmonotonic change of the critical flame radius with Lewis number is due to the fact that the absolute value of the Markstein length becomes smallest when  $Le$  is close to a critical value which is slightly less than unity (Law 2006).

By comparing the three different models of DM, SM and LM given by equations (5.11-5.13), we obtain the critical flame radius above which the linear or non-linear relationship between the stretched flame speed and stretch rate is satisfied. This critical flame radius can be used as a guide to choose the experimental data range for flame speed measurement by using either linear or nonlinear fitting approaches based on equation (5.11) or (5.12). Since the critical flame radius changes greatly with Lewis number, for mixtures such as rich hydrogen/air or lean propane/air with Lewis numbers greatly different from unity, the lower flame radius bound  $R_{fl}$  should be specified above the critical radius so that the linear (based on LM) or nonlinear (based on SM) extrapolation can be carried out.

### **5.2.2 Effects of Ignition and Unsteady Transition**

The above theoretical analysis is based on the quasi-steady assumption, with the

effects of ignition and unsteadiness are neglected. In order to study the effects of unsteady flame evolution at different ignition energies, A-SURF (1D) described in Chapter 3 is used to simulate outwardly propagating spherical flames. Detailed chemistry is included in the simulation: for H<sub>2</sub>/air flames, the recent mechanism of 9 species and 25 reactions developed by Li et al. (Li et al. 2004) is employed. The spherical chamber radius is set to be  $R_0=100\text{ cm}$  and the flame trajectory data with flame radius less than 5 cm are utilized. Therefore, both the pressure increase (<1%) and the compression-induced flow effect described in the next section are negligible. The flame is initiated by a small hot pocket of burned product surrounded by fresh mixture at the room temperature and pressure ( $T_0=298\text{ K}$ ,  $P_0=1\text{ atm}$ ). The size of the hot pocket,  $R_h$ , is between 0.9 mm and 2.0 mm, which changes with the equivalence ratio of H<sub>2</sub>/air. For very rich cases ( $\phi=5.0$  or 5.5), which have large Lewis numbers, a larger hot pocket is needed to obtain a propagating spherical flame (Chen et al. 2008b). In order to examine the effect of ignition energy on flame trajectories, at a fixed equivalence ratio, three different hot pocket sizes,  $R_h$ ,  $1.2R_h$ ,  $1.4R_h$ , were adopted to mimic the experiments with different ignition energies. The position of the flame front,  $R_f$ , is defined as the position of maximum heat release rate and the flame speed is calculated from the flame front history, i.e.  $S_b=dR_f/dt$ .

The propagating spherical H<sub>2</sub>/air flames at different equivalence ratios ( $\phi=0.5, 1.0, 2.0, 3.0, 3.5, 4.0, 4.5, 5.0, 5.5$ ) and different ignition hot pocket sizes are simulated. Figure 5.3 shows the flame speed with respect to the burned mixture,  $S_b$ , as a function of the flame radius,  $R_f$ , and flame stretch rate,  $K$ . The results show that the initial unsteady flame transition and different ignition energies (hot pocket sizes) lead to different flame

speed trajectories. Only above a critical flame radius,  $R_c$ , which is denoted by the open circles in figure 5.3, does the flame speed trajectory become independent of the ignition energy and converge to a low-dimensional manifold. With the increase of equivalence ratio, this critical flame radius increases dramatically. For  $\varphi=4.5$ , the critical radius is even larger than  $0.8\text{ cm}$ , which lies within typical experimental data ranges utilized for extrapolation of flame speed. For example, lower flame radius bounds,  $R_{L}$ , of  $0.5\text{ cm}$  or  $0.6\text{ cm}$  are often employed (Kwon et al. 1992; Tseng et al. 1993; Bradley et al. 1996; Tse et al. 2000; Farrell et al. 2004). Therefore, care is needed to fit the experimental data for flame speed measurements of mixtures with large Lewis numbers. Moreover, figure 5.3(b) shows that for flame radii larger than the critical radius (i.e. stretch rates less than the critical stretch rate, which are marked by the open circles),  $S_b$  changes linearly with  $K$ , except for very small Lewis numbers (the lean case at  $\varphi=0.5$ ). As a result, for these conditions, the linear extrapolation can be utilized to obtain unstretched flame speed.

For  $\text{H}_2/\text{air}$  flames, the critical radius from present simulations and the effective Lewis number based on contributions from both reactants in (Joulin and Mitani 1981; Law 2006) are shown in figure 5.4. The critical radius is shown to change non-monotonically with the equivalence ratio and is smallest for  $\varphi=2$ , which corresponds to the largest laminar flame speed and the smallest flame thickness. The nonmonotonic trend between the critical radius and equivalence ratio is similar to that between the flame thickness and equivalence ratio. This is caused by the fact that the duration of initial flame transition period (which is proportional to critical radius) strongly depends on the flame thickness.

In order to understand the cause for the strong flame trajectory dependence on the

ignition energy and Lewis number, the dependence of normalized flame speed on the Karlovitz number ( $Ka = K\delta/S_u^0$ ) of spherical H<sub>2</sub>/air flames is shown in figure 5.5(a). The maximum Karlovitz number changes greatly with the equivalence ratio, or more accurately, with the Lewis number. This predicted dramatic change of the maximum Karlovitz number is consistent with the theoretical prediction shown in figure 5.1(b). To show the effects of ignition energy, the theoretical results for a mixture with  $Le=2$  are shown in figure 5.5(b) for comparison. Theory predicts that the ignition energy does not affect the flame trajectories above the turning point of maximum Karlovitz number. This is due to the fact that energy deposition is treated as a boundary condition at the center and the unsteadiness is not included in the asymptotic theory. However, contrary to the theory, figure 5.5(a) shows that there is a strong unsteady effect near the maximum Karlovitz number. Due to the unsteady effect, the flame speed trajectory depends on the ignition energy. For  $\phi=4.5$ , the simulations reveal that, at large Karlovitz numbers, flames initiated by large ignition energies have large flame speeds. However, near the maximum Karlovitz number, flames initiated by smaller ignition energies have larger flame speed. This new phenomenon is called “flame speed reverse”, which originates from the unsteady flame evolution near the adiabatic extinction limit (the point of maximum Karlovitz number in figures 5.5(a) and 5.1(b)). Because of the existence of the flame speed reversal at large Lewis numbers, neither nonlinear fitting nor linear fitting of experimental data including the flame speed reverse period for flame speed determination is correct. Ignition energy and transient flame evolution significantly affect the flame trajectories and thus must be considered.

For flame radii larger than the critical radius (figure 5.3), flame speed becomes

only dependent on the Karlovitz number. The critical radius above which the unsteady flame transition ends can be found by observing the change of the flame thickness during flame propagation. Figure 5.6 shows the history of flame thickness (defined as the distance between the cold,  $T=400\text{ K}$ , and hot,  $T=1000\text{ K}$ , sides of the flame) during flame propagation for  $\text{H}_2/\text{air}$  at  $\phi=4.5$  initiated from three different ignition hot pocket sizes (cases  $a$ ,  $b$ ,  $c$ , marked also in figures 5.3 and 5.5). The results indicate that there is a significant change in the flame thickness during the initial period of unsteady flame transition. The substantial thickening of the flame initiated by the smallest ignition energy before it reaches the maximum Karlovitz number is the cause of the flame speed reversal. After the transition period, the flame thickness is almost constant and the three lines merge together onto the low-dimensional manifold for  $R_f > R_c$ . The change of flame thickness during flame propagation clearly demonstrates the effect of unsteadiness on the flame trajectory. In addition to the above results obtained under atmospheric conditions, numerical simulations of  $\text{H}_2/\text{air}$  flames at elevated pressures have also been conducted (figure 5.7). It is found that the flame speed reversal effect also exists at high pressures and that the critical radius decreases with pressure.

Therefore, the ignition energy has a significant impact on the flame trajectory and the unsteady flame transition causes a flame speed reversal phenomenon, which greatly narrows the experimental data range for flame speed extrapolation. Experiments (Chen et al. 2008a) on outwardly propagating spherical  $\text{H}_2/\text{air}$  flames have been conducted to validate the above theoretical and numerical results about Lewis number and ignition/unsteadiness effects.

### 5.2.3 Effect of Compression

In the previous section, the flow compression effect due to the interaction between the burned gas thermal expansion and the chamber walls is neglected and the flow velocity in the burned gas is assumed to be zero ( $U_b \approx 0$ ). As will be shown in this section, neglecting the compression-induced flow velocity,  $U_b$ , even for a small pressure increase could significantly reduce the accuracy of the flame speed measurements. In the following, an analytical expression of  $U_b$  will be derived and a *Compression-Corrected Flame Speed* (CCFS) will be presented.

The mass conservation in the spherical bomb gives

$$m_b + m_u \equiv m_0 \quad (5.14)$$

$$dm_u / dt = -dm_b / dt \quad (5.15)$$

in which  $m_b$  and  $m_u$  are, respectively, the mass of burned and unburned gases and  $m_0$  is the total mass which does not change with time. According to the definition of flame speed, we have

$$dm_u / dt = -4\pi R_f^2 \rho_u S_u \quad (5.16)$$

Based on the assumptions that the spherical flame is thin and the temperature is uniform in the burned gas region, we have

$$m_b = (4/3)\pi R_f^3 \rho_b \quad (5.17)$$

By further assuming that the burned gas behaves as an ideal gas and that the compression is isentropic during the flame propagation, we have

$$d\rho_b / \rho_b = dP / \gamma P \quad (5.18)$$

where  $\gamma$  is the ratio of heat capacities, and  $P$  is the pressure which is nearly uniform in a closed chamber (Lewis and Von Elbe 1961). Substituting equations (5.15) and (5.17) into

(5.16) and using the above isentropic relationship, one obtains (Lewis and Von Elbe 1961; Bradley and Mitcheson 1976; Hill and Hung 1988)

$$S_u = a \frac{dR_f}{dt} + a \frac{R_f}{3\gamma P} \frac{dP}{dt} \quad (5.19)$$

By comparing equations (5.9) and (5.19), the flow velocity of the burned gas behind the flame front is

$$U_b = - \frac{R_f}{3\gamma P} \frac{dP}{dt} \quad (5.20)$$

The pressure and its rate of change in equation (5.20) can be either measured directly in experiments or calculated from the flame front history obtained from the Schlieren images according to the following relationship (Bradley and Mitcheson 1976)

$$\frac{R_f}{R_0} = \left[ 1 - \frac{P_e - P}{P_e - P_0} \left( \frac{P_0}{P} \right)^{1/\gamma} \right]^{1/3} \quad (5.21)$$

where  $P_0$  and  $P_e$  are the initial and final chamber pressures, respectively, and  $R_0$  is the radius of a spherical chamber (which is the equivalent radius,  $R_0 = (3V/4\pi)^{1/3}$ , for a non-spherical chamber of volume  $V$ ).

With the increase of pressure, the unburned gas temperature,  $T_u$ , will also increase so that the density ratio,  $a$ , is not a constant but a function of  $T_u$

$$a(T_u) = T_u / T_{ad} = (1 + \Delta T / T_u)^{-1} \quad (5.22)$$

where  $\Delta T$  is the temperature increase caused by chemical heat release and it can be calculated from thermodynamic data. Assuming the unburned gas is compressed isentropically,  $T_u$  can be calculated from the pressure which can be evaluated from the flame front history according to equation (5.21),  $T_u = T_0 (P/P_0)^{(1-1/\gamma)}$ . Then  $T_u$  and thus  $a = a(T_u)$  can also be calculated from the flame front history.

Therefore, the compression-induced flow velocity,  $U_b$ , can be evaluated from the flame front history by using equations (5.20) and (5.21). As a result, flame speed extrapolated by using equation (5.9) instead of (5.10) is more accurate due to the inclusion of the compression effect. The unstretched flame speed,  $S_u^0$ , obtained by the linear extrapolation of  $S_u$  given by equations (5.9), (5.20) and (5.21), is called the *Compression-Corrected Flame Speed (CCFS)*.

To show the improvement of the accuracy in flame speed measurement by CCFS, A-SURF is used to simulate propagating spherical flames in a closed chamber for different fuels ( $H_2$ ,  $CH_4$  and  $C_3H_8$ ). Detailed chemistry is included in simulation, as specified previously in Section 4.2.1 for the  $H_2$ /air,  $CH_4$ /air, and  $C_3H_8$ /air flames.

In all the simulations, the spherical chamber radius is set to be  $R_0=6\text{ cm}$ . All the results in the following parts are presented in terms of flame radii normalized by the chamber size ( $R_f/R_0$ ). Therefore the same conclusions still hold for the cases using other chamber sizes (normalized results from simulations with  $R_0=12\text{ cm}$  show quantitatively similar results as those with  $R_0=6\text{ cm}$ ). The flame is initiated by a small hot pocket ( $\sim 1\text{ mm}$  in radius) of burned products surrounded by fresh mixture at room temperature and pressure ( $298\text{ K}$ ,  $1\text{ atm}$ ). At the inner and outer boundaries,  $r=0$  and  $r=R_0$ , respectively, zero-gradient conditions are enforced. The effects of ignition and unsteadiness discussed previously are excluded and only the data for flame radii larger than  $6\text{ mm}$  are used to calculate the flame speed in this section.

For the constant pressure method, similar to the Schlieren imaging in the experiments, the flame front history,  $R_f=R_f(t)$ , from the numerical simulation is used to calculate the flame speed. In the simulation, the position of flame front is defined as the

position of maximum heat release It was pointed out that the level of contours chosen to track the flame front might affect the flame front propagating speed (Bradley et al. 1996). However, this second-order effect is important only for very lean or rich pre-mixtures which have much thicker reaction zones. The chamber pressure can be either obtained from simulation or calculated from flame front history by solving equation (5.21). The difference between the pressures obtained from those two methods is negligible. The compression-induced flow velocity,  $U_b$ , is defined as the flow velocity at the position where 99.9% of the chemical heat is released.

Figure 5.8 shows the change of the flow field during flame propagation. There is a velocity jump at the flame front induced by thermal expansion resulted from chemical heat release in the flame reaction zone. The product and unburned mixture are ‘*expanded*’ inwardly and outwardly, respectively. When the relative flame radius is small, the velocity of burned gas is negligible and thus the assumption of zero burned gas velocity is reasonable. However, as shown in figure 5.8, the velocity of burned gas continuously increases during the flame propagation. Therefore, without including the movement of the burned gas, the flame speed would be under-predicted. This is further shown in figures 5.9~5.11, which are results from the same simulation of the outwardly propagating spherical stoichiometric CH<sub>4</sub>/air flame. Figure 5.9 shows the normalized compression-induced flow velocity of the burned gas behind the flame front,  $aU_b/S_L^0$ , as a function of normalized flame radius or relative pressure increase. The results from the theoretical relations given by equations (5.20) and (5.21) agree well with those from the simulation. Note that to the zeroth order of accuracy, we have  $S_u \approx S_L^0$  ( $S_u$  is the stretched flame speed while  $S_L^0$  is the planar unstretched flame speed). Therefore, according to

equations (5.9) and (5.10),  $aU_b/S_L^0$  is the relative error in evaluating the stretched flame speed,  $S_u$ , caused by neglecting the compression-induced flow,  $U_b$ . The results indicate that for normalized flame radius  $R_f/R_0$  larger than 0.4, the error will be greater than 5%. Thus, for larger flames, in order to derive accurate flame speeds from experimental measurements, the flow compression effect must be considered. As will be shown in figure 5.11, this error is further amplified during the linear extrapolation process to obtain the unstretched flame speed. Note that when the normalized flame radius  $R_f/R_0$  is less than 0.5, the relative pressure increase is below 18% and the increase of the temperature of unburned mixture is less than 12 K. The resulting change of the laminar flame speed is less than 1% and thus is negligible.

The flow compression effect on the stretched flame speed is further demonstrated in figure 5.10, in which different methods are employed to calculate the stretched flame speed,  $S_u$ . The normalized stretch rate is defined as  $K'=K\delta/S_L^0$ , with  $\delta=0.2$  mm and  $S_L=37.2$  cm/s being the unstretched adiabatic laminar planar flame thickness and flame speed, respectively. Figure 5.10 reveals that if the effect of flow compression is not considered, i.e.  $S_u=a(dR_f/dt)$ ,  $S_u$  decreases with increasing flame size when  $R_f/R_0>0.3$ . This is due to the fact the flame front propagating speed is reduced by the compression-induced flow (note that  $U_b$  is negative as shown in figure 5.9). The rapid decrease of the flame speed at large flame radii (or small stretch rate) renders the linear extrapolation to zero stretch rate inaccurate. Therefore, in order to obtain an accurate unstretched flame speed ( $S_u^0$ ) from the linear extrapolation of  $S_u$ - $K$  according to equation (5.8), an upper bound,  $R_{fU}$ , must be chosen to make  $R_{fU}/R_0<0.3$  such that the effect of the compression-induced flow is prevented. Otherwise the flame speed will be

under-predicted. For a small combustion chamber of  $R_0=6\text{ cm}$ , the  $R_{fU}$  that satisfies  $R_{fU}/R_0<0.3$  is  $1.8\text{ cm}$ . As such, the flame radius range,  $[R_{fL}, R_{fU}]$ , for which the constant pressure relations are accurate, is  $[0.6\text{ cm}, 1.8\text{ cm}]$ . This flame radius range might be too narrow for accurate linear extrapolation. Therefore, the compression-induced flow velocity,  $U_b$ , should be considered to extend the upper bound,  $R_{fU}$ . Figure 5.10 shows that when the flow velocity,  $U_b$ , is considered, i.e.  $S_u=a(dR_f/dt-U_b)$ , without including the temperature change,  $S_u$  will monotonically increase during flame propagation (increase of  $R_f$ ) until  $R_f/R_0>0.52$ . Therefore the upper bound,  $R_{fU}$ , is extended more than 70% by considering the compression-induced flow velocity,  $U_b$ . The decrease of  $S_u$  for  $R_f/R_0>0.52$  is caused by the change of density ratio,  $a$ , with the increase of the unburned gas temperature,  $T_u$ , as mentioned previously, and thus the density ratio is a function of  $T_u$  instead of being constant, i.e.  $a=a(T_u)$ , which is given by equation (5.22). Accordingly, figure 5.10 shows that if the change of density ratio is also considered, i.e.  $S_u=a(T_u)\cdot(dR_f/dt-U_b)$ ,  $S_u$  monotonically increases during the entire flame propagation process as is expected for a positive Markstein length mixture and a flame with increasing  $T_u$ . It should be noted that when the pressure increase is small ( $(P-P_0)/P_0<2\%$  or  $R_f/R_0<0.25$ ), the compression induced flow,  $U_b$ , is negligible and thus the stretched flame speeds calculated from all three methods are almost the same. However, the two CCFS methods yield linear relationships with stretch rate, as predicted by theory, for larger spans of data.

To reveal how the choice of the flame radius range affects the measured laminar flame speed by the flow compression effect, the accuracy of the unstretched flame speed with and without the flow compression correction using different flame radii ranges,  $[R_{fL},$

$R_f]$ , are shown in figure 5.11. The unstretched flame speed,  $S_u^0$ , is extrapolated from the plot of  $S_u-K$  according to equation (5.8) and  $S_L^0=37.2 \text{ cm/s}$  is the laminar flame speed of the unstretched planar flame at the room temperature and pressure obtained from the 1-D planar flame simulation. When the compression effect is neglected, i.e.  $S_u=a(dR_f/dt)$ , figure 5.11 shows that the flame radius range affects greatly the extrapolated unstretched flame speed,  $S_u^0$ , with the increase of the upper bound of the flame radius,  $S_u^0$ , significantly under-predicted (by more than 20%). This large discrepancy reveals that the flow compression effect on flame speed is magnified by the linear extrapolation to zero stretch rate. However, when the compression induced flow velocity,  $U_b$ , is considered and the CCFS is employed, i.e.  $S_u=a(dR_f/dt-U_b)$ , the discrepancies between the extrapolated unstretched flame speed,  $S_u^0$ , using different flame radii ranges are all below 5%. Therefore significant improvement in the accuracy of flame speed measurements is achieved using the CCFS, which considers the compression-induced flow. A typical data range utilized in previous experiments is [1.0 cm, 2.5 cm]. For chambers of radius larger than 10 cm (Brown et al. 1989; Dowdy et al. 1990; Tseng et al. 1993; Aung et al. 1997; Bradley et al. 1998; Gu et al. 2000), the accuracy of flame speed measurements neglecting the compression effect is below 5% according to figure 5.11. However, these experiments are for measurements below 5 atmospheres. For measurements of flame speed at high pressures (above 10 atmosphere), smaller chamber should be used for safety issues and only flames of small size can be used because hydrodynamic instability and/or thermal diffusive instability, making flame front wrinkled, will occur earlier at higher pressures (Rozenchan et al. 2003). When a chamber of 5 cm in radius is used, to use the data range of [1.0 cm, 2.5 cm] will result in errors of 15%. Only when the CCFS

is employed, the error becomes less than 5%.

Figure 5.12 shows the accuracy of the unstretched flame speed for stoichiometric  $H_2$ /air and  $C_3H_8$ /air flames, respectively. The results are similar to those of  $CH_4$ /air mixtures. All the results demonstrate that: 1), the compression-induced flow and flame radius range have significant impacts on the accuracy of the measured flame speed; 2), the compression-induced flow can be accurately predicted by the analytical correlation given by equations (5.20) and (5.21); 3), the accuracy of the flame speed measurements can be greatly improved using the CCFS; and 4), for high pressure experiments using small chambers, CCFS should be utilized to obtain accurate flame speed.

### **5.3 Constant Volume Method**

The constant volume method also uses a spherical vessel with central ignition. However, it calculates the flame speed based on the pressure history,  $P=P(t)$ , recorded after the flame has grown to a sufficiently large size so that the pressure variation is evident. Details of theoretical analysis on this method can be found in (Lewis and Von Elbe 1961; Bradley and Mitcheson 1976; Hill and Hung 1988) and are only briefly described below.

The constant volume method is based on the following assumptions (Hill and Hung 1988): the flame is thin, smooth, and spherical; the pressure is spatially uniform; the constituents of the burned and unburned gases behave as ideal gases; the dissociation products are in equilibrium; the unburned gas is compressed isentropically; and buoyancy effects are negligible. These assumptions allow for the calculation of properties of the burned and unburned gases in a constant volume combustion process.

First, we define the mass fraction of burned gas,  $x$ , as

$$x = m_b / m_0 = 1 - m_u / m_0 \quad (5.23)$$

where the burned mass is given by equation (5.17). The unburned and total masses are given by the following two equations, respectively,

$$m_u = (4/3)\pi(R_0^3 - R_f^3)\rho_u \quad (5.24)$$

$$m_0 = (4/3)\pi R_0^3 \rho_u^0 \quad (5.25)$$

where  $\rho_u^0$  is the initial mixture density. According to the isentropic assumption we have

$$\frac{\rho_u^0}{\rho_u} = \left(\frac{P_0}{P}\right)^{1/\gamma} \quad (5.26)$$

From equations (5.14), (5.16), (5.24-26), the following expressions for flame speed,  $S_u$ , can be obtained

$$S_u = \frac{R_0^3}{3R_f^2} \left(\frac{P_0}{P}\right)^{1/\gamma} \frac{dx}{dt} \quad (5.27)$$

$$\frac{R_f}{R_0} = \left[ 1 - (1-x) \left(\frac{P_0}{P}\right)^{1/\gamma} \right]^{1/3} \quad (5.28)$$

The above equations describe essentially the technique for determining the laminar flame speed from the pressure history (Lewis and Von Elbe 1961; Bradley and Mitcheson 1976; Hill and Hung 1988). Equilibrium calculations (Metghalchi and Keck 1980; Takizawa et al. 2005) at the constant volume condition are carried out to obtain the relationship of  $P$  with  $x$ ,  $\gamma$ , and the burned and unburned gas temperatures,  $T_b$  and  $T_u$ . These relationships are then applied to the experimentally measured pressure,  $P$ , and finally the flame speed,  $S_u$ , is obtained by solving equations (5.27) and (5.28). Detailed descriptions are given in (Metghalchi and Keck 1980; Takizawa et al. 2005). For simplicity, the commonly employed assumption of a linear relationship between the mass

fraction of the burned gas and pressure rise is employed (Lewis and Von Elbe 1961; Bradley and Mitcheson 1976; Hill and Hung 1988),

$$x = (P - P_0)/(P_e - P_0) \quad (5.29)$$

The validity of this assumption is confirmed by detailed numerical simulation in the next sub-section (figure 5.14b). Substituting equation (5.29) into (5.27) and (5.28), the relationship in (5.21) is readily obtained and the flame speed is given by

$$S_u = \frac{R_0}{3} \left(\frac{R_0}{R_f}\right)^2 \frac{1}{(P_e - P_0)} \left(\frac{P_0}{P}\right)^{1/\gamma_u} \frac{dP}{dt} \quad (5.30)$$

Therefore, from the pressure history  $P=P(t)$ , the flame position  $R_f$  can be obtained according to equation (5.21) and the stretched flame speed  $S_u$  can be evaluated by using equation (5.20).

### 5.3.1 Effect of Stretch Rate

In all previous experimental studies (Metghalchi and Keck 1980; Hill and Hung 1988; Farrell et al. 2004; Saeed and Stone 2004; Takizawa et al. 2005; Parsinejad et al. 2006; Huzayyin et al. 2008), the flame speed,  $S_u$ , obtained from the constant volume method is actually the stretched flame speed, not the unstretched flame speed,  $S_u^0$ . As mentioned before, the stretch effect on flame speed could be significant for mixtures with Lewis numbers greatly deviating from unity. In the following, the effects of flame stretch on the measured flame speed will be analyzed, and a method that includes a stretch correction in the determination of laminar flame speed will be introduced.

The stretch effect on flame speed is given by equation (5.8). By using  $L_u = aL_b$  (this relation is correct only under the assumption of thin flame front), it becomes

$$S_u = S_u^0 - L_u K \quad (5.31)$$

Note that to the zeroth order, we have  $S_u \approx S_u^0$ . So equation (5.31) can be written as

$$\frac{S_u^0 - S_u}{S_u^0} \approx \frac{L_u K}{S_u} \quad (5.32)$$

With the definition of stretch rate given in equation (5.5) and the flame radius in term of pressure in equation (5.21), the following expression for the flame stretch rate can be derived

$$K = \frac{2}{3} \left( \frac{R_0}{R_f} \right)^3 \left( 1 + \frac{P_e - P}{\gamma P} \right) \frac{1}{P_e - P_0} \left( \frac{P_0}{P} \right)^{1/\gamma} \frac{dP}{dt} \quad (5.33)$$

By using equations (5.21), (5.30), (5.32), and (5.33), the relative difference of the flame speed caused by stretch effects can be obtained as

$$\frac{S_u^0 - S_u}{S_u^0} \approx \frac{2L_u}{R_f} \left( \frac{\gamma - 1}{\gamma} + \frac{P_e}{\gamma P} \right) \quad (5.34)$$

According to the above equation, the error in the measured flame speed caused by neglecting the stretch effect can be evaluated. It is seen from equation (5.34) that the error is proportional to the Markstein length and the inverse of flame radius. Furthermore, when the flame size is small, the pressure increase is small and thus  $P_e/P$  is large, so the stretch effect is further magnified by the second term inside the brackets in equation (5.34). Therefore, for small spherical flames in mixtures with Lewis numbers greatly deviating from unity, the stretch effect on the flame speed is significant so stretch correction is necessary. Figure 5.13 shows the error caused by neglecting the stretch effect of equation (5.34) for a typical run with  $P_e/P_0=8.27$ ,  $\gamma=1.4$ ,  $L_u=0.25 \text{ mm}$  (close to the Markstein length of rich hydrogen/air and lean propane/air flames, as will be shown later) and chamber size  $R_0=6 \text{ cm}$ . It is observed that the stretch effect on the flame speed is greater than 10% when the pressure increase is below 20% ( $P/P_0 < 1.2$  or  $R_f/R_0 < 0.54$ ).

Therefore, the stretch correction is needed for accurate determination of the laminar flame speed.

In order to obtain a more accurate flame speed, a *Stretch-Corrected Flame Speed* (SCFS),  $S_u^0$ , is proposed here. The SCFS is obtained by applying a stretch correction according to equation (5.31), in which the stretched flame speed,  $S_u$ , is calculated from the measured pressure history according to equations (5.30) and (5.21), and the stretch rate,  $K$ , calculated according to equation (5.33). Note that in equation (5.31), the calculation of SCFS requires a value for the Markstein length,  $L_u$ . The Markstein length, which is usually measured either from propagating spherical flames using the constant pressure method discussed above or from counterflow flame experiments, can be obtained from linear extrapolation of the stretched flame speed,  $S_u$ , and flame stretch rate,  $K$ , calculated from the pressure history (according to equations 5.30, 5.21, 5.33) over spans of data where the pressure and temperature increase is small for the constant volume method. Since the temperature and pressure of the unburned gas increase during the flame propagation, the flame speed is affected not only by the stretch rate but also by the increases of the temperature and pressure of the unburned gas. Therefore, the Markstein length can not be obtained accurately from the linear extrapolation of  $S_u$  and  $K$  calculated from pressure history when the pressure increase is large (above 5%) for the constant volume method. However, there exists a portion of the flame propagation where the pressure rise is detectable experimentally, while the flame speed is nearly insensible to changes in temperature and pressure and thus is only affected by the stretch rate. As will be shown by numerical simulations below, the Markstein length corresponding to mixtures at the initial pressure can be accurately obtained from the pressure history

during this period and can be utilized in the SCFS method to improve the accuracy of the flame speed measurement.

For the constant volume method, the pressure history,  $P=P(t)$ , from the simulation is used to calculate the flame speed without stretch correction according to equations (5.30) and (5.21). The SCFS is calculated from the pressure history using the procedure proposed above. Before obtaining the SCFS, the validity of the theoretical relationships between the flame radius and pressure given by equation (5.21) and the linear relationship between the mass fraction of burned gas and pressure rise given by equation (5.29) is demonstrated by their excellent agreement with numerical simulation of propagation spherical flames in a closed spherical chamber. The results for a rich  $H_2$ /air flame at the equivalence ratio of  $\varphi=4$  are shown in figure 5.14, which reveals that the theoretical model agrees well with the direct numerical simulation. Similar results for other fuels are also obtained, indicating the robustness of the theoretical relationships given by equations (5.21) and (5.29).

In order to obtain the *Stretch-Corrected Flame Speed* (SCFS), the Markstein length,  $L_u$ , must be extracted from the pressure history. As mentioned before, the temperature and pressure of unburned gas increase during flame propagation. As a result, the Markstein length,  $L_u$ , which depends on pressure and temperature, may also change. In the following, the Markstein length is obtained from two different methods. The first method ( $L_u \neq const$ ) is to use  $R_f=R_f(t)$  results from numerical simulation to calculate the Markstein length through linear extrapolation of stretched flame speed,  $S_u$ , and stretch rate,  $K$ , at constant pressure and temperature calculated from the constant pressure method. This process is repeated to obtain the Markstein length at different temperature

and pressures corresponding to those for flames at different sizes in the constant volume method. Unfortunately, in most experimental measurements of flame speed, it is impossible to calculate the Markstein length accurately using the above method because a validated mechanism is usually not available. The second method ( $L_u = L_u^0 = \text{const}$ ) is to use the pressure history which is recorded in experiments to obtain the Markstein length via linear extrapolation of  $S_u$  and  $K$  calculated from pressure history (according to equations 5.39, 5.21, 5.33). In addition, in order to remove the effect of pressure and temperature increase, the data range used for the Markstein length calculation is limited to those with pressure increase lower than 5%. The results show that the Markstein length obtained by the second method agree well (less than 2% difference) with those obtained from the first method. The Markstein lengths obtained from the two different methods proposed above will be utilized to calculate the SCFS.

The propagating spherical flames of different fuels were simulated and the results are shown in figures 5.15 and 5.16. For a rich H<sub>2</sub>/air flame of the equivalence ratio of  $\phi=4$ , the Markstein length corresponding to mixtures at the initial pressure and temperature (1 atm, 298 K), is 0.3 mm which is predicted well by both methods. Figure 5.15(a) shows that without the stretch correction the flame speed from the constant volume method (using equations 5.30 and 5.21) agree well with those from PREMIX (PREMIX calculations are conducted at different sets of temperature and pressure according to the expected rise as the flame kernel grows in the constant volume vessel) only at a very large pressure increase (large  $R_f/R_0$ ). When the pressure increase or the relative flame radius is small, the discrepancy between the flame speed without and with stretch correction is more than 20%. This result shows clearly that stretch correction is

necessary in the constant volume experiment to obtain a reliable flame speed for small spherical flames. Figure 5.15 shows that the SCFS agrees very well with those from PREMIX, even for small pressure increases. Therefore, the accuracy of the measured flame speed is greatly improved by utilizing the SCFS.

Results indicate that the SCFS using the Markstein lengths from the above two methods ( $L_u \neq \text{const}$  and  $L_u = \text{const}$ ) agree very well. In fact, using a constant Markstein length from the second method only slightly over-predicts the stretch effect because the Markstein length and stretch rate decrease with increasing pressure. As shown in figure 5.15(b), the stretch rate (normalized by the stretch rate at  $R_f/R_0=0.1$ ) quickly decreases with increasing pressure. This explains why the difference between the SCFS obtained using the first and second methods is negligible. The success of the second method is significant for experimental measurements of flame speeds by using the constant volume method – the SCFS can be obtained directly from the pressure history without any knowledge of chemical kinetics and transport properties.

For a stoichiometric  $\text{H}_2/\text{air}$  flame of  $\phi=1$ , the unburned Markstein length is 0.03 *mm* at the initial pressure and temperature of (1 *atm*, 298 *K*). Therefore, as expected, the error caused by neglecting the stretch effect is small (below 5% in this case), which is also confirmed by results shown in figure 5.16(a). It is seen that for the stoichiometric  $\text{H}_2/\text{air}$  mixture, which has a small unburned Markstein length, the stretch effect is negligible and the discrepancy between the flame speed without and with stretch correction is small.

For a lean  $\text{H}_2/\text{air}$  flame of  $\phi=0.45$ , the unburned Markstein length is negative,  $L_u=-0.28$  *mm* at the initial pressure and temperature of (1 *atm*, 298 *K*). As such, positive

flame stretch will increase the flame speed according to equation (5.8). As shown in figure 5.16(b), flame speed without stretch correction is much larger than the planar unstretched flame speed predicted by PREMIX. The discrepancy between the flame speed without and with stretch correction can reach as high as 50% for this case. Figure 5.16(b) shows that after the stretch correction, the flame speed obtained from the constant volume method agrees well with those computed from PREMIX. Therefore, the above results show that the accuracy of the flame speed measurement can be greatly improved by utilizing the SCFS. Of course, in experiments for lean  $H_2$ /air flames, cellular instability will greatly affect the flame speed when the flame radius is larger than a critical value. Nevertheless, the results of lean  $H_2$ /air flame are presented here in order to demonstrate the validity of the analytical relation for the stretch effect given by equation (5.34), and the improvement of the flame speed measurements accuracy by using SCFS.

For a stoichiometric  $CH_4$ /air flame, similar results to those of the stoichiometric  $H_2$ /air shown in figure 5.16(a) are obtained. It is found that the stretch effect is negligible since the Markstein length is small, which agrees with the prediction from equation (5.34).

For a lean  $C_3H_8$ /air flame of  $\phi=0.8$ , the unburned Markstein length is  $0.19 \text{ mm}$  at the initial pressure and temperature of  $(1 \text{ atm}, 298 \text{ K})$ . Figure 5.16(c) shows that when the pressure increase or the relative flame radius is small, the discrepancy between the flame speed with and without the stretch correction is more than 20%. After the stretch correction, the flame speeds from the constant volume method agree very well with those from PREMIX. Again, the accuracy of the measured flame speed is shown to be greatly improved by utilizing the SCFS. All the results in figure 5.16 show that the SCFS based

on Markstein lengths obtained from the two methods are also in good agreement.

Therefore, all the numerical results of H<sub>2</sub>/air, CH<sub>4</sub>/air and C<sub>3</sub>H<sub>8</sub>/air mixtures show that for mixtures of large unburned Markstein lengths, the stretch effect on flame speed measurement in the constant volume method is significant and that the SCFS should be calculated to improve the accuracy of the flame speed measurements. Without stretch correction, only the data of spherical flame with normalized radius larger than 0.6 or presume increase greater than 50% can be utilized (figures 5.15a, 5.16b, 5.16c). After stretch correction, the SCFS agrees well with that from PREMIX and can be utilized as unstretched laminar flame speed for spherical flames with normalized radius larger than 0.1. Therefore, the present SCFS method not only greatly improves the accuracy of the flame speed measurements but also extends the parameter range of experimental conditions for which accurate measurements can be gathered. Since the proposed methods do not need information about transport and kinetic properties of the mixtures, these methods can be directly implemented in experimental measurements.

## 5.4 Conclusions

The constant pressure and constant volume methods utilizing propagating spherical flames for laminar flame speed measurements were studied theoretically and numerically. Different effects such ignition, unsteadiness, compression, and stretch on the accuracy of flame speed determination were investigated. New methods to obtain more accurate flame speeds in a broader experimental range by correcting for these effects were presented. The principal conclusions are:

1. For the constant pressure method, theoretical analysis reveals a critical flame radius only above which is the linear or non-linear extrapolation for flame speeds valid. It

is found that the critical radius changes non-monotonically with the Lewis number. For large Lewis numbers, the critical radius can be greater than the minimum flame radius used in the experimental measurements, leading to invalid flame speed extrapolation. The results also show that there is a critical Karlovitz number beyond which a spherical flame cannot exist, due to quenching caused by the combined effects of flame curvature and stretch. Furthermore, the ignition energy is shown to have a significant impact on the flame trajectory. It is found that the unsteady flame transition at different ignition energies causes a flame speed reversal phenomenon near the maximum Karlovitz number. The occurrence of flame speed reversal greatly narrows the experimental data range for flame speed extrapolation. Moreover, it is found that the compression induced flow can greatly affect both the instantaneous stretched and extrapolated unstretched flame speeds. When the compression effect is neglected, the choice of the flame radii range significantly affects the extrapolated unstretched flame speed. Due to the flow compression effect, the maximum flame radius, below which accurate measurements can be gathered in experiment, is severely restricted. An analytical expression is derived to evaluate the compression-induced flow velocity via the flame front history. A *Compression-Corrected Flame Speed (CCFS)* method for flame speed measurement is proposed. Numerical simulations using detailed chemical mechanisms for hydrogen/air, methane/air, and propane/air flames demonstrate that the present CCFS method not only increases the accuracy of the measured flame speed but also extend the parameter range of experimental conditions. For high pressure experiments in which small chambers are used, CCFS should be utilized to obtain accurate flame speed measurements.

2. For the constant volume method, an analytical expression is derived to evaluate the stretch effect on the determination of flame speeds. It is found that the stretch effect is proportional to the Markstein length and inversely proportional to the flame radius. For mixtures with Lewis numbers greatly deviating from unity, the stretch effect on the flame speed is significant. A *Stretch-Corrected Flame Speed* (SCFS) model is then proposed to obtain accurate flame speed directly from the experimental measurement. The accuracy of the measured flame speed is greatly improved by using the SCFS method, which is demonstrated by detailed numerical simulation.

The present results indicate that extrapolation of unstretched flame speeds in larger bombs at low pressures using typical flame radius ranges yield accurate results (within 5%) without consideration of compression effects. However, in smaller bombs, they reveal that the extrapolation is subject to large errors (~15%) if these effects are not considered. Moreover, the errors become even more serious. The proposed improvements to the theoretical models not only increases the accuracy of flame speed measurements but also enable flame speed measurements to be gathered from small bombs, which have significant advantages in terms of the pressure range, cost, and reduction of flame wrinkling and radiation effects, without sacrificing accuracy.

Note that the effect of radiative heat loss on the accuracy of flame speed measurement utilizing propagating spherical flames is not included in the present study. It has been shown in (Chen et al. 2008c) that radiation has three effects: 1) to decrease the flame temperature and thus flame speed; 2) to induce inward flow and slow down the flame propagation; and 3) to preheat the reactants due to absorption. The first effect is found to be important only for near-limit mixtures having very low laminar flame speed

(less than 10 cm/s) and the second effect is found to be important only for highly radiative mixture (for example, CO<sub>2</sub> diluted mixture in oxy-fuel combustion). The third effect will be discussed in the next chapter. For most mixtures (H<sub>2</sub>/air, CH<sub>4</sub>/air, C<sub>3</sub>H<sub>8</sub>/air, etc.) not close to their flammability limits and without CO<sub>2</sub> dilution, the effects of radiation can be neglected.

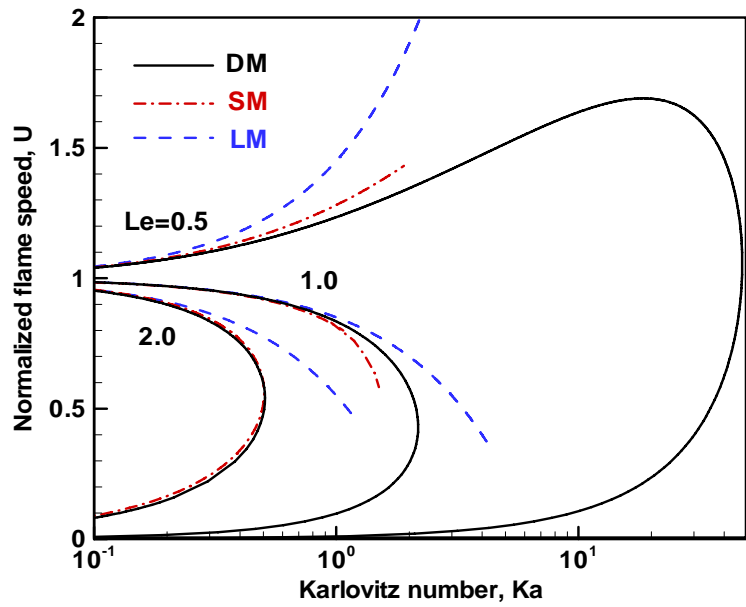
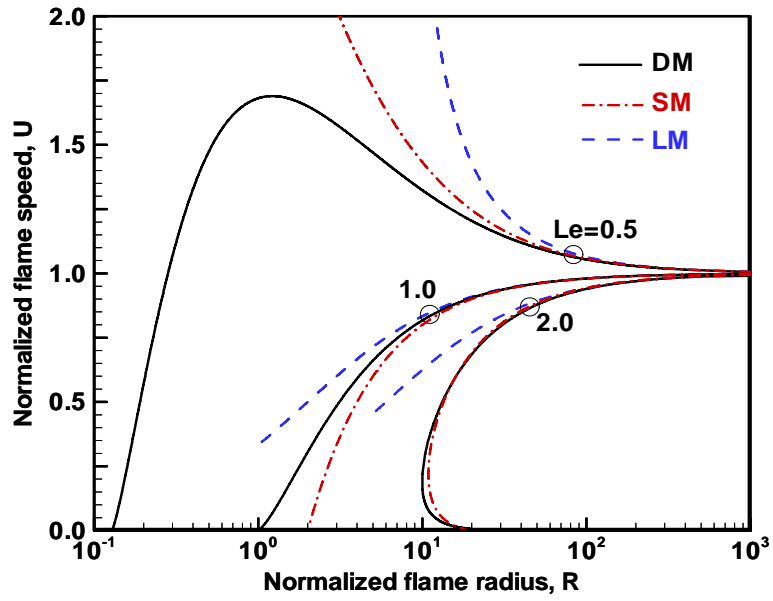


Figure 5.1: Normalized flame speed as a function of (a) flame radius and (b) Karlovitz number predicted by different models for different Lewis numbers.

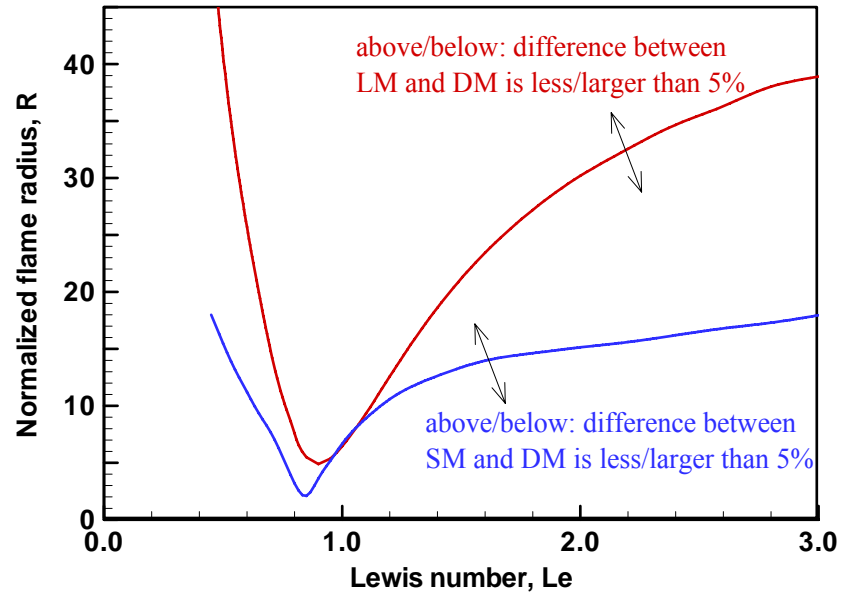


Figure 5.2: The critical flame radius above which the relative discrepancies between LM and DM and between SM and DM are less than 5% at different Lewis numbers.

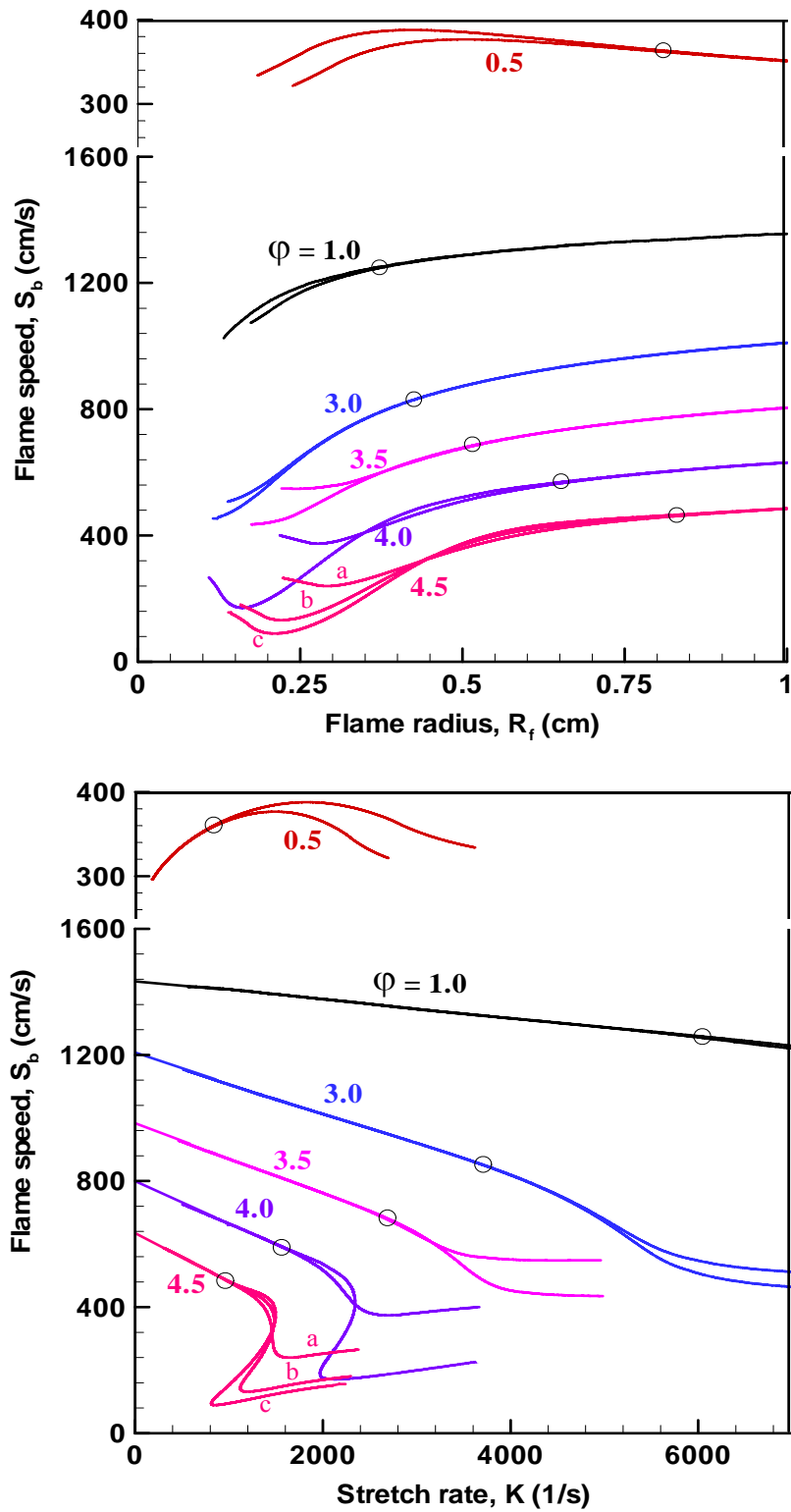


Figure 5.3: Flame speed as a function of (a) flame radius and (b) stretch rate for  $H_2$ /air at different equivalence ratios: results from simulation.

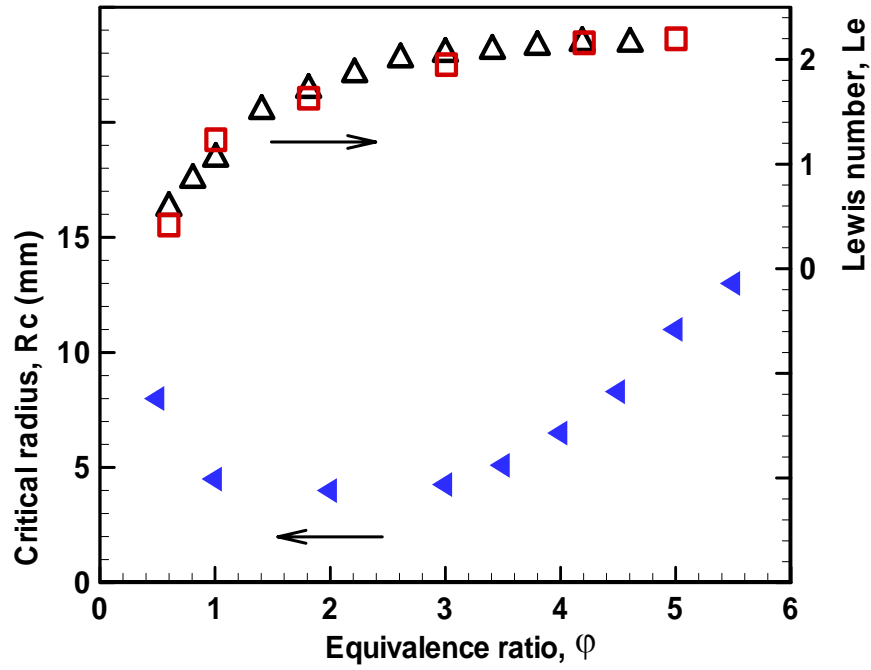


Figure 5.4: Critical flame radii and Lewis numbers for  $H_2$ /air at different equivalence ratios. Data denoted by open triangles are from (Law 2006) and those by squares are from (Joulin and Mitani 1981).

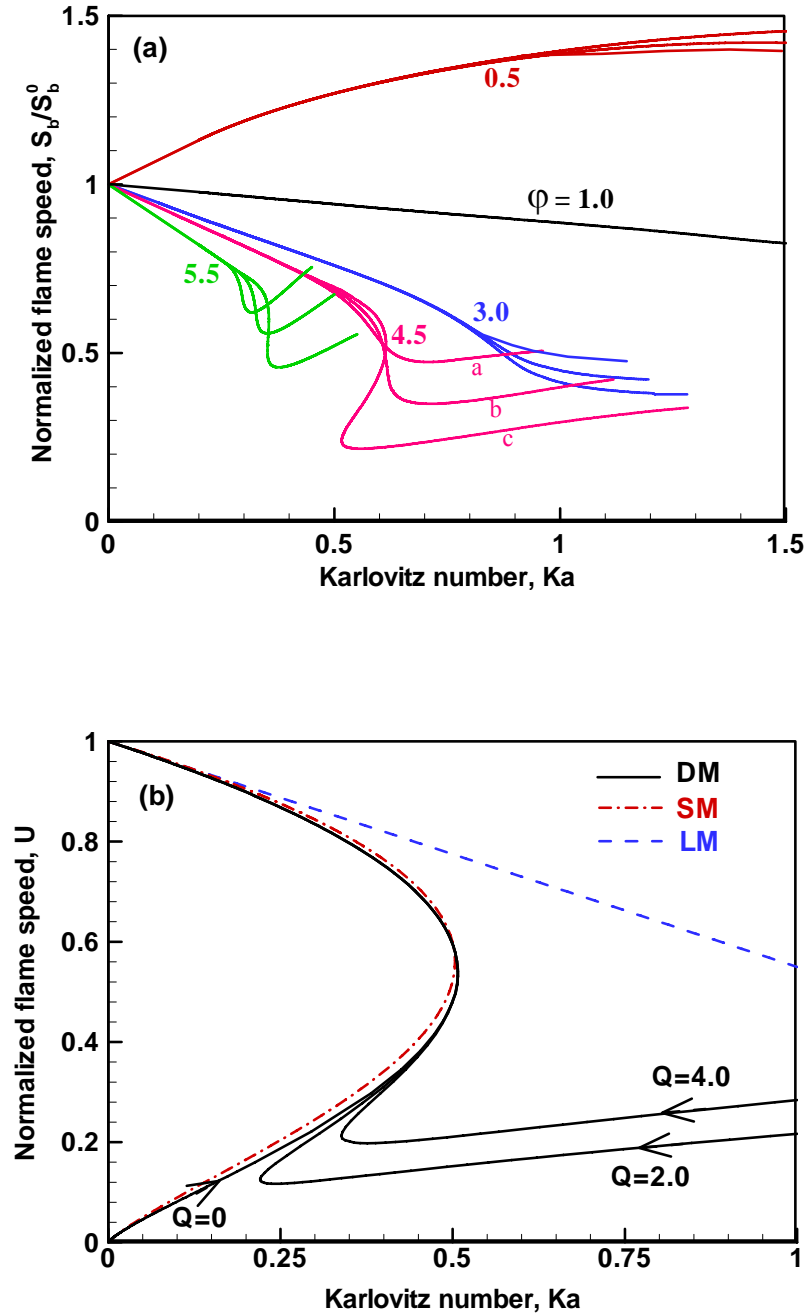


Figure 5.5: Normalized flame speed as a function of Karlovitz number: (a), from simulation of  $H_2$ /air for different equivalence ratios and ignition hot pocket sizes; (b), from theory for  $Le=2.0$  and different ignition powers.

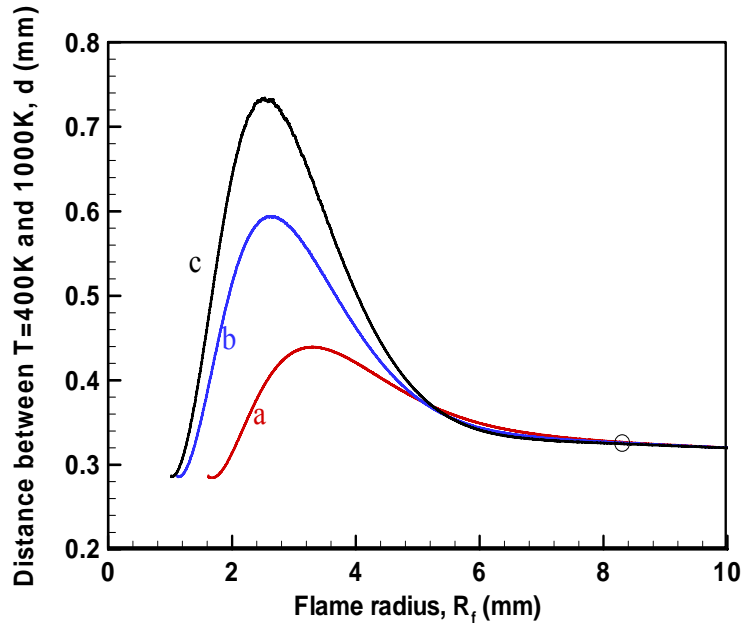


Figure 5.6: Variation of flame thickness during flame propagation from different initiation kernels for  $H_2/air$  ( $\phi=4.5$ ).

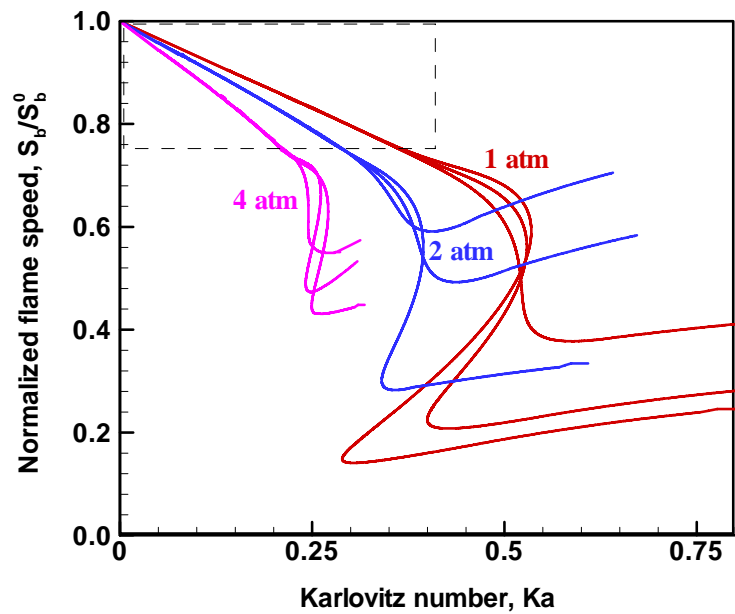


Figure 5.7: Normalized flame speed as a function of Karlovitz number for  $H_2/air$  ( $\phi=5.0$ ) at different pressures and ignition hot pocket size.

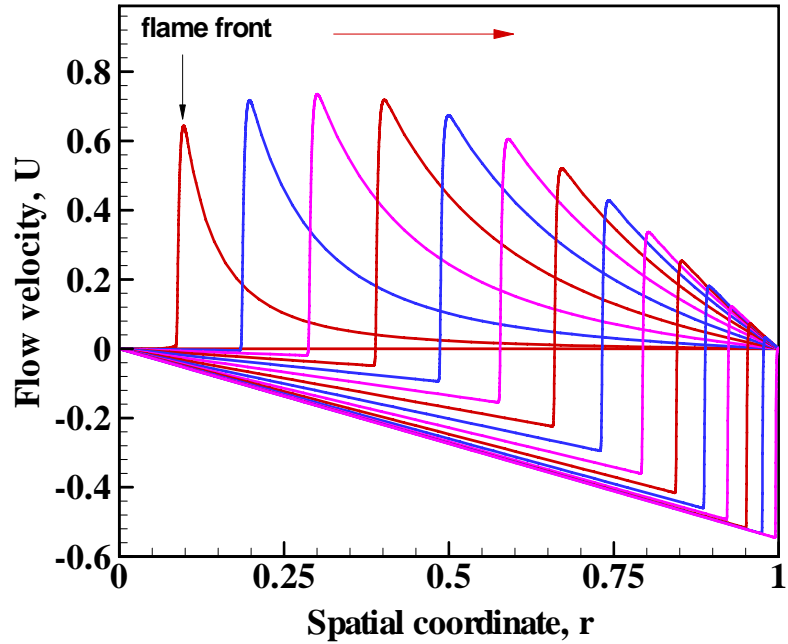


Figure 5.8: Change of flow field during flame propagation (velocity normalized by planar laminar flame speed and length normalized by spherical chamber radius).

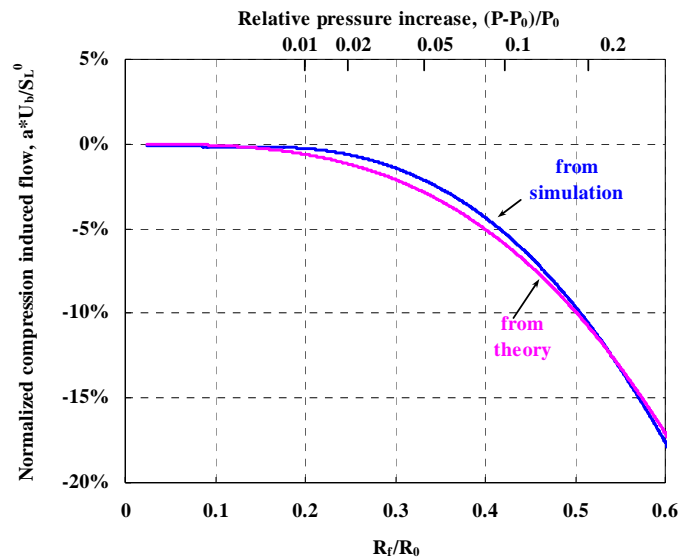


Figure 5.9: The compression induced flow velocity during the propagation of a spherical stoichiometric  $\text{CH}_4/\text{air}$  flame.

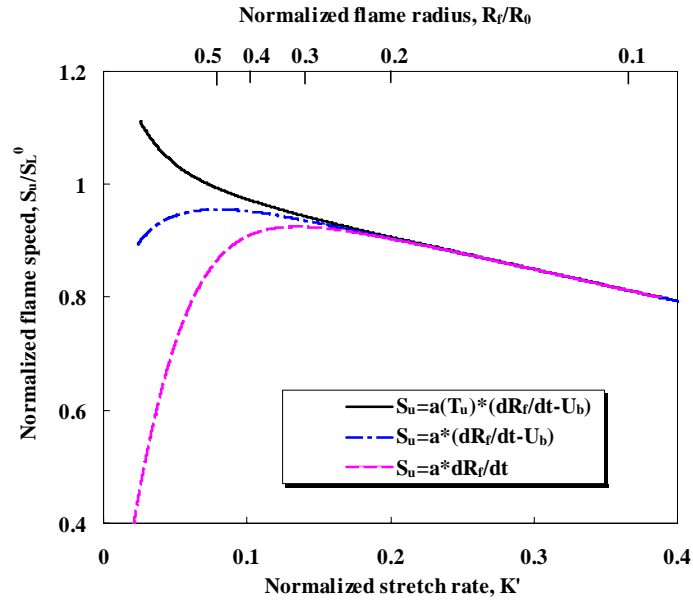


Figure 5.10: Normalized stretched flame speed as a function of normalized stretch rate and flame radius for a stoichiometric CH<sub>4</sub>/air flame.

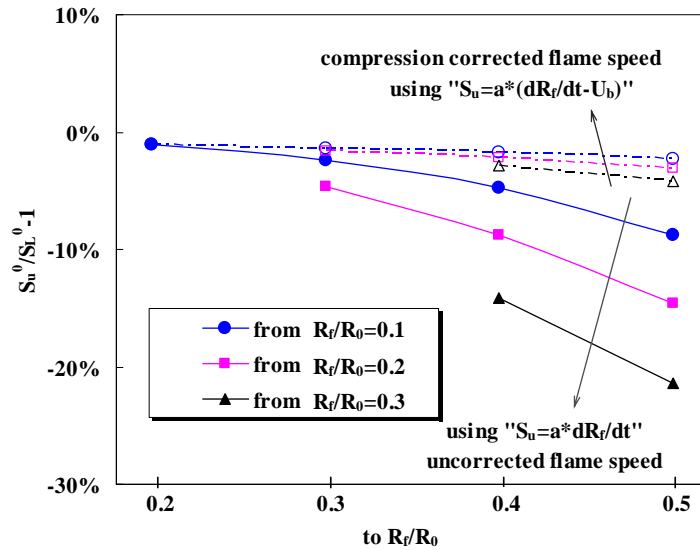


Figure 5.11: Accuracy of the unstretched flame speed with and without compression correction using different flame radius ranges for a stoichiometric CH<sub>4</sub>/air flame.

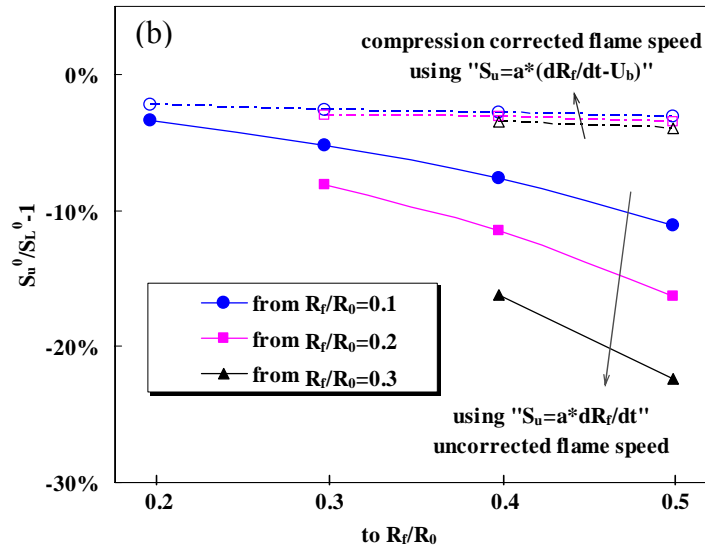
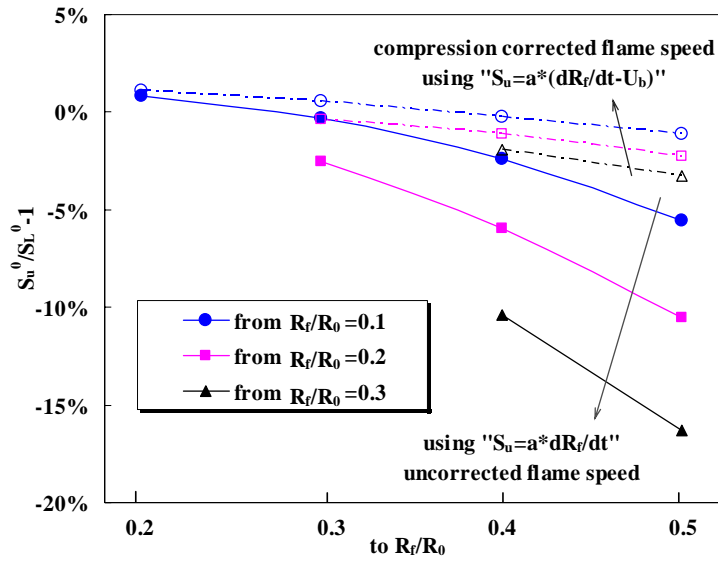


Figure 5.12: Accuracy of the unstretched flame speed with and without compression correction using different flame radius ranges for (a), a stoichiometric H<sub>2</sub>/air flame; (b), a stoichiometric C<sub>3</sub>H<sub>8</sub>/air flame.

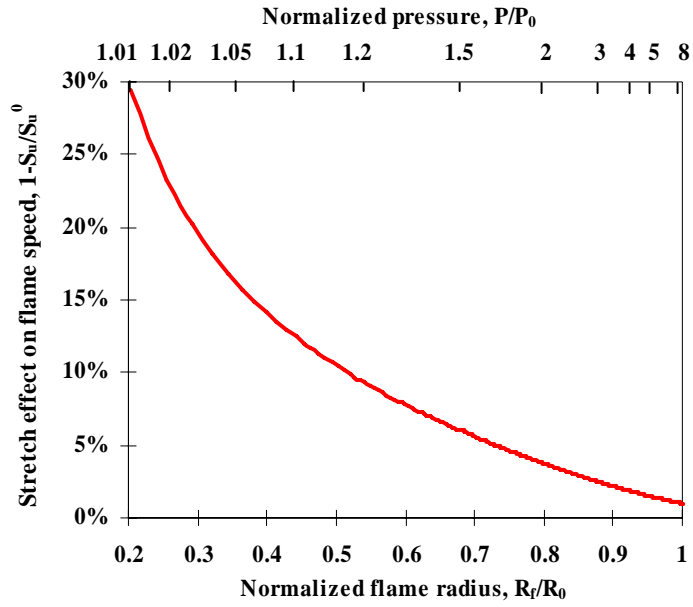


Figure 5.13: The stretch effect on the flame speed according to equation (5.34) with  $P/P_0=8.27$ ,  $\gamma=1.4$ ,  $L_u=0.25$  mm,  $R_0=6$  cm.

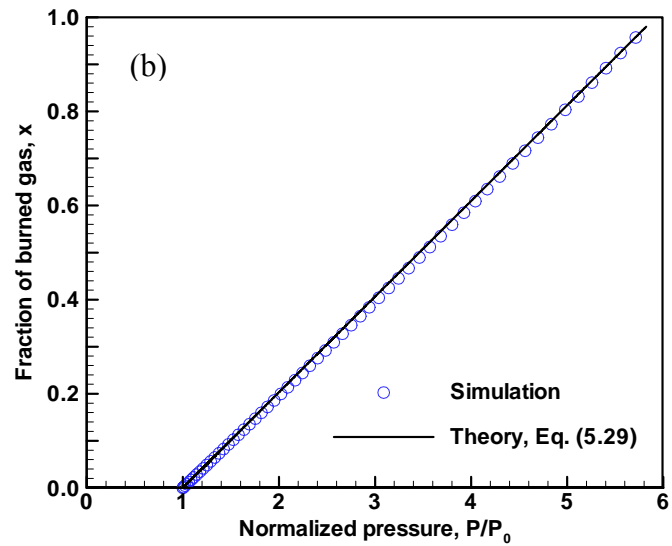
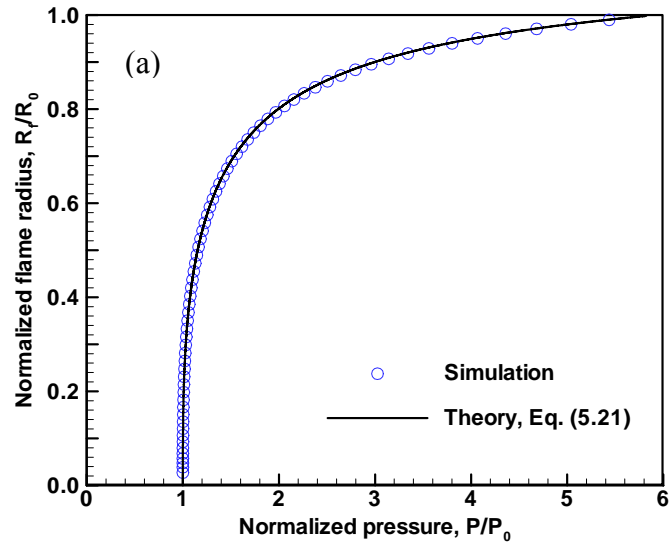


Figure 5.14: The change of (a) normalized flame radius and (b) fraction of burned gas with normalized pressure during the propagation of a spherical  $H_2$ /air flame of  $\varphi=4$  in a closed spherical bomb.

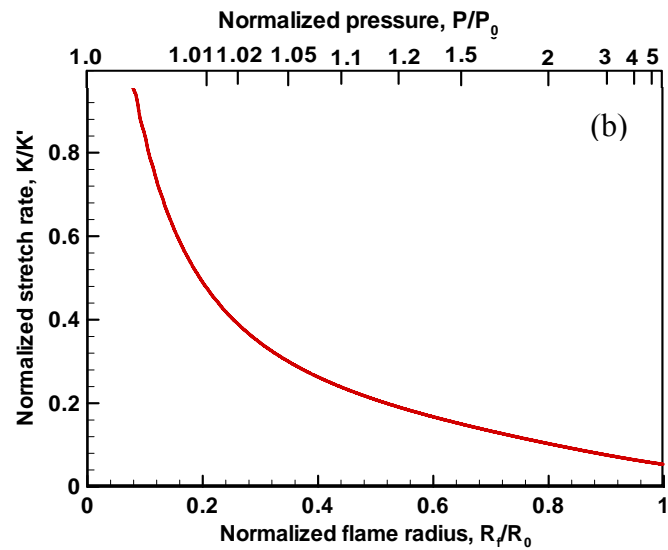
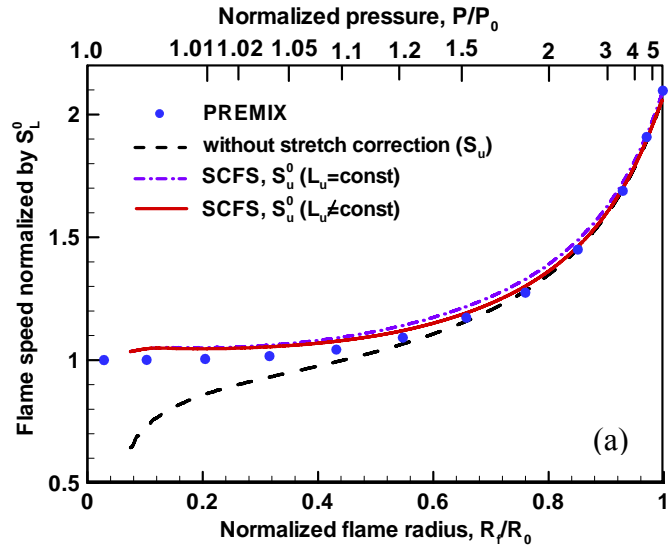
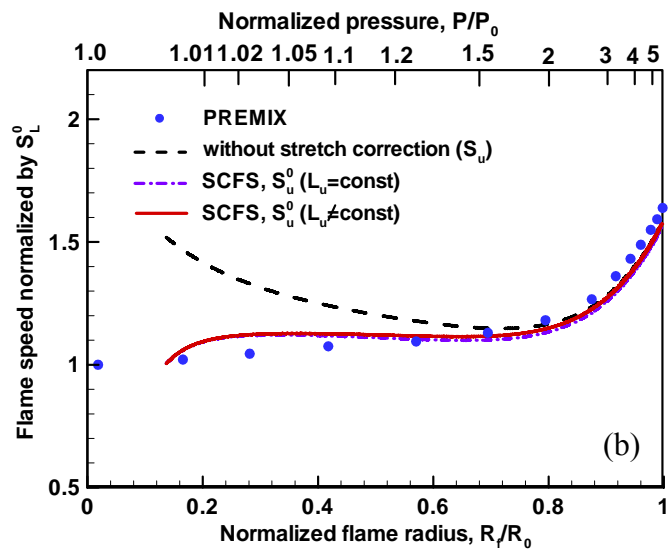
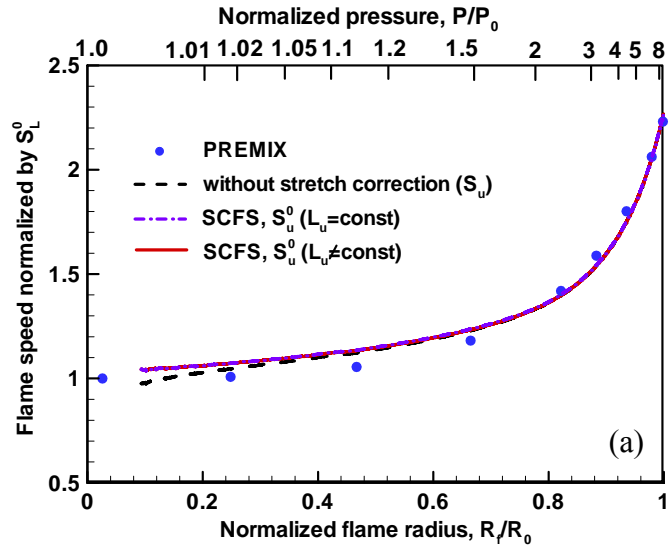


Figure 5.15: (a) Flame speed with and without stretch correction and (b) normalized stretch rate as a function of normalized flame radius and pressure for a  $H_2$ /air flame of  $\phi=4$ .



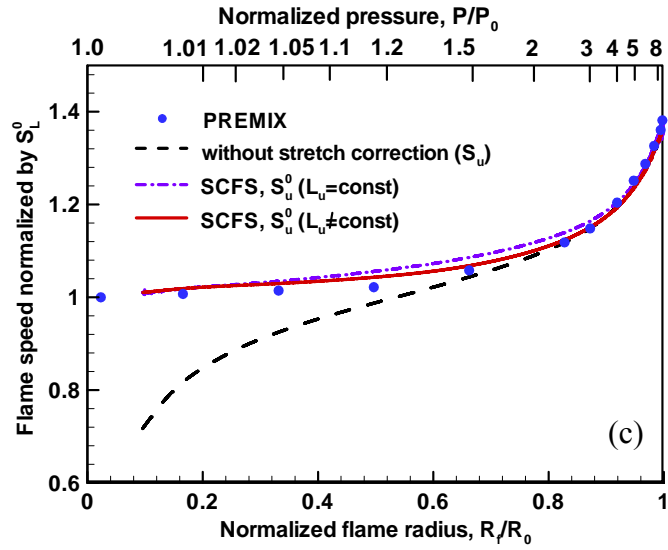


Figure 5.16: Flame speed with and without stretch correction as a function of normalized flame radius and pressure for (a), a  $H_2/air$  flame of  $\phi=1$ ; (b), a  $H_2/air$  flame of  $\phi=0.45$ ; (c), a  $C_3H_8/air$  flame of  $\phi=0.8$ .

# Chapter 6: Effect of Radiation on Flame Propagation and Extinction

In this chapter, the effect of radiation on flame propagation and extinction is investigated. In the first part, the effect of radiative heat loss on both outwardly and inwardly propagating spherical flames is studied using asymptotic analysis for a simplified quasi-planar thermo-diffusion flame structure. In the second part, the effects of spectral-dependent radiation and absorption on the flammability limits and flame speed are investigated experimentally and numerically for CO<sub>2</sub> diluted outwardly propagating CH<sub>4</sub>/O<sub>2</sub>/He flames at normal and elevated pressures. In the third part, the combined effects of radiation, curvature, and stretch on the extinction of premixed counterflow and tubular flames are analyzed.

## 6.1 Radiation Effect on Propagating Spherical Flames

### 6.1.1 Introduction

Radiation heat transfer is well known to be a dominant mechanism for near-limit flames. Extensive studies have been conducted to investigate the effects of radiation, stretch, and curvature on flame extinction by using the counterflow flames, outwardly propagating spherical flames (OPF), and tubular flames, all of which have positive flame stretch rate. To study the effect of negative flame stretch rate, the inwardly propagating spherical flames (IPF) can be utilized. The quenching of IPF has been studied theoretically and numerically in (Frankel and Sivashinsky 1984; Flaherty et al. 1985; Sun and Law 1998). The quenching was found to take place at non-zero velocity of the flame front for mixtures with Lewis number less than unity due to the negative stretch rate of

IPF. For mixtures with Lewis number larger than unity, it was shown that extinction also occurs for IPF due to depletion of the upstream mixture (Sun and Law 1998). Both the OPF and IPF were studied in (Sun et al. 1999) to show the linear relationship between stretched flame speed and flame stretch rate. However, radiative heat loss was not considered in all of the above studies on IPF. As a result, how radiation affects the propagation and extinction of IPF is not well understood. Furthermore, as discussed in the previous chapter, the method utilizing propagating spherical flames in a closed chamber is currently one of the most favourable methods for measuring laminar flame speeds and Markstein lengths. Radiation transfer is inevitable in practical experiments and the effect of radiation on flame speed measurements has been investigated in previous studies (Taylor 1991; Chen et al. 2007a; Chen et al. 2008c). However, there is no study about radiation effect on the Markstein length. Therefore, how the Markstein length is affected by radiation remains unclear.

The objective of this study is to answer the above two questions. Both the OPF and IPF with radiative loss will be investigated and the emphasis is on studying the effects of radiative loss and preferential diffusion on the flame propagation speed, Markstein number, and flame extinction.

### **6.1.2 Mathematical Model and Asymptotic Solutions**

Figure 6.1 shows the schematic diagrams of the OPF and IPF investigated in the present study. The mathematical model for the OPF and IPF is similar to that presented in Chapter 2. Unlike Chapter 2 where emphasis is on the initiation of OPF, here we focus on the propagation and extinction of OPF and IPF. The large flame radius assumption used in (Frankel and Sivashinsky 1983; Frankel and Sivashinsky 1984) is employed here,

under which the nondimensional governing equations, (2.9a, 2.9b), can be simplified as

$$-\left(U + \frac{2}{R}\right) \frac{dT}{d\xi} = \frac{d^2T}{d\xi^2} - h \cdot T + \omega \quad (6.1)$$

$$-(LeU + \frac{2}{R}) \frac{dY}{d\xi} = \frac{d^2Y}{d\xi^2} - Le \cdot \omega \quad (6.2)$$

where  $\xi = r - R(t)$  is the moving coordinate attached to the propagating flame front,  $R=R(t)$ , in which the thermo-diffusion structure of the flame is quasi-planar, i.e.  $R \gg \xi$  (Frankel and Sivashinsky 1983).

Following the same asymptotic analysis procedure presented in Chapter 2, the following algebraic system of equations for normalized flame propagation speed,  $U$  ( $U = |dR/dt| = |V - 2/R|$ ), normalized flame radius,  $R$ , and normalized flame temperature,  $T_f$ , are obtained (the normalization is presented in Chapter 2)

$$T_f \sqrt{V^2 + 4h} = \pm \left[ V + \frac{2}{R} \left( \frac{1}{Le} - 1 \right) \right] = \exp\left( \frac{Z}{2} \frac{T_f - 1}{\sigma + (1 - \sigma)T_f} \right) \quad (6.3)$$

where ‘+’ is for OPF and ‘-’ for IPF. Eliminating the flame temperature and setting  $L = 2Zh$ , where  $h \sim O(1/Z)$  and  $L \sim O(1)$ , we have

$$\left( \frac{dR}{dt} + \frac{2}{R} \right)^2 \ln \left[ \left( \frac{dR}{dt} + \frac{2}{R} \right)^2 \right] = (Z - 2) \frac{2}{R} \left( \frac{1}{Le} - 1 \right) \left( \frac{dR}{dt} + \frac{2}{R} \right) - L \quad (6.4)$$

Using the above relationship, the effect of radiative loss on OPF and IPF could be investigated by comparing the normalized flame propagation speed,  $U = |dR/dt|$ , at different flame radii,  $R$ , and radiative loss intensities,  $L$ . The preferential diffusion effect can also be studied by changing the Lewis number in equation (6.4). The general theory presented in Chapter 2, equation (2.14), which works for OPF for all flame radii range, is found to reduce to the present result, equation (6.4), in the limit of  $R \gg 1$  for OPF. Figure

6.2 shows the flame propagation speed as a function of flame radius for OPF predicted by the present simplified model, equation (6.4), and the detailed model, equation (2.14). It is seen that the prediction from the simplified model agrees well with that from the detailed model at different Lewis numbers and radiative losses. It is noted that the detailed model only works for OPF and there is no counterpart theory for IPF; while the simplified model under the assumption of large flame radius works for both OPF and IPF.

The present simplified model recovers previous results in different limiting cases. Without radiative loss,  $L=0$ , equation (6.4) reduces to that of adiabatic propagating spherical flames studied in (Frankel and Sivashinsky 1983). Moreover, by changing the curvature from  $2/R$  to  $1/R$  in equation (6.4), the same result for nonadiabatic propagating cylindrical flames as that presented in (Mitani 1980) is obtained. In the limit of  $R \rightarrow \infty$ , equation (6.4) recovers the classical theory of flammability limit for planar flames (Joulin and Clavin 1979)

$$(U^0)^2 \ln[(U^0)^2] = -L \quad (6.5)$$

where  $U^0$  is utilized to denote the nondimensional (normalized by adiabatic planar flame speed) plane flame speed with radiative loss. According to equation (6.5), the flammability limit for planar flame is  $L^* = 1/e$  and  $U^{0*} = e^{-1/2}$ .

For both OPF and IPF, the Karlovitz number is defined as  $K=(2/R)(dR/dt)$  (Clavin 1985; Law 2006). When it is small,  $|K| \ll 1$ , there is a linear relationship between  $U$  and  $K$  (Clavin 1985)

$$U \approx U^0 - Ma \cdot K \quad (6.6)$$

where  $Ma$  is the Markstein number. Using Taylor expansion for equation (6.4) at small  $K$ , the linear relationship, equation (6.6), as well as the following expression for the Markstein number is obtained

$$Ma = \frac{1}{U^0} - \frac{(Z/2 - 1)(Le^{-1} - 1)}{(U^0)[2 \ln(U^0) + 1]} \quad (6.7)$$

According to equations (6.5) and (6.7), it is seen that the Markstein number is affected not only by the Lewis number but also by the radiative loss. For adiabatic case ( $L=0$ ,  $U^0=1$ ), the adiabatic Markstein length is (the subscript  $0$  means at zero radiative loss, i.e. adiabatic; while the superscript  $0$  means at zero stretch rate, i.e. unstretched)

$$Ma_0 = Le^{-1} - (Z/2)(Le^{-1} - 1) \quad (6.8)$$

which is the same as that derived for adiabatic counterflow premixed flames (Law 2006). In (Law 2006), the following relationship is proposed for stretched premixed flames with small radiative losses ( $L \ll 1$ )

$$U \approx 1 - \left[ \frac{1}{Le} - \frac{Z}{2} \left( \frac{1}{Le} - 1 \right) \right] K - \frac{L}{2} \quad (6.9)$$

according to which the Markstein length is not affected by radiative loss and is a constant given by equation (6.8). This is not contradictory with the present result. The relationship given by equation (6.9) works only for small radiative loss, while the results given by equations (6.6) and (6.7) work well not only for small radiative loss but also for large radiative loss. As a result, the present theory works for a broader range of radiative loss and thus the radiation effect on flame propagation speed as well as Markstein length at different Lewis numbers can be investigated using equation (6.4).

### 6.1.3 Results and Discussions

Figure 6.3 shows the normalized flame propagation speed as a function of flame radius for OPF and IPF with different radiative loss intensities,  $L$ , and Lewis numbers,  $Le$ . The same Zel'dovich number,  $Z=10$ , as used in Chapter 2 is used here. The results for OPF are consistent with those shown in figures 2.3(a), 2.4(a), and 2.5(a). At a given Lewis number and radiative loss, there are two solutions of flame propagation speed for one specific flame radius: the fast stable one and the slow unstable one (only the fast branch is shown for  $Le=1.0$ ). Extinction occurs at the turning point where the fast branch meets the slow branch (there is no extinction for  $Le=1.0$ ). Figure 6.3 clearly shows that the  $U-R$  relation and flame extinction is strongly affected by the Lewis number and radiative loss. For the same Lewis number, the  $U-R$  diagram of OPF shows totally opposite trends compared with that of IPF. This is because the OPF has positive stretch rate,  $K=(2/R)(dR/dt)>0$ , while the IPF has negative stretch rate,  $K=(2/R)(dR/dt)<0$ . For a Lewis number less (larger) than some critical Lewis number,  $Le^*$  (which is less than 1.0), the positive stretch rate of OPF strengthens (weakens) the flame while the negative stretch rate of IPF weakens (strengths) the flame (Law 2006). As a result, for  $Le=0.5$ , the flame propagation speed (the fast stable branch) of both OPF and IPF decreases monotonically during the propagation; while for  $Le=1.0$  and  $Le=2.0$ , it monotonically increases during the propagation (note that the magnitude of stretch rate change inversely with flame radius).

To investigate the effects of radiation and flame stretch on spherical flame propagation and extinction, the normalized flame propagation speed as a function of stretch rate is shown in figure 6.4. As shown in figures 6.3 and 6.4, for  $Le=0.5$ , the flame

extinction occurs for IPF even when the radiative heat loss is smaller than the one corresponding to the planar flame flammability limit,  $L^* = 1/e$ ; while OPF (which is called self-extinguish flame, SEF) still exists even for mixtures below the flammability limit,  $L = 0.4 > 1/e = L^*$ . For OPF, the existence of SEF for small Lewis numbers is because the flame stretch enhancement is greater than radiative loss when the flame radius is small (Ronney 1985; Ronney 1988). For IPF, extinction is caused by the continuously decreasing flame stretch rate (it is negative and its absolute value increasing during flame propagation) which weakens the flame during flame propagation before the extinction point is reached. The opposite trend is shown for  $Le=2.0$ . Similar results from simulations of adiabatic IPF at different Lewis numbers were found in (Flaherty et al. 1985; Sun and Law 1998), which confirms the validity of the present theoretical prediction. Furthermore, figures 6.3 and 6.4 also show that the radiative loss strongly affects both OPF and IPF and flame extinction occurs earlier at higher radiative loss.

Therefore, at the same radiative loss, for mixture with small Lewis number ( $Le < Le^*$ ), the OPF/IPF propagates faster/slower than the planar propagating flame and the flammability limit is extended/narrowed due to the positive/negative flame stretch; while for mixture with large Lewis number ( $Le > Le^*$ ), the opposite trend happens. The change of flammability limit caused by stretch rate coupled with preferential diffusion effect (Lewis number effect) is further shown in figures 6.5. The turning point on the solid curve, which is the solution as  $R \rightarrow \infty$ , corresponds to the flammability limit for the planar flame, and only the upper fast branch is stable and thus physically realistic. The dashed and dash-dotted lines represent solutions for flames at finite radii (thus finite stretch rate). The flammability region is either extended or reduced, depending on the

value of the Lewis number and the sign of stretch rate: for mixture with small Lewis number ( $Le < Le^*$ ), it is extended for positive stretch (OPF) and reduced for negative stretch (IPF); while for mixture with large Lewis number ( $Le > Le^*$ ), it is extended for negative stretch (IPF) and reduced for positive stretch (OPF). The present results on stretch rate and Lewis number effects for OPF and IPF are consistent with those for OPF in (Bechtold et al. 2005) and counterflow flames presented in (Law 2006).

Figure 6.4 shows that the Markstein length (which is equal to  $-1.0$  multiplying the gradient in the  $U-K$  plot at  $K$  close to zero) is strongly affected by radiative loss. The Markstein length can be evaluated based on equation (6.7). Figure 6.6 shows the Markstein number for different Lewis numbers and radiative loss. It is seen that for small radiative loss, the Markstein length is close to that of the adiabatic flame,  $Ma_0$ . However, when the radiative loss is large, the Markstein length is strongly affected by radiative loss, especially when  $L$  is close to the value corresponding to the flammability limit,  $L^*$ . Moreover, the change of the Markstein length due to radiative loss also strongly depends on the Lewis number.

Figure 6.7 shows the normalized Markstein number as a function of Lewis number for different radiative loss. It is found that the normalized Markstein number varies non-monotonically with the Lewis number and it reaches infinity at  $Le=0.8$  due to the appearance of zero  $Ma_0$  for  $Z=10$  (according to equation (6.8),  $Ma_0$  is zero at  $Le=1-2/Z$ ). With increasing radiative loss, the magnitude of the Markstein number always increases for  $Le < 0.8$ . For  $0.8 < Le < 1.0$ , the magnitude of the Markstein length can be smaller than the adiabatic Markstein length. For  $Le > 1.0$ , the normalized Markstein number is always greater than unity and increases with radiative loss.

#### 6.1.4 Summary

The OPF and IPF at large flame radii were studied using asymptotic analysis. A general correlation between flame propagation speed and flame radius for both OPF and IPF was derived and utilized to study the effects of radiative loss and preferential diffusion on the flame propagation speed, Markstein number, and flame extinction. The following conclusions are made:

1. The flame propagation speed, Markstein number, and flame extinction are strongly affected by the Lewis number as well as the radiative loss. Opposite trends for the change of flame propagation speed during flame propagation are shown for OPF and IPF for different Lewis numbers. The positive/negative stretch rate of OPF/IPF is shown to enhance/weaken the flame at small Lewis numbers and to weaken/enhance the flame at large Lewis numbers.

2. The flammability region is found to be extended for positive stretch (OPF) and reduced for negative stretch (IPF) for mixtures with small Lewis numbers; and it is extended for negative stretch (IPF) and reduced for positive stretch (OPF) for mixtures with large Lewis number.

3. A correlation for the Markstein length at different Lewis numbers and radiative loss was presented. The Markstein length is strongly affected by radiative loss and Lewis number.

## **6.2 Radiation Reabsorption Effect on Flame Speed and Flammability**

### **Limits**

#### **6.2.1 Introduction**

In the previous section, radiative loss is simplified as a linear function of temperature in theoretical analysis. However, in practical problems, thermal radiation not only changes nonlinearly with temperature but also strongly depends on the mixture composition and pressure. Furthermore, radiation has a strong spectral dependence and can act not only as a heat sink due to emission but also as a heat source due to absorption. In this part, the CO<sub>2</sub> diluted outwardly propagating CH<sub>4</sub>/O<sub>2</sub>/He flames will be used to study the effects of the spectral dependent radiation and absorption on flame speed and flammability limit.

#### **6.2.2 Experimental and Numerical Specifications**

The experimental measurements of flame speed were conducted in a dual-chambered, pressure-release type high pressure combustion facility at normal gravity (Qin and Ju 2005). This type of dual chamber design was first reported by Tse et al. (Tse et al. 2000). Due to the effect of buoyancy, the maximum test pressure was limited to 5 *atm*. The combustible mixture was spark-ignited at the center of the inner chamber with minimum ignition energy so as to minimize ignition disturbances. The flame propagation sequence was imaged with Schlieren photography and a high-speed digital video camera (Photron Fastcam APX) with 4  $\mu$ s shutter speed and a framing rate of 8000 fps. 1024 pixels were used for 5 *cm* width domain in the horizontal direction. Data reduction was performed only for flame radii between 1.0 and 2.5 *cm*. Pressure increase is negligible since the volume of the chamber is approximately 100 times larger

than the flame size at which the flame speed was measured. Therefore, the CCFS is not employed here. The reactant mixtures were prepared using the partial pressure method. Helium was introduced to adjust the mixture Lewis number and to suppress the flame instability (Law 2006). Mixtures of  $\text{CH}_4-(0.3\text{O}_2+0.2\text{He}+0.5\text{CO}_2)$  were examined and all runs were performed in a quiescent environment at an initial temperature of  $298\pm 3\text{ K}$  and initial pressures ranging from 1 to 5 *atm*. The results presented at each point were the average of three tests.

For the spherical flame simulation, A-SURF was used here to simulate the outwardly propagating spherical  $\text{CH}_4/\text{O}_2/\text{He}/\text{CO}_2$  flames at different equivalence ratios and pressures. For methane oxidation, the GRI-MECH 3.0 mechanism (Smith et al.) was used and the detailed transport and thermodynamic properties were predicted from the CHEMKIN database (Kee et al. 1989). To initiate the computation, a hot spot with radius of 1.5 *mm* and temperature of 1800 *K* was set in the center initially to mimic the spark ignition in the experiments. The stretched flame speed was first obtained from the flame front (point of maximum heat release) history and then linearly extrapolated to zero stretch rate to yield the unstretched flame speed. The most accurate and efficient radiation modeling, FSNB-CK (Chen et al. 2007a), was incorporated into A-SURF to investigate the effect of spectral-dependent radiation.

### 6.2.3 Results and Discussions

Figure 6.8 shows Schlieren photographs of  $\text{CH}_4-(0.3\text{O}_2+0.2\text{He}+0.5\text{CO}_2)$  flames at different equivalence ratios at 1 *atm*. For fast-burning mixtures (stoichiometric or near stoichiometric mixtures,  $\phi=0.8$  in figure 6.8), buoyancy effect is not observed from flame images and the flame front is spherically symmetric. For lean mixtures, the effect of

buoyancy is noticeable and the flame front reaches the top edge of the photograph before reaching the bottom. Here, we define the 1-g downward flammability limit,  $\Phi_d$ , as in the limiting mixture in which the flame can propagate throughout the entire chamber. For the present  $\text{CH}_4\text{-(}0.3\text{O}_2\text{+}0.2\text{He+}0.5\text{CO}_2\text{)}$  mixture, the downward flammability limit is  $\Phi_d=0.50$ . Below this limit, e.g. for leaner mixtures ( $\phi=0.49$  in figure 6.8), the flame cannot propagate downward against buoyancy forces. After reaching the top of the inner chamber, the flame spreads out and propagates downward. Although the mixture at this condition is still flammable, the flame front location is hard to determine and flame speed data are not extracted for these cases. At elevated pressures, buoyancy effect is enhanced with the increase of mixture density. For example, at 5 atm the downward flammability limit becomes  $\Phi_d=0.57$ .

Figure 6.9 shows the measured and predicted flame speeds of  $\text{CH}_4\text{-(}0.3\text{O}_2\text{+}0.2\text{He+}0.5\text{CO}_2\text{)}$  flames at different equivalence ratios at 1 atm. For comparisons, three radiation models were employed. First is the optically thin model (OPTM) (Ju et al. 1997) in which no radiation absorption is considered. The second is the SNB gray band model in 1D planar geometry (SNB-GB1D) (Kim et al. 1991; Liu et al. 1998) in which gray gas model is used at each band (375 bands in total) and radiation absorption is solved in the one-dimensional slab rather than in spherical geometry. The third one is the FSNB-CK model (Chen et al. 2007a) in which spectral radiation is solved in the spherical coordinate. Furthermore, the volumetric radiative loss and temperature distributions predicted from OPTM, SNB-GB1D and FSNB-CK for a flame at equivalence ratio of 0.6 and flame radius of 2.4 cm are plotted in figure 6.10.

Figure 6.9 shows that the optically thin model under-predicts the flame speed.

This is because OPTM model over-predicts the radiative heat loss and the flame temperature decreases significantly in the burned zone (figure 6.10). However, for the FSNB-CK model, it is seen that because of radiation absorption, the radiative loss in the burned zone becomes much smaller. A significant amount of radiative loss from the burned zone is reabsorbed by the unburned mixture (see the part with negative heat loss in figure 6.10). This means that the radiation absorption in CO<sub>2</sub>-diluted flames increases the flame speed by reducing the net heat loss and that the optically thin model is not applicable. As the equivalence ratio decreases, figure 6.9 shows that radiation absorption plays an important role in increasing the flame speed and extending the flammability limit. On the other hand, the SNB gray band model in 1D geometry over-predicts the flame speed. This over-prediction comes from two sources. One is that the employment of one-dimensional radiation geometry in which less radiation emission in the burned gas than that in the spherical flame was calculated (compare the radiation predicted by FSNB-CK(planar) and FSNB-CK(spherical) in figure 6.10); and the second is that the gray narrow band assumption increases the radiation absorption (compare the radiation predicted by FSNB-CK(planar) and SNB-GB1D in figure 6.10). The present FSNB-CK model greatly improves the accuracy of the flame speed prediction. A slight over-prediction may result from the linear extrapolation method for flame speed because, strictly speaking, the radiation enhancement does not linearly increase with the flame radius. This improvement is because the radiation in spherical flame geometry is appropriately solved and the spectral radiation in each band is accurately treated by using the cumulative function of  $k$ -distribution from the direct Laplace transform instead of the simple gray gas assumption.

Theoretical analysis in (Joulin and Deshaies 1986) shows that radiation absorption has less effect as pressure increases because the total chemical heat release increases with the pressure. In order to examine the effect of pressure, the radiation absorption effect and comparison of different radiation models for  $\text{CH}_4+(0.3\text{O}_2+0.2\text{He}+0.5\text{CO}_2)$  mixtures at 2 *atm* and 5 *atm* is shown in figure 6.11. It is seen that radiation absorption becomes much stronger than that at 1 *atm*. Different from the theory (Joulin and Deshaies 1986), the present result shows that radiation absorption increases with pressure. This is because an infinite optical thickness was assumed in the theory (Joulin and Deshaies 1986) so that all the radiative loss from the burned zone is absorbed by the unburned mixture. In the present experiment, the optical thickness is finite (about 1.0~6.0 estimated from OPTM) so that the increase of pressure enlarges the optical thickness and radiation absorption. Again, for the same reason, it is clearly seen that the present FSNB-CK model predicts the flame speed much better than SNB-GB1D. With a further increase of pressure to 5 *atm*, figure 6.11 shows that the radiation absorption effect further increases.

To further demonstrate the pressure effect on radiation absorption, the normalized flame speed increase due to radiation absorption at different equivalence ratios is plotted in figure 6.12. It is seen that radiation absorption enhancement on the flame speed is linearly dependent on pressure. This linear dependence is caused by the increase of the optical thickness. In addition, figure 6.12 shows that with decreasing equivalence ratio, the effect of radiation absorption on flame speed becomes more significant. Therefore, it can be concluded that although the pressure increase leads to an increased chemical heat release, the effect of radiation absorption on flame speed enhancement still increases and

it becomes increasingly important for lean flames.

As discussed above, radiation absorption depends on the optical thickness. Therefore, it is of interest to show how radiation absorption enhancement on the flame speed depends on the flame size so that a flamelet model can be used to correct the radiation absorption effect in turbulence modeling. According to the theory in (Joulin and Deshaies 1986), the flame speed is related to the Boltzmann number,  $B$ , by

$$(S_L / S_L^0) \ln(S_L / S_L^0) = B, \quad B = E\sigma(T_{ad}^4 - T_0^4) / (2R\rho_0 S_L^0 C_P T_{ad}^2) \quad (6.10)$$

where  $E$ ,  $R$ ,  $\sigma$ , and  $C_P$  denote the activation energy, universal gas constant, Stefan-Boltzmann constant, and the specific heat, respectively.  $T_{ad}$  is the adiabatic flame temperature, and  $\rho_0$  and  $T_0$  are the unburned gas density and temperature. Therefore,  $B$  represents the radiation absorption effect on the increase of flame speeds. The effective  $B$  numbers estimated from theory (Joulin and Deshaies 1986) and computation (by using  $S_L$  from simulation and the first equation of equation (6.10)) as a function of flame size are plotted in figure 6.13. Note that in calculating the  $B$  number, the flame stretch effect is already excluded by comparing the radiative flames with the adiabatic flames. It is seen that the radiation absorption effect predicted by the theory is two orders of magnitude higher than that predicted by the FSNB-CK model. In addition, the theory predicts a constant  $B$  number with increasing flame radius. This is also because of the assumption of large optical thickness. The FSNB-CK model predicts a negative  $B$  number at small flame radius and an increasing dependence of  $B$  on the flame radius. This means that at small flame radius, although radiation absorption can enhance the flame speed, the final flame speed remains below the adiabatic flame speed. However, with increasing flame radius, the optical thickness increases, yielding an increase in the  $B$  number. Again, for

the optically thin model, the predicted  $B$  number is much lower. At high pressures, similar trends are also found except that the  $B$  number becomes positive at 2 atm. Therefore, by computing the  $B$  number for a given optical thickness, the radiation absorption effect could be employed in flamelet models for turbulent modeling.

#### 6.2.4 Summary

The spectral-dependent radiation absorption effect on flame speed enhancement was measured by using CO<sub>2</sub>-diluted CH<sub>4</sub>-O<sub>2</sub> mixtures at normal and elevated pressures. The following conclusions are drawn from this study:

1. Radiation absorption increases the flame speed and extends the flammability limit. This enhancement effect also increases with pressure. The spectral-dependent radiation absorption needs to be included in any quantitative predictions of flame speed and flammability limit with CO<sub>2</sub> addition.

2. The FSNB-CK radiation model can well reproduce the measured flame speed. The SNB narrow-band gray model over-predicts the flame speed while the optically thin model significantly under-predicts the flame speed.

3. The radiation absorption effect increases with flame size and pressure. The theory based on gray gas model over-predicts the radiation absorption by two-orders. The effective Boltzmann number is extracted from the present radiation modeling and can be applied to flamelet modeling in turbulent flow.

4. Flame geometry has a significant effect on flame radiation. In spherical flame modeling, the one-dimensional slab radiation model over-predicts the radiation absorption.

## **6.3 Radiation Effect on Premixed Counterflow and Tubular Flames**

### **6.3.1 Introduction**

It is well known that curved flame fronts prevail in turbulent combustion and the effect of curvature on flame propagation is important, especially for near-limit flames. Therefore, in order to extend the flammability and to improve flame stability, it is particularly important to understand how the coupling of thermal radiation, flame curvature, and stretch affects the flame speed and extinction limits. In the previous two sections, the effect of radiation is studied for propagating spherical flames, in which the flame stretch and flame curvature both change and it is difficult to investigate the pure curvature effect. In this part, the steady tubular and counterflow flames are investigated and by comparing the flame dynamics of these two flames at the same stretch rate and radiation intensity, the curvature effect on the near-limit radiative flames are demonstrated.

### **6.3.2 Mathematical Model and Asymptotic Solutions**

In order to study the effect of flame curvature, two kinds of flame configurations are considered in this study. The first one is the premixed tubular flame shown in figure 6.14(a). Combustible mixture is injected toward the concentric inner tube (stagnation surface) from the inner wall of the porous outer tube. A positively stretched tubular flame with well-defined flame curvature can be stabilized between the inner and outer tubes (Takeno et al. 1986; Mosbacher et al. 2003; Wang et al. 2006). The inner tube is introduced here to change the flame curvature (Mosbacher et al. 2003; Wang et al. 2006; Yokomori et al. 2006). The second configuration is the premixed planar counterflow flame shown in figure 6.14(b). This flame is also positively stretched but has no flame

curvature. Therefore, by comparing the flame dynamics of these two flames at the same stretch rate and radiation intensity, the curvature effect on the near limit radiative flames can be readily demonstrated.

For both flame geometries, the potential flow assumption, which is commonly used in the large activation energy asymptotic analysis (Sohrab and Law 1984; Ju et al. 2000; Matthews et al. 2006), is employed here. By introducing a geometry factor  $N$  with  $N=0$  for the counterflow flame and  $N=1$  for the tubular flame (with  $\tilde{R}_I$  and  $\tilde{R}_O$  being the inner and outer tube radius, respectively), the potential flow field for both configurations can be written as

$$\tilde{u} = -\tilde{k}(\tilde{r}^2 - \tilde{R}_I^2)/[(1+N)\tilde{r}] \quad (6.11)$$

$$\tilde{w} = \tilde{k}\tilde{z} \quad (6.12)$$

where  $\tilde{u}$  and  $\tilde{w}$  are velocities in the radial ( $\tilde{r}$ -axis for tubular flame with  $N=1$ ,  $\tilde{x}$ -axis for counterflow flame with  $N=0$ ,  $\tilde{x} = \tilde{r}$ ,  $\tilde{R}_I = 0$ , and  $\tilde{R}_O \rightarrow \infty$ ) and the axial directions ( $\tilde{z}$ -axis), respectively, and  $\tilde{k}$  is the inlet velocity gradient.

According to the definition of flame stretch rate (Williams 1985) and the simplified expression derived by Matalon (Matalon 1983), the flame stretch rate can be written as:

$$\frac{1}{\tilde{A}} \frac{d\tilde{A}}{d\tilde{t}} = -[\tilde{\nabla} \times (\tilde{V} \times \tilde{n})] \cdot \tilde{n} + v_n (\tilde{\nabla} \cdot \tilde{n}) \quad (6.13)$$

where  $\tilde{V}$  is the flow velocity and  $\tilde{n}$  is the unit normal vector of the flame surface,  $v_n$  is the normal component of the flame front propagating velocity and  $\tilde{\nabla} \cdot \tilde{n}$  is the flame curvature. For the steady flames considered in this study,  $v_n$  is zero. Therefore, the

stretch rate, which only depends on the flow field given by equations (6.11) and (6.12) becomes

$$\frac{1}{\tilde{A}} \frac{d\tilde{A}}{d\tilde{t}} = -\frac{1}{\tilde{r}^N} \frac{d}{d\tilde{r}} (\tilde{r}^N \tilde{u}) = \tilde{k} \quad (6.14)$$

which indicates that the two flame configurations will have the same stretch rate  $\tilde{k}$  if the inlet velocity is specified according to equations (6.1) and (6.2). Note that the flame stretch rate  $\tilde{k}$  is independent of the inner tube radius  $\tilde{R}_f$ . Therefore, by fixing  $\tilde{k}$  and varying  $\tilde{R}_f$  for the tubular flame configuration ( $N=1$ ), flames at the same stretch rate but different curvatures (different flame radii  $\tilde{R}_f$ ) can be obtained (Takeno et al. 1986; Kobayashi and Kitano 1989; Mosbacher et al. 2003; Yokomori et al. 2006). When  $\tilde{R}_f \rightarrow \infty$  and  $N=1$ , the tubular flame has zero flame curvature and it becomes counterflow flame ( $N=0$ ); when  $\tilde{R}_f = 0$  and  $N=1$ , the flame curvature reaches its maximum value and it is the traditional tubular flame configuration (without the inner tube) employed in previous studies (Takeno and Ishizuka 1986; Takeno et al. 1986; Nishioka et al. 1988; Kobayashi and Kitano 1989; Nishioka et al. 1991; Kobayashi and Kitano 1993; Ju et al. 1999b; Matthews et al. 2006). Therefore the present model is more general and it will be shown that previous results on both counterflow flames and tubular flames can be recovered.

Since we are interested in the dynamics of the near-limit flames, the combustible mixture is sufficiently off-stoichiometric so that the flame strength is only determined by the concentration of the fuel. By assuming constant density, constant thermal properties, and one-step irreversible chemical reaction, the nondimensional conservation equations for energy and fuel mass fraction can be written as

$$-k \frac{r^2 - R_I^2}{r} \frac{dT}{dr} = \frac{1}{r^N} \frac{d}{dr} \left( r^N \frac{dT}{dr} \right) + \omega - q_r \quad (6.15)$$

$$-k \frac{r^2 - R_I^2}{r} \frac{dY}{dr} = \frac{1}{Le} \frac{1}{r^N} \frac{d}{dr} \left( r^N \frac{dY}{dr} \right) - \omega \quad (6.16)$$

Parameters with and without the carrot symbol denote the dimensional and non-dimensional variables, respectively. The variables,  $r$ ,  $T$  and  $Y$  are, respectively, the axial coordinate, temperature, and fuel mass fraction normalized by  $\tilde{\delta}_f^0$ ,  $\tilde{Y}_\infty \tilde{Q} / \tilde{C}_p$ , and  $\tilde{Y}_\infty$ , where  $\tilde{\delta}_f^0 = \tilde{\lambda} / (\tilde{\rho} \tilde{C}_p \tilde{S}_L^0)$  is the flame thickness of adiabatic planar flame,  $\tilde{\lambda}$  the thermal conductivity,  $\tilde{\rho}$  the density,  $\tilde{C}_p$  the specific heat capacity at constant pressure,  $\tilde{Q}$  the reaction heat-release per unit mass of fuel, and  $\tilde{Y}_\infty$  the fuel mass fraction in the fresh mixture. Additionally,  $Le = \tilde{\lambda} / \tilde{\rho} \tilde{C}_p \tilde{D}$  is the Lewis number and  $\tilde{D}$  the mass diffusivity of fuel. The normalized stretch rate is  $k = \tilde{k} \tilde{\rho} \tilde{C}_p (\tilde{\delta}_f^0)^2 / [(N+1)\tilde{\lambda}]$ . The adiabatic laminar burning velocity  $\tilde{S}_L^0$  for a first-order one-step reaction is (Williams 1985):

$$\tilde{S}_L^0 = \left\{ 2 \cdot \frac{\tilde{\lambda}}{\tilde{\rho} \tilde{C}_p} \cdot \tilde{B} \cdot \frac{Le}{Z^2} \cdot \exp\left(-\frac{T_a}{T_{ad}}\right) \right\}^{1/2} \quad (6.17)$$

where  $Z = T_a / T_{ad}^2$  is the Zeldovich number,  $\tilde{B}$  the pre-factor of the Arrhenius expression,  $T_{ad}$  the normalized adiabatic flame temperature, and  $T_a$  the normalized activation temperature.

On the right-hand side of equation (6.15),  $q_r$  is the nondimensional volumetric radiative heat loss. It is approximated by using the optically thin grey gas model of (Ju et al. 1997)

$$q_r = 4\tilde{\sigma}\tilde{K}_p(\tilde{T}^4 - \tilde{T}_\infty^4)(\tilde{\delta}_f^0)^2\tilde{C}_p/(\tilde{Y}_\infty\tilde{Q}\tilde{\lambda}) \quad (6.18)$$

where  $\tilde{\sigma}$  is the Stefan-Boltzmann constant,  $\tilde{K}_p$  the Planck mean absorption coefficient of the mixture, and  $\tilde{T}_\infty$  the temperature of the incoming fresh mixture.

In the limit of large activation energy, chemical reaction occurs only within a very thin zone of high temperature, whose thickness is much smaller than that of the radiation zone (Sohrab and Law 1984; Ju et al. 1997). Therefore, the reaction rate can be replaced by the Dirac Delta function (Sivashinsky 1977; Joulin and Clavin 1979; Law 2006)

$$\omega = \exp\left(\frac{T_a}{2T_{ad}} - \frac{T_a}{2T_f}\right) \cdot \delta(r - R_f) \quad (6.19)$$

where  $T_f$  and  $R_f$  are the flame temperature and radius, respectively. By integrating the conservation equations (6.15) and (6.16) around the flame front ( $r=R_f$ ), the jump relations for temperature and fuel mass fraction can be obtained as (Sivashinsky 1977; Joulin and Clavin 1979)

$$\left.\frac{dT}{dr}\right|_{R_f^-} - \left.\frac{dT}{dr}\right|_{R_f^+} = \frac{1}{Le} \left( \left.\frac{dY}{dr}\right|_{R_f^+} - \left.\frac{dY}{dr}\right|_{R_f^-} \right) = \exp\left(\frac{T_a}{2T_{ad}} - \frac{T_a}{2T_f}\right) \quad (6.20)$$

The symmetric (for  $R_I=0$ ) or adiabatic (for  $R_I>0$ ) condition is used at the inner boundary ( $r=R_I$ ). At the inlet ( $r=R_O$ ), the Hirschfelder boundary condition for the fuel concentration, as suggested by Matthews et al. (Matthews et al. 2006), is used instead of the plug flow boundary condition. By defining the flame as the location where fuel concentration goes to zero, the boundary conditions for temperature and fuel mass fraction can be given as

$$\begin{aligned} r = R_I : & \quad dT/dr = 0, \quad dY/dr = 0 \\ r = R_f : & \quad T = T_f, \quad Y = 0 \\ r = R_O : & \quad T = T_\infty, \quad Le^{-1}dY/dr = k(1-Y)(r^2 - R_I^2)/r \end{aligned} \quad (6.21)$$

It should be noted that for the counterflow flame ( $R_0 \rightarrow \infty$ ), the inlet boundary condition (6.21c) reduces to the plug flow boundary condition ( $Y=1$ ), which is used in previous theoretical studies of counterflow flames (Ju et al. 2000).

In the limit of large activation energy, it is reasonable to assume that the magnitude of the radiative loss term in the energy equation is one-order smaller than those of the convection and diffusion terms. This assumption has been widely used in combustion theory (Joulin and Clavin 1979; Buckmaster 1997) and its validity has been confirmed by previous analysis. The radiation term given by equation (6.18) can be written as

$$q_r = h(T^4 - T_\infty^4), \quad h = 4\tilde{\sigma}\tilde{K}_p(\tilde{\delta}_f^0)^2\tilde{Y}_\infty^3\tilde{Q}^3/(\tilde{\lambda}\tilde{C}_p^3) \ll 1 \quad (6.22)$$

The validity of  $h \ll 1$  is shown in (Chen and Ju 2008). It is noted that the nonlinear radiative heat loss is considered in the present study. It was shown by Ju et al. (Ju et al. 2000) that the linearized radiative heat loss results in a narrower flammable region and a larger flammability limit compared with the nonlinear radiative heat loss model. Therefore, by using the nonlinear radiation model, the present model can more accurately demonstrate the dynamics of radiation dominated near-limit flames.

Since the delta-function model for reaction rate is used here, in the limit of large activation energy, the governing equations can be solved analytically in the burned gas ( $R_I \leq r \leq R_f$ ) and unburned gas ( $R_f \leq r \leq R_O$ ) regions separately. The fuel mass fraction in the burned gas region is zero according to the fuel lean assumption and that in the unburned gas region is obtained by solving equation (6.16) together with the boundary conditions in equation (6.21), which gives

$$Y^+(r) = \frac{\int_{R_f}^r \tau^{kLeR_f^2 - N} e^{-kLe\tau^2/2} d\tau}{\int_{R_f}^{R_o} \tau^{kLeR_f^2 - N} e^{-kLe\tau^2/2} d\tau + [kLe(R_o^2 - R_f^2)]^{-1} R_o^{kLeR_f^2 - N + 1} e^{-kLeR_o^2/2}} \quad (6.23)$$

Here the superscripts ‘+’ and ‘-’ denote the states on the unburned and burned sides of the flame front, respectively. To determine the temperature distribution, the energy equation (6.15) with boundary conditions in equation (6.21) can be solved asymptotically, i.e.  $T = T_0 + hT_1 + O(h^2)$ , with the accuracy to the first order,  $O(h)$ . The temperature distribution in the burned gas region ( $R_f \leq r \leq R_o$ ) is

$$T^-(r) = T_f - h^-(T_f^4 - T_\infty^4) \int_r^{R_f} \left[ \int_{R_f}^\tau (s/\tau)^{N - kR_f^2} e^{k(s^2 - \tau^2)/2} ds \right] d\tau \quad (6.24)$$

and that in the unburned gas region ( $R_f \leq r \leq R_o$ ) is

$$T^+(r) = T_0^+(r) + h^+ T_1^+(r) \quad (6.25)$$

$$T_0^+(r) = T_\infty + (T_f - T_\infty) G(r) / G(R_f) \quad (6.26)$$

$$T_1^+(r) = \frac{G(r)}{G(R_f)} \int_{R_f}^{R_o} \frac{\varphi(s) [T_f - T_0^+(s)]}{dT_0^+(s)/ds} ds - \int_r^{R_o} \frac{\varphi(s) [T_0^+(r) - T_0^+(s)]}{dT_0^+(s)/ds} ds \quad (6.27)$$

where  $G(r) = \int_r^{R_o} \tau^{kR_f^2 - N} e^{-k\tau^2/2} d\tau$  and  $\varphi(r) = [T_0^+(r)]^4 - T_\infty^4$ .

The gradients of temperature and fuel mass fraction at the flame front can be obtained from their distributions given by equations (6.23-6.27). By using the jump relations in equation (6.20), one obtains the following algebraic system of equations for the flame radius,  $R_f$ , and flame temperature,  $T_f$

$$Le^{-1} \cdot F^+(R_f, Le) = \frac{T_f - T_\infty}{\int_{R_f}^{R_o} (s/R_f)^{kR_f^2 - N} e^{k(R_f^2 - s^2)/2} ds} + L^+(R_f, T_f) + L^-(R_f, T_f) \quad (6.28)$$

$$Le^{-1} \cdot F^+(R_f, Le) = e^{T_a(T_{ad}^{-1} - T_f^{-1})/2} \quad (6.29)$$

where

$$F^+(R_f, Le) = \frac{R_f^{kLeR_f^2-N} e^{-kLeR_f^2/2}}{\int_{R_f}^{R_o} \tau^{kLeR_f^2-N} e^{-kLe\tau^2/2} d\tau + [kLe(R_o^2 - R_f^2)]^{-1} R_o^{kLeR_f^2-N+1} e^{-kLeR_o^2/2}} \quad (6.30)$$

$$L^+(R_f, T_f) = h^+ \frac{\int_{R_f}^{R_o} \varphi(\tau) \left[ \int_{\tau}^{R_o} (s/\tau)^{kR_f^2-N} e^{k(\tau^2-s^2)/2} ds \right] d\tau}{\int_{R_f}^{R_o} (s/R_f)^{kR_f^2-N} e^{k(R_f^2-s^2)/2} ds} \quad (6.31)$$

$$L^-(R_f, T_f) = h^-(T_f^4 - T_\infty^4) \cdot \int_{R_f}^{R_o} (s/R_f)^{N-kR_f^2} e^{k(s^2-R_f^2)/2} ds \quad (6.32)$$

Equations (6.28) and (6.29) yield a general solution for both tubular flames ( $N=1$ ) and counterflow flames ( $N=0$ ). The solution for the flame radius,  $R_f$ , and flame temperature,  $T_f$ , as a function of stretch rate,  $k$ , can be obtained by solving the above equations numerically for different  $h$ ,  $R_I$ ,  $R_O$ ,  $N$  and  $Le$ . The flame speed, which is equal to the flow speed at the flame front, can be calculated from the flame radius and the potential flow field given by equations (6.11) and (6.12). According to equation (6.29), the term on the left-hand side of equation (6.28) denotes the total chemical heat release. The first term on the right-hand side of equation (6.28) represents the heat flux induced by thermal conduction to the unburned side, while the second and third terms represent the heat flux induced by radiative loss in the unburned and burned regions, respectively. The adiabatic flame temperature of stretched flames can be obtained by setting the radiative loss terms ( $L^\pm$  or  $h^\pm$ ) to zero.

Equations (6.28) and (6.29) reduce to previous results of adiabatic tubular flames (Matthews et al. 2006) in the limit of  $N=1$ ,  $R_I=0$ , and  $L^\pm=0$ ; and those of counterflow flames (Sohrab and Law 1984; Ju et al. 2000) in the limit of  $N=0$ ,  $R_I=0$ , and  $R_o \rightarrow \infty$ . Furthermore, by specifying  $R_I > R_O$  (now the outer tube is of radius  $R_I$  while the inner one of radius  $R_O$ ), solutions to tubular flames of negative curvature (unlike the tubular flame

of positive curvature shown in figure 6.14(a), a tubular flame of negative curvature is established when combustible mixture is injected toward the outer tube through the porous inner tube) can be obtained from the present results.

### 6.3.3 Results and Discussions

The present results, equations (6.28) and (6.29), provide a general theoretical description of flame speed, flame temperature and extinction limits. By specifying different flame curvatures (by changing  $R_l$  or  $N$ ), flame stretches (by changing  $k$ ), and radiative heat loss intensities (by changing fuel concentration or the concentrations of radiative gases,  $h^\pm$ ), the effects of flame curvature, radiation, and stretch rates can be systematically investigated. Furthermore, the preferential diffusion effect can be demonstrated by comparing results at different Lewis numbers (by changing  $Le$ ).

In the following calculations, the integrations in equations (6.28) and (6.29) are evaluated by using QUADPACK (Piessens et al. 1983) and the thermal and chemical parameters are chosen to mimic methane/air mixture. They are  $\tilde{Q} = 4.75 \cdot 10^7 J / Kg$ ,  $\tilde{C}_p = 1400 J / Kg / K$ ,  $\tilde{B} = 2.5 \cdot 10^{10} m^3 / mol / s$ ,  $\tilde{\rho} = 1.0 Kg / m^3$ ,  $\tilde{T}_\infty = 300 K$ ,  $\tilde{T}_a = 25000 K$ ,  $\tilde{K}_p = 2.0 m^{-1}$ , and  $\tilde{\lambda} / (\tilde{\rho} \tilde{C}_p) = 5 \cdot 10^{-5} m^2 / s$ . The Lewis number of methane/air flames is close to unity. Therefore, unit Lewis number is utilized in the following except in the last subsection, in which the effects of Lewis number is investigated and different Lewis numbers could be obtained by adding Helium into the methane/air mixture (Chen et al. 2007a).

In the following, the effects of flame curvature, radiation, stretch, and Lewis number on flame extinction will be discussed. Note that the outer tube radius is set to be infinity ( $R_O = \infty$ ), so the heat conduction to the outer tube, which was studied by

Kobayashi et al. (Kobayashi and Kitano 1989) and Matthews et al. (Matthews et al. 2006), is not considered here. Besides, in the present study and all previous studies, the surface radiation is not considered in the tubular geometry. The existence of the inner and outer tubes could interact with the gas-phase radiation losses. This is a subject for future study.

### 6.3.3.1 Flame Extinction and Bifurcations of Tubular Flames

It is well known that radiative heat loss depends strongly on the volume of the hot emitting gas. Therefore, the appearance of flame curvature in tubular flame yields a smaller volume of the burned gas per unit area of the flame front than that of the planar counterflow flame. As a result, an increase of flame curvature reduces the radiative heat loss and thus improves the combustion. On the other hand, an increase of flame curvature increases the heat conduction loss from the burned gas side to the unburned gas side (caused by the so-called defocusing effect) and the flame speed is decreased. So flame curvature also weakens the flame strength. The above two competing effects of flame curvature, together with that of radiation will be shown to greatly affect the flame extinction.

To quantitatively evaluate the effect of radiative heat loss, the fraction of radiative heat loss is introduced (Ju et al. 1997; Chen and Ju 2007):

$$Fr = \int_{R_I}^{R_O} q_r (2\pi r)^N dr / \int_{R_I}^{R_O} \omega (2\pi r)^N dr = \int_{R_I}^{R_O} q_r (2\pi r)^N dr / \left[ (2\pi R_f)^N e^{T_a(T_{ad}^{-1} - T_f^{-1})/2} \right] \quad (6.33)$$

where the numerator denotes the total radiative heat loss in both the unburned and burned zones and the denominator denotes the total chemical heat release rate.

Figure 6.15 shows the dependences of flame radius, flame temperature and fraction of radiative heat loss of tubular flames ( $R_I=0$ ,  $R_O=\infty$ ,  $N=1$ ) on stretch rate at

$Le=1.0$  and  $\tilde{Y}_\infty = 0.0376$ . It is seen that the non-adiabatic tubular flames exhibit an isola response, with dual extinction limits at higher and lower values of stretch rate ( $b$  and  $d$ ). According to previous stability analysis mentioned in (Matthews et al. 2006), the branch of large flame radius (thus large flame speed) is stable (solid lines in figure 6.15) while the branch of small flame radius (thus small flame speed) is unstable (dashed lines in figure 6.15).

It is seen that the mixture can burn in a range of stretch rate between  $1.3 \text{ s}^{-1}$  and  $6.7 \text{ s}^{-1}$ . For stretch rates larger than  $3.5 \text{ s}^{-1}$  (point  $a$ ), an increase of the stretch rate causes the decrease of flow residence time and flame radius. Therefore, the fraction of radiative heat loss decreases and flame temperature increases. Flame extinction occurs at point  $b$ . For counterflow flames, this extinction is usually called stretch-induced extinction limit (Sohrab and Law 1984; Sung and Law 1996; Buckmaster 1997; Ju et al. 1997; Ju et al. 1999a; Ju et al. 2000). However, for tubular flames the flame curvature (inverse of flame radius) reaches its maximum value at the extinction point  $b$  and thus the curvature effect might also help to accelerate flame extinction. The validity of this conclusion will be proved in the next section.

On the other hand, with the decrease of stretch rate (from point  $a$  to  $c$  to  $d$ ), the flow residence time increases, which enhances the radiative heat loss; while the flame curvature also increases, which reduces radiation by decreasing the volume of radiation emitting gas. The two processes compete with each other and result a non-monotonic change of radiation fraction and flame temperature, as shown in figure 6.15. From point  $a$  to  $c$ , the effect of residence time dominates and thus radiation fraction increases and flame temperature decreases; from point  $c$  to  $d$ , the effect of curvature dominates and thus

radiation fraction decreases and flame temperature increases. The flame is eventually quenched at point  $d$ . Therefore, unlike the counterflow flame whose low stretch rate extinction limit is only caused by an increase of radiation, that of tubular flame is caused by the combined effects of flame curvature and radiation. Therefore, both the stretch and radiation extinction limits of tubular flames are strongly affected by flame curvature.

Results of tubular flames at other fuel concentrations ( $\tilde{Y}_\infty = 0.0392, 0.04$ ) are shown in figure 6.16 in order to demonstrate the effect of different radiation intensities ( $h = 0.017, 0.011, 0.009$  for  $\tilde{Y}_\infty = 0.0376, 0.0392, 0.04$ , respectively). Different flame regimes are predicted. For  $\tilde{Y}_\infty = 0.0376$ , the flammable region is an isola with flame position near the stagnation line ( $r=0$ ). This is usually called Near Stagnation Flame (NSF). However, with the increase of fuel concentration and thus decrease of radiative heat loss intensity, figure 6.16 shows that there are two distinct flame branches for  $\tilde{Y}_\infty = 0.0392$ : one branch is a NSF similar to that of  $\tilde{Y}_\infty = 0.0376$ , the other one is far from the stagnation line and thus is called a FSF. For both branches, the solid lines stand for stable solutions while the dashed lines are unstable solutions. With the decrease of radiative heat loss intensity  $h$  (or increase of  $\tilde{Y}_\infty$ ), the flame can survive radiation from emitting volume much larger than that of NSF, which is the reason why the FSF appears. With further decrease of radiative heat loss intensity, the strength of FSF increases and its extinction limit moves to the higher stretch rate side. At the same time, the NSF is also strengthened and it can survive despite the larger radiation emitting volume (thus large  $\tilde{R}_f$ ). Therefore, flame branch bifurcations appear with the increase of fuel concentration (decrease of radiative heat loss intensity). Figure 6.16 shows that, for  $\tilde{Y}_\infty = 0.04$ , the FSF

branch  $ag$  and NSF branch  $hb$  merge with each other to form branch  $ab$ , and so do the FSF branch  $fg$  and NSF branch  $hd$  to form branch  $fed$ . It is seen that for  $\tilde{Y}_\infty = 0.04$  there are two stable solutions for stretch rate between  $0.33 \text{ s}^{-1}$  and  $2.72 \text{ s}^{-1}$ , of which the one of higher temperature (on  $ab$  branch) is called normal flame, while the one of lower temperature (on  $de$  branch) is called the weak flame (Ju et al. 1999a; Ju et al. 1999b).

Similar flame bifurcations shown in figure 6.16 have also been found in the detailed numerical simulation of tubular and counterflow methane-air flames (Ju et al. 1997; Ju et al. 1999b) and theoretical analysis of counterflow flames (Buckmaster 1997), which confirms the validity of the present general theoretical description of the combined effects of flame curvature, radiation, and stretch given by equations (6.28) and (6.29). The different flame regions of counterflow flames predicted by the present theoretical correlation is the same as those shown in Buckmaster's analysis (Buckmaster 1997) and thus are not repeated here.

### ***6.3.3.2 Curvature and Radiation Effects on Extinction Limits***

To further study the combined effect of flame curvature and radiation, the tubular flames of different inner tube radii  $\tilde{R}_f$  are studied for mixture of  $Le=1.0$  and  $\tilde{Y}_\infty = 0.0376$ . The dependence of flame position (stable branches in solid lines and unstable branches in dashed lines) and flame temperature (only stable branches) on stretch rate are shown in figure 6.17. It is seen that by continuously increasing the inner tube radius, the isola response for counterflow flames is recovered. Note that the flame position  $\tilde{R}_f - \tilde{R}_f$  and the flame temperature are strongly affected by the inner tube size. Flame position  $\tilde{R}_f - \tilde{R}_f$  and flame temperature both increase with the increase of flame curvature (decrease of  $\tilde{R}_f$ ) since flame curvature reduces the radiative heat loss.

Furthermore, the flame position, flame temperature, and stretch rate at both extinction limits are significantly changed by choosing different inner tube radii. As shown in figure 6.18, the stretch rate at the upper extinction limit (stretch extinction limit) decreases *monotonically* with the increase of flame curvature (decrease of the inner tube radius). However, it is interesting to note that the dependence of the lower extinction limit (radiation extinction limit) on flame curvature is *not monotonic*. Similar non-monotonic dependences for flame position and flame temperature on flame curvature at the radiation extinction limits can also be seen in figure 6.17. This result shows that flame curvature and radiation coupling has distinct effects on the stretch extinction limit and the radiation extinction limit.

For extinction at high stretch rate, when the inner tube radius is large, flame is very close to the stagnation surface ( $\tilde{R}_f - \tilde{R}_l \approx 0$  for  $\tilde{R}_l = 1, 5 \text{ mm}$  in figure 6.17) and the radiation fraction reaches its minimum value (according to figure 6.15(3)). So the radiation effect at upper extinction limit could be negligible. This is further confirmed by the nearly constant flame temperature at the stretch extinction limit for different  $\tilde{R}_l$  shown in figure 6.17. Therefore, the change of extinction stretch rate is purely caused by flame curvature. When the inner tube radius is smaller than  $1 \text{ mm}$ , the  $\tilde{R}_f - \tilde{R}_l$  at extinction increases significantly with decrease of  $\tilde{R}_l$ , and then flame temperature decreases because of the increase of radiative heat loss. Therefore, the change of extinction stretch rate is caused by combined effects of flame curvature and radiation.

For extinction at low stretch rate, flame extinction is also caused by the combined effects of flame curvature and radiation. As mentioned before, an increase of flame curvature has two effects: (1), the reduction of the radiative heat loss and consequent

improvement in combustion; and (2), the decrease of flame speed and consequent reduction in the flame strength. The two processes compete with each other in the determination of the low stretch rate extinction limits. For large inner tube radius ( $\tilde{R}_l > 1.6 \text{ mm}$ ), the first effect dominates, thus the stretch rate at extinction decreases with the increase of flame curvature (decrease of inner tube size); while for small inner tube radius ( $\tilde{R}_l < 1.6 \text{ mm}$ ), the second effect dominates, thus the stretch rate at extinction increases with the increase of flame curvature (decrease of inner tube size).

Therefore, flame curvature has significant effects on extinction of premixed tubular flames since the extinction limits can be greatly changed by choosing different inner tubes to change flame curvature. Note that all the cases studied above are for mixtures of  $Le=1.0$ , so the stretch effect caused by preferential diffusion is not covered. The Lewis number effect will be demonstrated in the next section.

### ***6.3.3.3 Effects of Preferential Diffusion (Lewis Number Effect)***

The impact of radiation and flame curvature coupling on near limit flames will be enriched by the appearance of preferential diffusion. The effects of Lewis number on the tubular flames are shown in figure 6.19. It can be seen that the flammable region is greatly expanded by decrease of Lewis number. With decrease in the Lewis number, the stretch rate at upper limit increases while that at lower limit decreases. Furthermore, the flame radius decreases and flame temperature increases with the decrease of Lewis number at both extinction limits. This effect can be easily understood from equations (6.28) and (6.29). Equations (6.28) and (6.29) shows that the lower the Lewis number, the higher the adiabatic flame temperature and thus flame can survive much larger radiative heat loss and flame curvature. Note that the flame temperature increase at upper

extinction limit is much larger than that at lower extinction limit. This is because the Lewis number effect is proportional to the magnitude of stretch rate. Similar results for counterflow flames are also obtained from the present theory and are consistent with those of the previous study (Ju et al. 2000).

To demonstrate further the effects of Lewis number, radiation, and curvature on the extinction of tubular flames, the stretch rates at two different extinction limits for different inner tube radii and Lewis numbers are shown in figure 6.20. For fixed inner tube radius, the Lewis number effect is the same: the stretch rate at the upper limit increases while that at the lower limit decreases with decreasing Lewis number. Therefore, the preferential diffusion of mass over heat ( $Le < 1$ ) extends the flammable region for all the tubular flames with different curvatures. For fixed Lewis number, the stretch rate at the upper stretch extinction limit decreases monotonically. However, depending on the Lewis number, the radiation extinction limit can be either monotonically or non-monotonically dependent on the flame curvature. At large Lewis numbers (e.g.  $Le=1.1$ ), the stretch effect is dominant. Therefore, an increase of flame curvature leads to a monotonical increase of the extinction limit. There is a critical curvature above which no premixed tubular flames can be obtained (for  $Le=1.1$ , no solution for  $R_f < 1.5 \text{ mm}$ ). However, at lower Lewis numbers (e.g.  $Le=0.9$  and  $1.0$ ), the effect of radiation and flame curvature coupling becomes dominant. The radiation extinction limit varies non-monotonically with the flame curvature. In addition, flame curvature does not lead to flame extinction. As shown in figure 6.20, at a large flame radius, the decrease of the flame radius causes a decrease (or broadening) of the extinction limit. As the flame curvature increases, the radiation extinction limit reaches a

minimum value. A further increase of the flame curvature causes an increase of the extinction limit. Therefore, there is a critical Lewis number that separates the monotonic and nonmonotonic curvature dependence regimes. This critical Lewis number will be larger than unity and increases with increasing radiation intensity.

#### **6.3.4 Summary**

The flame dynamics of near-limit premixed tubular flames are studied by using the large activation energy asymptotic method. A general correlation for flame speed, flame temperature and extinction limits is obtained and it is used to study the combined effects of flame curvature, radiation, and stretch on flame extinction. The following conclusions are made:

1. The coupling between radiation and flame curvature leads to multiple flame bifurcations and extinction limits at different radiation intensities (different fuel mass concentrations). For mixtures with high radiation intensity, the flammable region is an isola and only the NSF is observed. With decreasing radiative loss intensity, two distinct flame branches NSF and FSF are first predicted and then they will merge with each other.

2. It is shown that both the stretch and radiation extinction limits are strongly affected by flame curvature. The stretch extinction limit is found to monotonically decrease with increasing flame curvature. However, depending on the Lewis number, the radiation extinction limit can be either monotonically or non-monotonically dependent on the flame curvature. For Lewis numbers larger than a critical value, increasing flame curvature results in a monotonic increase of the extinction limit and there is a critical curvature at which flame extinguishes. For Lewis numbers smaller than the critical value,

increasing flame curvature leads to a non-monotonic dependence of the radiation extinction limit and flame curvature does not lead to flame extinction.

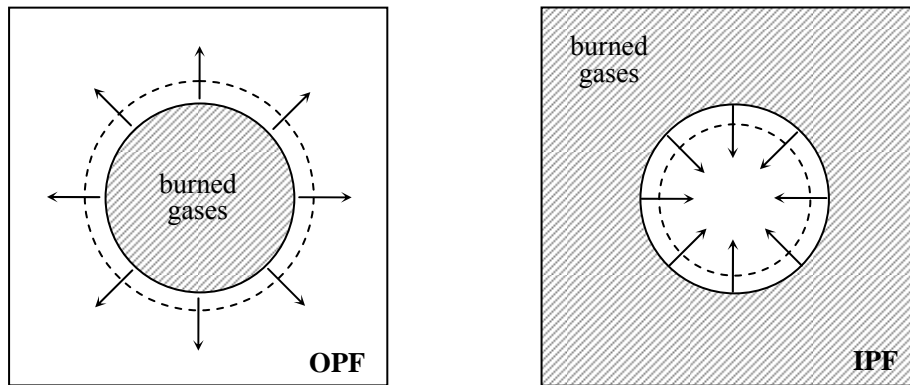


Figure 6.1: The schematic diagrams of (a) the outwardly propagating spherical flame (OPF) and (b) the inwardly propagating spherical flame (IPF) (Frankel and Sivashinsky 1983).

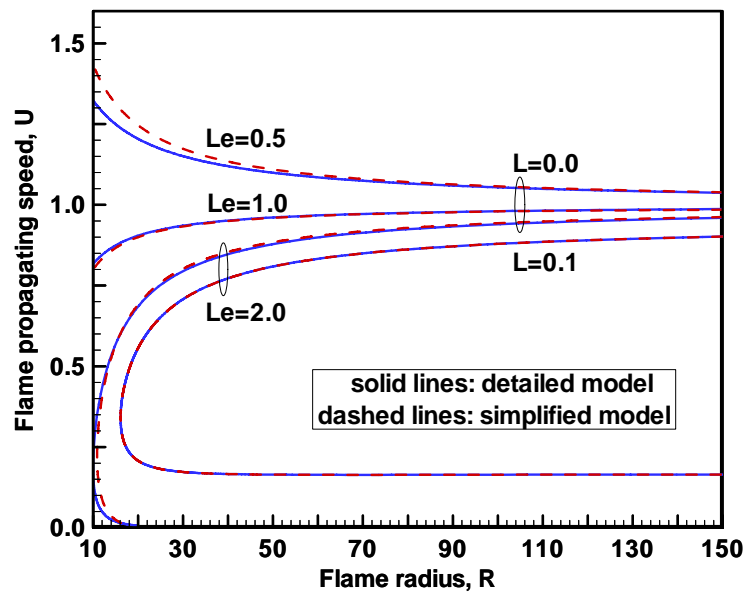


Figure 6.2: The flame propagation speed as a function of flame radius for OPF predicted by different models.

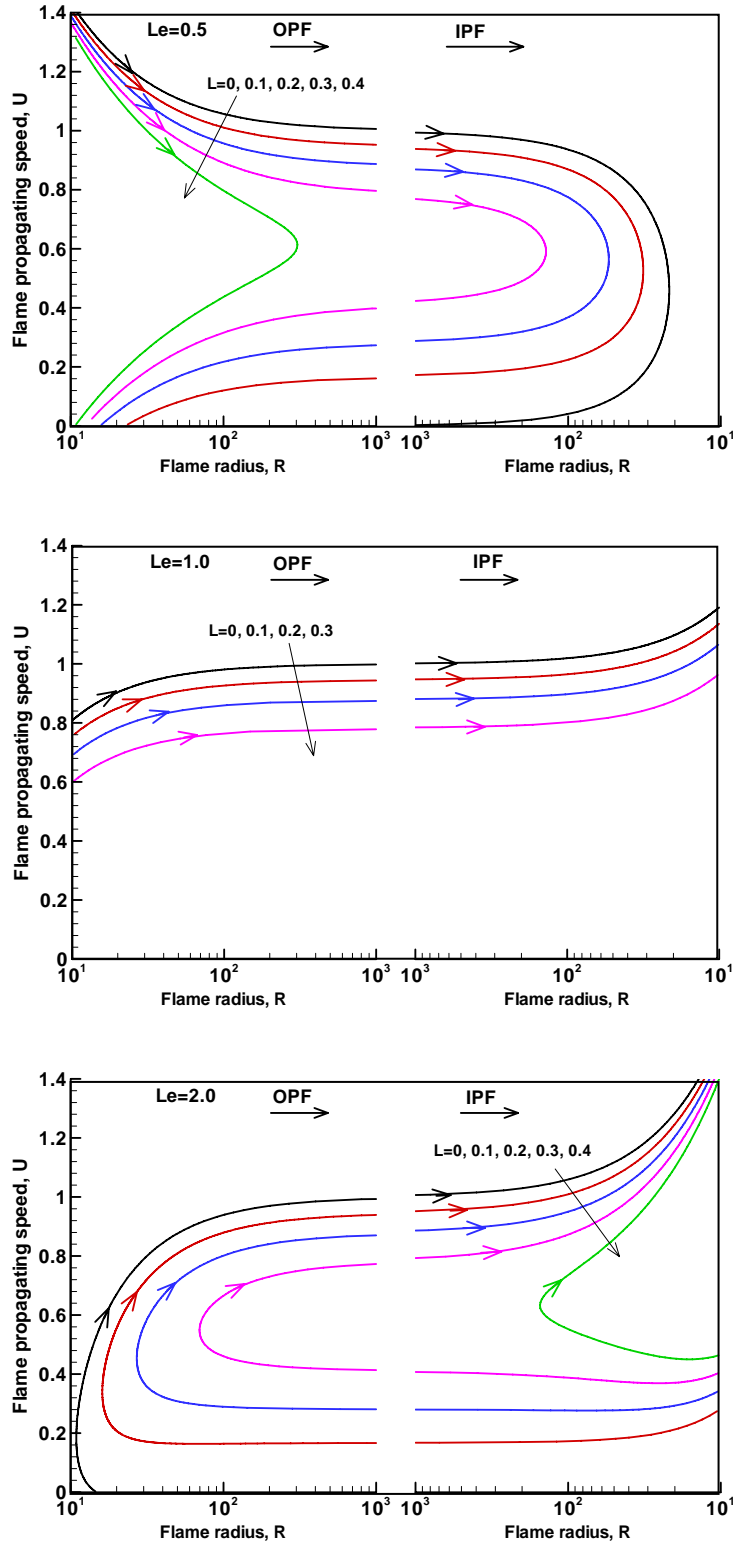


Figure 6.3: The flame propagation speed as a function of flame radius for OPF and IPF at different radiative loss intensities and Lewis numbers.

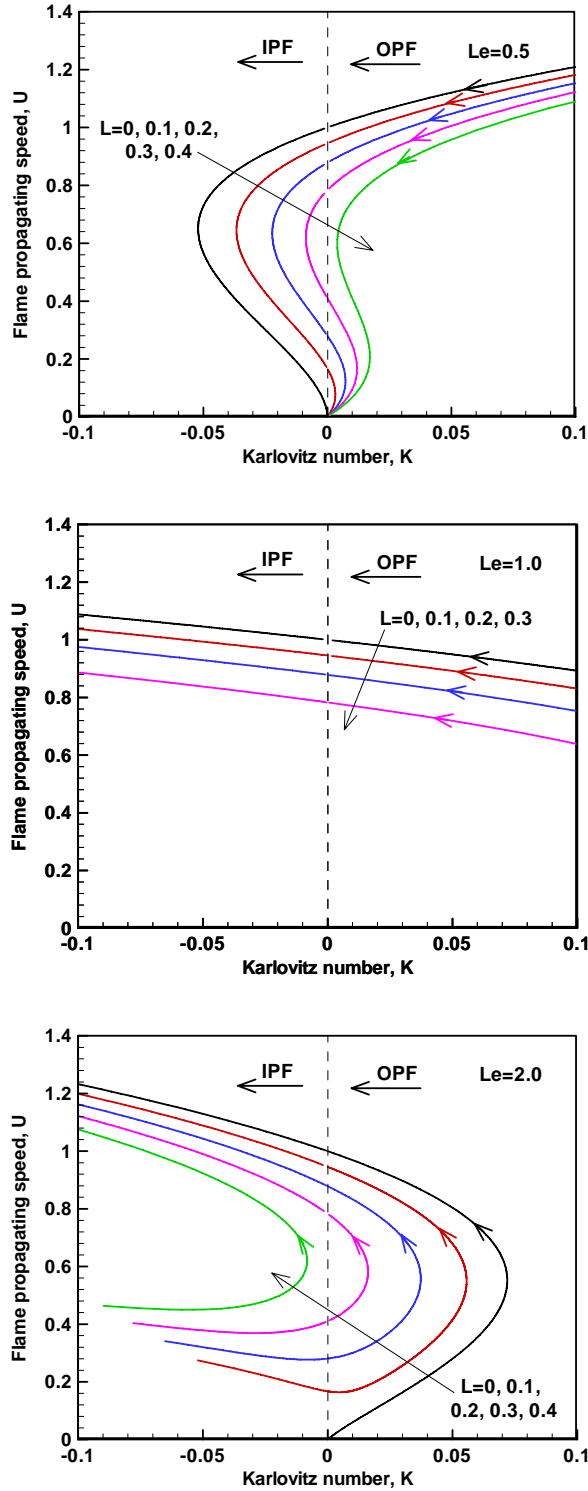


Figure 6.4: The flame propagation speed as a function of Karlovitz number for OPF and IPF at different radiative loss intensities and Lewis numbers.

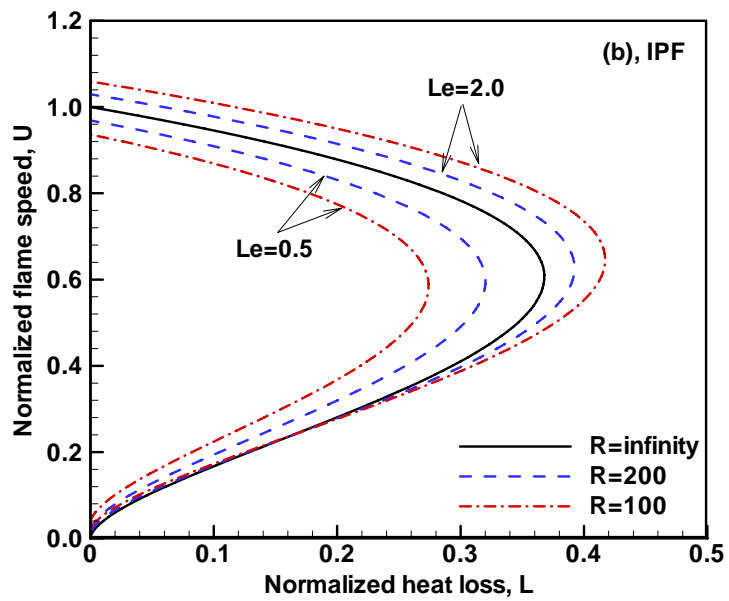
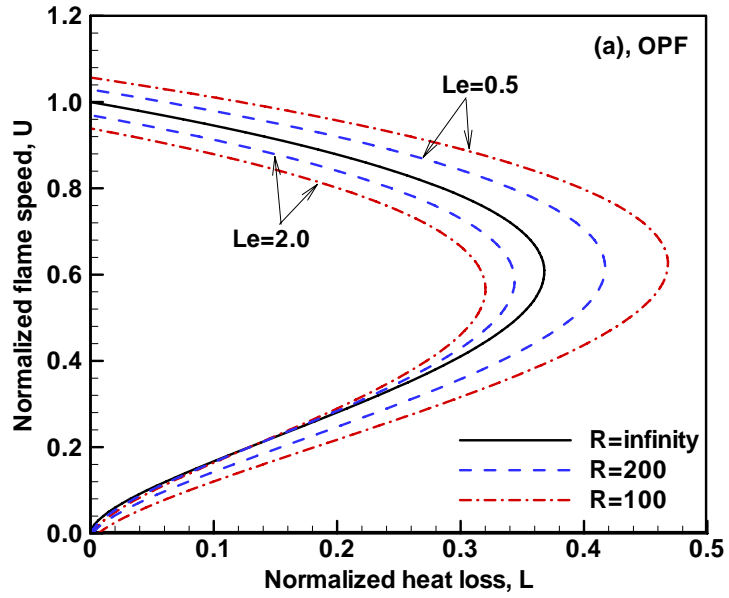


Figure 6.5: The flame propagation speed as a function of radiative loss intensity for OPF and IPF at different flame radii and Lewis number. The solid curve corresponds to the planar configuration.

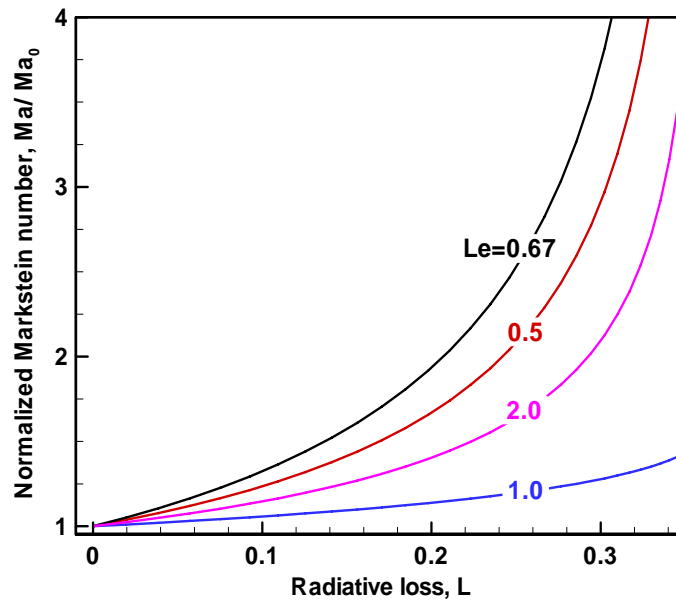
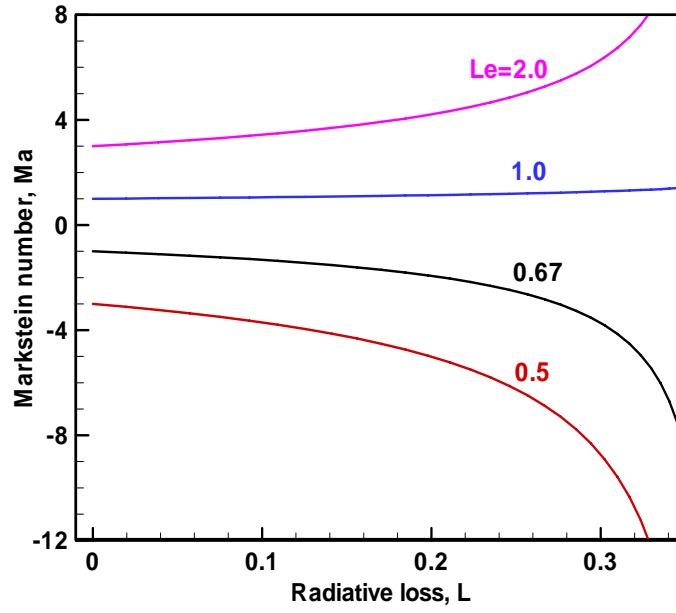


Figure 6.6: The effect of radiative loss on Markstein number.

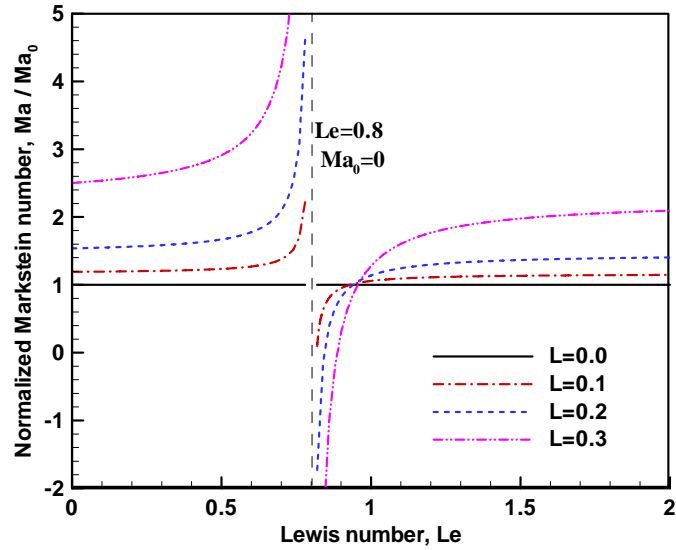


Figure 6.7: The normalized Markstein number as a function of Lewis number at different radiative losses.

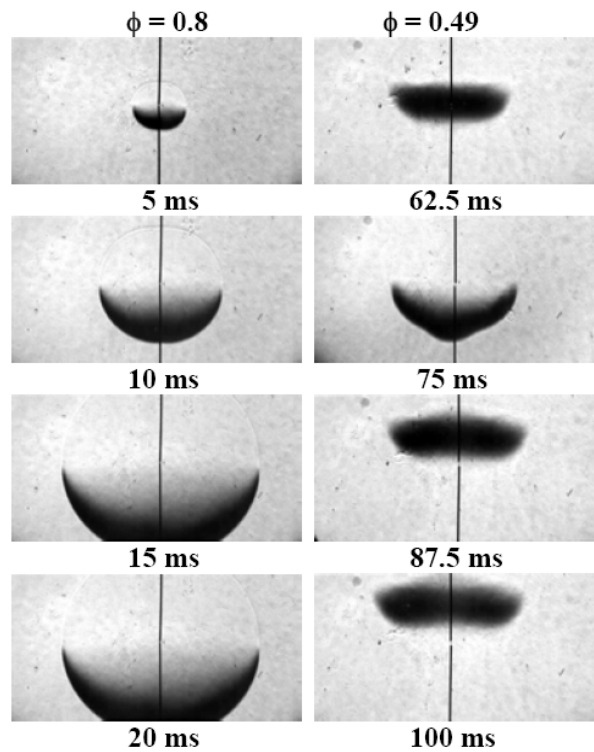


Figure 6.8: Schlieren photographs of  $\text{CH}_4\text{-(}0.3\text{O}_2\text{+}0.2\text{He+}0.5\text{CO}_2\text{)}$  flames at different equivalence ratios at 1 atm.

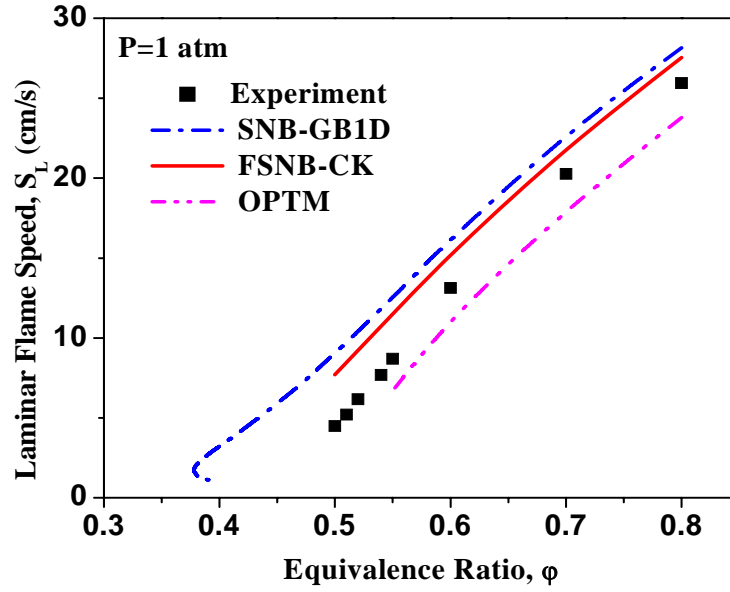


Figure 6.9: Measured and predicted laminar flame speeds of  $\text{CH}_4\text{-(}0.3\text{O}_2\text{+}0.2\text{He+}0.5\text{CO}_2\text{)}$  flames as a function of equivalence ratio at 1 atm.

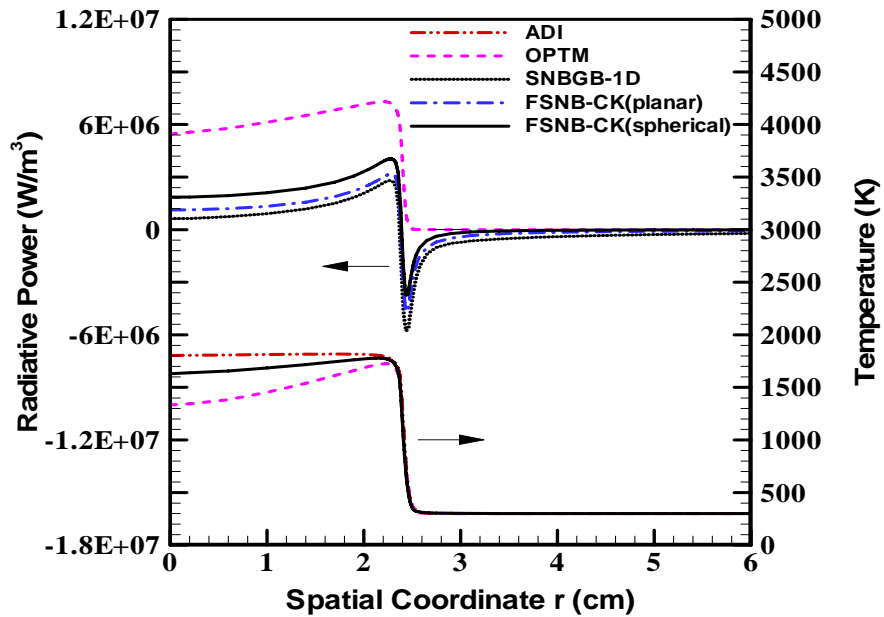


Figure 6.10: Temperature and volumetric heat loss distributions in spherical  $\text{CH}_4\text{-(}0.3\text{O}_2\text{+}0.2\text{He+}0.5\text{CO}_2\text{)}$  flame at  $\phi=0.6$  and  $P=1$  atm.

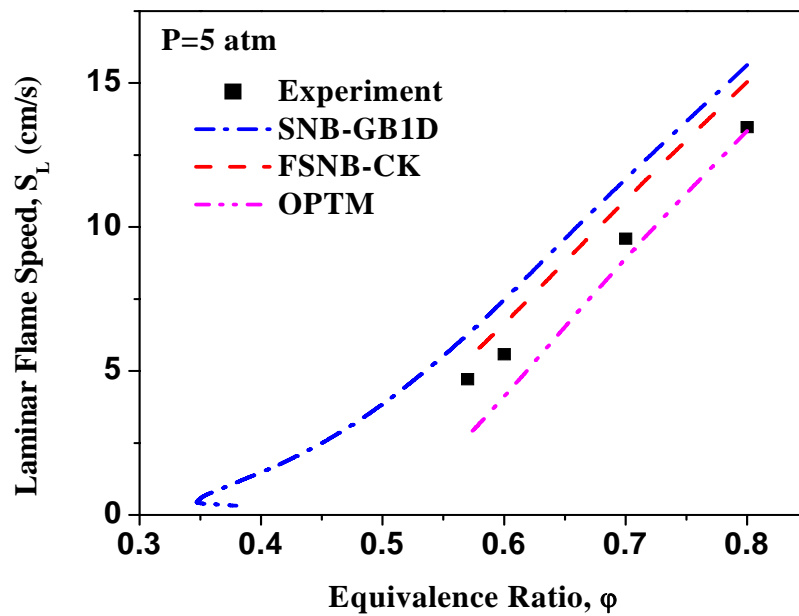
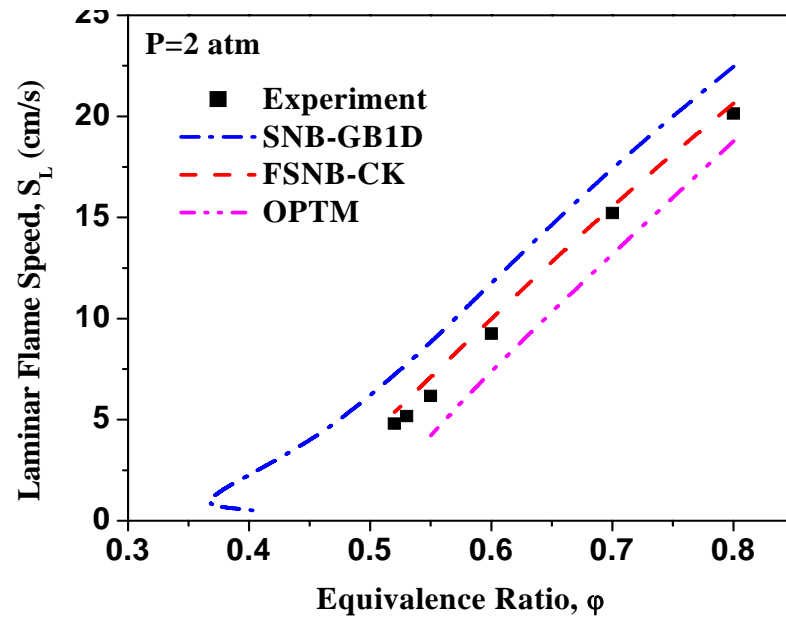


Figure 6.11: Measured and predicted laminar flame speeds of  $\text{CH}_4-(0.3\text{O}_2+0.2\text{He}+0.5\text{CO}_2)$  flames as a function of equivalence ratio at 2 atm and 5 atm.

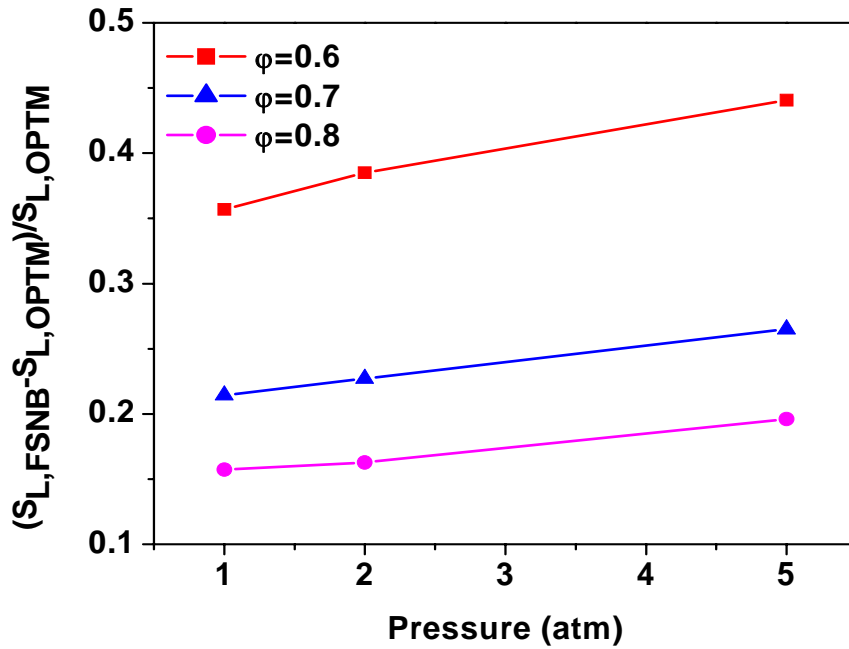


Figure 6.12: Effects of radiation absorption on flame speed at different pressure and equivalence ratios.

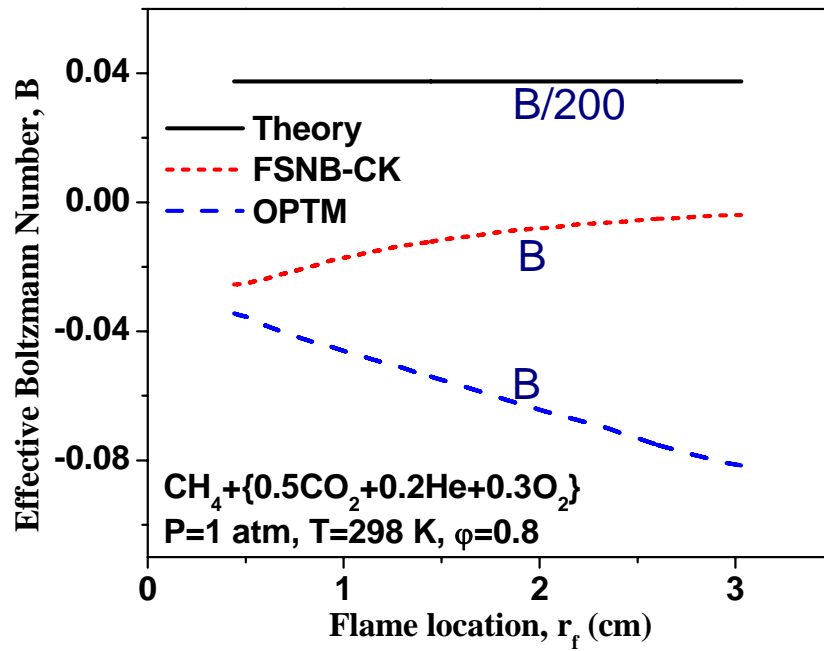


Figure 6.13: The predicted effective Boltzmann number versus flame size at 1 atm.

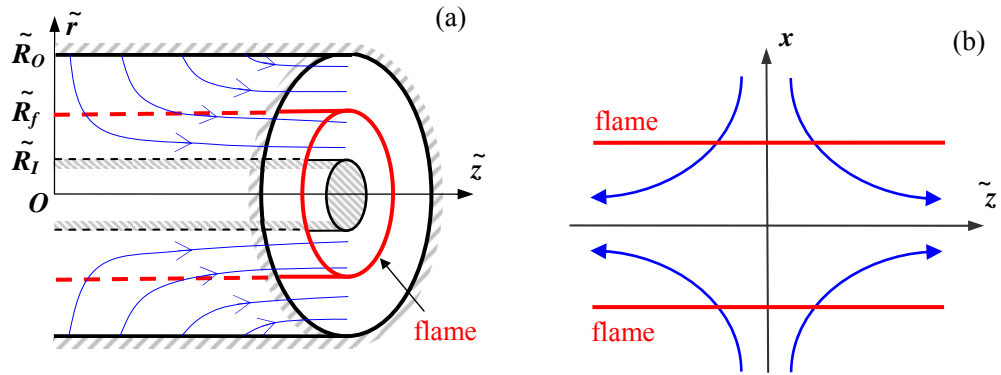


Figure 6.14: The schematic diagrams of the (a) tubular and (b) counterflow flames.

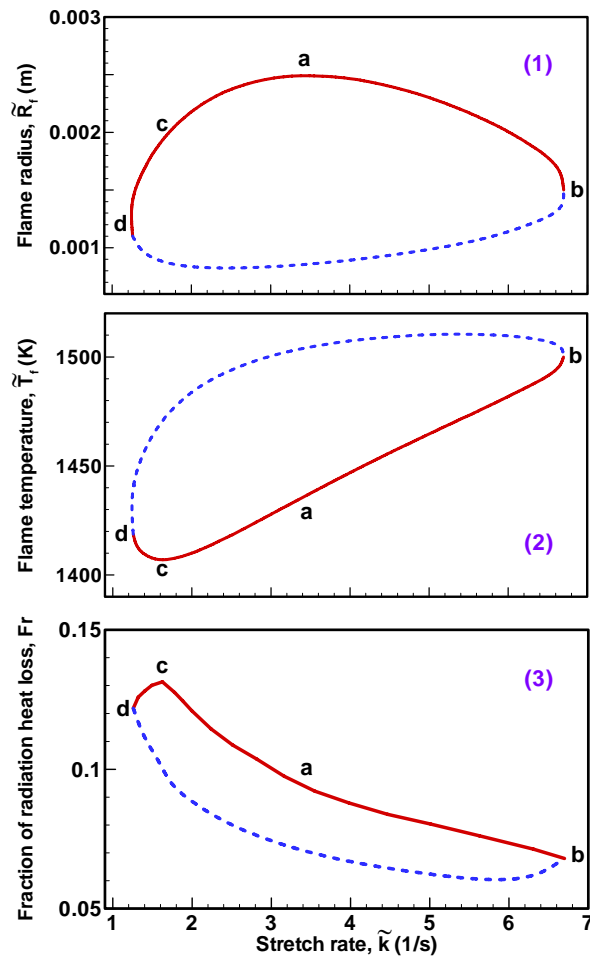


Figure 6.15: Dependences of flame radius (1), flame temperature (2), and fraction of radiative heat loss (3) of tubular flames ( $R_I=0$ ,  $R_O=\infty$ ,  $N=1$ ) on stretch rate for mixture of  $Le=1.0$  and  $\tilde{Y}_\infty=0.0376$ .

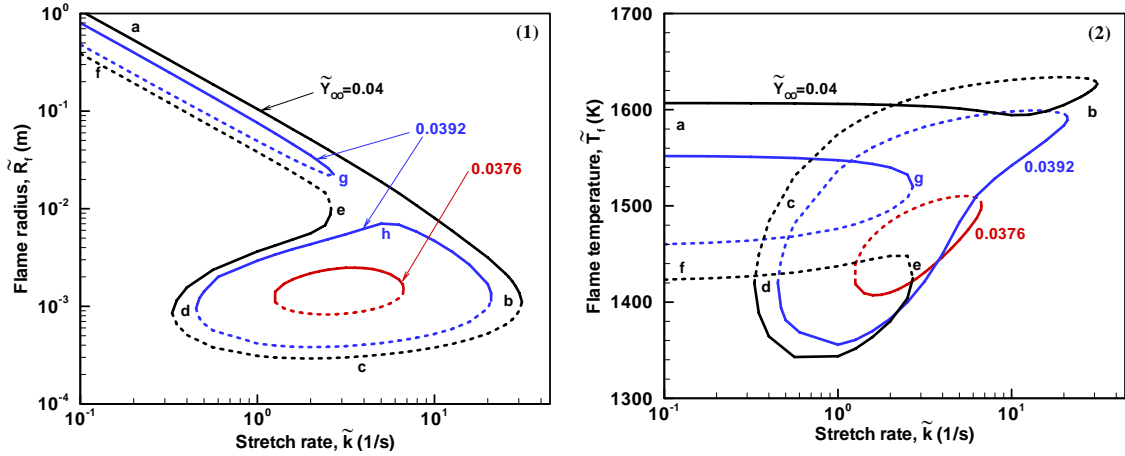


Figure 6.16: Flame radius (1) and flame temperature (2) of tubular flames ( $R_I=0$ ,  $R_O=\infty$ ,  $N=1$ ) as a function of stretch rate for mixtures of different fuel mass fractions and  $Le=1.0$ .

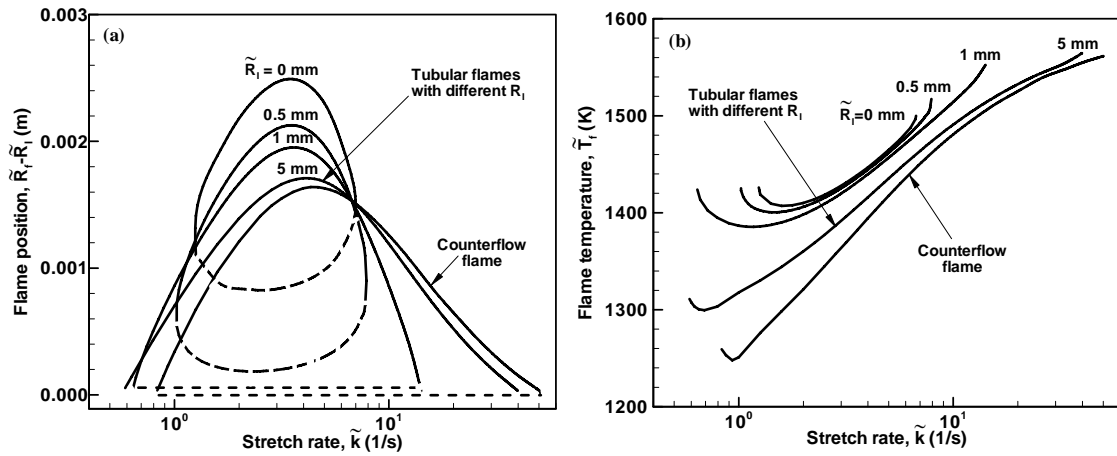


Figure 6.17: Flame radius (a) and flame temperature (b) as a function of stretch rate for tubular flames ( $N=1$ , different  $R_I$ ) and counterflow flames ( $N=0$ ) at  $Le=1.0$ ,  $\tilde{Y}_{\infty}=0.0376$ , and  $R_O=\infty$ .

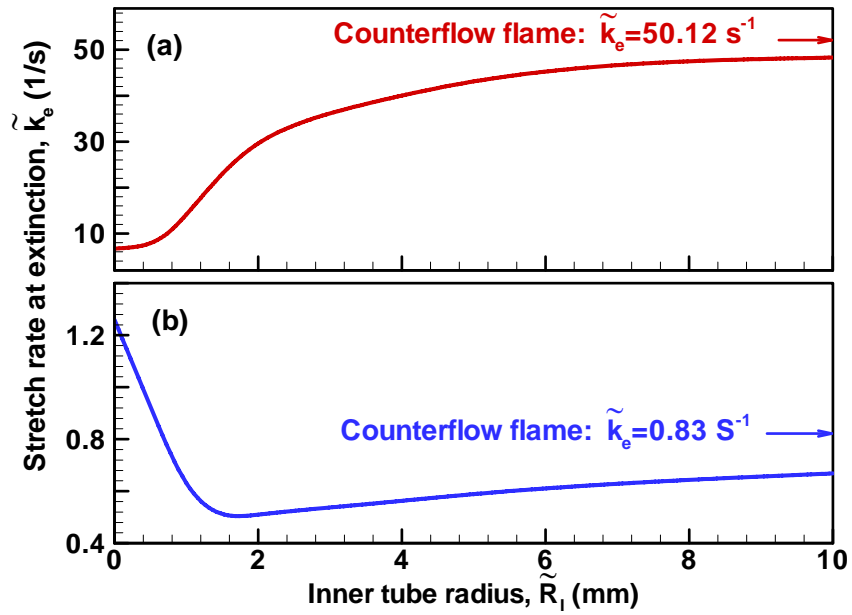


Figure 6.18: Stretch rate at extinction limits as a function of inner tube size for tubular flames and counterflow flame at  $Le=1.0$ ,  $\tilde{Y}_\infty=0.0376$ , and  $R_O=\infty$ .

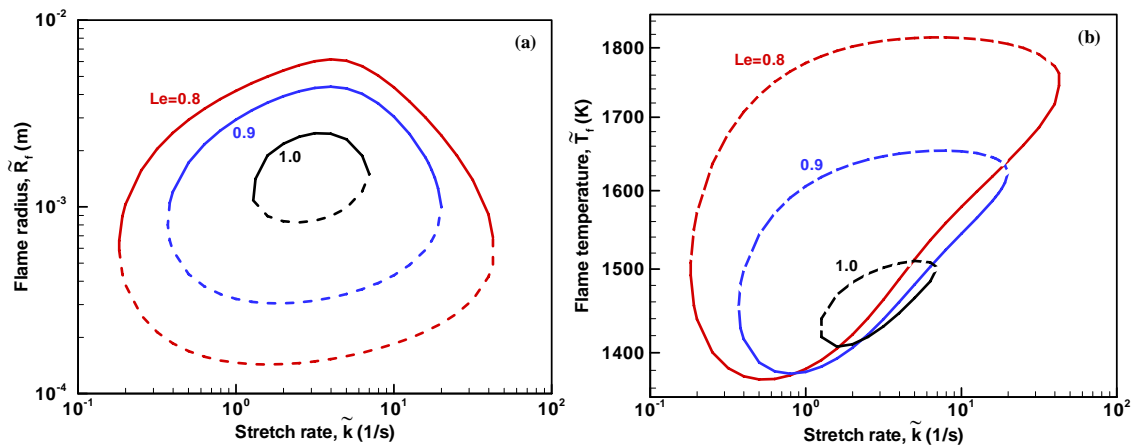


Figure 6.19: Flame radius (a) and flame temperature (b) of tubular flames ( $R_I=0$ ,  $R_O=\infty$ ,  $N=1$ ) as a function of stretch rate for mixtures of  $\tilde{Y}_\infty=0.0376$  and different Lewis numbers.

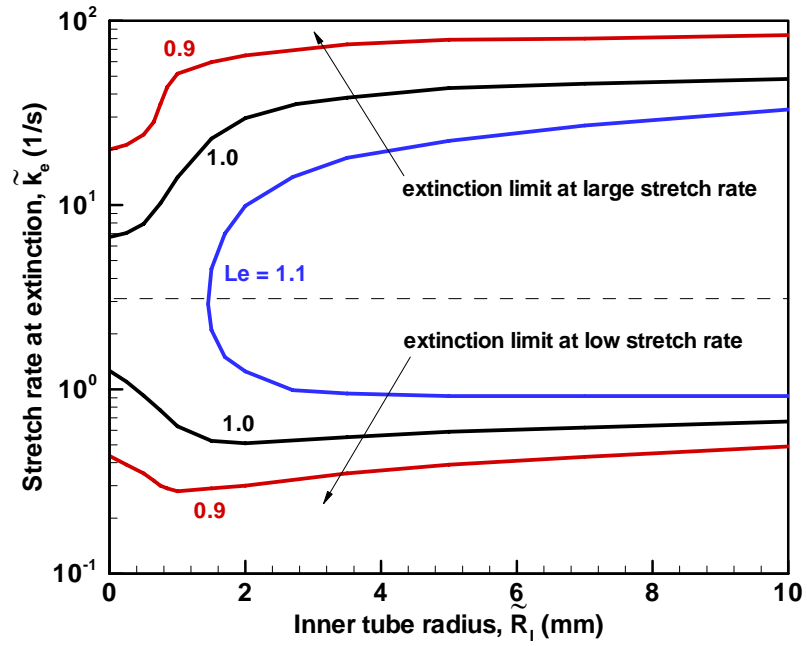


Figure 6.20: Stretch rate at extinction limits as a function of inner tube size for tubular flames at  $\tilde{Y}_\infty = 0.0376$ , and  $R_O = \infty$ .

# **Chapter 7: Ignition and Burning Properties of DME/methane Mixtures**

In previous chapters, the ignition and burning properties of different fuel/air mixtures were studied. The transport effects on the flame dynamics were emphasized while the chemical kinetic effect was covered. In this chapter, we shall demonstrate the potential role of chemical kinetics on the ignition and burning intensity of flames by using dimethyl ether/methane mixtures as an example.

## **7.1 Introduction**

The objective of the present study is to investigate kinetic coupling effects of DME addition on the high-temperature ignition and burning properties of methane–air mixtures. First, experimentally measured laminar flame speeds of DME-air and CH<sub>4</sub>-air mixtures are compared with predictions by different existing DME mechanisms including a recently developed high temperature model by Zhao et al. (Zhao et al. 2008). This mechanism is then used to study the effects of DME addition on the ignition enhancement in both homogeneous and non-homogeneous systems. Finally, the flame speeds of DME/CH<sub>4</sub>-air mixtures were measured using outwardly propagating spherical flames. The results are compared with model predictions and the effect of kinetic coupling on the burned Markstein length is discussed.

## **7.2 Experimental/numerical Specifications and Kinetic Model Selection**

The laminar flame speed and Markstein length of DME/CH<sub>4</sub>-air premixed flames were measured by using outwardly propagating spherical flames in the dual-chambered,

pressure-release-type, high pressure combustion chamber (Qin and Ju 2005). Pre-mixtures were prepared by using the partial pressure method from pure methane and DME compressed gas sources. The purities of the DME and CH<sub>4</sub> were 99.8% and 99.9%, respectively. Experiments were conducted for DME/CH<sub>4</sub>-air mixtures: ( $\alpha$ CH<sub>3</sub>OCH<sub>3</sub> + (1- $\alpha$ )CH<sub>4</sub> + air), with values of the volume fraction,  $\alpha$ , ranging from zero to unity. The combustible mixture was spark-ignited at the center of the chamber with the minimum ignition energy so as to preclude significant ignition disturbances. The flame propagation sequence was imaged by using Schlieren photography. A high-speed digital video camera operating at 8000 frames per second was used to record the propagating flame images. The stretched flame speed was first obtained from the flame history and then linearly extrapolated to zero stretch rate to obtain the unstretched flame speed. The results presented here are the averaged value of at least two tests for each experimental condition. All experiments were performed at an initial temperature of 298±3 K and atmospheric pressure. In order to examine the available kinetic mechanisms, the measured flame speeds were compared with the numerical results obtained using PREMIX (Kee et al. 1985). Furthermore, A-SURF is utilized to carry out simulations of outwardly propagating spherical DME/methane/air flames at atmospheric and elevated pressures. The laminar flame speed and burned Markstein length were obtained from numerical simulations.

The effect of adding DME on the ignition enhancement of methane was investigated numerically in two different systems, a homogeneous flame configuration to examine the kinetic ignition enhancement, and a nonpremixed counterflow configuration to examine the effect of transport. The ignition time of homogeneous mixtures at constant

pressure and enthalpy was calculated by using SENKIN (Lutz et al. 1987). For the nonpremixed simulations, the quasi-steady temperature and species distributions of counter flowing DME/CH<sub>4</sub> (298 K at the boundary) and hot air jets (1400 K at the boundary) were determined under a frozen flow constraint. At time zero, chemical reactions were allowed in the pre-calculated frozen flow field. Ignition time was recorded when the first increase in the temperature field exceeded 400 K, indicating thermal runaway. Simulations were conducted using an unsteady potential counterflow flame code described by Ju et al. (Ju et al. 1997). To further examine the effect of flow residence time on ignition enhancement, the stretch rate in the frozen flow configuration was varied from low stretch to that near the ignition limit.

In order to properly model and interpret the present work, the chemical kinetic model used in the calculations must be capable of predicting the pure fuel–air laminar flame speed and high temperature shock tube ignition properties. One might expect that comprehensively developed detailed mechanisms for DME oxidation would also be capable of predicting high temperature kinetic properties for methane oxidation. The measured laminar flame speeds of pure DME-air and CH<sub>4</sub>-air mixtures at atmospheric pressure and room temperature are shown in figures 7.1 and 7.2, respectively, along with the predictions utilizing a number of different DME mechanisms.

It is seen that the earlier DME mechanisms published by Curran and co-workers (Curran et al. 1998; Curran et al. 2000; Fischer et al. 2000; Zheng et al. 2005) (2000-Mech and 2003-Mech) are not able to well reproduce the measured flame speeds for both lean and rich mixtures. Although a more recently updated version (Curran 2005), 2005-Mech, predicts flame speeds much better than the previous ones, there is still a

large discrepancy for lean DME–air and CH<sub>4</sub>–air flames. Recently, a new high-temperature model that includes the revised decomposition parameters, updates in the sub-model and thermo-chemistry for the hydrogen oxidation, and a revised C<sub>1</sub>-C<sub>2</sub> species sub-model developed in recent experimental and modelling studies on ethanol pyrolysis and oxidation, has been developed (Zhao et al. 2008). The mechanism was constructed and tested hierarchically against a large volume of high temperature experimental data for hydrogen, carbon monoxide, formaldehyde, and methanol oxidation. The new high-temperature DME reaction mechanism (denoted here as 2008-Mech) consists of 263 reversible elementary reactions and 46 species, and its predictions compare well with the high-temperature flow reactor data for DME pyrolysis and oxidation, for oxidation at high temperatures in a jet-stirred reactor, for high-temperature shock tube ignition, for species profiles from burner-stabilized flames and for laminar flame speeds of DME–air flame (figure 7.1). The model also results in excellent prediction of CH<sub>4</sub>-air flame speed data (figure 7.2). On the basis of the ability to reproduce these same reference conditions, we utilize the 2008-Mech in the remainder of comparisons reported in this chapter.

## **7.3 Results and Discussions**

### **7.3.1 Ignition Enhancement by DME Addition**

Figure 7.3 shows the effects of DME and hydrogen addition on the ignition delay of homogeneous DME/CH<sub>4</sub>–air and H<sub>2</sub>/CH<sub>4</sub>–air mixtures. The results show that the addition of DME to CH<sub>4</sub>–air has a dramatic enhancement in CH<sub>4</sub>–air ignition, particularly, at small amounts of DME addition. It is seen that for 10% of DME addition, the ignition time can be reduced by at least an order of magnitude. As the DME addition level reaches

40%, a further increase in DME blending has little effect on reducing the ignition time. It is noted that the enhancement due to DME addition can be much larger than that of hydrogen addition, given that the volume fraction of the added fuel is below 70%.

In order to understand the factors involved in the enhancement of methane ignition by DME addition, radical path analysis was conducted. Figures 7.4 and 7.5 show the radical pool development and CH<sub>3</sub>-reaction path analysis during the ignition of DME/CH<sub>4</sub>-air mixtures for 0% and 10% (in volume) DME addition, respectively (the contribution to  $d[CH_3]/dt$  by the  $i^{th}$  reaction is defined as the generation or production rate of CH<sub>3</sub> due to  $i^{th}$  reaction,  $d[CH_3]/dt|_i$ , normalized by the summation of the absolute value due to all the reactions,  $\sum_i |d[CH_3]/dt|_i$ ). It is seen that addition of 10% DME drastically increases the radical pool concentration growth. As the DME concentration further increases, however, this effect is lessened which gives rise to the nonlinear ignition enhancement observed in figure 7.3 (more results on radical pool development and sensitivity analysis are shown in figures 4 and 5 in (Chen et al. 2007c)).

For CH<sub>4</sub>-air mixtures without DME, figure 7.4, the initial radical production is governed by the reaction  $CH_4+O_2 \rightarrow CH_3+HO_2$ , which has no significant contribution to the radical pool growth later in the induction period. The methyl radicals formed react with O<sub>2</sub> to yield CH<sub>2</sub>O and OH, or CH<sub>3</sub>O and O, with CH<sub>3</sub>O decomposing to form CH<sub>2</sub>O and H. Through abstraction reactions, CH<sub>2</sub>O forms HCO which subsequently yields HO<sub>2</sub> and CO through oxidation. The recombination reaction  $2CH_3(+M) \rightarrow C_2H_6(+M)$  is the main channel opposing the initial radical pool growth. When both CH<sub>3</sub> and HO<sub>2</sub> are available in sufficient concentrations,  $CH_3+HO_2 \rightarrow CH_3O+OH$  becomes an important radical source. The above processes all depend on developing a significant pool of CH<sub>3</sub>

and HO<sub>2</sub> before radical pool growth of OH, O, and H can occur. Since the governing reaction  $\text{CH}_4 + \text{O}_2 \rightarrow \text{CH}_3 + \text{HO}_2$  is slow relative to the similar reaction and/or thermal decomposition rates of higher alkanes, the ignition time for pure CH<sub>4</sub>-air mixtures is, in comparison, relatively longer.

Once a small amount of DME is present, the system is strongly driven by the unimolecular decomposition of DME (figure 7.5). This reaction is the major initial source of radicals and continues to contribute to radical production thereafter. With DME addition to methane, the radical pool growth occurs much more rapidly (figure 7.5), as it is not limited by the rate with which methyl radicals alone can produce more reactive species. In the case of DME addition, unimolecular decomposition yields CH<sub>3</sub>O and CH<sub>3</sub> at the above temperatures, and subsequent abstraction reactions of CH<sub>3</sub> and radicals generated from CH<sub>3</sub>O produce CH<sub>3</sub>OCH<sub>2</sub> which in turn yields additional radical growth through decomposition to CH<sub>3</sub> and CH<sub>2</sub>O. These reaction sequences lead to a relatively large concentration of HO<sub>2</sub>, which in turn provides an alternative mechanism for CH<sub>3</sub> to yield radicals (CH<sub>3</sub>+HO<sub>2</sub> vs. CH<sub>3</sub>+O<sub>2</sub>). CH<sub>2</sub>O reacts with OH, H or CH<sub>3</sub> through  $\text{CH}_2\text{O} + \text{X} \rightarrow \text{HCO} + \text{HX}$  (X = OH, O, H, CH<sub>3</sub>). Formyl radicals further oxidize to produce CO and HO<sub>2</sub>. CH<sub>3</sub>O decomposes through  $\text{CH}_3\text{O} + \text{M} \rightarrow \text{CH}_2\text{O} + \text{H} + \text{M}$ , or reacts with O<sub>2</sub> to obtain CH<sub>2</sub>O and HO<sub>2</sub>. Moreover, the large concentrations of HO<sub>2</sub> also produce H<sub>2</sub>O<sub>2</sub> and subsequent production of OH through  $\text{H}_2\text{O}_2 + \text{M} \rightarrow \text{OH} + \text{OH} + \text{M}$ . Thus, by adding DME to methane not only is CH<sub>3</sub> more easily generated, other sources and channels are also available for generating radicals, as a result it enhances ignition.

Figure 7.6 shows the evolution of temperature and H-radical mass fraction in nonpremixed ignition. The ignition kernel is seen to develop on the hot air side (the

stagnation plane is located at  $x=2.26 \text{ cm}$ ). The effect of DME addition on the ignition time in nonpremixed counterflow systems is shown in figure 7.7. It is seen that, unlike the homogenous case, the ignition enhancement strongly depends on the stretch rate. At large stretch rates, the ignition is kinetically limited (the characteristic transport time is shorter than that of ignition) so that a small amount of DME addition causes a rapid reduction of the ignition time. For example, at a high stretch rate ( $a = 300 \text{ s}^{-1}$ ), the short flow residence time prevents the slow radical process from quickly building up the radical pool, so that the ignition time of pure methane in nonpremixed counterflow is considerably long. It is a kinetic limited process. However, at low stretch rates, the ignition time is limited by the characteristic transport time (transport limited). In this regime, the ignition time only slightly decreases with increasing DME concentration. Furthermore, it is noted that for both low and high stretch rates, the minimum ignition times for large amounts of DME addition are of the same order, indicating the limiting by transport as the kinetic ignition time is shortened. Therefore, it can be concluded that for nonpremixed ignition, there are two different regimes. In the kinetic limited regime, DME addition significantly reduces the ignition time. However, in the transport limited regime, the ignition enhancement by DME addition is less significant.

Furthermore, figure 7.7 shows that, for very low DME percentages, the homogeneous ignition time is larger than that of nonpremixed ignition at low strain rates. This is caused by the presence of transport in nonpremixed ignition. For nonpremixed ignition, thermal and mass transports have two effects: 1) to bring heat to the ignition kernel and preheat the fuel by the hot air, and 2) to remove the radicals produced in the ignition kernel, hence slowing down the radical pool growth. In cases of low strain rates

of large ignition delay times, the first effect becomes important because the endothermic decomposition reactions of DME are enhanced by the convective heat transfer and the radical transported away from the ignition kernel is low at small radical gradients.

To further demonstrate the effects of stretch and DME addition on methane ignition in nonpremixed configuration, the evolution of the maximum mass fraction of  $\text{CH}_3$ , the major radical species controlling the ignition time, as discussed previously, is shown in figure 7.8. It is seen that with increasing DME addition (from 2% to 10%), similar to the homogeneous case, the ignition time is reduced. Its effect, however, greatly depends on the stretch rate. For example, at low stretch rates ( $20 \text{ s}^{-1}$ ), the ignition is only slightly enhanced when the DME addition changes from 2% to 10%, although the initial  $\text{CH}_3$  concentration is heavily affected. On the other hand, at high stretch rates ( $200 \text{ s}^{-1}$ ), ignition time is significantly shortened by increasing the DME addition from 2% to 10%. This result further confirms the existence of two different regimes for non-premixed ignition.

### **7.3.2 Flame Speed and Burned Markstein Length of DME/ $\text{CH}_4$ Dual Fuel**

Figure 7.9 shows the dependence of the measured and predicted laminar flame speeds of DME blended methane-air flames on the DME addition level at different equivalence ratios. It is seen that with increasing DME, the laminar flame speeds of DME/ $\text{CH}_4$ -air flames increase almost linearly with the addition, although the rate of increase is slightly larger at small DME addition levels. It is well known that the magnitude of the laminar flame speed depends on the thermal diffusivity, Lewis number, activation energy and chemical heat release of the fuel/air mixture (Law 2006). The increase of laminar flame speeds caused by DME addition is mainly due to the relatively

lower activation energy and higher chemical heat release of DME compared with methane. As found in (Chen et al. 2007b), the adiabatic flame temperature increases monotonically while the activation energy decreases monotonically with the amount of DME addition in the dual fuel. Besides, the same trend of flame speed changing with DME addition for rich DME/CH<sub>4</sub>-air flames is also found (Chen et al. 2007b).

Figure 7.9 also shows that the numerical results calculated from the 2008-Mech agree reasonably well with the experimental data. This result indicates that although DME addition can increase the initial radical production for the acceleration of ignition, the fuel oxidation rate which is dominated by chain-propagation and termination reactions does not change significantly. As a result, the burning rate of a binary fuel mixture can be approximated as a linear function of the mixture fraction of the blended fuel.

The burned Markstein length of DME/methane dual fuel at atmospheric pressure and room temperature, obtained from numerical simulation using A-SURF, is shown in figure 7.10. Unlike the laminar flame speed, the change of the burned Markstein lengths of the dual fuel shows different trends: increase at fuel lean ( $\phi=0.8$ ), decrease at fuel rich ( $\phi=1.2$ ), and slight increase at stoichiometric ( $\phi=1.0$ ). The Markstein length is interpreted as the sensitivity of the flame response to stretch rate variations and is closely related to the global Lewis number of the mixture. The change of the burned Markstein length with DME addition implies that the global Lewis number,  $Le$ , is sensitive to DME addition. The relationship of the global Lewis number and the burned Markstein length is given by the following equation (Clavin 1985):

$$\frac{L_b}{\delta_f^0} = \frac{1}{1-\sigma} \left[ \frac{Z(Le-1)}{2} \cdot \int_0^{(1/\sigma-1)} \frac{\ln(1+x)}{x} dx - \ln(\sigma) \right] \quad (7.1)$$

where  $\delta_f^0$  is the flame thickness,  $Z$  the Zel'dovich number, and  $\sigma$  the density ratio between burned and unburned gases. Since there is only slight change of the density ratio,  $\sigma$ , due to DME addition, the change of the burned Markstein length,  $L_b$ , is mainly caused by that of  $\delta$  and  $Z(Le-1)$ . With increasing DME addition, the thermal diffusivity,  $\lambda/\rho C_p$ , decreases and the flame speed,  $S_u^0$ , increases. Therefore, the flame thickness,  $\delta = \lambda/\rho C_p S_u^0$ , will decrease with DME addition. Moreover, as shown in (Chen et al. 2007b), the overall activation energy monotonously decreases with DME addition; thus the Zel'dovich number,  $Z$ , also decreases with increasing DME addition.

Furthermore, the mass diffusivity of the dual fuel decreases with increasing DME addition. However, it only changes Lewis number for the lean case (to increase the global Lewis number) because the global Lewis number depends strongly on the mass diffusivity of the fuel for the lean case and oxygen for the rich case, respectively. Consequently, there is only slight change of the global Lewis number with DME addition for rich case because it depends on the mass diffusivity of oxygen. For the fuel lean case ( $\phi=0.8$ ), the increase of burned Markstein length is mainly due to the large increase of the global Lewis number, which dominates over the decrease of the flame thickness and the Zel'dovich number. For the stoichiometric case ( $\phi=1.0$ ), the increase of the global Lewis number is nearly balanced by the decrease of the flame thickness and the Zel'dovich number. Therefore there is only slight change of the burned Markstein length. For the fuel rich case ( $\phi=1.2$ ), the Lewis number depends on the mass diffusivity of oxygen and DME addition has little effect on the global Lewis number. So the decrease of the flame thickness and Zel'dovich number results in a decrease of the burned Markstein length with DME addition.

Figure 7.11 shows the laminar flame speeds and burned Markstein lengths of DME/CH<sub>4</sub>/air flames at different equivalence ratios ( $\phi=0.8, 1.0, 1.2$ ) and pressures ( $P = 1, 2, 4, 8 \text{ atm}$ ). All the results are from numerical simulation using A-SURF. It is seen that the laminar flame speeds of DME/CH<sub>4</sub>/air flames decrease rapidly with increasing pressure, showing a similar trend to other hydrocarbon fuels. The flame speeds at 8 atm are only half of those at 1 atm for all the equivalence ratios and DME blending levels. Similar to the results at atmospheric pressure, the laminar flame speeds of DME/CH<sub>4</sub>/air flames monotonously increase with DME addition for all the equivalence ratios and pressures. It is also due to the relatively lower activation energy and higher chemical heat release of DME compared with methane. However, unlike the laminar flame speeds, the burned Markstein length of the binary fuel at elevated pressures shows different trends with increasing DME addition: increase at fuel lean ( $\phi=0.8$ ), decrease at fuel rich ( $\phi=1.2$ ), and little increase at stoichiometric ( $\phi=1.0$ ). The results are consistent with those at atmospheric pressure. The different trends for fuel lean and rich cases are caused by the same fact that the global Lewis number depends strongly on the mass diffusivity of fuel for lean case and oxygen for rich case, respectively, and thus it changes with DME addition only for fuel lean cases. For fuel rich case, the decrease of the flame thickness and Zel'dovich number results in the decrease of the burned Markstein length with DME addition according to equation (7.1).

To reveal the pressure effect, the normalized laminar flame speeds and burned Markstein lengths of DME/CH<sub>4</sub>-air mixtures at different pressures for fuel lean and rich cases are shown in figure 7.12. All the laminar flame speeds and burned Markstein lengths are normalized by the corresponding results of pure CH<sub>4</sub>/air mixtures ( $\alpha=0\%$ ) at

the same pressure. It is shown that for both fuel lean and rich cases, the enhancement of laminar flames due to DME addition becomes stronger at higher pressures. As to the burned Markstein lengths, the changes at low pressures (*1 atm* and *2 atm*) are similar, while with further increase of pressure, the changes (increase for fuel lean case and decrease for fuel rich case) become larger. Therefore, relative changes in both laminar flame speeds and unburned Markstein lengths are greatly affected by pressure.

## 7.4 Conclusions

In the present work, the effects of DME addition to methane-air mixtures on ignition, flame speeds, and burned Markstein length were studied experimentally and computationally. New experimental data were obtained for the study of the kinetic coupling between DME and methane and for the validation of existing chemical mechanisms. The following conclusions can be drawn from the present work:

1. In homogeneous ignition, small amounts of DME addition to methane lead to a significant decrease in the ignition time. The effect is even more profound than that of hydrogen addition. This significant ignition enhancement is caused by the rapid build-up of  $\text{CH}_3$  and  $\text{HO}_2$  radicals when DME addition is present in the system. The resulting chain propagation reaction via  $\text{CH}_3$  and  $\text{HO}_2$  replaces the slow reactions via  $\text{CH}_3$  and  $\text{O}_2$  in the pure methane case and thus accelerates the ignition.

2. In non-homogeneous ignition, it is found that the ignition enhancement is strongly affected by the stretch rate. There exist two ignition regimes: a kinetic limited regime and a transport limited regime. In the kinetic limited regime, small amounts of DME addition cause a dramatic decrease of ignition time. However, in the transport limited regime, ignition enhancement by DME addition is much less effective.

3. In contrast to the nonlinear behaviour in ignition enhancement, the flame speeds of DME/CH<sub>4</sub>-air mixture are linearly proportional to the DME fraction. It is also found that the enhancement of flame speed by DME addition becomes stronger at higher pressures. Unlike the laminar flame speeds, the Markstein lengths of the binary fuel change dramatically at small DME concentrations and have different trends: increase at fuel lean ( $\phi=0.8$ ), decrease at fuel rich ( $\phi=1.2$ ), and little increase at stoichiometric ( $\phi=1.0$ ). These changes are also found to be significantly affected by pressure.

4. The comparison between the experimental data with model predictions showed that the 2000-Mech, 2003-Mech, and 2005-Mech do not well reproduce the flame speed data for both DME and methane-air flames, although the 2005-Mech performs much better than its previous versions. The results also showed that the high temperature mechanism (2008-Mech) is able to reproduce the speeds of both DME-air and methane-air flames, and those for DME addition to methane.

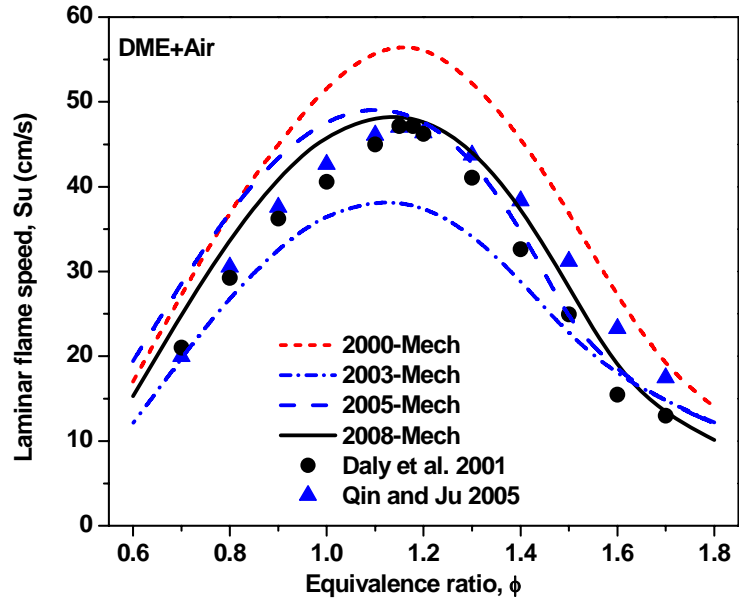


Figure 7.1: Laminar flame speeds of DME/air mixtures as a function of equivalence ratio at 298K, atmospheric pressure.

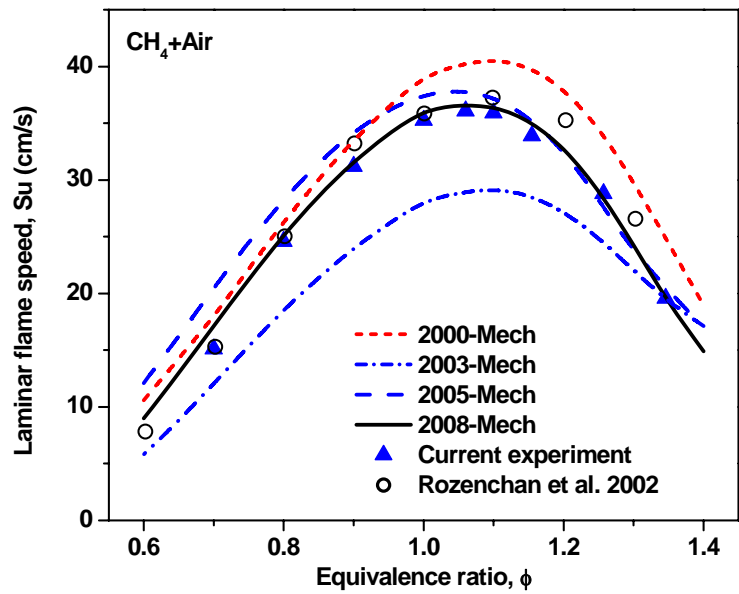


Figure 7.2: Laminar flame speeds of CH<sub>4</sub>/air mixtures as a function of equivalence ratio at 298K, atmospheric pressure.

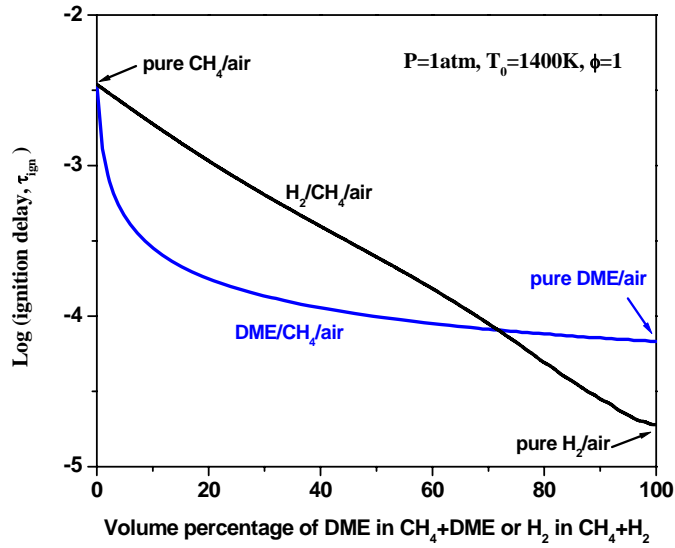


Figure 7.3: Effects of DME and hydrogen addition on homogeneous ignition delay of methane/air.

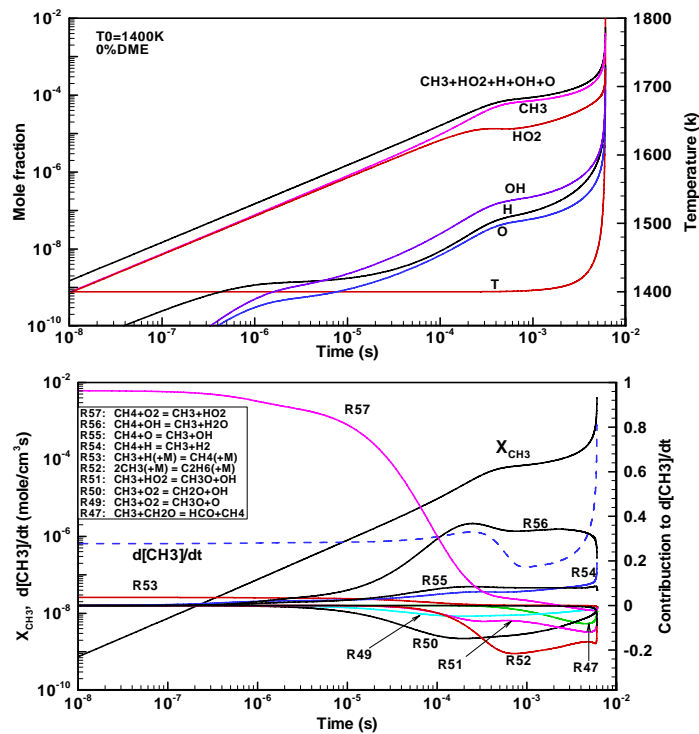


Figure 7.4: Radical pool growth and  $\text{CH}_3$ -reaction path analysis during homogeneous ignition of  $\text{DME}/\text{CH}_4$ -air mixtures (without DME addition).

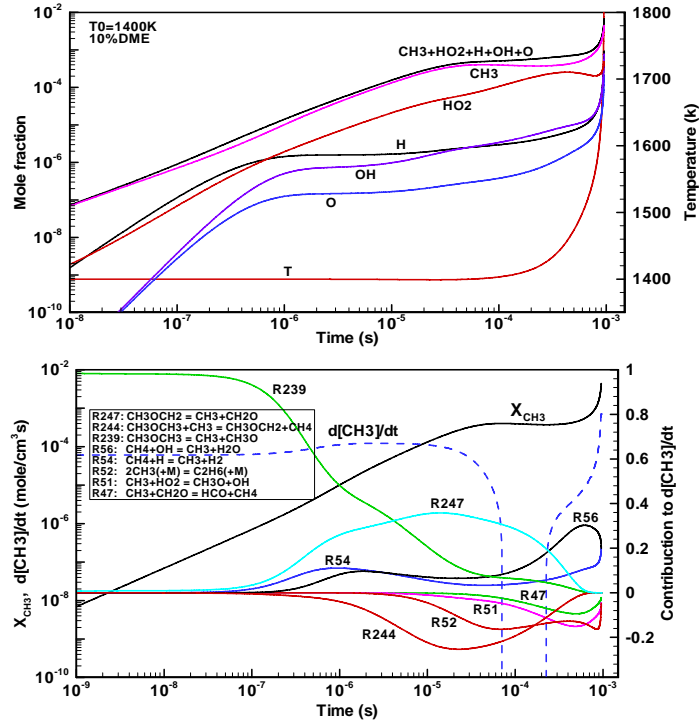


Figure 7.5: Radical pool growth and CH<sub>3</sub>-reaction path analysis during homogeneous ignition of DME/CH<sub>4</sub>-air mixtures (vol. 10% DME addition).

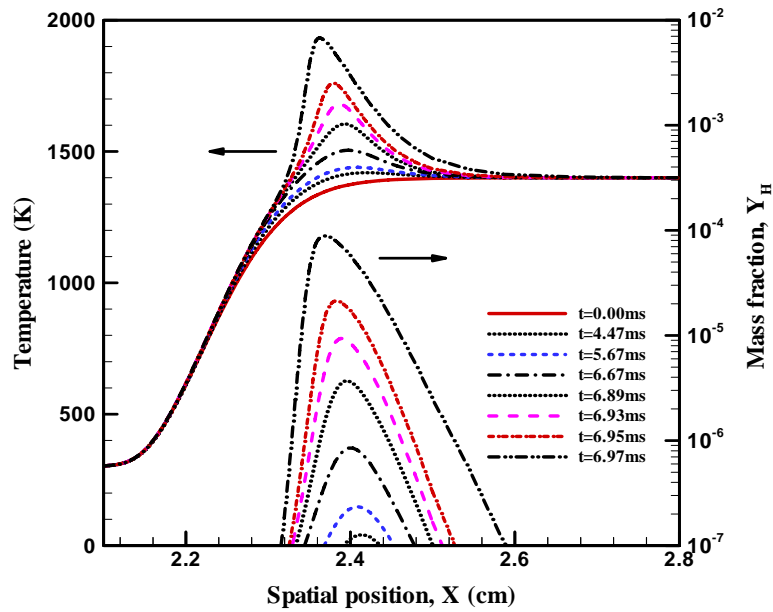


Figure 7.6: Evolution of temperature and H-radical mass fraction in non-premixed ignition (10% DME addition).

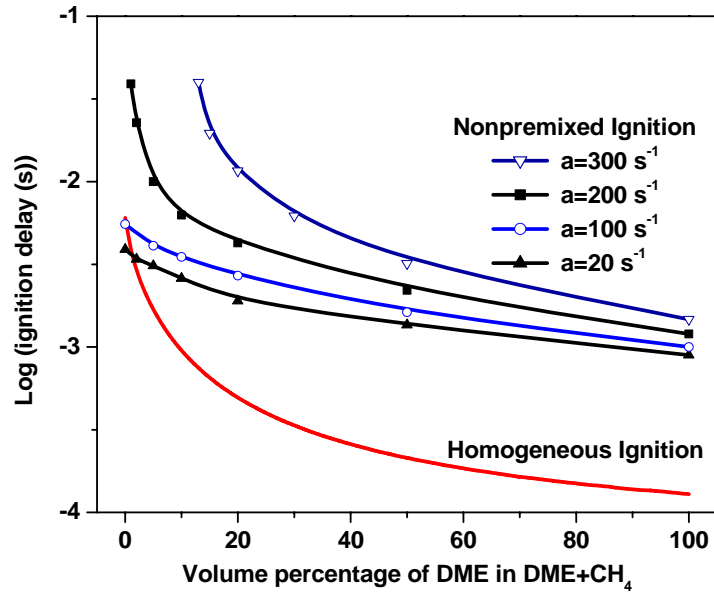


Figure 7.7: Effects of DME addition on ignition delay of methane at atmospheric pressure.

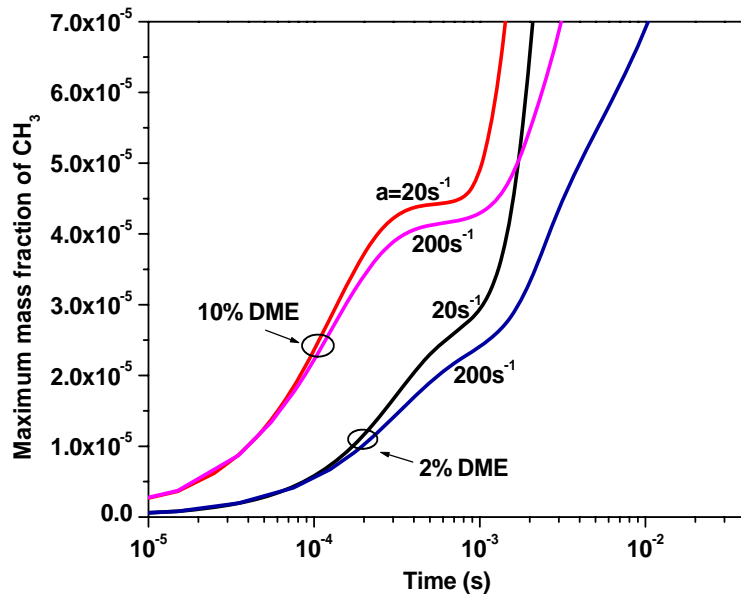


Figure 7.8: Evolution of the maximum mass fraction of  $\text{CH}_3$  in non-premixed ignition at different stretch rates and DME addition levels.

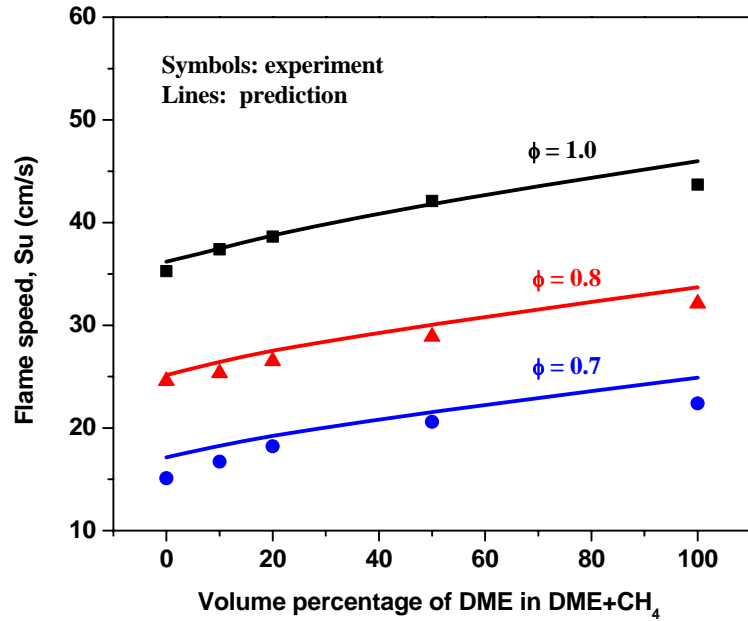


Figure 7.9: Variation of laminar flame speeds of DME/CH<sub>4</sub>-air mixtures at different equivalence ratios and DME blending at 298K, atmospheric pressure.

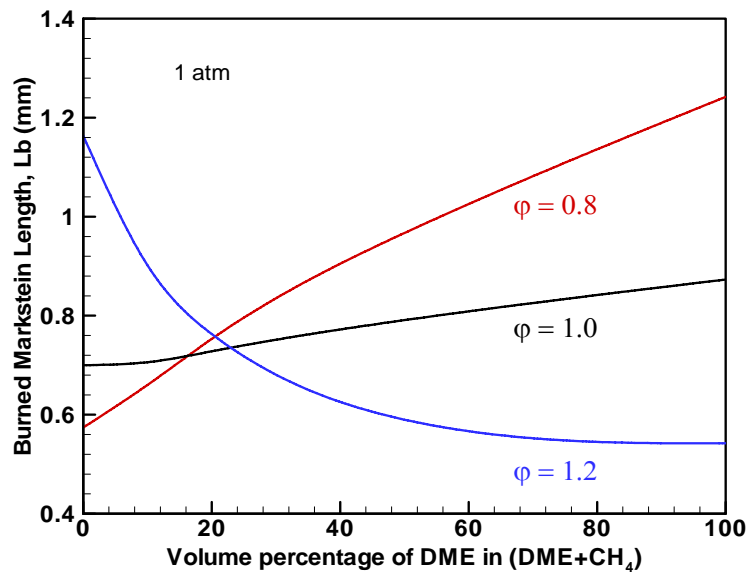


Figure 7.10: Burned Markstein lengths of DME/CH<sub>4</sub>-air mixtures at different equivalence ratios and DME blending at atmospheric pressure.

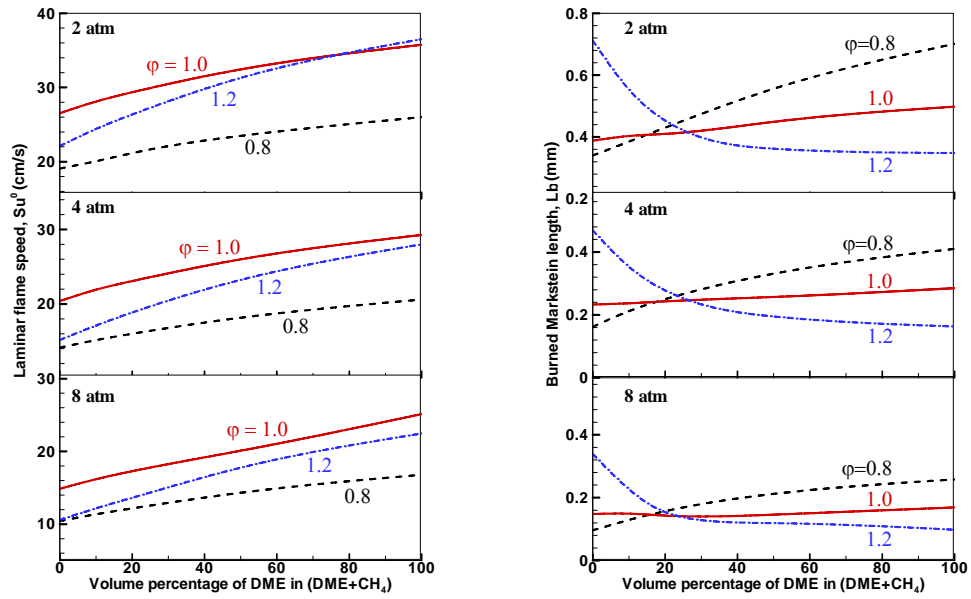


Figure 7.11: Laminar flame speeds and burned Markstein lengths of DME/CH<sub>4</sub>-air mixtures at different equivalence ratios and pressures.

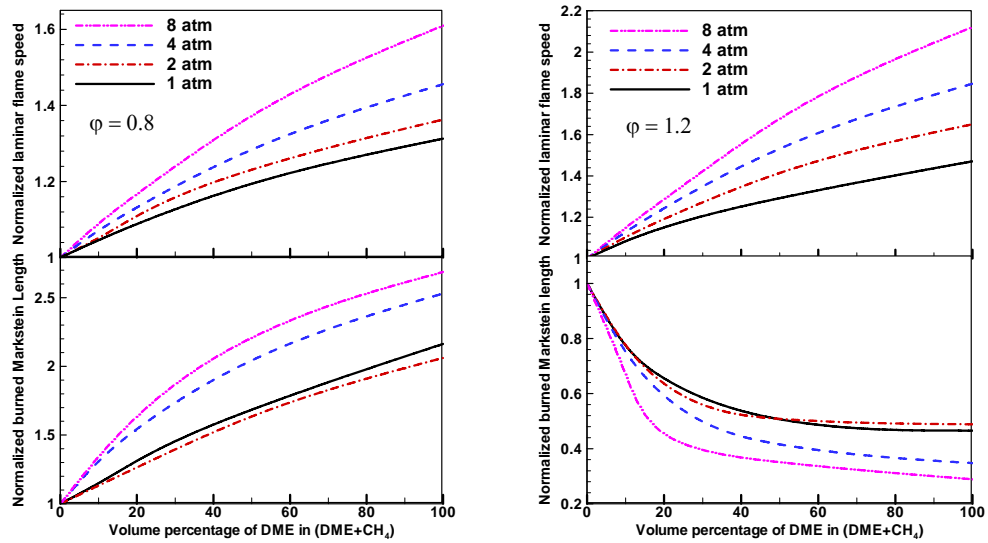


Figure 7.12: Normalized laminar flame speeds and burned Markstein lengths of DME/CH<sub>4</sub>-air mixtures at different equivalence ratios and pressures.

# Chapter 8: Summary and Recommendations

## 8.1 Summary

In this dissertation, initiation, propagation, and extinction of premixed flames are systematically investigated using asymptotic theoretical analysis, detailed numerical simulations, and/or experimental measurements.

Specifically, in Chapter 2, a general theory to describe different flame regimes and transitions among the flame kernel, the flame ball, the self-extinguishing flame, the outwardly propagating spherical flame, and the propagating planar flame is obtained. Based on this general theory, the dynamics of flame kernel evolution with and without ignition energy deposition is studied and the effects of radiative heat loss and Lewis number on flame propagation are investigated. It is found that the radiative heat loss from the unburned and burned zones play different roles in affecting the flame propagation speed. With the increase of flame radius, the radiative heat loss from the burned zone increases, while that from the unburned zone decreases. As a result, there is a peak radiation loss at an intermediate flame radius, which dramatically affects the flame regimes. It is also found that the radiative heat loss from the unburned zone results in a new flame regime: the isolated self-extinguishing flame with two radiation extinction limits at small and large flame radii, respectively. In addition, radiative loss is found to significantly affect the transition history of flame initiation when an external energy is deposited.

In Chapter 3, a time-accurate and space-adaptive numerical solver for Adaptive Simulation of Unsteady Reactive Flow (A-SURF) has been developed. It is shown that

A-SURF can accurately and efficiently simulate one-dimensional propagating flames with detailed chemical mechanisms. A-SURF is currently the only numerical solver which simulates propagating flames based on the compressible governing equations (thus resolving acoustics) using detailed chemical mechanisms and adaptive meshes.

In Chapter 4, the controlling factor for spherical flame initiation and how it relates to the minimum ignition energy are investigated by asymptotic analysis and detailed numerical simulations. The results show that it is the critical flame radius, rather than the flame thickness or flame ball radius, that controls the spherical flame initiation. The minimum ignition energy for successful spherical flame initiation is found to be proportional to the cube of the critical flame radius. Furthermore, preferential diffusion between heat and mass (Lewis number effect) is found to play an important role in the spherical flame initiation and it strongly affects the flame kernel evolution after ignition. It is shown that both the critical flame radius and the minimum ignition energy increase significantly with the Lewis number. Therefore, for transportation fuels with large Lewis numbers, blending of small molecule fuels will significantly reduce ignition energy.

In Chapter 5, the constant pressure and constant volume methods utilizing propagating spherical flames for laminar flame speed measurements are studied theoretically and numerically. For the constant pressure method, the validity of the linear relationship between flame speed and stretch and the effects of ignition, unsteady flame transition, and compression on the accuracy of flame speed determination are investigated. Theoretical analysis reveals a critical flame radius; only above which is the linear or non-linear extrapolation for flame speeds valid. It is found that the critical radius changes non-monotonically with the Lewis number and that, at large Lewis numbers, it

can be larger than the minimum flame radius used in experiments, leading to invalid flame speed extrapolation. Besides, the ignition energy is shown to have a significant impact on flame trajectories. It is found that the unsteady flame transition at different ignition energies causes a flame speed reversal phenomenon that greatly narrows the experimental data range for flame speed extrapolation. Furthermore, the compression induced flow is shown to greatly affect both the instantaneous stretched and extrapolated unstretched flame speeds. A Compression-Corrected Flame Speed (CCFS) method for flame speed measurement is proposed to include the compression effect. It is demonstrated that the present CCFS method not only increases the accuracy of the measured flame speed but also extends the parameter range of experimental conditions. For the constant volume method, the stretch effect is studied and an analytical expression is derived to evaluate the stretch effect on the determination of laminar flame speeds. It is shown that the stretch effect is proportional to the Markstein length and inversely proportional to the flame radius. A Stretch-Corrected Flame Speed (SCFS) model is then proposed to obtain accurate flame speed directly from the experimental measurements.

In Chapter 6, the effect of radiation on flame propagation and extinction is investigated. In the first part, the outwardly and inwardly propagating flames (OPF and IPF) are studied with the emphasis on the effects of radiative loss and preferential diffusion on the flame propagation speed, Markstein number, and flame extinction. Opposite trends for the change of the flame propagation speed and flame extinction/flammability limits are found for the OPF and IPF at different Lewis numbers and a correlation for Markstein length at different Lewis numbers and radiative losses is obtained. In the second part, the spectrally dependent radiation absorption effect on flame

speed enhancement is measured by using CO<sub>2</sub>-diluted CH<sub>4</sub>/O<sub>2</sub> mixtures at normal and elevated pressures. The radiation absorption is found to increase the flame speed and to extend the flammability limit. It is also shown that the spectrally dependent radiation absorption needs to be included for quantitative predictions of flame speed and flammability limit with CO<sub>2</sub> addition: the FSNB-CK radiation model can well reproduce the measured flame speed, while the SNB narrow-band gray model over-predicts the flame speed and the optically thin model significantly under-predicts the flame speed. In the third part, the flame dynamics of near limit premixed tubular flames are investigated to reveal the combined effects of flame curvature, radiation, and stretch on flame extinction. The coupling between radiation and flame curvature is found to lead to multiple flame bifurcations and extinction limits for different radiation intensities. It is also shown that both the stretch and radiation extinction limits are strongly affected by flame curvature: the stretch extinction limit monotonically decreases with the increase of flame curvature; while the radiation extinction limit, depending on the Lewis number, either monotonically or non-monotonically changes with flame curvature.

In Chapter 7, the effects of DME addition to methane/air mixtures on the ignition, flame speeds, and Markstein lengths are studied experimentally and computationally. In homogeneous ignition, small amounts of DME addition to methane are found to significantly decrease the ignition time. This significant ignition enhancement is caused by the rapid build-up of CH<sub>3</sub> and HO<sub>2</sub> radicals when a small amount of DME is added to the system. In non-homogeneous ignition, it is found that the ignition enhancement is strongly affected by the stretch rate and there exist two ignition regimes: a kinetic limited regime and a transport limited regime. In contrast to the nonlinear behaviour appeared in

ignition enhancement, the flame speeds of DME/CH<sub>4</sub>-air mixture are found to be linearly proportional to the DME fraction. Moreover, it is found that the enhancement of the flame speed by DME addition becomes stronger at higher pressures. Unlike the laminar flame speeds, the Markstein lengths of the dual fuel change dramatically at small DME concentrations and have different trends: increase at fuel lean ( $\phi=0.8$ ), decrease at fuel rich ( $\phi=1.2$ ), and little increase at stoichiometric ( $\phi=1.0$ ). These changes are also found to be significantly affected by the pressure.

## **8.2 Recommendations for Future Work**

Based on the results of the present study, the following are some recommendations for potential improvements on our understanding of premixed flame initiation, propagation, and extinction.

For ignition, our theoretical and numerical analyses show that there exists a critical flame radius controlling the spherical flame initiation and that the minimum ignition energy is proportional to the cube of the critical flame radius. However, very few experiments have been conducted to study the critical flame radius and its relationship to the minimum ignition energy. Recent experiments by Kelly et al. (Kelley et al. 2008) on hydrogen/air ignition at different equivalence ratios and pressures confirmed that there was a critical flame radius for spherical flame initiation and successful ignition depended on whether the initially ignited flame kernel could attain this critical radius. However, the minimum ignition energy was not measured and thus its relationship with the critical flame radius was not examined. Similar to the detailed numerical simulations shown in Chapter 4, ignition experiments on different H<sub>2</sub>/O<sub>2</sub>/He/Ar and CH<sub>4</sub>/O<sub>2</sub>/He/Ar mixtures are currently on our laboratory's schedule. By changing the helium and argon fractions

while fixing their combined volume, the preferential diffusion effect as well as the correlation between the critical flame radius and the minimum ignition energy will be revealed. Moreover, it is of practical interest to study the ignition of fuel mixtures since different fuel blends could be utilized for ignition control. According to the present study, both the critical flame radius and the minimum ignition energy increase significantly with the Lewis number. Therefore, for transportation fuels with large Lewis numbers, adding small-molecule fuel will significantly reduce the ignition energy.

For flame propagation, either the constant pressure method or the constant volume method was used in all the previous experiments. With the help of the Compression-Corrected Flame Speed (CCFS) and the Stretch-Corrected Flame Speed (SCFS) developed in Chapter 5, both methods could be utilized for the same run by experiments conducted in a spherical chamber with windows for Schlieren imaging and sensors for pressure recording (i.e. both the flame front and pressure histories could be recorded). Using these methods, accurate flame speed data should be experimentally determined at high pressures and high temperatures since many practical combustion devices operate near these conditions. Moreover, compared with the laminar flame speeds, the discrepancies among the Markstein lengths obtained from measurements are much larger. Therefore, efforts need to be spent on accurately measuring the Markstein length using the constant pressure method. In addition, comparison between the constant pressure method and the counterflow flame method needs to be conducted since different laminar flame speeds and Markstein lengths are reported from experiments for the same mixture at the same conditions.

For flame extinction, the combined effects of radiation, stretch, and curvature are only investigated theoretically based on the premixed tubular flames. Experiments utilizing a tubular burner should be conducted to validate the theoretical predictions. Besides, numerical simulations of premixed tubular flames with detailed chemical mechanisms will also help to understand these combined effects on flame extinction. In addition, experiments on radiation absorption effect reported in Chapter 6 were conducted at normal gravity. For near-limits flames, the laminar flame speeds are lower than 10 *cm/s* and thus the buoyancy effect can not be neglected. Microgravity experiments should be conducted to further understand the radiation absorption effect on laminar flame speeds and flammability limits. These experiments will also help to reveal the radiation effect on the accuracy of flame speed measurements using propagating spherical flames. Furthermore, the correlation between the Markstein length and the radiative heat loss derived in Chapter 6 could be checked by results from microgravity experiments.

## References

- Addabbo, R., Bechtold, J.K. and Matalon, M. (2003). *Proceedings of the Combustion Institute* **29**: 1527-1535.
- Akram, M. (1996). *AIAA Journal* **34**: 1835-1842.
- Andrews, G.E. and Bradley, D. (1972). *Combustion and Flame* **18**: 133-153.
- Arcounianis, C., Bae, C., Crookes, R. and Kinoshita, E. (2008). *Fuel* **87**: 1014-1030.
- Aung, K.T., Hassan, M.I. and Faeth, G.M. (1997). *Combustion and Flame* **109**: 1-24.
- Bechtold, J.K., Cui, C. and Matalon, M. (2005). *Proceedings of the Combustion Institute* **30**: 177-184.
- Bechtold, J.K. and Matalon, M. (1987). *Combustion and Flame* **67**: 77-90.
- Bradley, D., Gaskell, P.H. and Gu, X.J. (1996). *Combustion and Flame* **104**: 176-198.
- Bradley, D., Hicks, R.A., Lawes, M., Sheppard, C.G.W. and Woolley, R. (1998). *Combustion and Flame* **115**: 126-144.
- Bradley, D., Lawes, M., Liu, K., Verhelst, S. and Woolley, R. (2007). *Combustion and Flame* **149**: 162-172.
- Bradley, D. and Mitcheson, A. (1976). *Combustion and Flame* **26**: 201-217.
- Brown, P.N., Byrne, G.D. and Hindmarsh, A.C. (1989). *SIAM Journal on Scientific and Statistical Computing* **10**: 1038-1051.
- Buckmaster, J.D. (1976). *Combustion and Flame* **26**: 151-162.
- Buckmaster, J.D. (1997). *Combustion Theory and Modelling* **1**: 1-11.
- Buckmaster, J.D., Joulin, G. and Ronney, P.D. (1990). *Combustion and Flame* **79**: 381-392.
- Buckmaster, J.D. (1982). *Quarterly Journal of Mechanics and Applied Mathematics* **35**: 249-263.
- Buckmaster, J.D., Joulin, G. and Ronney, P.D. (1991). *Combustion and Flame* **84**: 411-422.
- Buckmaster, J.D. and Lundford, G.S.S. (1982). *Theory of laminar flames*, Cambridge University Press.
- Burke, M.P., Chen, Z., Ju, Y. and Dryer, F.L. (2009). *Combustion and Flame*, In press.
- Champion, M., Deshaies, B., Joulin, G. and Kinoshita, K. (1986). *Combustion and Flame* **65**: 319-337.
- Chen, Z., Burke, M.P. and Ju, Y. (2008a). *Proceedings of the Combustion Institute* **32**: Accepted.
- Chen, Z., Burke, M.P. and Ju, Y. (2008b). AIAA 2008-0977.

- Chen, Z., Burke, M.P. and Ju, Y. (2008c). SIAM: 12th International Conference on Numerical Combustion, Monterey, California, USA.
- Chen, Z. and Ju, Y. (2007). *Combustion Theory and Modelling* **11**: 427-453.
- Chen, Z. and Ju, Y. (2008). *International Journal of Heat and Mass Transfer* **51**: 6118-6125.
- Chen, Z., Qin, M., Xu, B., Ju, Y.G. and Liu, F.S. (2007a). *Proceedings of the Combustion Institute* **31**: 2693-2700.
- Chen, Z., Qin, X. and Ju, Y. (2007b). 18th International Symposium on Transport Phenomena, Daejeon, Korea.
- Chen, Z., Qin, X., Ju, Y.G., Zhao, Z.W., Chaos, M. and Dryer, F.L. (2007c). *Proceedings of the Combustion Institute* **31**: 1215-1222.
- Chung, S.H. and Law, C.K. (1988). *Combustion and Flame* **72**: 325-336.
- Clavin, P. (1985). *Progress in Energy and Combustion Science* **11**: 1-59.
- Clavin, P. (1994). *Annual Review of Fluid Mechanics* **26**: 321-352.
- Clavin, P. and Williams, F.A. (1982). *Journal of Fluid Mechanics* **116**: 251-282.
- Curran, H.J. (2005). *Private Communication*.
- Curran, H.J., Fischer, S.L. and Dryer, F.L. (2000). *International Journal of Chemical Kinetics* **32**: 741-759.
- Curran, H.J., Pitz, W.J., Westbrook, C.K., Dagaut, P., Boettner, J.C. and Cathonnet, M. (1998). *International Journal of Chemical Kinetics* **30**: 229-241.
- Darrieus, G. (1938). Communication presented at La Technique Moderne.
- Deshaias, B. and Joulin, G. (1984). *Combustion Science and Technology* **37**: 99-116.
- Dowdy, D.R., Smith, D.B., Taylor, S.C. and Williams, A. (1990). *Proceedings of the Combustion Institute* **23**: 325-332.
- Egolfopoulos, F.N., Cho, P. and Law, C.K. (1989). *Combustion and Flame* **76**: 375-391.
- Ekici, O., Ezekoye, O.A., Hall, M.J. and Matthews, R.D. (2007). *Journal of Fluids Engineering-Transactions of the Asme* **129**: 55-65.
- Farrell, J.T., Johnston, R.J. and Androulakis, I.P. (2004). Molecular structure effects on laminar burning velocities at elevated temperature and pressure. SAE paper, 2004-01-2936.
- Fischer, S.L., Dryer, F.L. and Curran, H.J. (2000). *International Journal of Chemical Kinetics* **32**: 713-740.
- Flaherty, J.E., Frankel, M.L., Roytburd, V. and Sivashinsky, G.I. (1985). *Combustion Science and Technology* **43**: 245-257.
- Frank-Kamenetskii, D. (1955). Diffusion and heat exchange in chemical kinetics, Princeton University Press, Princeton.

- Frankel, M.L. and Sivashinsky, G.I. (1983). *Combustion Science and Technology* **31**: 131-138.
- Frankel, M.L. and Sivashinsky, G.I. (1984). *Combustion Science and Technology* **40**: 257-268.
- Freni, A. and Sibulkin, M. (1990). *Combustion Science and Technology* **73**: 395-413.
- Glassman, I. (1996). *Combustion*, 3<sup>rd</sup> edition. Academic Press.
- Gottlieb, S. and Shu, C.W. (1998). *Mathematics of Computation* **67**: 73-85.
- Groot, G.R.A., van Oijen, J.A., de Goey, L.P.H., Seshadri, K. and Peters, N. (2002). *Combustion Theory and Modelling* **6**: 675-695.
- Gu, X.J., Haq, M.Z., Lawes, M. and Woolley, R. (2000). *Combustion and Flame* **121**: 41-58.
- Guo, H., Ju, Y., Maruta, K., Niioka, T. and Liu, F. (1998). *Combustion Science and Technology* **135**: 49-64.
- Hassan, M.I., Aung, K.T. and Faeth, G.M. (1998). *Combustion and Flame* **115**: 539-550.
- He, L. and Law, C.K. (1999). On the dynamics of transition from propagating flame to stationary flame ball, AIAA 99-0325.
- He, L. (2000). *Combustion Theory and Modelling* **4**: 159-172.
- Hill, P.G. and Hung, J. (1988). *Combustion Science and Technology* **60**: 7-30.
- Hinshelwood, C.N. (1940). *The kinetics of chemical changes*, Oxford University Press, London.
- Huang, Y., Sung, C.J. and Eng, J.A. (2004). *Combustion and Flame* **139**: 239-251.
- Huzayyin, A.S., Moneib, H.A., Shehatta, M.S. and Attia, A.M.A. (2008). *Fuel* **87**: 39-57.
- Ishizuka, S. (1993). *Progress in Energy and Combustion Science* **19**: 187-226.
- Jomaas, G. (2008). Propagation and stability of expanding spherical flames, Princeton University. **Ph.D. Thesis**.
- Joulin, G. (1985). *Combustion Science and Technology* **43**: 99-113.
- Joulin, G. and Clavin, P. (1979). *Combustion and Flame* **35**: 139-153.
- Joulin, G. and Deshaies, B. (1986). *Combustion Science and Technology* **47**: 299-315.
- Joulin, G. and Mitani, T. (1981). *Combustion and Flame* **40**: 235-246.
- Ju, Y., Maruta, K. and Niioka, T. (2001). *Applied Mechanical Review* **54**: 257-277.
- Ju, Y., Masuya, G., Liu, F., Hattori, Y. and Riechelmann, D. (2000). *International Journal of Heat and Mass Transfer* **43**: 231-239.
- Ju, Y., Masuya, G. and Ronney, P.D. (1998). *Proceedings of the Combustion Institute* **27**: 2619-2626.
- Ju, Y.G., Guo, H.S., Liu, F.S. and Maruta, K. (1999a). *Journal of Fluid Mechanics* **379**: 165-190.

- Ju, Y.G., Guo, H.S., Maruta, K. and Liu, F.S. (1997). *Journal of Fluid Mechanics* **342**: 315-334.
- Ju, Y.G., Matsumi, H., Takita, K. and Masuya, G. (1999b). *Combustion and Flame* **116**: 580-592.
- Karlovitz, B., Denniston Jr., D.W., Knapschaefer, D.H. and Wells, F.E. (1953). *Proceedings of the Combustion Institute* **4**: 613-620.
- Kee, R.J., Grcar, J.F., Smooke, M.D. and Miller, J.A. (1985). A FORTRAN program for modeling steady laminar one-dimensional premixed flames, Sandia National Laboratory Report SAND85-8240.
- Kee, R.J., Rupley, F.M. and Miller, J.A. (1989). CHEMKIN-II: A FORTRAN package for the analysis of gas-phase chemical kinetics, Sandia National Laboratory Report SAND89-8009B.
- Kelley, A.P., Jomaas, G. and Law, C.K. (2008). AIAA 2008-1054.
- Kelly, A.P. and Law, C.K. (2007). Fall technical meeting: Eastern states sections of the combustion institute, Virginia, Paper B-11.
- Kim, T.K., Menart, J.A. and Lee, H.S. (1991). *Journal of Heat Transfer-Transactions of the Asme* **113**: 946-952.
- Kobayashi, H. and Kitano, M. (1989). *Combustion and Flame* **76**: 285-295.
- Kobayashi, H. and Kitano, M. (1993). *Combustion Science and Technology* **89**: 253-263.
- Kwon, S., Tseng, L.K. and Faeth, G.M. (1992). *Combustion and Flame* **90**: 230-246.
- Landau, L. (1944). *Acta Physicochimica Urss* **19**: 77-85.
- Law, C.K. (2006). *Combustion physics*, Cambridge University Press.
- Law, C.K., Sung, C.J., Wang, H. and Lu, T.F. (2003). *AIAA Journal* **41**: 1629-1646.
- Levy, A. and Weinberg, F.J. (1959). *Proceedings of the Combustion Institute* **7**: 296-303.
- Lewis, B. and Von Elbe, G. (1961). *Combustion flames and explosive of gases*, Academic Press, New York.
- Li, J., Zhao, Z.W., Kazakov, A. and Dryer, F.L. (2004). *International Journal of Chemical Kinetics* **36**: 566-575.
- Liu, F., Gulder, O.L., Smallwood, G.J. and Ju, Y. (1998). *International Journal of Heat and Mass Transfer* **41**: 2227-2236.
- Lozinski, D., Buckmaster, J. and Ronney, P. (1994). *Combustion and Flame* **97**: 301-316.
- Lutz, A.E., Kee, R.J. and Miller, J.A. (1987). SENKIN: A FORTRAN program for predicting homogeneous gas phase chemical kinetics with sensitivity analysis, Sandia National Laboratory Report SAND87-8248.
- Maas, U. and Warnatz, J. (1988). *Combustion and Flame* **74**: 53-69.
- Markstein, G.H. (1951). *Journal of the Aeronautical Sciences* **18**: 199-209.
- Markstein, G.H. (1964). *Nonsteady flame propagation*, Pergamon Press.

- Maruta, K., Yoshida, M., Ju, Y. and Niioka, T. (1996). *Proceedings of the Combustion Institute* **26**: 1283-1289.
- Matalon, M. (1983). *Combustion Science and Technology* **31**: 169-181.
- Matthews, M.T., Dlugogorski, B.Z. and Kennedy, E.M. (2006). *Combustion and Flame* **144**: 838-849.
- Metghalchi, M. and Keck, J.C. (1980). *Combustion and Flame* **38**: 143-154.
- Mitani, T. (1980). *Combustion Science and Technology* **23**: 93-101.
- Mosbacher, D.M., Wehrmeyer, J.A., Pitz, R.W., Sung, C.J. and Byrd, J.L. (2003). *Proceedings of the Combustion Institute* **29**: 1479-1486.
- Müller, S. (2000). Adaptive multiscale schemes for conservation laws, Springer.
- Nishioka, M., Inagaki, K., Ishizuka, S. and Takeno, T. (1991). *Combustion and Flame* **86**: 90-100.
- Nishioka, M., Takeno, T. and Ishizuka, S. (1988). *Combustion and Flame* **73**: 287-301.
- Parsinejad, F., Arcari, C. and Metghalchi, H. (2006). *Combustion Science and Technology* **178**: 975-1000.
- Peters, N. (2000). Turbulent combustion. New York, Cambridge University Press.
- Piessens, R., Doncker-Kapenger, E., Ueberhuber, C. and Kahaner, D. (1983). QUADPACK, a subroutine package for automatic integration, Springer Verlag.
- Poinsot, T. and Veynante, D. (2005). Theoretical and numerical combustion, R.T. Edwards, Inc.
- Qin, X. and Ju, Y.G. (2005). *Proceedings of the Combustion Institute* **30**: 233-240.
- Rallis, C.J. and Garforth, A.M. (1980). *Progress in Energy and Combustion Science* **6**: 303-329.
- Ronney, P.D. (1985). *Combustion and Flame* **62**: 121-133.
- Ronney, P.D. (1988). *Proceedings of the Combustion Institute* **22**: 1615-1623.
- Ronney, P.D. (1990). *Combustion and Flame* **82**: 1-14.
- Ronney, P.D. (1994). *Optical Engineering* **33**: 510-521.
- Ronney, P.D. and Sivashinsky, G.I. (1989). *SIAM Journal on Applied Mathematics* **49**: 1029-1046.
- Ronney, P.D. and Wachman, H.Y. (1985). *Combustion and Flame* **62**: 107-119.
- Rozenchan, G., Zhu, D.L., Law, C.K. and Tse, S.D. (2003). *Proceedings of the Combustion Institute* **29**: 1461-1470.
- Ruan, J.M., Kobayashi, H., Niioka, T. and Ju, Y.G. (2001). *Combustion and Flame* **124**: 225-230.
- Saeed, K. and Stone, C.R. (2004). *Combustion and Flame* **139**: 152-166.

- Semelsberger, T.A., Borup, R.L. and Greene, H.L. (2006). *Journal of Power Sources* **156**: 497-511.
- Semenov, N.N. (1935). *Chemical kinetics and chain reactions*, Oxford University Press, London.
- Sivashinsky, G.I. (1977). *Combustion Science and Technology* **15**: 137-146.
- Sloane, T.M. and Ronney, P.D. (1993). *Combustion Science and Technology* **88**: 1-13.
- Smith, G.P., Golden, D.M., Frenklach, M., Moriarty, N.W., Eiteneer, B., Goldenberg, M., Bowman, C.T., Hanson, R.K., Song, S., Gardiner, W.C., Jr., Lissianski, V.V. and Qin, Z., [http://www.me.berkeley.edu/gri\\_mech/](http://www.me.berkeley.edu/gri_mech/).
- Sod, G.A. (1978). *Journal of Computational Physics* **27**: 1-31.
- Sohrab, S.H. and Law, C.K. (1984). *International Journal of Heat and Mass Transfer* **27**: 291-300.
- Spalding, D.B. (1957). *Proceedings of the Royal Society of London Series a-Mathematical and Physical Sciences* **240**: 83-100.
- Strang, G. (1968). *SIAM Journal on Numerical Analysis* **5**: 506-517.
- Sun, C.J. and Law, C.K. (1998). *Proceedings of the Combustion Institute* **27**: 963-970.
- Sun, C.J., Sung, C.J., He, L. and Law, C.K. (1999). *Combustion and Flame* **118**: 108-128.
- Sun, M. (1998). Numerical and experimental studies of shock wave interaction with bodies, Tohoku University. **Ph.D. Thesis**.
- Sun, M. and Takayama, K. (1999). *Journal of Computational Physics* **150**: 143-180.
- Sung, C.J. and Law, C.K. (1996). *Proceedings of the Combustion Institute* **26**: 865-873.
- Takeno, T. and Ishizuka, S. (1986). *Combustion and Flame* **64**: 83-98.
- Takeno, T., Nishioka, M. and Ishizuka, S. (1986). *Combustion and Flame* **66**: 271-283.
- Takizawa, K., Takahashi, A., Tokuhashi, K., Kondo, S. and Sekiya, A. (2005). *Combustion and Flame* **141**: 298-307.
- Taylor, S.C. (1991). Burning velocity and the influence of flame stretch, University of Leeds. **Ph.D. Thesis**.
- Thiele, M., Selle, S., Riedel, U., Warnatz, J. and Maas, U. (2000). *Proceedings of the Combustion Institute* **28**: 1177-1185.
- Thiele, M., Warnatz, J., Dreizler, A., Lindenmaier, S., Schiessl, R., Maas, U., Grant, A. and Ewart, P. (2002). *Combustion and Flame* **128**: 74-87.
- Toro, E.F. (1999). *Riemann solvers and numerical methods for fluid dynamics*, Springer.
- Tromans, P.S. and Furzeland, R.M. (1988). *Proceedings of the Combustion Institute* **21**: 1891-1897.
- Tse, S.D., Zhu, D.L. and Law, C.K. (2000). *Proceedings of the Combustion Institute* **28**: 1793-1800.

- Tseng, L.K., Ismail, M.A. and Faeth, G.M. (1993). *Combustion and Flame* **95**: 410-426.
- Tsuji, H. (1982). *Progress in Energy and Combustion Science* **8**: 93-119.
- van Leer, B. (1984). *SIAM Journal on Scientific and Statistical Computing* **5**: 1-20.
- Van maaren, A., Thung, D.S. and Degoey, L.P.H. (1994). *Combustion Science and Technology* **96**: 327-344.
- Vazquez-Espi, C. and Linan, A. (2001). *Combustion Theory and Modelling* **5**: 485-498.
- Vazquez-Espi, C. and Linan, A. (2002). *Combustion Theory and Modelling* **6**: 297-315.
- Wang, P., Wehrmeyer, J.A. and Pitz, R.W. (2006). *Combustion and Flame* **145**: 401-414.
- Williams, F.A., <http://maeweb.ucsd.edu/~combustion/>.
- Williams, F.A. (1985). *Combustion theory*, Benjamin-Cummins, Menlo Park, CA.
- Wu, M.S., Ronney, P.D., Colantonio, R.O. and Vanzandt, D.M. (1999). *Combustion and Flame* **116**: 387-397.
- Yao, M., Qin, J. and Zheng, Z. (2005). *Proceedings of the Institution of Mechanical Engineers Part D-Journal of Automobile Engineering* **219**: 1225-1236.
- Yokomori, Y., Chen, Z. and Ju, Y. (2006). AIAA 2006-0161.
- Zeldovich, Y.B., Barenblatt, G.I., Librovich, V.B. and Makhviladze, G.M. (1985). *The mathematical theory of combustion and explosions*, New York: Consultants Bureau.
- Zhao, Z., Chaos, M., Kazakov, A. and Dryer, F.L. (2008). *International Journal of Chemical Kinetics* **40**: 1-18.
- Zheng, X.L., Lu, T.F., Law, C.K., Westbrook, C.K. and Curran, H.J. (2005). *Proceedings of the Combustion Institute* **30**: 1101-1109.